NUREG/CR-6527
SAND97-1039

Final Results of the XR2-1 BWR Metallic Melt Relocation Experiment

Manuscript Completed: April 1997
Date Published: August 1997

Prepared by
R. O. Gauntt, SNL
L. L. Humphries, SAIC

Sandia National Laboratories
Albuquerque, NM 87185

Science Applications International Corporation
Albuquerque, NM 87106

Y. Chen, NRC Project Manager

Prepared for
Division of Systems Technology
Office of Nuclear Regulatory Research
U.S. Nuclear Regulatory Commission
Washington, DC 20555-0001
NRC Job Code L1468

CONTENTS

Figures

Tables

SUMMARY

The XR2-1 test was the third in a series of out-of-pile severe accident experiments conducted at Sandia National Laboratories for the Nuclear Regulatory Commission. The objective of this experiment program is to investigate the material relocation processes and relocation pathways in a dry boiling water reactor (BWR) core following a severe accident such as an unrecovered station blackout accident. The XR2 test section was prototypic in composition and in geometry and simulated the lower reactor core including ½ meter of the fuel assembly, the nose piece, the core plate, the control blade and velocity limiter, and the fuel support structure with coolant inlet nozzles. The imposed test conditions (initial thermal state and the melt generation rates) simulated the conditions for the postulated accident scenario and the prototypic design ensured that thermal masses and physical flow barriers were modeled adequately.

To simulate downward draining control blade material reaching the lower core, 20 kilogram of control blade material was fed into the upper end of the test section over a period of 1000 seconds. The feed material was delivered over a prescribed pattern over the control blade at a controlled, constant rate. Following the control blade material, 40 kg of molten zircaloy-4 was poured over the open ends of the fuel assemblies, simulating the subsequent degradation of fuel rod cladding and assembly can walls. The zircaloy material was also poured over a period of 1000 seconds and was restricted to within the assembly canisters.

The test was was instrumented with over 87 type K thermocouples, 26 type C thermocouples, and 3 optical pyrometers. A real-time X-ray imaging system was also used to record the motion of molten metals at the bottom of the fuel rods. Following the test, the entire package was x-rayed and X-ray tomography was employed to further characterize the end state of the test package.

The fuel assemblies were severely degraded during the conduct of the test, channel walls were destroyed by the aggressive eutectic action of the molten control blade material, and fuel rods were deformed and stripped of cladding. The upper 1/2 of the fuel rods showed severe degradation where many of the fuel pellets had fallen into the lower half of the fuel assembly forming regions of rubblized geometry about 1/4 m from the nose pieces. The upper 1/3 of the fuel assembly was completely absent, having collapsed into the lower test bundle.

The real-time X-ray imaging system showed flow blockages and pools forming early on in the test, but the molten material was able to break free so that molten material would drain suddenly to lower reaches of the test packages. Thermocouple responses indicate very large-scale and sudden melt relocation events leading to material relocating to regions beneath the core plate.

Fourty-seven kilograms, or more than 70 percent of the material available for melt (feed material and material that melted at the top of the package), was found below the core plate elevation in the inlet nozzle (~6 kg), resting on the control blade velocity limiter (~21 kg), or in the lower catch basin (~20 kg). It is believed that material drained through the assembly nose piece and out

through the inlet nozzle into the lower catch basin. In addition, material drained through the control blade guide tubes, over the control blade velocity limiter and then into the catch basin. The composition of the material in the catch basin is not known, though it is expected that both zircaloy and control blade material would be found there. Lower structures such as the core plate and fuel support piece appear to have remained intact, and downward cascading material apparently drained through existing flow paths.

The XR2-1 experiment has demonstrated the potential for molten metal relocation to the lower plenum in a BWR core through existing pathways in the lower core structures. This experiment does exhibit some of the characteristics of the "Continuous-Drainage" melt progression pathway in that important quantities of molten metal drained from the "core region". However, destruction of the core plate did not occur, and about half of the molten metals accumulated in blockages on or above the core plate region. Fuel material, rubblized by the draining metals was compacted slightly into the lower core plate region. In that the core plate remained at the end of the experiment, with accumulations of additional metal and an over burden of rubblized fuel material, the end state also bears some resemblance to the TMI-2 configuration. Had the test not been terminated when it was, protracted heating of the test section by the radiant heat from the melter assembly may have led to continued metallic draining from the core region. The current results can be further projected in time into the reactor scale regime by additional analyses. Quantitative extrapolation of the experiment results to a reactor evaluation will require the use of a tool like MERIS. The analysis would account for sustained heating from above, embedded decay heating, and the differences in radial heat transfer. Such analyses were beyond the scope of this work, but could be accomplished with minor additions to the MERIS model.

The XR2-1 experiment has shown that under the "dry core" conditions investigated, the metallic core materials that melt and drain from the upper core regions have the potential to drain from the core region entirely without the formation of robust coherent blockages in the lower core. Temporary blockages that suspended pools of molten metal were observed to form which later remelted, allowing the metals to continue draining downward. The fuel rods in the XR2-1 test showed significant damage in the form of rubblization in the uppermost part of the test bundle, however, X-ray examination revealed that distorted, but rod-like, structure was still retained in the lower part of the test bundle. The lower core plate structure in the test bundle remained intact at the conclusion of the test, however, it should be emphasized that failure of the core plate during the test was not expected.

The ultimate fate of the core plate, and the overlying ceramic fuel materials with respect to the transfer of materials to the lower vessel depends on the thermal and mechanical response of the lower core, core plate, and control blade drive tubes. The XR2-1 test provides the initial conditions for these subsequent events, which may be explored by analytical synthesis. The MERIS code is one analytical tool that may be useful in this regard, but other models for structural response must also be applied. If the weight of the core is distributed uniformly over the underlying structures, including the lower core plate, analyses have indicated that the lower core plate structure can be expected to fail under the thermal and mechanical loads from the overlying core materials. Structural response analyses should, however consider the possible effects of fusing of the core plate to the drive tubes by the refrozen metallic melts, and the extent to which the core weight load is distributed over the core plate and the drive tubes. In the event

that the core plate fails, then providing the overlying core materials behave in a fluid-like manner, the failure of the core plate could result in the ceramic core materials "draining" to the lower plenum and coming to rest on top of the previously relocated metallic materials. This "draining" of the fuel material could be impeded, however, if the fuel materials are not sufficiently "rubblized" to negotiate the open spaces between and within the control blade guide tubes. In this case, the support capacity of the drive tubes must be considered. Finally, it must also be kept in mind that the XR2-1 test investigated a single typical thermal state of the lower core region by using an axial thermal gradient of ~2000 K/m. Differing thermal conditions could influence these results.

ACKNOWLEDGEMENTS

The inception, design, fabrication, assembly, conduct and analysis of the XR2-1 test described in this report is attributed to the combined efforts of more than a few talented and dedicated individuals. Those individuals are recognized in the following along with a general description of their contributions.

Robert W. Wright: Dr. Wright was the NRC technical manager for the Ex-Reactor Project up until his retirement in 1995, only months before the conduct of the XR2-1 test. Dr. Wright provided strong technical guidance to this project since its inception,

Yi-shung Chen: The NRC technical manager for the Ex-Reactor Project since 1995,

Randall O. Gauntt: Ex-Reactor project leader responsible for the test objectives, design of overall testing approach, and management of project,

Larry L. Humphries: Analytical support, heat transfer analyses, MERIS analysis, and lead author of final report,

John Bentz: Test installation, data systems and systems development,

Randy Chambers: Preparation of mechanical drawings for fabrication and assembly,

John Garcia: Facility manager and lead assembly technician for the XR2-1 test section,

Chuck Hanks: Data system programming, data acquisition, and operation of power systems,

Paul Helmick: Project engineer contributing to the design, fabrication and assembly of the Ex-Reactor testing systems and task scheduling,

Rodney C. Schmidt: Responsible for MERIS code development,

Richard Simpson: Video systems and test installation, zircaloy pre-oxidation studies,

Weldon Teague: Facility modifications and test installation,

Doug Trump: Assistant in test section assembly and test installation,

John Murray and Kyle Thompson: real time radiography systems

Larry Ott and Fred Griffen (ORNL): Analytical support in determining test conditions,

Siegfrid Hagen and Peter Hoffman (FZK Karlsruhe): providing advise and recommendations on materials behaviors,

Kenneth O. Reil: Manager of Reactor Safety Experiments Department providing experience and guidance to the team.

Final Results of the XR2-1 BWR Metallic Melt Relocation Experiment

1. INTRODUCTION

1.1 Background

The Ex-Reactor (XR) experiments were conducted at Sandia National Laboratories to aid in the resolution of a major uncertainty in the core melt progression process associated with a severe accident in a boiling water reactor (BWR), where loss of reactor core coolant inventory has occurred. Specifically, the class of accidents of concern are those that involve core melting under dry core conditions, such as an unrecovered station blackout accident with manual vessel depressurization.[1] In these accidents, a manual vessel depressurization is expected to be carried out by the plant operators when the core water level drops to ~35 percent below the top of the core. This procedure is intended to cool down the reactor core before the onset of severe fuel damage from oxidation and over-temperature conditions by making use of the steam blowdown cooling effect, and to permit the activation of any potentially available low pressure coolant injection systems. After vessel depressurization, the water level in the vessel is expected to be below the lower core plate, but above the jet pump intake nozzles. The procedure also delays severe damage to the core by about a half hour, assuming that reintroduction of water into the core does not subsequently occur. In the event that core cooling is not regained, the severe core damage processes resulting from the continued core heatup will take place under "dry core" conditions because of the low water level in the reactor vessel, with very low steam flow through the core.

Without vessel depressurization, "wet core" conditions would exist, with the lower core generating large amounts of steam from the boiling coolant present. Wet core conditions were present in the Three Mile Island, Unit 2 (TMI-2) accident, which, as a result of subsequent core melt progression processes, are believed (in general) to lead to a blocked core configuration with the formation of a growing molten ceramic fuel pool. The water in the lower core causes relocating molten core materials to freeze, forming a dense crust. Subsequent melt collects upon the crust blockage until a molten pool forms. Later, as the pool growth reaches a boundary of the core, the contents of the molten pool (principally molten ceramic fuel) will be released and relocation to the lower vessel head follows, as occurred in the TMI-2 accident. The blocked core "TMI-like" melt progression scenario is illustrated in Figure 1-1.

In the case of the BWR "dry core" melt progression scenario, it is not clear that the blocked core

molten pool configuration discussed above will result, since the heat sink associated with water in the lower core is not present. An alternative "continuous drainage" melt progression pathway has been proposed for these dry-core conditions, which does not lead to the formation of a large in-core molten ceramic pool, but instead, follows a continuous drainage behavior, where molten material drains from the core region without the formation of any stable crusts or blockages. This alternative melt progression pathway is also illustrated in Figure 1-1, and can be seen to lead to very different melt relocation behavior and different vessel head loading conditions. The TMI-like blocked core pathway results in a sudden relocation of ~3000 K molten ceramic fuel material, which subsequently comes into contact with the lower vessel head. The alternative continuous drainage pathway results in the gradual and continuous drainage of materials from the core region, first the lower melting point metallic core materials (control blades and zircaloy materials), and later solid or molten ceramic fuel materials. In this case, the metallic materials will collect on the lower head, followed later by overlying ceramic fuel materials. These two melt progression pathways lead to important differences in the timing and mode of vessel failure, in addition to differences in the rate, temperature and composition of those materials that are ultimately released into the containment environment. Therefore, it is important to understand which melt progression scenario will result from each set of conditions, so that the consequences of these two different pathways can be assessed.

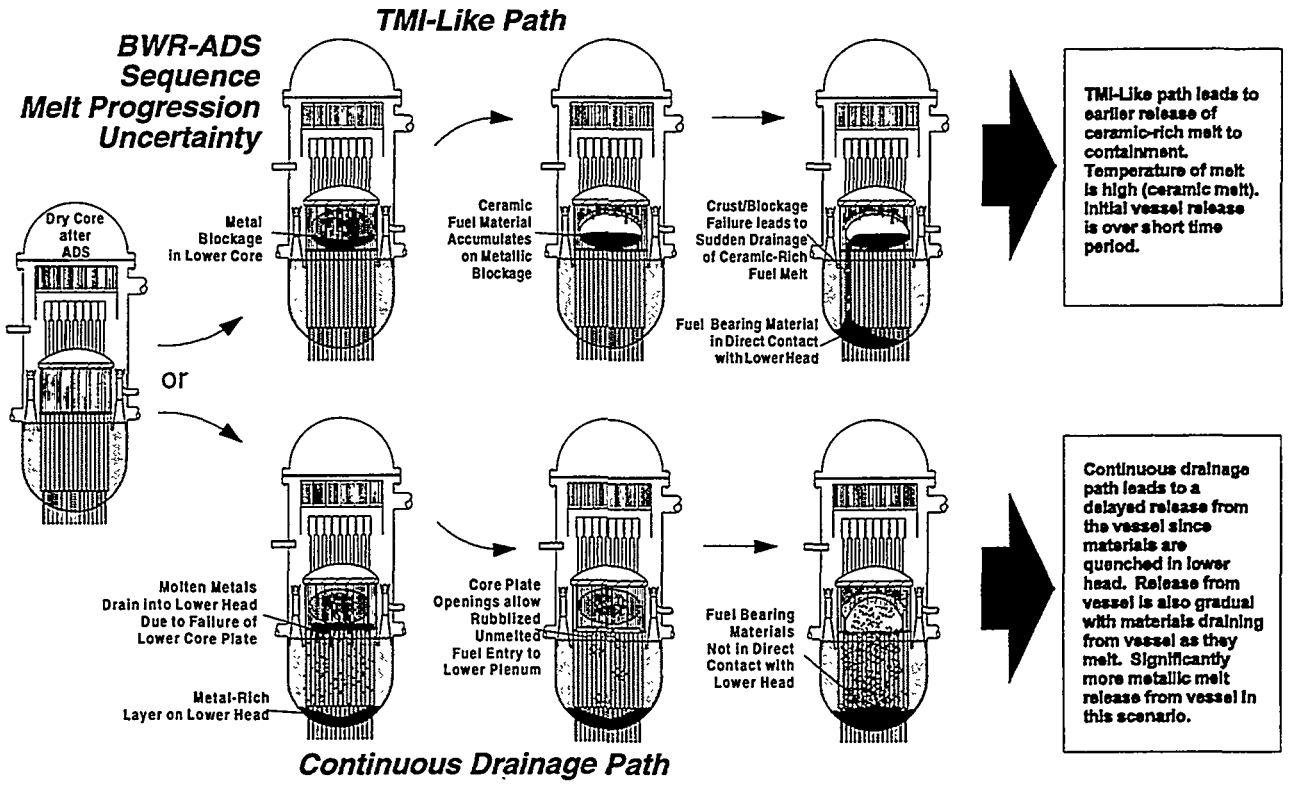

Figure 1-1. Illustration of the melt progression branchpoint uncertainty for "dry core" and "wet core" scenarios.

Complicating the analytical assessment of these pathways is the complexity of the BWR lower core geometry, which is composed of fuel canisters with rods, control blades, and inter-canister gaps, as well as lower canister nosepieces, control rod drive tubes, the lower core plate structure, and numerous flow pathways. These geometrical complexities are illustrated in Figure 1-2. These complexities, together with uncertainties concerning material eutectic interactions (Zr-Fe for example), stability of core structures during melt relocation, and the freezing and blockage behavior of relocating metallic melts has prompted an experimental, and companion analytical program to address this melt progression issue. The Ex-Reactor experiments were intended to provide the experimental evidence necessary to develop and assess predictive models for this phase of the melt progression process, which are required to resolve the uncertainty in this crucial melt progression pathway branchpoint.

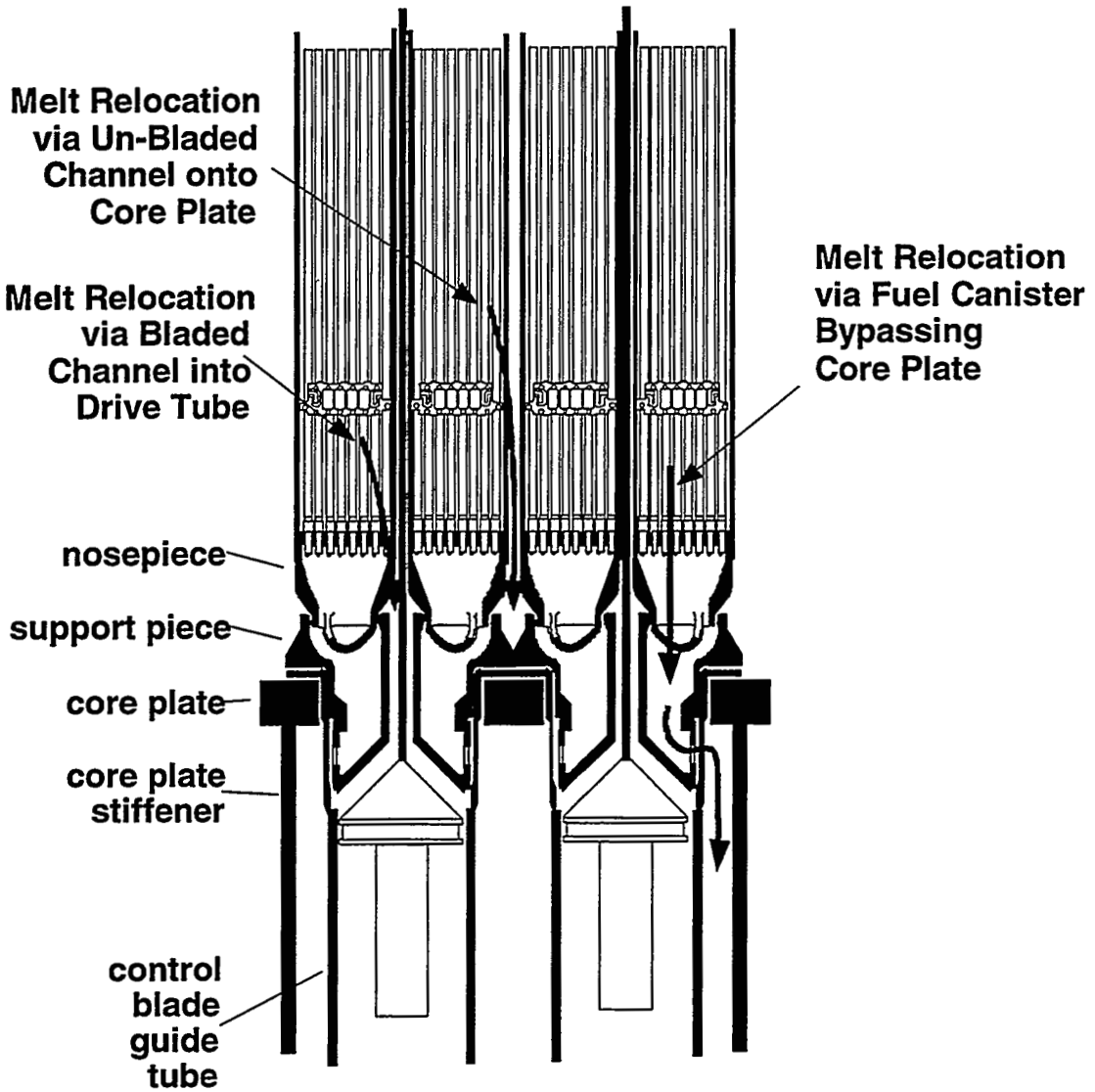

Figure 1-2. Diagram of the complex lower core structure in the BWR.

1.2 The XR Experiment Program

In order to determine the conditions under which BWR dry core melt progression will follow either the "blocked core, TMI-like" path, or alternatively, the continuous drainage pathway, a series of experiments were designed to characterize the behavior of the draining metallic core materials in the geometry of the BWR lower core region. If the molten metallic core materials form stable blockage configurations in the lower BWR core region under dry core conditions, then it is considered likely that the TMI-like melt progression pathway, involving the formation of a ceramic fuel melt pool, will also apply to BWRs. However, under typical dry-core conditions, there is only marginally sufficient thermal heat sink available to freeze the relocating stainless steel control blade melt and the subsequent relocating zircaloy channel box and cladding materials. This, together with the complex BWR lower core geometry, with many possible melt drainage pathways (Figure 1-2) and many potential material interaction effects, would suggest that stable blockages might not form, and that the continuous drainage melt progression pathway might be favored.

The formation of eutectic material compositions can greatly effect the extent to which molten material is able to relocate through the lower core structures. It is known that B_4C and stainless steel react to form a eutectic with melting point below both steel and B_4C. Studies[2] have shown that the solidus for such a eutectic may be as low as 1473 K. This is much lower than the melting point for either steel or B_4C, i.e., ~1700 K and 2725 K, respectively. Furthermore, there is a eutectic reaction between the iron and the zircaloy metals resulting in a eutectic with melting point as low as 1600 K for an iron rich system and 1200 K for a zirconium rich system (see the phase diagram in Appendix C). Again, the eutectic melting point is below the melting points of either component (the melting point of zircaloy is 2100 K). Material interactions of this type can lead to the erosion of channel box walls and fuel rod cladding at temperatures below the melting point of zircaloy. The reaction between zircaloy melt (draining from melting channel boxes and fuel rod cladding high in the core) and resolidified control blade material that forms blockages in the lower core (the control blade material higher in the core melts before the zircaloy) may also result in the opening of those early blockages and further promote the downward draining of materials.

The general approach taken in the Ex-Reactor experiments is to simulate the bottom of the BWR core geometry in full scale, using prototypic materials, at the time that the molten metallic core materials are beginning to drain from the upper regions of the core into the lowermost regions. The full scale, prototypic nature of these experiments eliminates the uncertainties that would be present in a scaled down experiment, and the results observed should be representative of what would be expected in a BWR under these accident conditions.

The fuel rod cladding surfaces and the zircaloy-4 fuel canister walls were oxidized in steam to form a 20 to 40 micrometer thick oxide layer to simulate conditions present in an operating BWR core. A primary variable in the proposed XR test series was the axial thermal gradient, which was proposed to range from 1000 to 2000 K/m. The total temperature difference over the test bundle length is 1000 K, ranging from 600 K at the bottom to 1600 K at the top. A 0.5-m test

bundle length was required to achieve the proposed ~2000K/m gradient. A test investigating 1000 K/m would employ a nominal 1-m test bundle.

The Ex-reactor program consisted of two series of experiments designed to accomplish the goals set out above. The first series of experiments, XR1[3], simply modeled the control blade, the control blade melt material, and the channel box walls. This series investigated both 1000 and 2000 K/m temperature gradients by utilizing a 106-cm and a 53-cm test section in the XR1-1 and XR1-2 tests respectively. These experiments were intended to provide some initial insight into the interaction of the molten control blade material with the channel box walls and to assist in the development of the technology needed in designing the more complicated XR2 experiments. The XR2 experiment more fully modeled the geometry at the bottom of the BWR core by adding fuel rods, the core plate, the nose piece, the velocity limiter, and the fuel support structure.

Figure 1-3 shows a cross sectional view of the two test section designs used in these experiments. In the view at left, a simple channel design used in the XR1 tests is shown where only the fuel canister walls (channel box) and the control blade features are included. The view at right shows the cross section for the more prototypic geometry XR2 tests, which include arrays ofzircaloy-clad fuel rods in addition to the channel box and control blade structures. The lateral scale of the XR2 test section is designed to represent all of the lateral degrees of freedom with respect to the draining of molten materials, and was selected based on symmetry principles (the XR2 test section is approximately a 1/8 symmetric section extracted from the 4-canister repeating array of the BWR core).

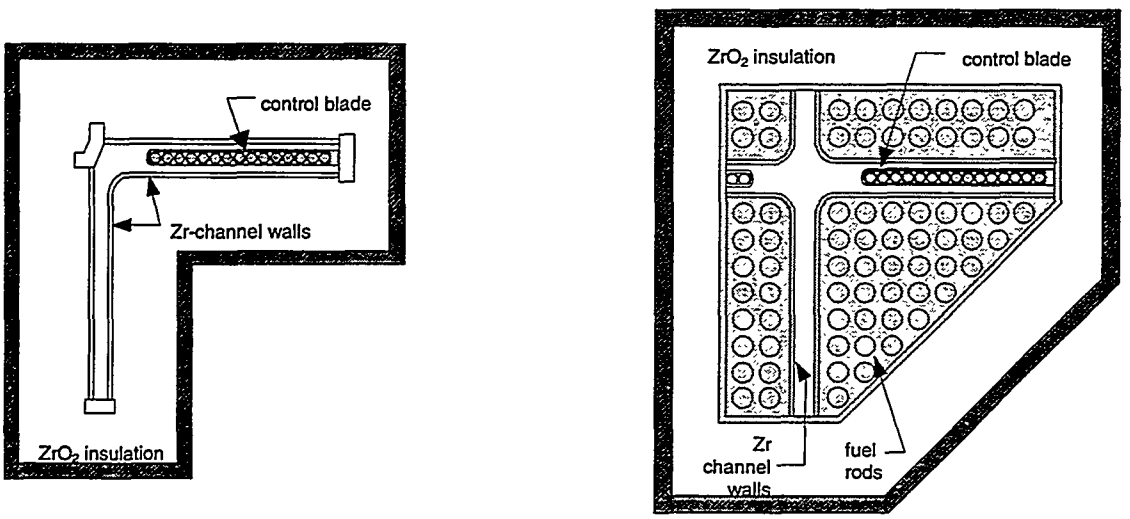

a) XR1 test section

b) XR2 test section

Figure 1-3. Cross-sectional views of test bundles for the XR1 and XR2 tests.

To achieve the required temperature gradient the test section is heated at its top by the radiant cavity melter above. A smooth axial temperature profile is achieved by imposing a downward flow of Ar gas which convects heat down into the test section. The internal decay heating of the lower fueled region was neglected in this experiment.

The tests were conducted by pouring molten metallic materials (molten steel and B_4C from control blades and molten zircaloy from fuel rod cladding and channel boxes) into the upper, open end of the heated test section, thereby simulating the melting and draining of the upper core metallic materials down through the overheating reactor. The melt pour was accomplished by feeding wire feedstock into a hot radiant melter system where it melted and then dripped onto the test section below. The test sections were pre-heated in order to impose a prototypic axial thermal gradient over the length of the test section. The objective was to characterize the nature of any blockages that were formed as the melt enters the test geometry, and to provide information on melt drainage pathways through the lower core region.

1.3 Summary of the Report

Section 2 of this report describes the design of the XR2 experiment components: the test facility, the wire feed system, the radiant cavity melter, the test package and the type and location of thermocouples and other instrumentation. It also discusses the test conditions imposed on the test package. It should be emphasised that this experiment used full scale, prototypic geometries and prototypic materials and test conditions that are representative of a BWR under the presumed accident conditions.

Section 3 presents the chronology of the test as well as the test results. It discusses the pre-heat of the test package to the desired initial conditions, the delivery of the stainless steel/B_4C composite material, and the subsequent delivery of molten zircaloy. It points out indications during the test of molten material transfer and blockage development as suggested by thermocouple responses and the real-time X-ray apparatus. Finally, it presents views of the end-state condition of the test package by photos, Xrays, and tomography as well as estimates of the volume of material found in regions below the core plate.

Section 4 discusses the MERIS model of the test and compares calculated results with measured observations. It also discusses both the strengths and weaknesses of the code in predicting the outcome of the XR2 test.

Section 5 presents a short discussion on the conclusions drawn from this test and the MERIS modeling of this test. A discussion of radiant heat transfer is presented in Appendix A. A description of an EXCEL version 5 workbook for archiving the data is attached in Appendix B. Thermal physical properties of materials used in the XR2 test are included in Appendix C. The XR2 thermocouple data are presented in Appendix D. Finally, a set of XR2 drawings are included as Appendix E.

2. THE XR2-1 EXPERIMENT DESIGN

A discussion of the XR2-1 test facility, the wire feed system, the melter system, the test section, and the imposed test conditions follows. It should be pointed out that the XR2-1 experiment required the development of two unique, never-before-tested systems which were critical to the success of the experiment: the wire delivery system and the radiant cavity melter. Both systems offered technical challenges that had to be overcome before the test could take place. The wire delivery system was required to deliver 31 spools of zirconium wire and 10 spools of steel/B_4C composite wire (a total of ≅ 2700 m of zircaloy and 1300 m of steel/B_4C composite) to the melter system at a predetermined delivery rate without the wires snagging or melting inside the wire guide tubes. If the wires melted inside the wire guides (passing through a 2400 K temperature gradient) there was a risk that the molten material would wet the tube walls and could freeze up inside the narrow tubes, blocking the wires progress before entering the melter. As for the melter system, it was required to heat the wires to beyond their melting points strictly from radiant heat transfer alone since the incoming wire could not come in close contact with the hot inner surfaces of the melter. This meant that the radiant cavity must be heated to beyond 2700 K. At these high temperatures, the design becomes constrained by severe material limitations, and the potential for overheating the test chamber becomes an important issue. Furthermore, the melter system served a dual function — besides melting feed material, it also supplied the heat source necessary to preheat the lower test section — and care had to be taken in its design and operation in order to balance these two roles.

2.1 XR2-1 Test Facility

The XR2 test package and radiant melter system were placed inside the FITS test chamber as depicted in Figure 2-1. The test chamber was filled with argon gas to provide an inert environment, to prevent test section oxidation at the required test temperatures.

The test section was instrumented with thermocouples to measure the thermal gradient prior to introducing the molten metals, and to characterize the melt flow and blockage behavior of the melt flowing into the test section. In addition to the thermocouples, a real-time X-ray imaging system provided a video image of the melt as it drained to the bottom of the test section, showing flow behavior and blockage formation. The imaging system provided a projection view looking laterally along the width of the control blade channel and axially from the bottom of the nose pieces to roughly the bottom third of the fuel assemblies. The system consisted of a 400 kiloelectronvolt (keV) X-ray head which radiated a high photon flux through the XR test package. A scintillation screen situated on the other side of the XR test section provided an image of the Xrays which penetrated the test section and reached the screen. This image was recorded using a high sensitivity video camera for subsequent post test examination.

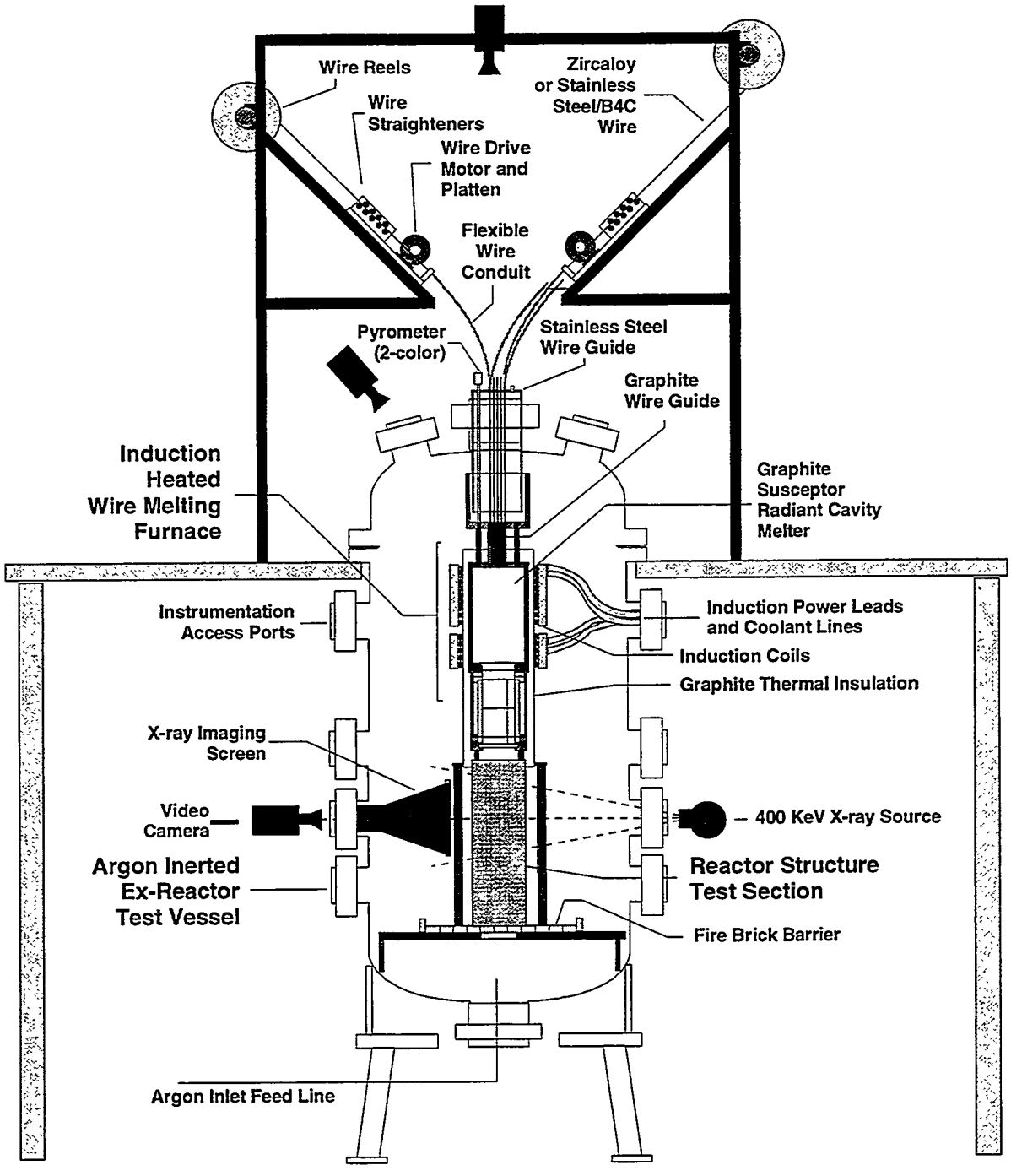

Figure 2-1. The FITS test facility with the XR2 test package, melter system, and wire feed system.

2.2 Wire Feed System

The feed material was fabricated into thin, 16 mm (.063 in) diameter wires which were fed into a hot radiant cavity where they melted and dripped onto the XR2 package assembly below. In this way, feed material could be delivered evenly over prescribed areas of the package and at a controlled delivery rate. Figure 2-2 provides the reader with a view of the top of the XR2 fuel bundle overlayed with the position and size of the wire guide tubes together with an estimate of the wire "wander" or uncertainty in the position of droplet formation based on early melter tests. Note that during the Steel/B_4C melt phase, only the 10 wire guide tubes located over the control blade region were used, the balance of those tubes were used during the zircaloy melt phase.

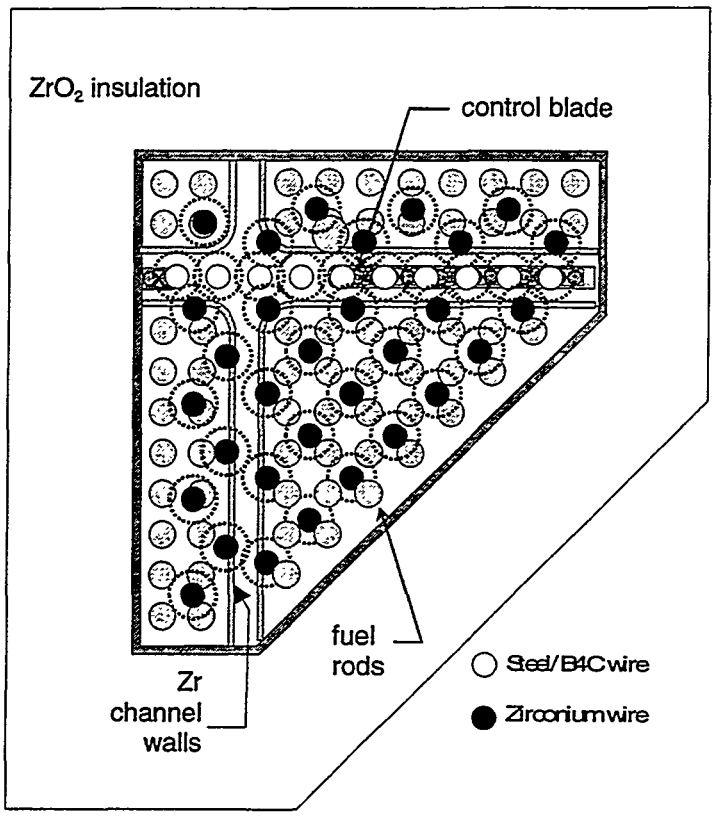

Figure 2-2. XR2 test bundle array and wire guide tube pattern.

The steel/B_4C wires were constructed of a B_4C core surrounded by a stainless steel sheath. The outer diameter of the B_4C core was 0.5 mm, resulting in a mass ratio of 43 kg stainless steel to every 1 kg B_4C.

Details of the wire feed system are depicted in Figure 2-3. Wire feed stock was pulled off reels and through a series of rollers or wire straighteners by motorized platens. The wire straighteners were capable of removing small kinks and bends in the wires to prevent

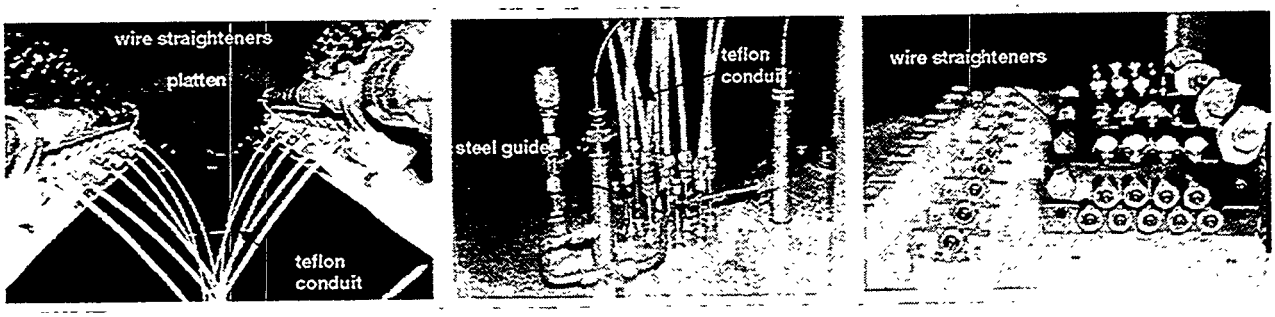

Figure 2-3. Wire feed system.

snagging as the wire was fed into the melter system. The wire delivery system was capable of feeding wire over a wide range of feed rates. Pre-experiment tests demonstrated that the system could feed wire at velocities ranging from 2.5 centimeter (cm) per second to over 15 cm per second.

Each wire was then fed through flexible teflon conduits into its own individual wire guide. The upper length of each wire guide was fabricated of stainless steel tubing. Because of the high temperatures expected at the upper surface of the melter lid, it was necessary to transition these wire-guides with 23 cm (9 inch) long, graphite stand-off tubes as shown in Figure 2-4. The wire guides served as ports into the melter system and the FITS chamber. The close tolerance between the wire and the inside diameter of the steel wire guide together with the introduction of argon purge gas at the lower ends of the steel wire guide served to prevent the contamination of the vessel by the the outer environment.

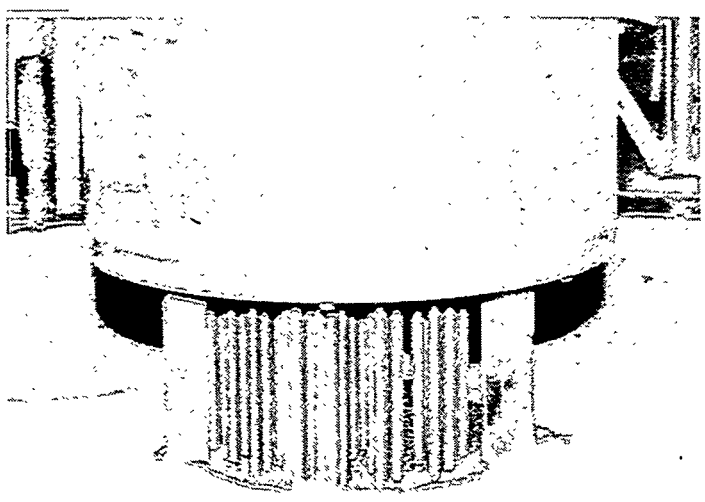

Figure 2-4. Melter stand-off tubes.

2.3 Radiant Cavity Melter System

The XR2 melter system was designed to serve two critical functions: to provide the radiant heat energy to melt the steel/B_4C composite and zircaloy feed materials, and to provide the necessary downward heat flux to preheat the XR2 package below. These two functions defined a design operating space for the melter system, i.e., the melter needed to be hot enough to ensure a complete phase transition for the feed materials, yet not so hot that the downward heat flux would exceed the desired axial profile in the package below. In addition, preliminary melter designs demonstrated that the high surface tension and chemical reactivity of molten zirconium dictated that the contact between the molten zirconium and melter structural materials should be avoided. The open cavity design that evolved is shown in Figure 2-5.

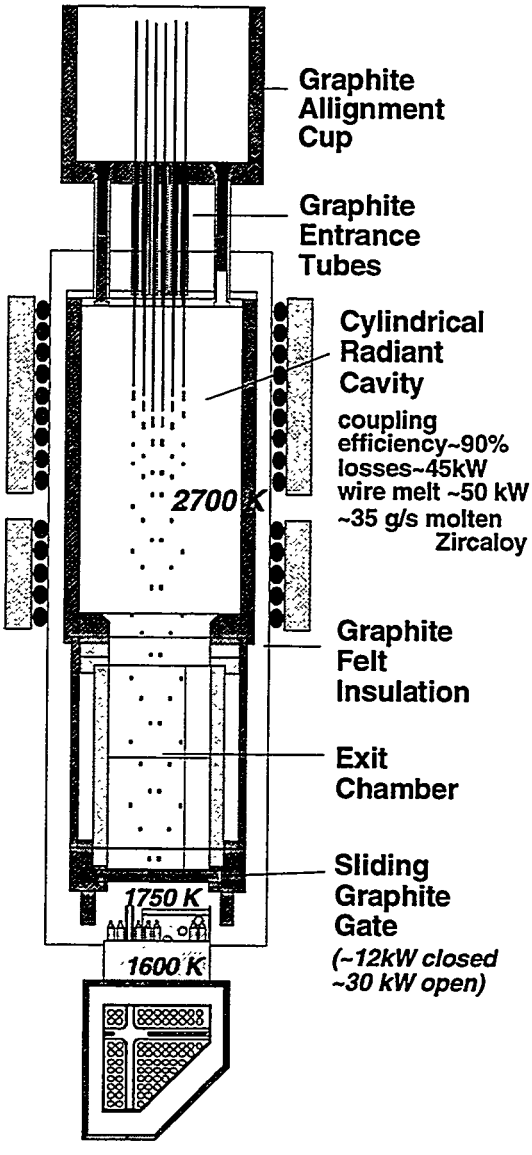

Figure 2-5. XR2 melter design.

The radiant cavity consisted of a 5.08 cm thick, 53 cm x 33 cm OD graphite cylinder which was heavily insulated and surrounded by upper and lower induction coils (see Figure 2-6). The cylinder was wrapped on all outer surfaces with more than 5.08 cm of graphite fiber insulation in order to minimize heat losses from the melter system. The power supply was capable of providing up to 250 kilowatt (kW) to the coils to bring the system up to temperature and to account for heat losses, and enthalpy input to the melt. The coupling efficiency between the coil and the graphite cylinder (the susceptor) was nearly 88 - 90 percent. The remaining 10-12 percent of the coil input power was lost in heating the induction coils and other surrounding materials. The two induction coils were cooled hydraulically in order to maintain their temperatures within a permissible operating range. Each coil could be operated independently, providing a means of tailoring the axial temperature profile in the cavity. For example, early in the preheating stage, before the melter achieves highly efficient radiant temperatures, more power was applied to the bottom coil in an attempt to flatten the temperature profile in the melter due to the large heat drain to the package below.

materials were used in the construction of other components. The control blade was

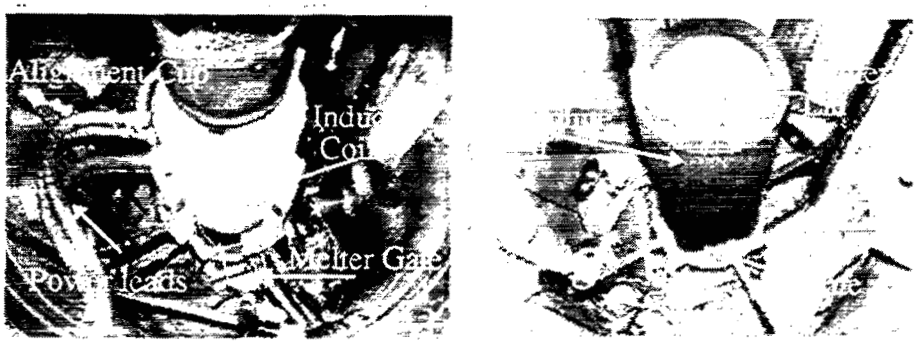

Figure 2-6. Melter coils and graphite felt insulation.

In order to bring the zirconium feed wire to its melting point of 2100 K, it is necessary to heat the melter to between 2700 K and 3000 K. At these temperatures, the radiant heat load from the melter cavity to the lower package is excessive. Two measures were incorporated into the melter design in order to minimize this problem. First, an insulated sliding gate was placed between the package and the melter cavity. This gate, which was constructed of 0.635 cm of graphite felt sandwiched between two 0.635 cm thick sheets of K-carb graphite sheets, could be closed remotely while bringing the melter and package up to the operating temperature and then opened during the melt pour (see Figure 2-7).

Figure 2-7. Melter gate assembly.

A more passive means of reducing the heat load on the lower package, was to include a long, heavily insulated exit duct between the melter cavity and the top of the melter gate assembly, effectively reducing the view factor from the melter cavity to the test package below (Figure 2-8). The exit duct was well insulated in order to minimize the heat load to the test chamber and reduce heat losses from the melter cavity. It was made as long as physically possible within the constraints of the test chamber (about 48 cm from the top of the package to the lower surface of the melter cavity bottom end piece), and the cross-sectional area of the inner opening was minimized to the test package shape. Calculations have shown that this transition region reduced the heat flux to the package by roughly 70 percent. A short discussion of radiation heat transfer methods and a means of estimating the heat flux from the cavity to the lower test package is presented in Appendix A.

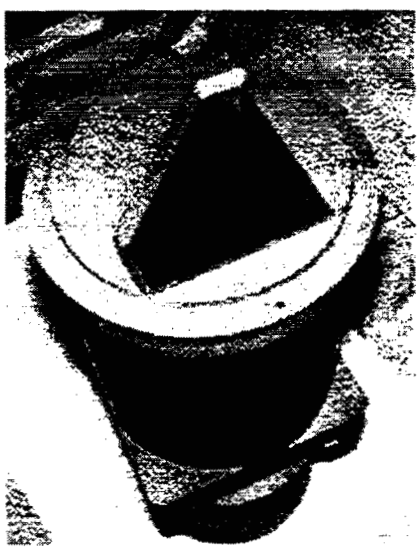

Figure 2-8. Melter exit duct region.

To further assist the downward flow of heat into the test section below, a 100 liter per minute flow of Ar gas was initiated by drawing a slight vacuum at the base of the test section. This gas flow helped to transfer heat

deeper into the test section, generating a nearly linear temperature profile in the package below.

2.4 XR2-1 Test Package

Central to the XR2 experiment was the test section, which was designed and fabricated to replicate as close as possible the lower ½ to 1 meter of an operating BWR core geometry. The design criteria of the test section is that it should be capable of accurately representing the thermal mass, material interactions, and the complicated flow paths that exist for the presupposed accident conditions. Components used in the test section were full-scale. Several of the more complicated pieces such as the nose pieces, the support pieces, the grid spacers, the core plate, and the lower control blade velocity limiter were structures that were actual components fabricated for use in a BWR core (see Figure 2-9). Also, prototypic materials were used in the construction of other components. The control blade was constructed of stainless steel with B_4C-filled tubes. Fuel rods were clad with zircaloy-2 tubing and filled with full size depleted UO_2 fuel pellets. Furthermore, the fuel rod cladding surfaces and the zircaloy-4 fuel canister walls were oxidized in steam to form a 20 to 40 μm thick oxide layer prior to assembly to accurately simulate conditions normally present in an operating BWR core. The package was then insulated with 5.08 cm of ZrO_2 fibrous insulation to minimize lateral heat losses out of the package.

2.5 XR2-1 Test Conditions

The purpose of the XR2 test was to examine the behavior of downward relocating molten metallic core materials in a dry BWR core such as might result from a short-term station blackout with depressurization. To make this test credible, it was important that the test section be subjected to the same or similar thermal conditions as might exist at the time that molten metal reaches the lower ½ to 1 m of a BWR core in such an accident scenario. These thermal conditions were determined from a best estimate calculation performed using the SCDAP/ RELAP5 code. This calculation included a detailed description of the lower region with fine axial noding and modeled both the core plate and the nose pieces, as described in Reference 1. In addition, these calculations predicted both the timing and the material melting rates for the upper-core metallic structural materials. The results of these

calculations are shown in Figure 2-10 and Figure 2-11.

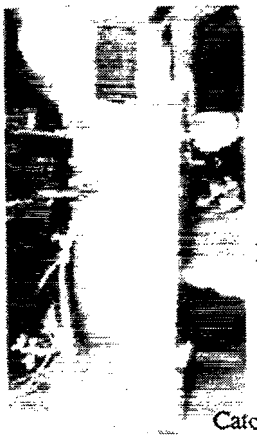

XR2-1 Package

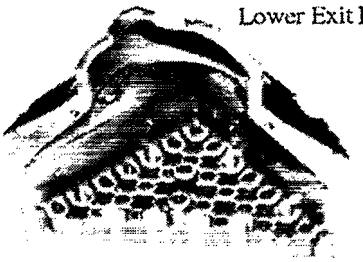

Half Nose Piece

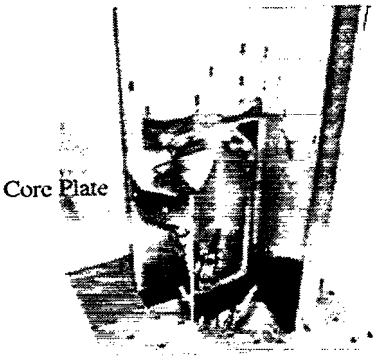

Fuel Support Piece

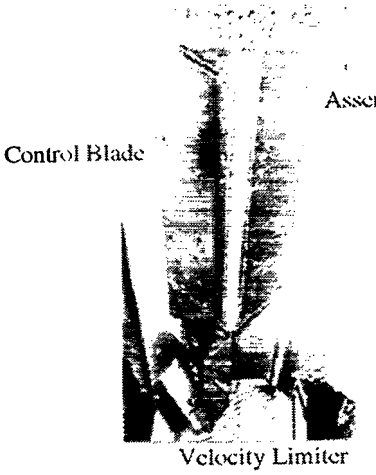

Assembly and Control Blade

Figure 2-9. XR2-1 test package.

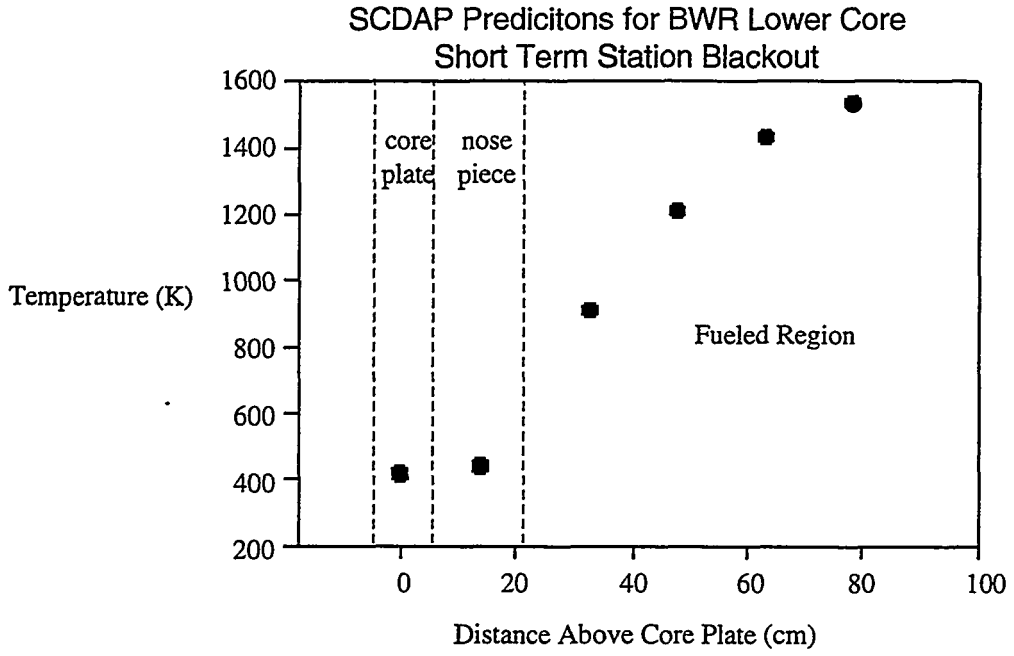

Figure 2-10. Axial thermal gradient in the lower BWR core for Dry-Core conditions (Station blackout with depressurization).

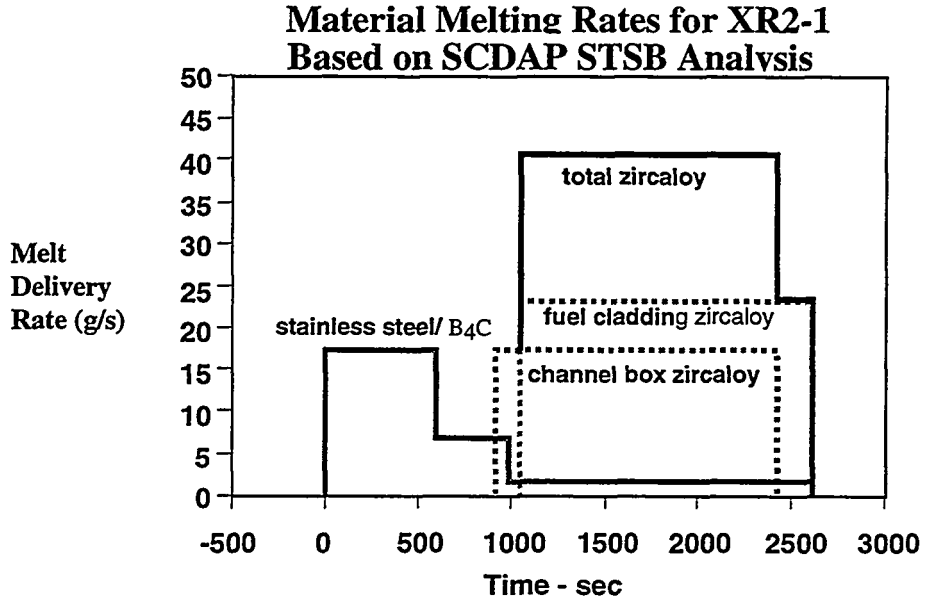

Figure 2-11. Flow rate of molten metallic materials from upper core into the lower 0.5 m, XR2 assembly cross-section.

The results of these best estimate calculations were used to prescribe conditions imposed in the XR test series. Results of this and other studies using the MELCOR code (cited by John E. Kelly of Sandia National Laboratories) indicate that the temperature gradient at the bottom of a BWR core could range from 1000 K/m to 2000 K/m depending on the control rod positioning strategy. In both studies, however, the temperature at the core plate remained at 500 K. The XR1 test series investigated both a 1000 K/m and a 2000 K/m temperature gradient. The XR1-1 test modeled the 1000 K/m gradient by using a 1-m test specimen while the XR1-2 test modeled the higher, 2000 K/m gradient using a 0.5-m test specimen. The temperature at the bottom of the test specimen was ~500 K while the upper temperature was heated to ~1500 K. The XR2 test modeled the higher, 2000 K/m temperature gradient by using a ~0.5-m test specimen. This higher thermal gradient would tend to assist the downward motion of molten material into the test specimen.

The mass of molten material calculated by the SCDAP/RELAP5 best estimate calculation was used in determining the flow rate of material to be introduced into the XR2 test. Molten control blade material was poured into the test assembly at a rate of 18 grams per second (gm/sec) for 1000 seconds followed by zircaloy at a rate of 35 gm/sec for the following 1000 seconds.

2.6 XR2 Package Instrumentation and Data

The XR2 Package was instrumented with over 87 type K thermocouples, 26 type C thermocouples, and 2 optical pyrometers. Sixty-nine thermocouples were placed in the test bundle on fuel rods, can walls, and the control blade. The balance of the thermocouples were placed on the the core plate, the fuel support pieces, the nose piece, the lower control blade, and other strategic places within the test chamber.

Figure 2-12 shows the axial layout of the XR2 test package. Thermocouples were placed at four different elevations along fuel rods, can walls, and control blades. These elevations are at equal spaced intervals along the active fuel rods. Figure 2-13 shows thermocouple locations at each elevation. Note that not every elevation has thermocouples at each thermocouple location. At core region 1 (CR1), only fuel rods 1, 3, 8, and 11 (FR1, FR3, FR8, and FR11) were instrumented with type C thermocouples. Similarly, only locations CB1 and CB4 on the control blade at core region 1 were instrumented.

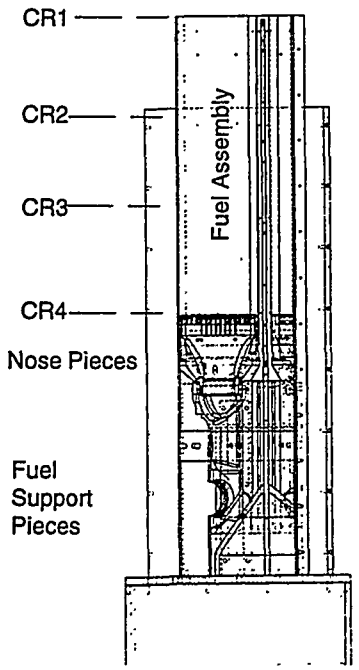

Figure 2-12. XR2 axial thermocouple locations.

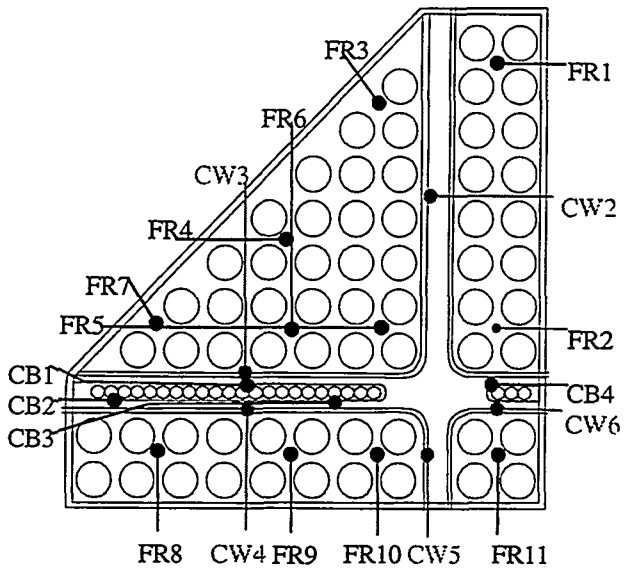

Figure 2-13. XR2 test bundle thermocouple locations.

The nose pieces at the bottom of the fuel bundles were instrumented. The half nose piece (HNP) corresponding to the half fuel assembly seen in the cross section of Figure 2-13 has three thermocouples embedded in its surface. These locations are indicated on the drawing of Figure 2-14. Each of the two quarter nose pieces (QNPA and QNPB) were instrumented with two thermocouples as shown in Figure 2-15. Likewise, thermocouple locations in the double fuel support, the single fuel support, both the upper and lower surfaces of the core plate (CPT and CPB respectively), and the lower control blade are indicated on Figure 2-16 through Figure 2-19.

In addition to both type C and type K thermocouples in the package, the XR2 test incorporated two water cooled, 2-color optical pyrometers located outside the melter. These pyrometers were arranged with view ports that allowed the measurement of temperatures at the inside surface of both the top and bottom melter end-pieces. Two type C thermocouples were placed at the end of each view port as a means of testing the pyrometer calibration. To complete the temperature characterization of the melter assembly, there were three more type C thermocouples located at the center sidewall of the radiant cavity, the midplane of the outer graphite cylinder in the exit chamber, and in the melter gate assembly.

The data was recorded about once every 30 seconds during the heat-up and cool-down phases of the experiment and about once every 3 or 4 seconds during the actual melt delivery phases. There are over 1300 data points for each of the 100 or so data channels resulting in a large

database for analysis. Plots of the thermocouple data for the XR2 test are included in Appendix D. In addition, an Excel® spreadsheet has been included to archive this data and facilitating data management. A short user's guide has also been included in Appendix B.

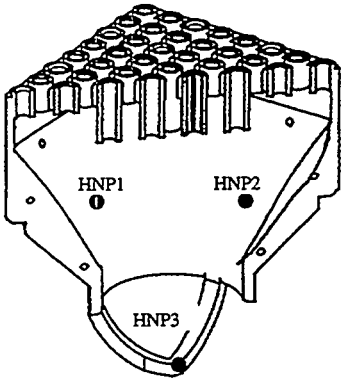

Figure 2-14. Half nose piece (HNP) thermocouple locations

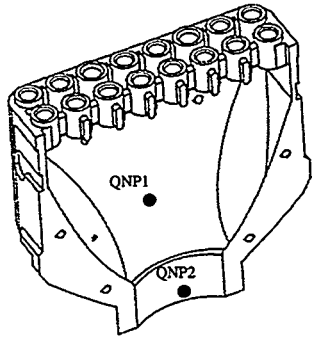

Figure 2-15. Quarter nose piece (QNP) thermocouple locations.

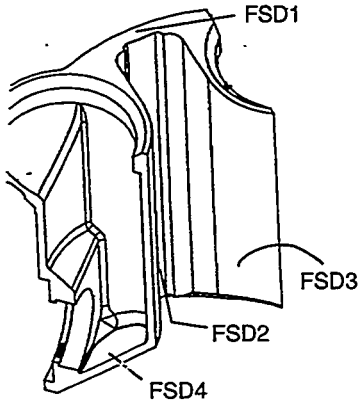

Figure 2-16. Fuel support Double (FSD) thermocouple locations.

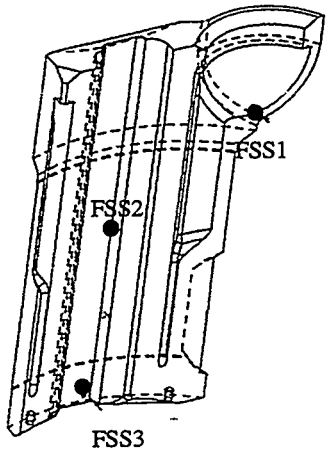

Figure 2-17. Fuel Support Single (FSS) thermocouple locations.

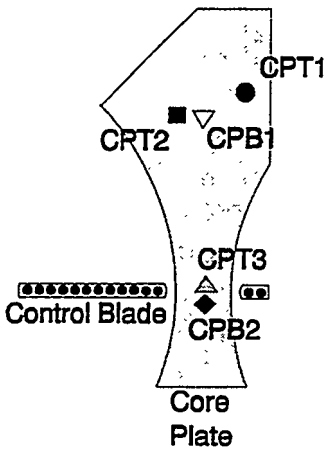

Figure 2-18. Core plate thermocouple locations.

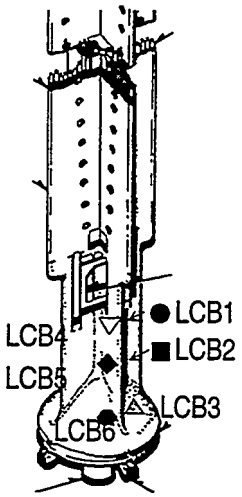

Figure 2-19. Lower control blade thermocouple locations.

3. THE XR2-1 TEST RESULTS

The XR2 experiment was conducted in the FITS test facility at Sandia National Laboratories at roughly 7:00 p.m. on October 12, 1995. The test was run at night to take advantage of the cooler ambient temperatures, improving heat rejection from the FITS test chamber. All test systems including the wire feed system, the radiant cavity melter, and the gas preheat system as well as all diagnostic systems, performed as required. There were no problems or malfunctions that were serious enough to compromise the validity of the test results.

3.1 Conduct of Test

The XR2-1 test was conducted in three stages: the melter and package preheat phase, the steel/B_4C composite melt phase, and the zircaloy melt phase (see Table 3-1). Details of these three test stages are presented in the following three sections. Prior to heating the XR2 package and melter assembly, the test chamber was evacuated and filled with argon gas to provide an inert environment. The melter and package were brought up to the desired temperature at which time the lower gate was opened and steel/B_4C composite wire was fed into the melter cavity. The steel/B_4C composite melt was fed at the rate of 18.0 gm/sec for 1000 seconds for a total of 18 kg of wire (see

Figure 3-1). At that time, the zircaloy wire was delivered to the test section at a rate of 35 gm/sec for 1000 seconds, for a total of 35 kg of zircaloy wire. The test was then terminated, the melter gate was closed, and power to the coils was shut off.

Table 3-1.XR2-1 test conduct.

Event	Time (hr)	Time (seconds)
Initialize data recording	0	0
Stage 1: Begin package preheat, melter at 1700 K	1:50	6600
Package preheat accomplished	3:34	12840
Close melter gate and heat melter to operating temperature	3:42	13320
Melter reaches operating temperature of 2650 K	4:45	17100
Stage 2: Open melter gate and start feeding stainless steel wire	4:46	17213
Stage 3: Terminate stainless steel feed and initiate Zr feed	5:03	18212
Terminate zircaloy wire feed and close melter gate	5:19	19158
Shut down melter power, continue logging data	5:20	19200

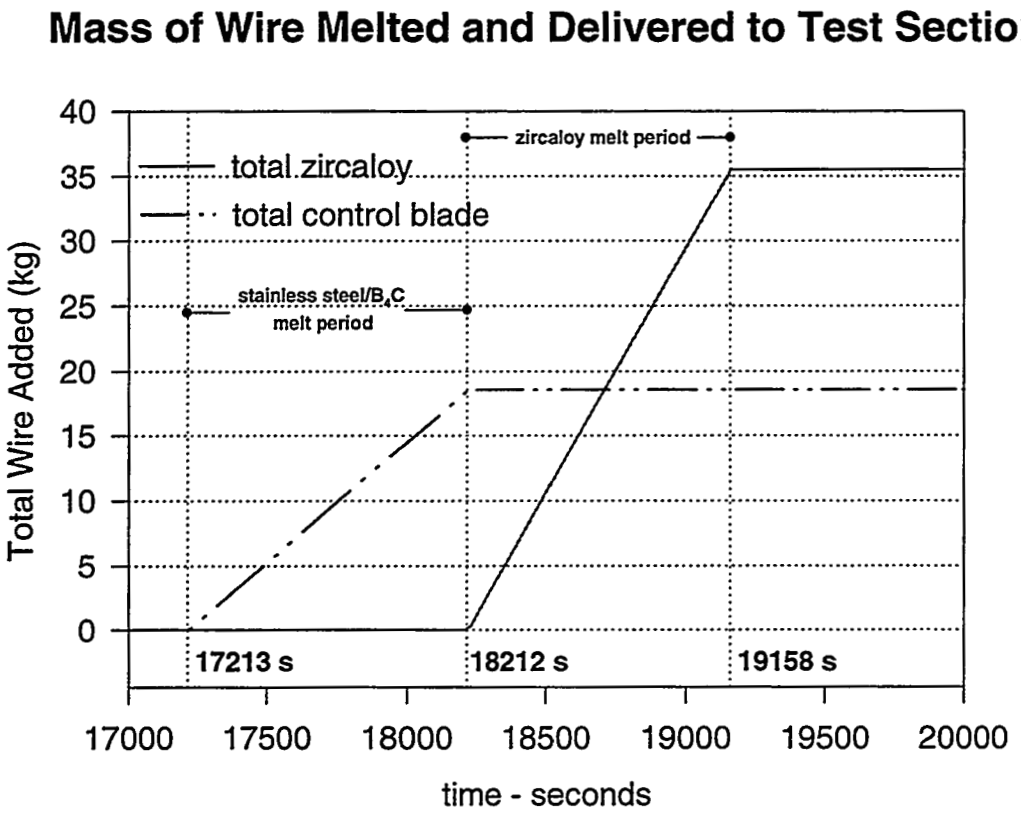

Figure 3-1. Feedstock material melted and delivered to XR2 test package.

3.2 Melter and Package Preheat

The first stage of the XR2 test, the melter and package preheat, was by far the longest, requiring 17,153 seconds or 4 hours and 45 minutes. This involved bringing the melter cavity up to a design temperature that was determined to be high enough to assure that radiant heat transfer from the cavity to the wire was sufficient to completely melt the wire. The cavity temperature was carefully chosen in order to impose the necessary downward heat flux to the XR2 package to obtain the desired initial temperature gradient in the package. Figure 3-2 shows the power input to the melter and the melter temperatures. With the lower gate closed, the melter was heated to 1700 K. At 6600 seconds the gate was opened and the melter temperature was maintained for over an hour. This was done in order to bring the lower package up to temperature while the melter was still at a reasonably low temperature, thereby minimizing the heat load to the test chamber. Once the package was pre-heated, the insulated gate was closed and the melter was heated to its operational temperature of about 2700 K. Preliminary calculations predicted that if the melter cavity were heated to 2700 K, the top of the XR2 package would reach the target temperature of about 1600 K. The bottom of the package was electrically heated to about 600 K. In addition, when the melter was heated to 1700 K and the gate was opened, a 100 liter/minute (lpm) flow of argon gas was established downward through the XR2 package to assist in heat transport to the lower reaches of the test bundle. The gas flow was capable of smoothing out the axial temperature profile in the package (as shown in Figure 3-3) providing a nearly linear axial profile from 600 K at the bottom to 1600 K at the package top. Just before the gate was opened, the temperature at the bottom of the insulated lower gate was 1750 K and there were only ≈ 5 kW

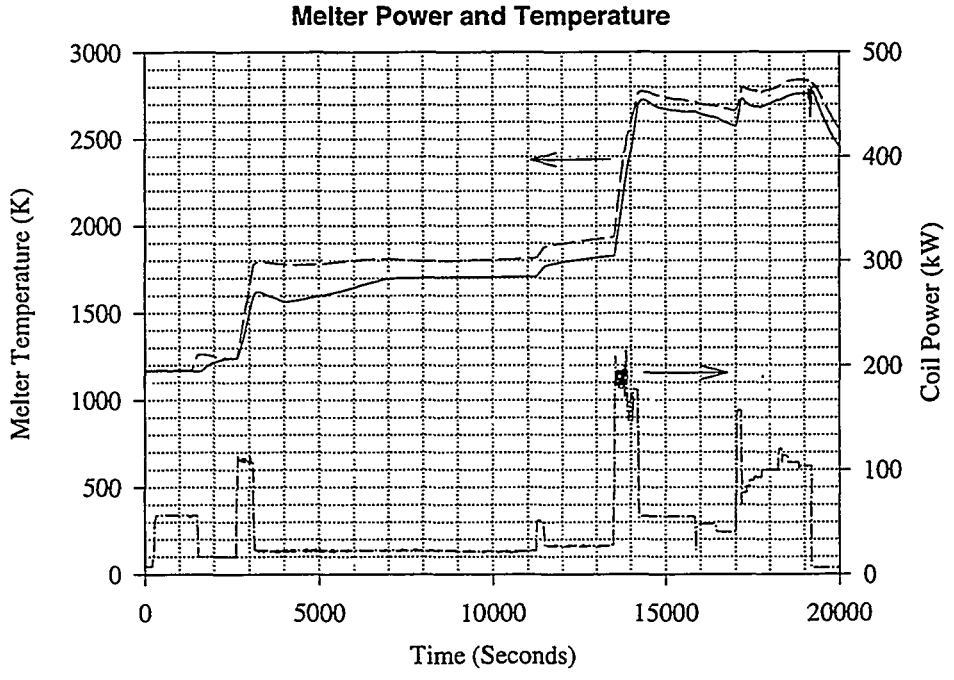

Figure 3-2. Coil power and melter temperatures during heat-up phase.

of heat conducted out through the XR2-1 package. When the gate was opened and the wire drive system was started to allow the introduction of molten material into the package, the radiant heat flux shining onto the package increased to nearly 20 kW. The temperature at the top of the package correspondingly rose until the diminishing radiant heat flux balanced the heat conducted out through the package. Calculations showed that within 10 minutes of opening the gate, temperatures at the top of the package would exceed the zircaloy melting point.

Thermally, the XR-2 melter system behaved as expected. At a cavity temperature of 2700 K, the predicted energy requirement of 45 kW agreed very well with the actual required energy input of 41 kW (see Table 3-2). In addition, calculated temperatures closely matched actual thermocouple measurements.

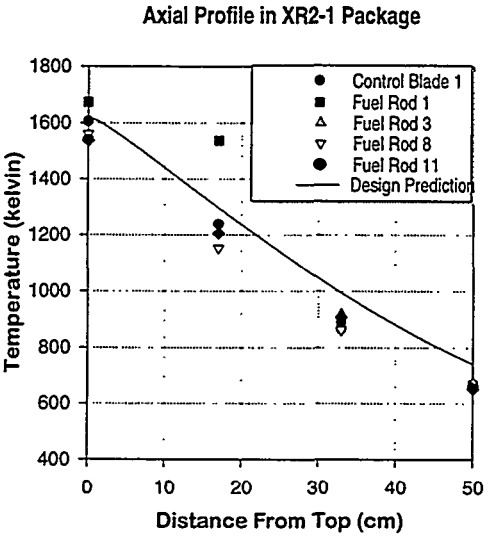

Figure 3-3. Axial temperature profiles in the lower XR2-1 package preceding melt introduction.

Table 3-2. Comparison of predicted and observed thermal indicators just before the gate is opened at 17,100 seconds.

Location	Observed Temperature (Kelvin)	Predicted Temperature (Kelvin)	Heat Loss (kW) Observed	Heat Loss (kW) Predicted
Melter Sides (Calculated)				**35**
Melter Top (Calculated)				**5**
Melter Bottom (Calculated)				**5**
Melter Total (Calculated/Observed)			**41**	**45**
Cavity	**2713**	**2700**		
Gate	**1750**	**1790**		
Package Top	**1605**	**1620**		

3.3 Stainless Steel/ B_4C Delivery

At 17,153 seconds into the experiment, the lower melter gate was opened and within seconds the stainless steel/B_4C composite wire was fed into the test package. Temperatures at the upper elevations began to rise as a consequence of the increased radiant heat flux to the package as shown in Figure 3-4. It is believed that the zircaloy melting point was reached near the top of the package in approximately 4 minutes after opening the gate. The zircaloy spacer grid near the top of the fuel rods began to melt in only a minute or two. Evidence of this can be found in the thermal responses of lower fuel rod thermocouples as early as 17,230 seconds.

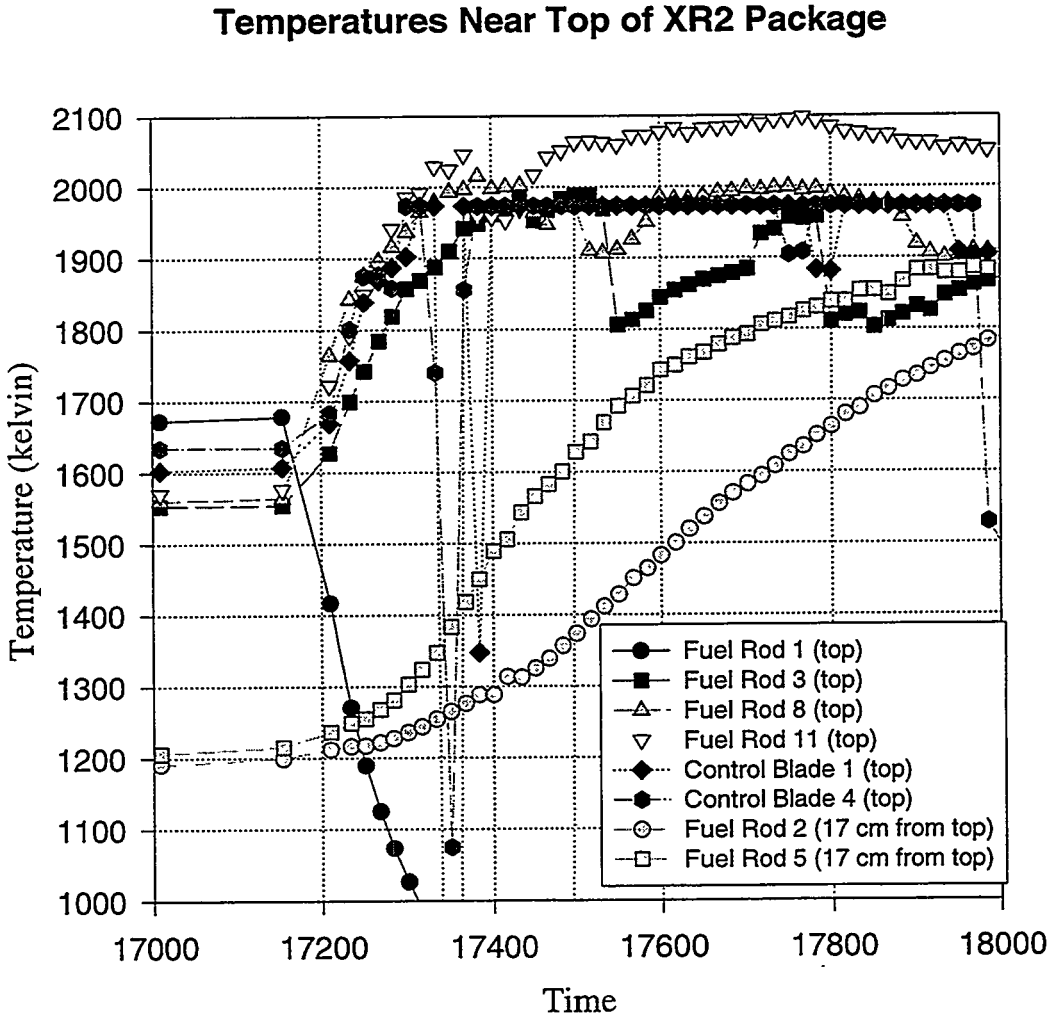

Figure 3-4. Temperature rise at top of XR2 package following the opening of the gate.

At core region 2 (approximately 17 cm or 6½ inches from the top as shown in Figure 3-1), the temperature rise is somewhat slower and was not expected to exceed the zircaloy melting point as a result of radiant heat transfer alone. The upper denuded fuel rods were expected to provide shadowing from the intense radiant heat flux above so that melting would be localized in the upper 10 to 13 centimeters.

The composite wire was fed continuously into the XR2-1 package at a rate of 12 gm/sec for nearly 1000 seconds. In addition, the top of the control blade began to melt almost immediately from the incident radiant heat flux. These two sources provided material for relocation into the lower end of the assembly. The first indications of molten material moving into core region 2 (17 cm from the top) were at 17,240 seconds into the experiment or about 1½ minutes after opening the gate. There were also indications at this time of molten material falling on the lower control blade drive. Almost simultaneously, material fell onto the core plate, as evidenced by the thermocouple traces of Figure 3-5. Notice that the only thermocouples significantly affected by this relocation were those located nearest the control blade both on the upper and lower surface. These thermocouples continued to record small sporadic relocation events to the core plate for the following three to four minutes, followed by three or four minutes in which there was little or no evidence of further material relocating to the core plate. Then, at approximately 17,900 seconds there was a sudden and very sizable relocation of molten material along the entire core plate. This trend is very similar to that observed for the XR1 tests (see Reference 3), i.e., initially some core blade material fell to the core plate, followed by a period in which very little molten material found its way there, followed by a sudden and very sizable relocation of material to the core plate roughly 10 minutes into the melt pour.

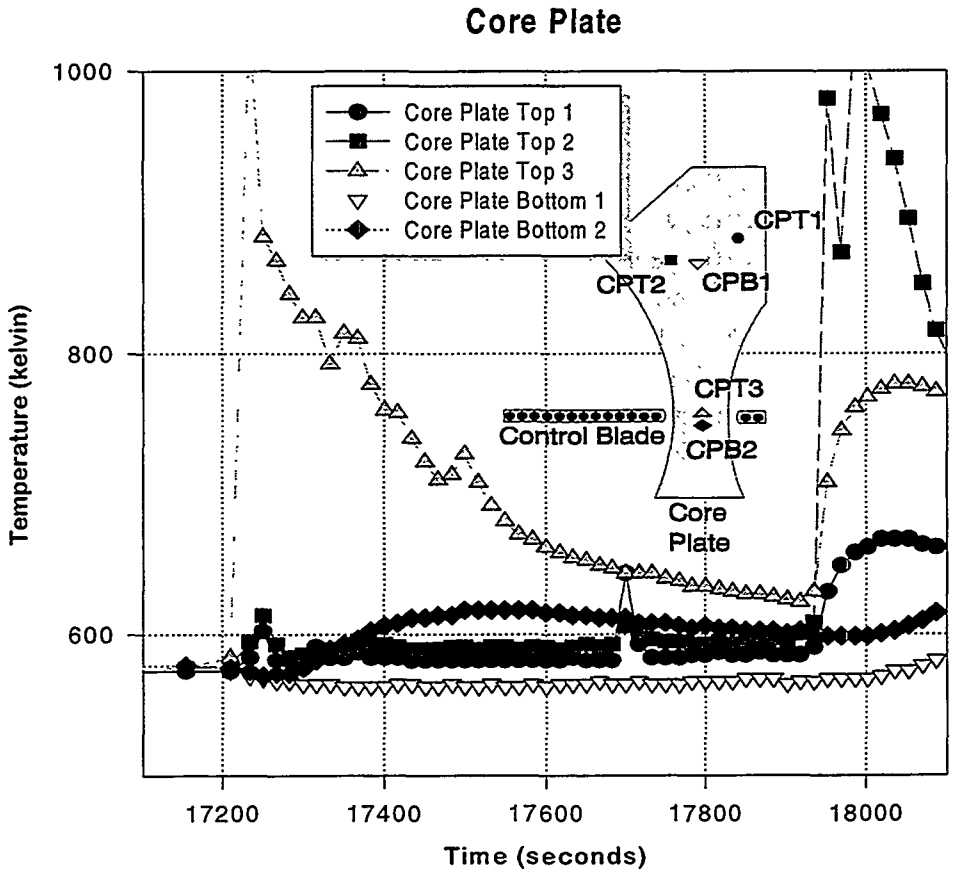

Figure 3-5. Temperature response in core plate thermocouples during composite wire feed.

Thermocouple signatures in the lower control blade drive and fuel support piece indicate that initially, material was able to drain to the lower reaches of the package though perhaps somewhat slowly. As material continued to drain, it froze and filled the gaps between the control blade and can walls, forcing some material to drain laterally along the control blade to the relatively open channel above the core plate. There are several thermocouple indications of material dripping rapidly down nearly the full length along the end of the control blade at approximately 17,290 seconds. When it reached the relatively cold core plate, the molten control blade material froze relatively quickly and could not spread laterally along the entire core plate as evidenced by the unaffected thermocouples on the core plate far from the control blade. Eventually, material accumulated along the end of the control blade and molten material was forced to fill up the control blade gaps between the fuel assembly canisters. Real-time X-ray images (see Figure 3-6) indicated that by 17,992 seconds, this molten pool filled in the control blade gap above the lower support piece, probably plugging the control blade access slot. Figure 3-7 shows the axial temperature profiles as the molten material was poured along the control blade. Even though thermocouples at the bottom of the control blade registered temperatures under 1200 K, thermocouples located 16.5 cm (6½ inches)

from the bottom of the active length recorded temperatures at or above the melting point (~1500 K) of the iron/B_4C eutectic. Consequently, it is expected that most of the active length of the control blade was liquefied by the end of the composite material pour.

Figure 3-6. Real-time x-ray frames.

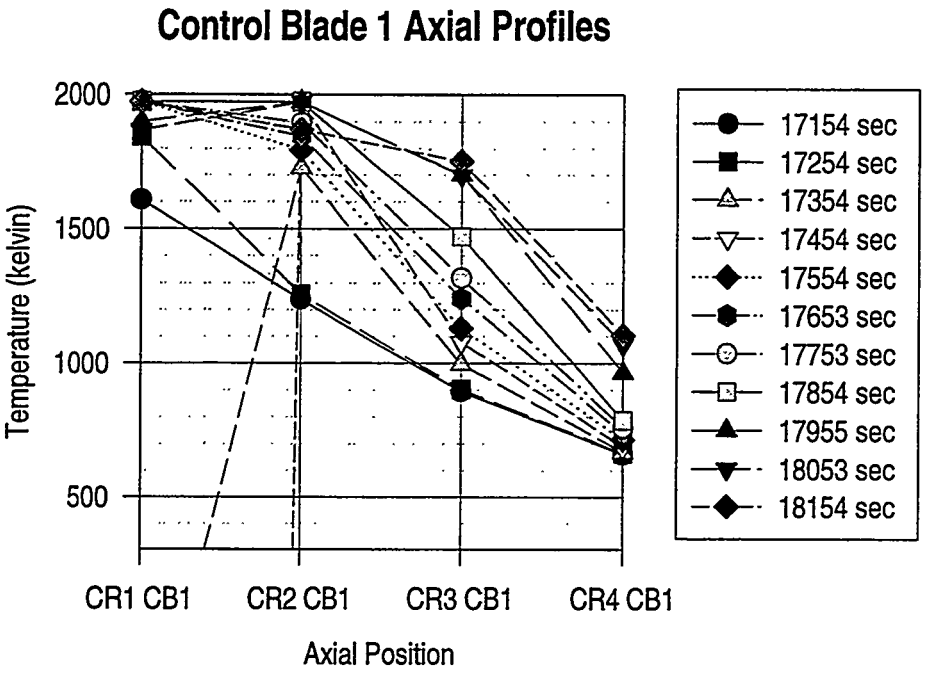

Figure 3-7. The developing axial temperature profile at the center of the control blade after the gate is opened.

3.4 Zircaloy Melt Delivery

The zircalloy melt pour stage began at 18,212 seconds. At the beginning of this stage, considerable melting had already occurred in the upper three or four inches of the package. The grid spacer and some of the upper cladding and can walls had most likely already melted and relocated into the lower package. When the zircaloy melt pour phase was initiated, it is apparent that this melt initially did not drain through the bottom of the test section, and instead formed a blockage region in the test bundle. The blockage formation and melt accumulation was observed using the real-time X-ray imaging system. A molten pool was forming above the tie plate and some material even dripped past the tie plate onto the nose piece. The zircaloy melt continued to accumulate until shortly after 18,500 seconds, when a large and sudden melt release event was observed at many locations in the lower test bundle, including the lower core plate and regions below the core plate. This relocation event resulted in significant heating of the core plate and lower test section, as seen from the thermal responses in Figure 3-8 and Figure 3-9. Zircaloy

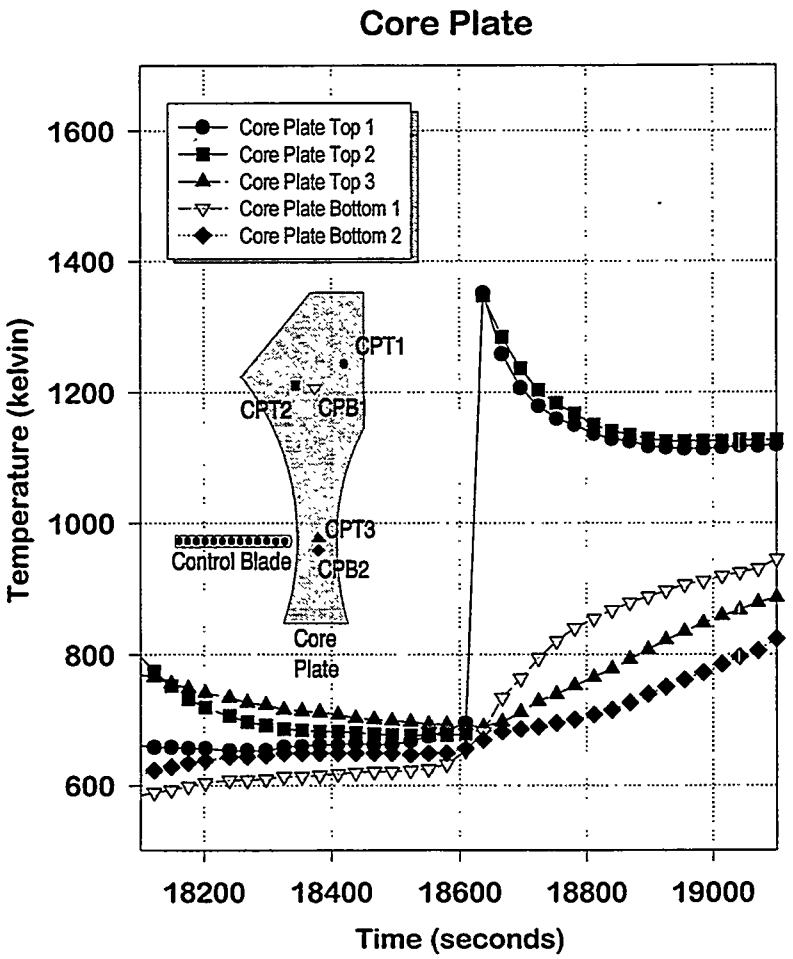

Figure 3-8. Temperature response in core plate thermocouples during zircaloy wire feed.

melt released in this event drained to the bottom of the test section below the core plate, finding access through the fuel nose piece and the flow inlet nozzle in the fuel support piece, as shown in Figure 3-10. This pathway is suggested by the coincidental thermocouple responses at the bottom of the inlet nozzle and in the catcher basin. A significant mass of cascading molten material also appears to have drained onto the core plate at essentially the same time, suggesting a parallel path for a rapidly draining plug of molten material. This parallel path would indicate extensive damage to the upper can walls at this point in time in order for the molten material to drain both to the inlet nozzle and the inter-can gaps. The real-time X-ray images indicate that the upper pool level above the core plate may have extended above the tops of the lower nose pieces. This would mean that the pool level was above the top of the support piece making it possible for melt to drain through the control blade access slots. In fact, there are some indications early on of molten material draining through the short control blade slot, but there are no immediate temperature signatures at locations on the long control blade slot or the velocity limiter indicating that this channel was probably blocked by control blade material.

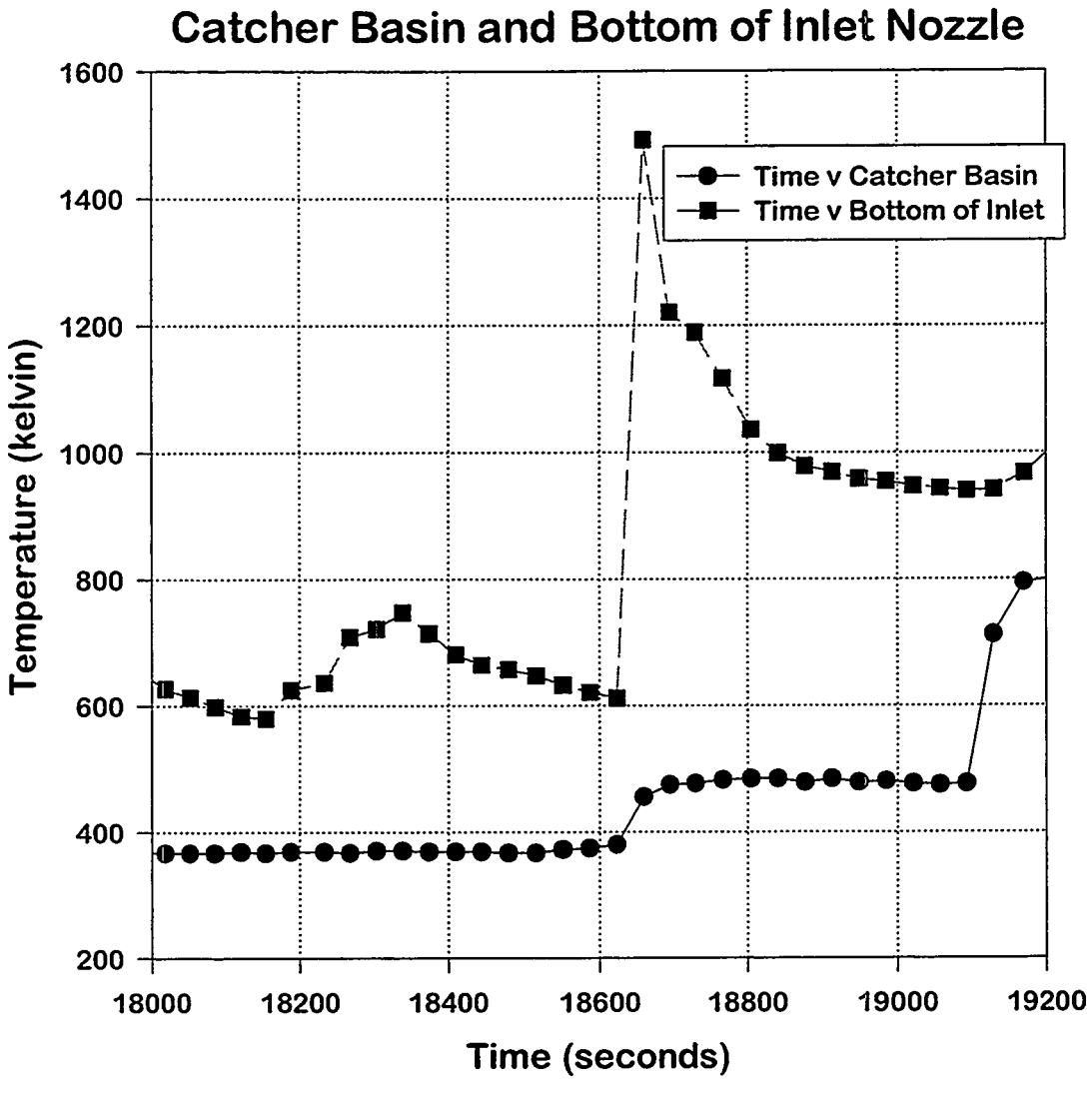

Figure 3-9. Temperature response in catch basin and inlet nozle at 18,600 seconds.

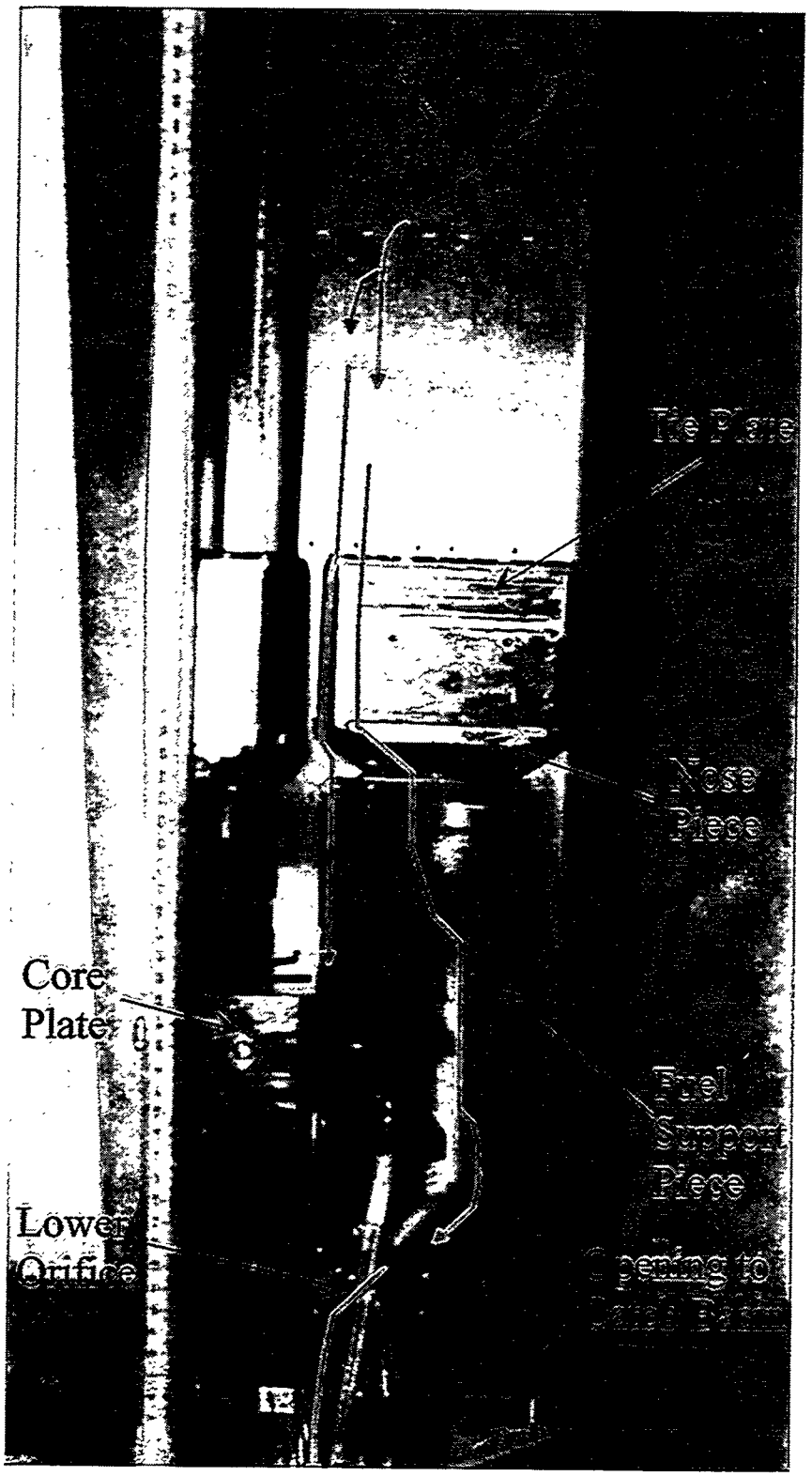

Figure 3-10. Parallel melt relocation paths at 18500 seconds.

Material continued to accumulate above the core plate and the inlet nozzle may have begun to fill with material. Lower structures, including the velocity limiter and guide tubes, showed a gradual, yet very significant increase in temperature (Figure 3-11), suggesting that material might be slowly entering the guide tube or that surrounding structures such as the fuel support piece may be heating the velocity limiter. The material that relocated to the inlet nozzle, core plate, and nose piece gradually reheated and remelted control blade material that was blocking the core plate penetration until about 19,100 seconds, when there was a rapid drainage of material through this channel onto the velocity limiter and into the lower catch basin. Temperatures on the velocity limiter jumped over 400 kelvin in response to the relocation of molten material along its surface. Real-time X-ray images showed material suddenly draining from both the control blade channel and the molten zircaloy pool in the unbladed bypass channel above the core plate.

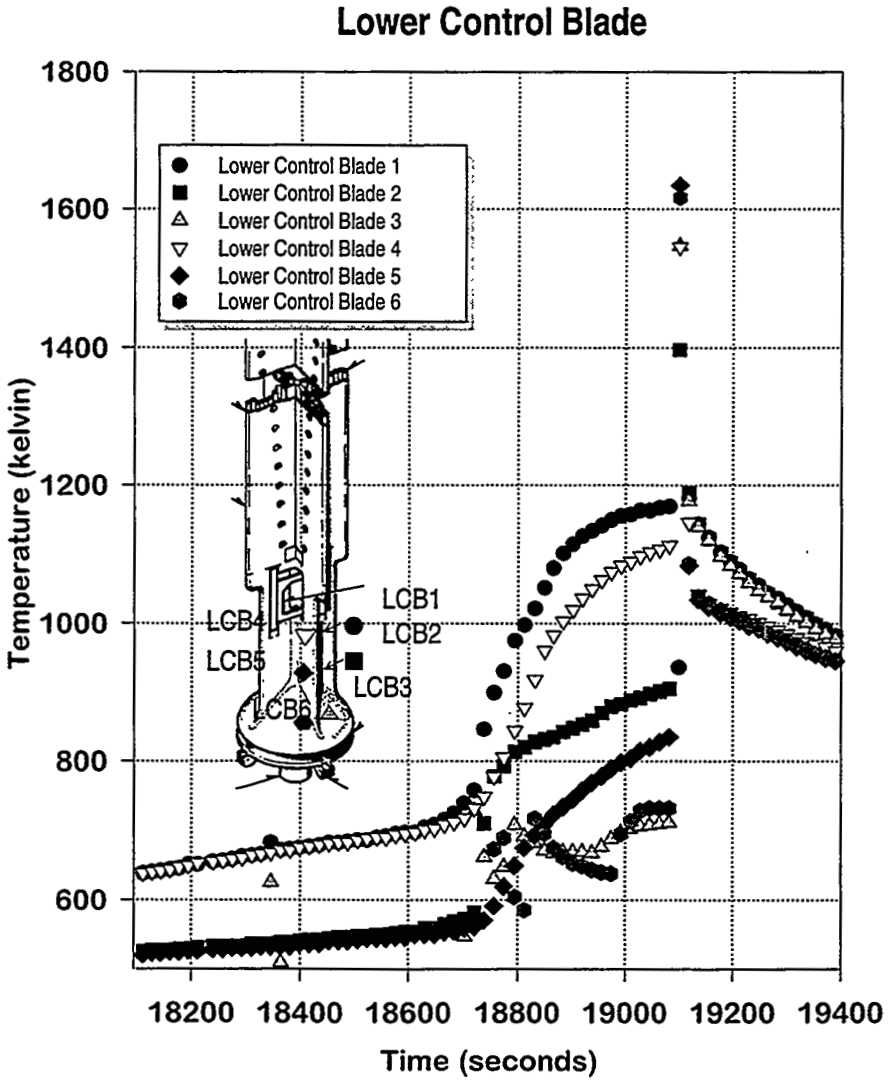

Figure 3-11. Temperatures in lower control blade drive thermocouples.

3.5 Post-Test Condition of XR2 Package

The post-test condition of the XR2-1 test section reveals a large degree of disruption of the upper bundle features, as seen by comparing Figure 3-12 (pre-test) and Figure 3-13 (post-test). The orderly rod array, channel walls, and control blade at the top of the bundle have been significantly disturbed with virtually no recognizable features remaining. In addition, some vertical compaction of the bundle occurred. The fuel rods in the top of the test section were denuded of cladding by the draining molten zircaloy and the radiant heat load to the top of the bundle, allowing the eroded UO_2 pellets to collapse to a rubble geometry.

Figure 3-14, showing two x-ray projection views of the XR2-1 post-test condition, reveals that some fuel rod features remain in the lower regions of the test section, although the rods are distorted and displaced. Blockages of refrozen melt are seen across the test bundle above the core plate, as well as on and below the core plate. Refrozen melt is visible within the fuel canister nose pieces and in the nozzle inlet region below the core plate. (The nozzle inlet region is the main coolant flow path by which water flows from the lower plenum below the core plate, up through the fuel support pieces, into the fuel canister nosepieces and up through the fuel channels in the normally operating BWR - see Figure 1-2 for clarification). The nozzle inlet region is largely filled with refrozen melt, as is the control blade access slot in the drive tube region. Finally, a large accumulation of melt is seen to have solidified at the lower-most catch basin of the test section, apparently arriving there by way of the control blade access slot and the fuel canister nozzle inlet pathways. The top surface of the refrozen material in the lower catch basin is flat, indicating that this material arrived at a high enough transfer rate and with sufficient superheat to attain a flat upper surface, as opposed to a "stalagmite" geometry typical of dribbling melts with little superheat. It is possible that the material that drained to the lower catch basin was a "eutectic" mixture of Zr and Fe (zircaloy and control blade material) which formed when the molten Zr attacked the lower blockages. The composite material resulting from the eutectic interaction could have a solidus temperature well below the liquidus of either the Zr or control materials separately. Eutectic liquidus temperatures for the Zr-Fe system can be as low as 1220 K for zirconium rich mixtures (see Figure C-11 for the Zr/FE phase diagram).

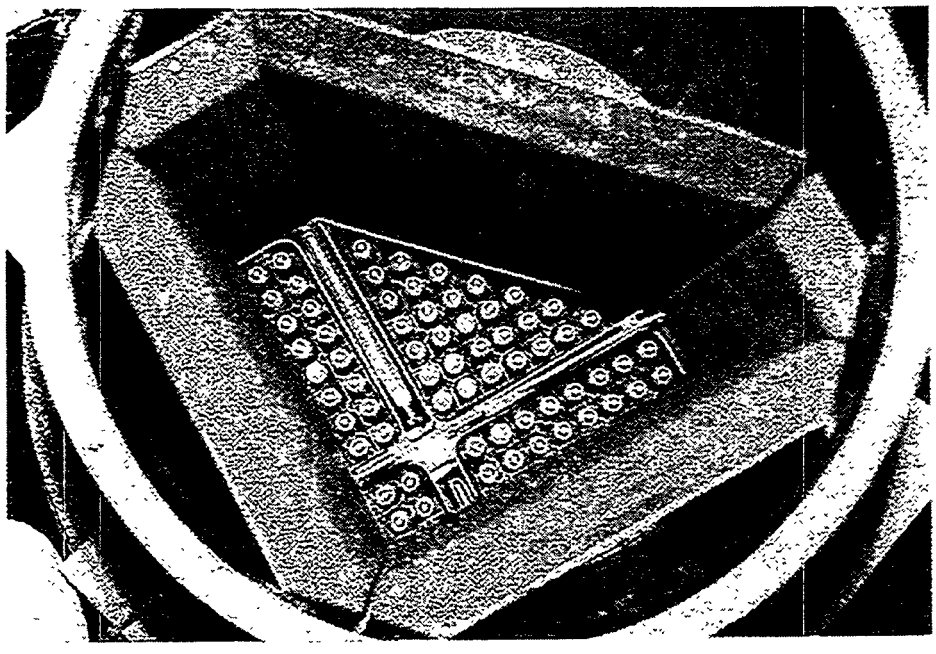

Figure 3-12. Pre-test top view of the XR2-1 test section showing fuel rods, channel walls and control blade.

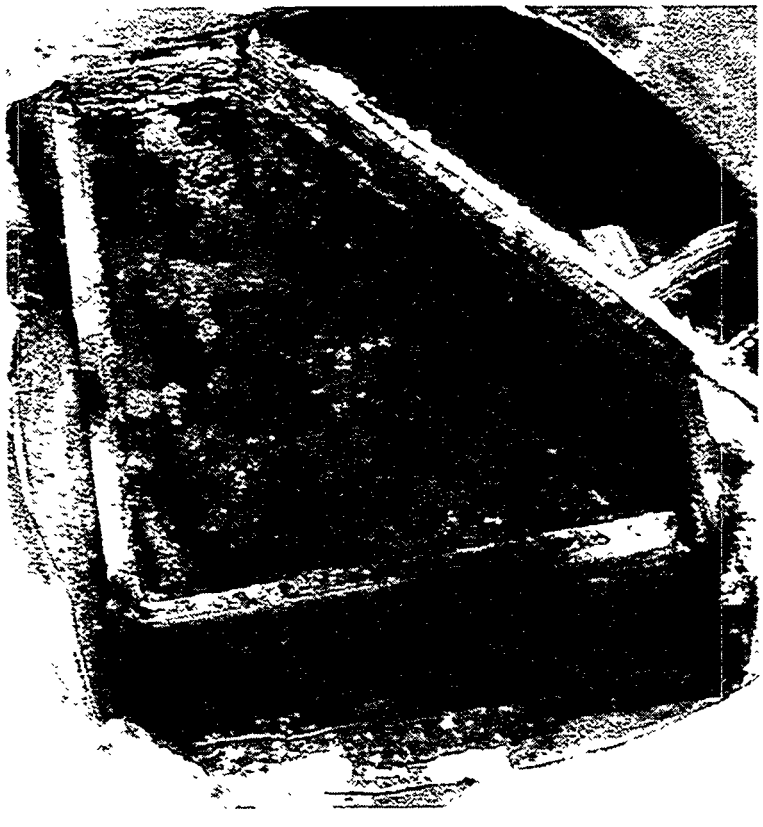

Figure 3-13. Post-test top view of the XR2-1 test section showing substantial disruption of ordered geometry.

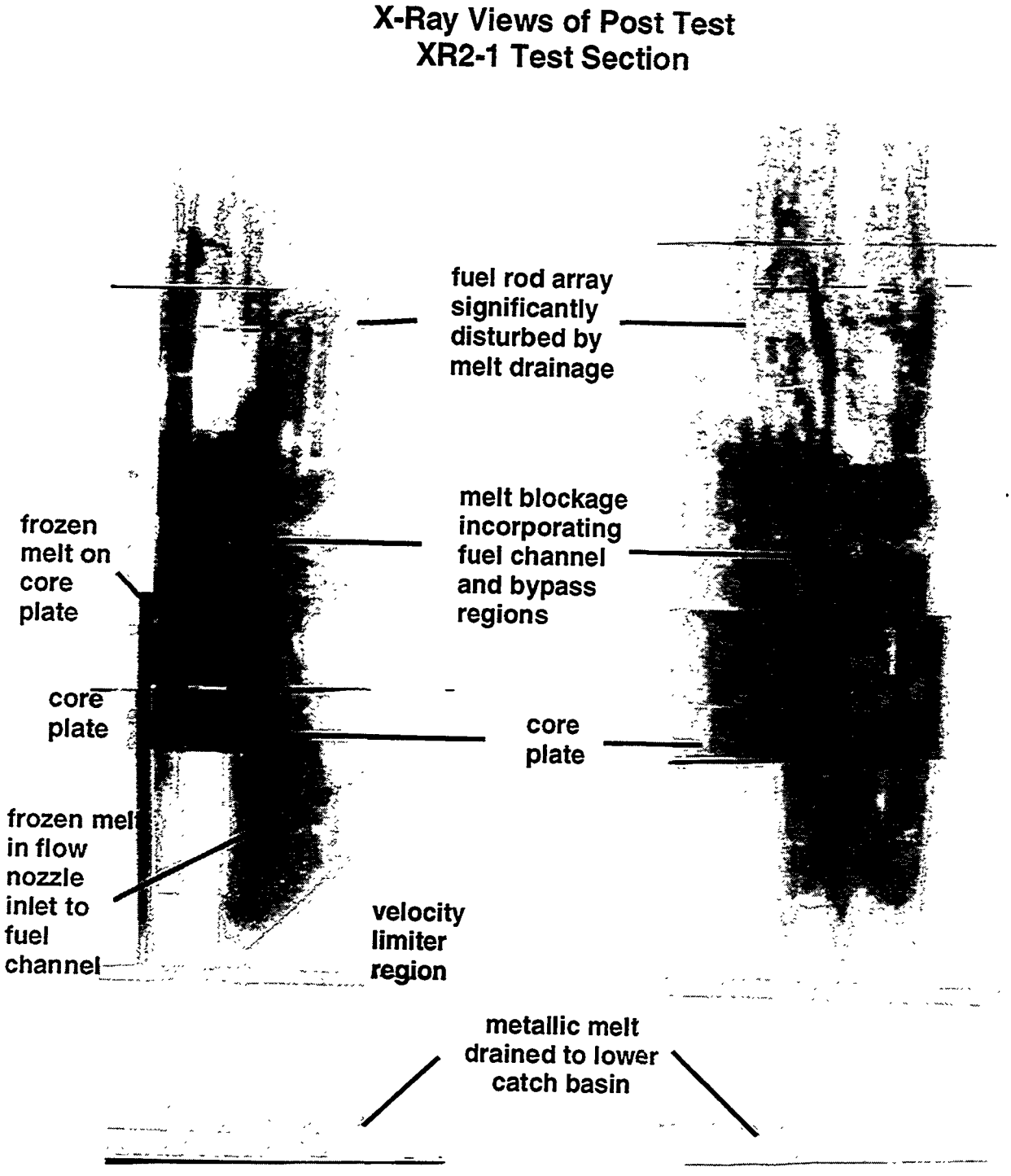

Figure 3-14. X-ray projection views of the XR2-1 test section (post-test).

A more detailed view of the post-test condition of the package was obtained by x-ray tomographic inspection of the package. The upper part of the XR2-1 package, from just below the upper surface of the core plate extending to the top of the remaining fuel rod debris (~60 cm above), was scanned at 960 elevations, resulting in an axial pixel height of 0.0625 cm. In the lateral direction there were 256 pixels, each with a width of 0.14 cm. Each scan provides a horizontal cross sectional image of material densities at that particular elevation. Axial sections were then generated from these scans to give additional views from the two orthogonal directions.

Figure 3-15 shows the horizontal cross section at a given elevation as it existed in its pre-test geometry compared with the tomographic cross section at the end of the test. Note that at the top of the fuel bundle, only a few fuel rods situated in cooler locations near the outer boundaries remain — most of this region is void of material of any kind. However, from the tie plate to roughly half way up the fuel bundle, it is possible to identify nearly all of the original fuel rods, many of which are found roughly in their original lattice arrangement at the tie plate elevation. The axial views (Figure 3-16 to Figure 3-23) show clusters of individual fuel pellets throughout the lower half of the rodded region, apparently falling there from the voided region above. In addition, it appears that many of the fuel rod remnants are fused together with shapeless masses of re-solidified metallic melt, the fuel material acting as a heat sink to the downward relocating molten material. In an actual accident situation, these fuel rods would provide a strong heat source, inhibiting blockage formation further promoting the downward motion of molten metal. It is also likely that the fusion of the fuel pellets by the metallic zircaloy has resulted in "eutectic" interactions, forming higher melting point U-Zr-O materials fusing the UO_2 pellets together. The fusion of the fuel rod remnants into clumps may inhibit further rubblization or settling of the fuel material. This pattern of resolidified material surrounding clusters of displaced and deformed fuel rods is found throughout the lower rodded region with one or two exceptions. It is very clear from these figures that there is a large void (nearly 900 cm^3) located above the core plate near the bottom of the fuel assemblies (roughly 2 cm above the tie plate). This void has roughly the shape of the core plate and is nearly 9 cm from top to bottom. Also, at these same elevations, there is a large mass of resolidified material (~294 cm^3) located where the control blade used to be.

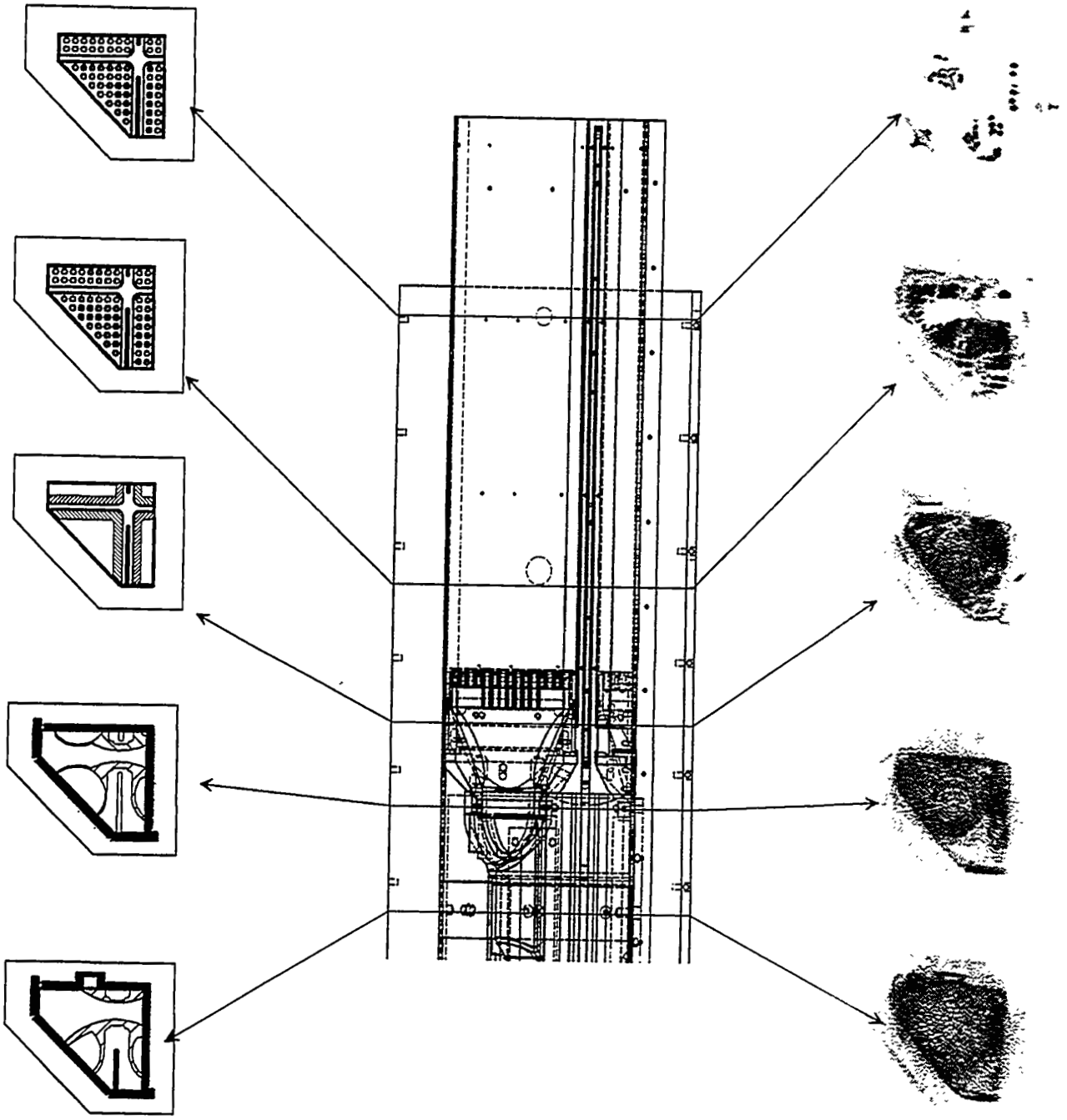

Figure 3-15. Horizontal tomographic cross sections through the XR2-1 package at various elevations.

From some of the axial views (X140 in particular) it is possible to recognize the outline of the nose pieces, indicating that they remained intact. The half nose piece appears to be completely full of solidified melt. This is consistent with what was seen in both the post-test X-ray projections and the real-time X-ray views. Horizontal cross sectional views through the nose piece also show that the gap between nose pieces above the core plate was tightly packed with material. Axial views along the core plate (Y130 - Y180) show that the region above the core plate extending to the tie-plate elevation was uniformly dense indicating that molten material

drained into this region with sufficient superheat to spread out laterally before solidifying. The upper surface is roughly level, though slightly depressed at the junction between the bladed and unbladed channels indicating material draining from the region above the core plate into the control blade gap.

The tomographic images indicate that the nozzle inlet must also be full (X100 - X130 of Figure 3-17 and Figure 3-18). The X-ray projection confirms this at its lower opening which was beyond the view of the tomographic scans. In contrast, the control blade guide tube was mostly empty from the top of the core plate to the top of the fuel support piece(X140 - X170 and Y70 - Y100 of Figure 3-18, Figure 3-19, Figure 3-20, and Figure 3-21). However, material is found at the end of the guide tube, perhaps draining from the mass accumulated above the core plate onto the velocity limiter. Views Y70 to Y100 show that material had accumulated on the lower control blade extending as high as the top of the core plate. The x-ray projections also indicated that the region between the velocity limiter and the fuel support piece was completely filled with resolidified material.

Small quantities of resolidified material were also found in the fiber insulation outside the outer zircaloy package walls. This material apparently eroded the zircaloy wall and drained through the insulation down the side of the package. Two points of origin were identified, both near the midplane of the rodded section of the test package. These points of origin might indicate the location of temporary pools that formed early on in the test.

Structural features that can be clearly recognized in these tomographic images include the double fuel support piece, the single fuel support piece, the half nose piece, the quarter nose piece adjacent to the control blade, the fuel rods, the fuel pellets, the core plate, the outer can walls, and the insulation. There were no signs of the control blade above the nose piece though the lower control blade is likely visible in the guide tube in views Y90 and Y100 (see Figure 3-21).

From the X-ray projections and the tomographic views, it is possible to make estimates of material volumes at the end of the test for various locations within the test package, the results of which are summarized in Table 3-3. It is important to remember that the total volumes of previously molten material identified includes both the material introduced as melt by the wire-fed melter system as well as test bundle materials that subsequently became molten as a result of heat transfer and eutectic interactions. Nearly 9 liters of once molten material have been accounted for in this table, the remaining 0 to 14 percent is most likely found in the fuel rod region, the insulation, and in estimation error. Seven liters of material relocated to regions below the core plate, i.e., into the catcher box, the velocity limiter, or the inlet nozzle. This accounts for roughly 70-82 percent of the total available molten volume.

Since the composition of relocated material is not known, it is not possible to know for sure the mass of material below the core plate. However, if the density of the material is approximated as 6.74 gm/cm^3 it is estimated that nearly 47 kilograms was found below the core plate elevation in the inlet nozzle (~6 kg), resting on the control blade velocity limiter (~21 kg), or in the lower catch basin (~20 kg). The density 6.74 gm/cm^3 is the mass averaged density for the total material inventory fed into the system through the wire feeders.

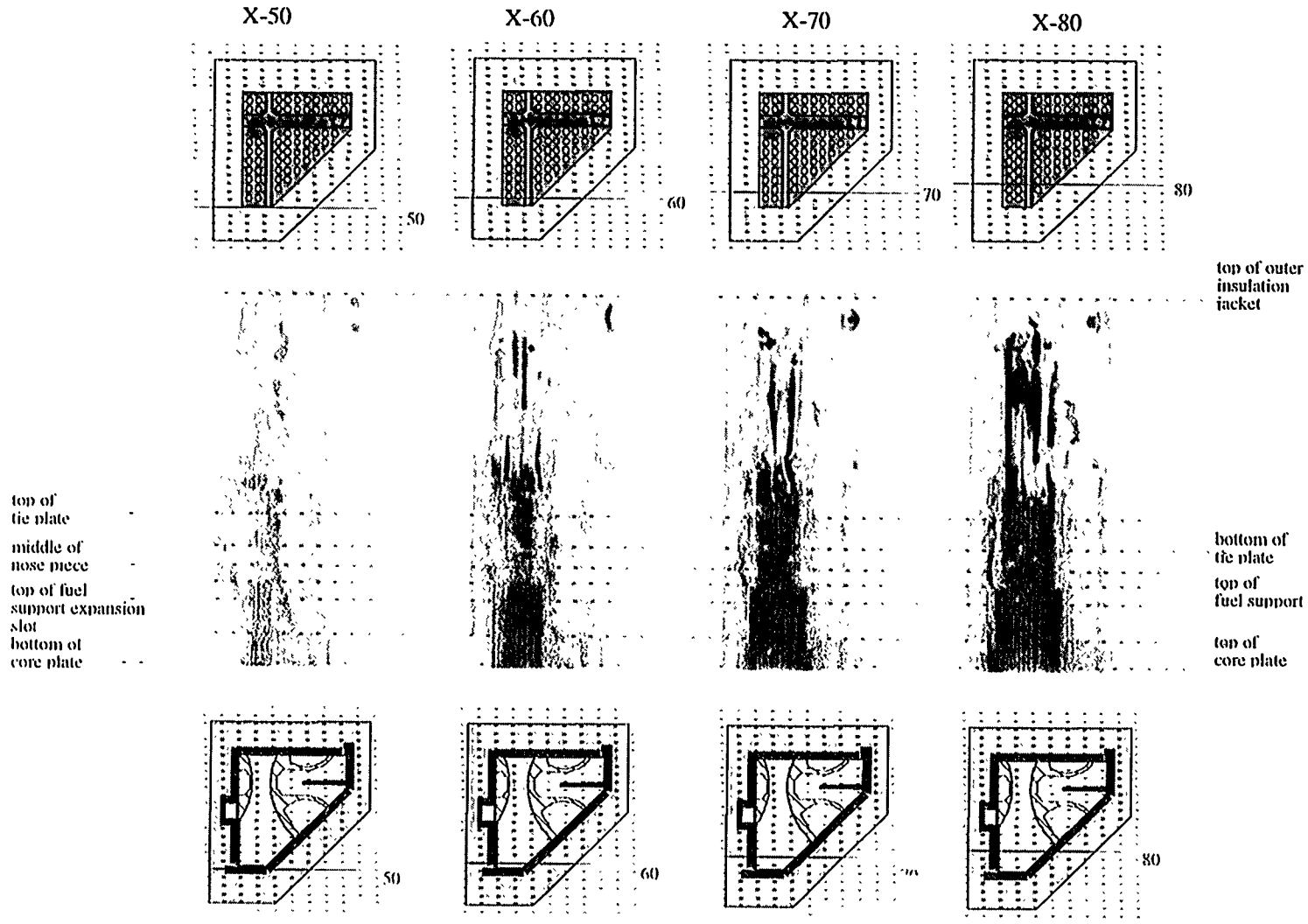

Figure 3-16: Axial x-ray tomographic slices through the XR2 test package (X-50 through X-80).

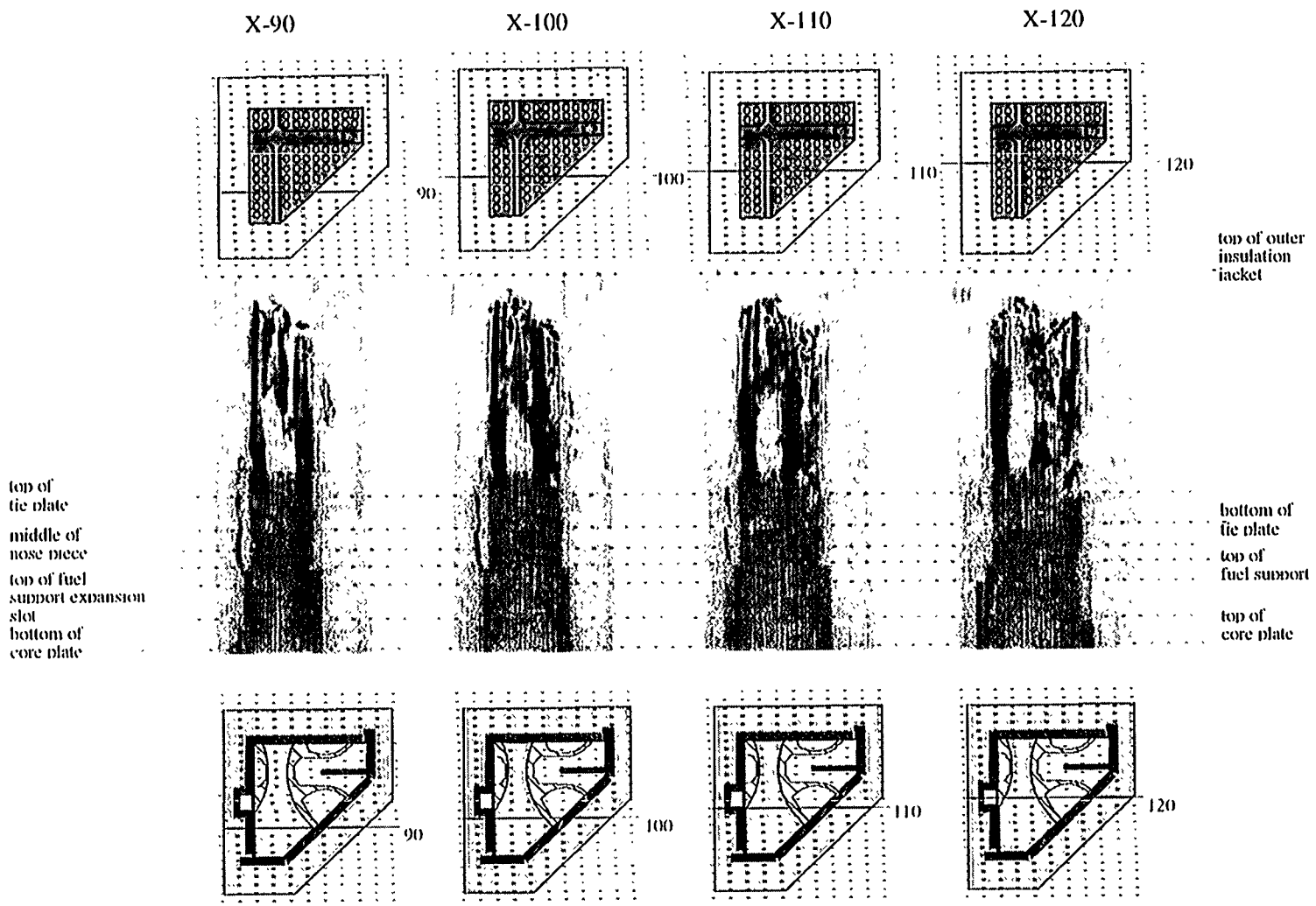

Figure 3-17: Axial x-ray tomographic slices through the XR2 test package (X-90 through X-120).

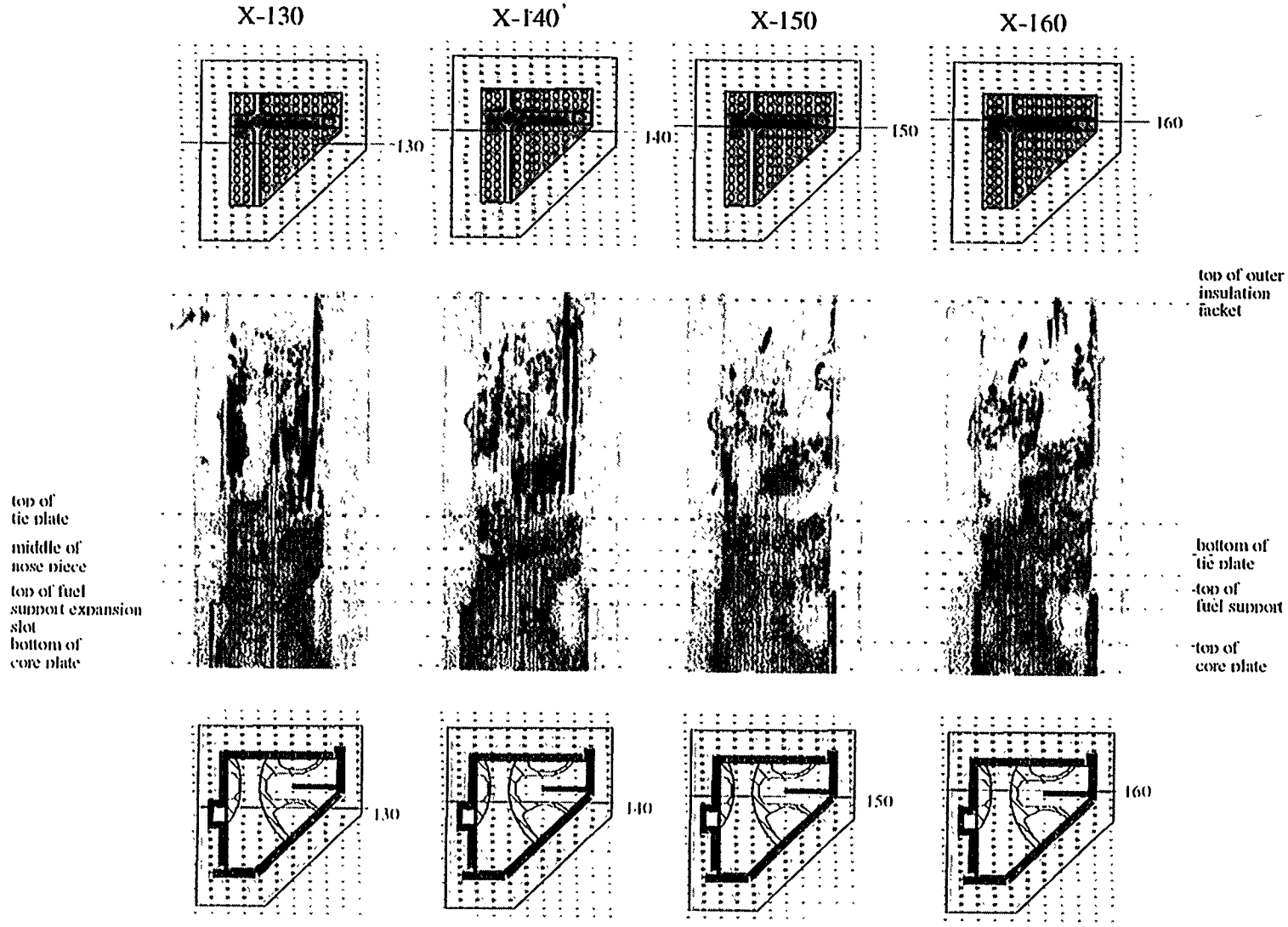

Figure 3-18: Axial x-ray tomographic slices through the XR2 test package (X-130 through X-160).

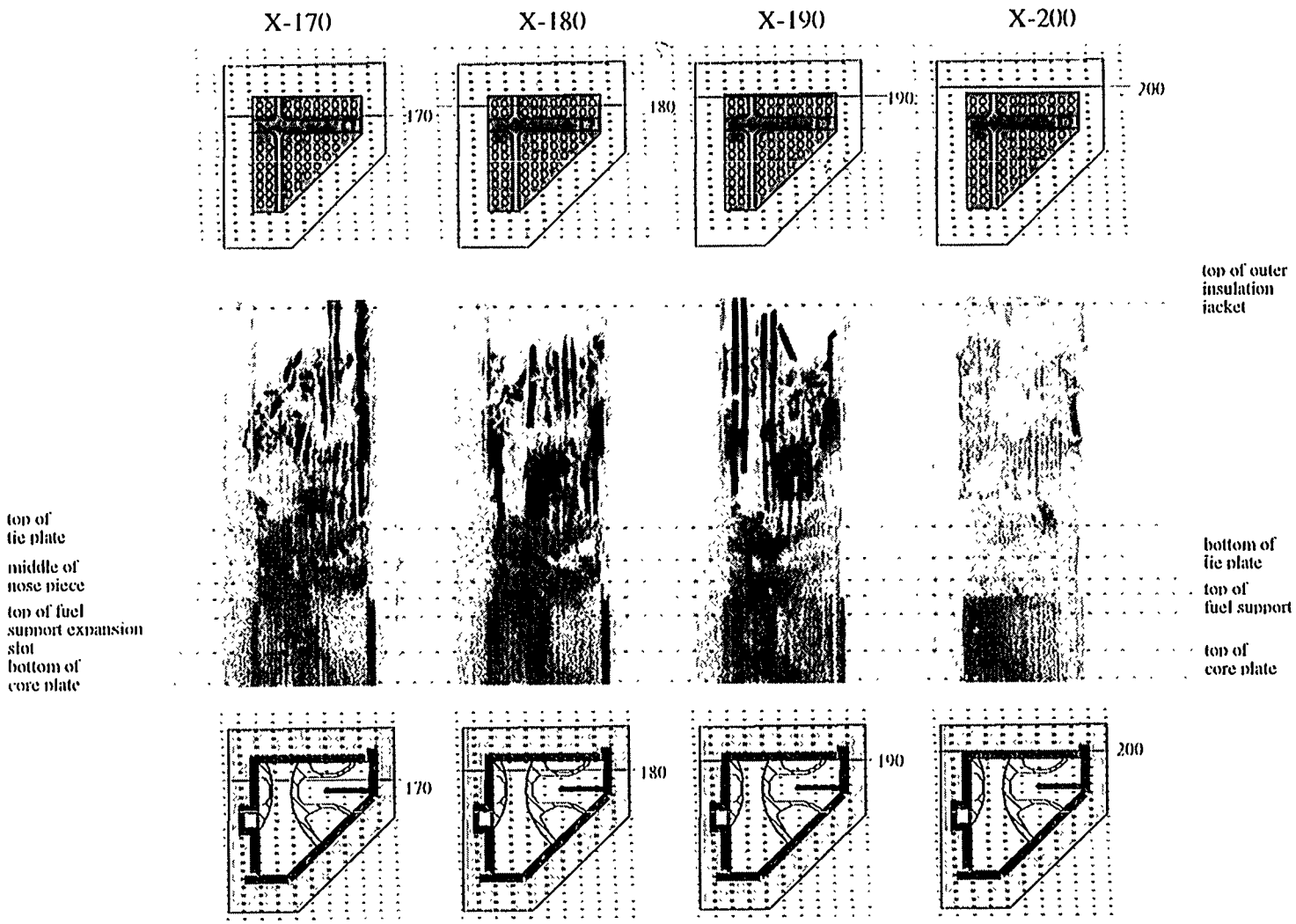

Figure 3-19: Axial x-ray tomographic slices through the XR2 test package (X-170 through X-200).

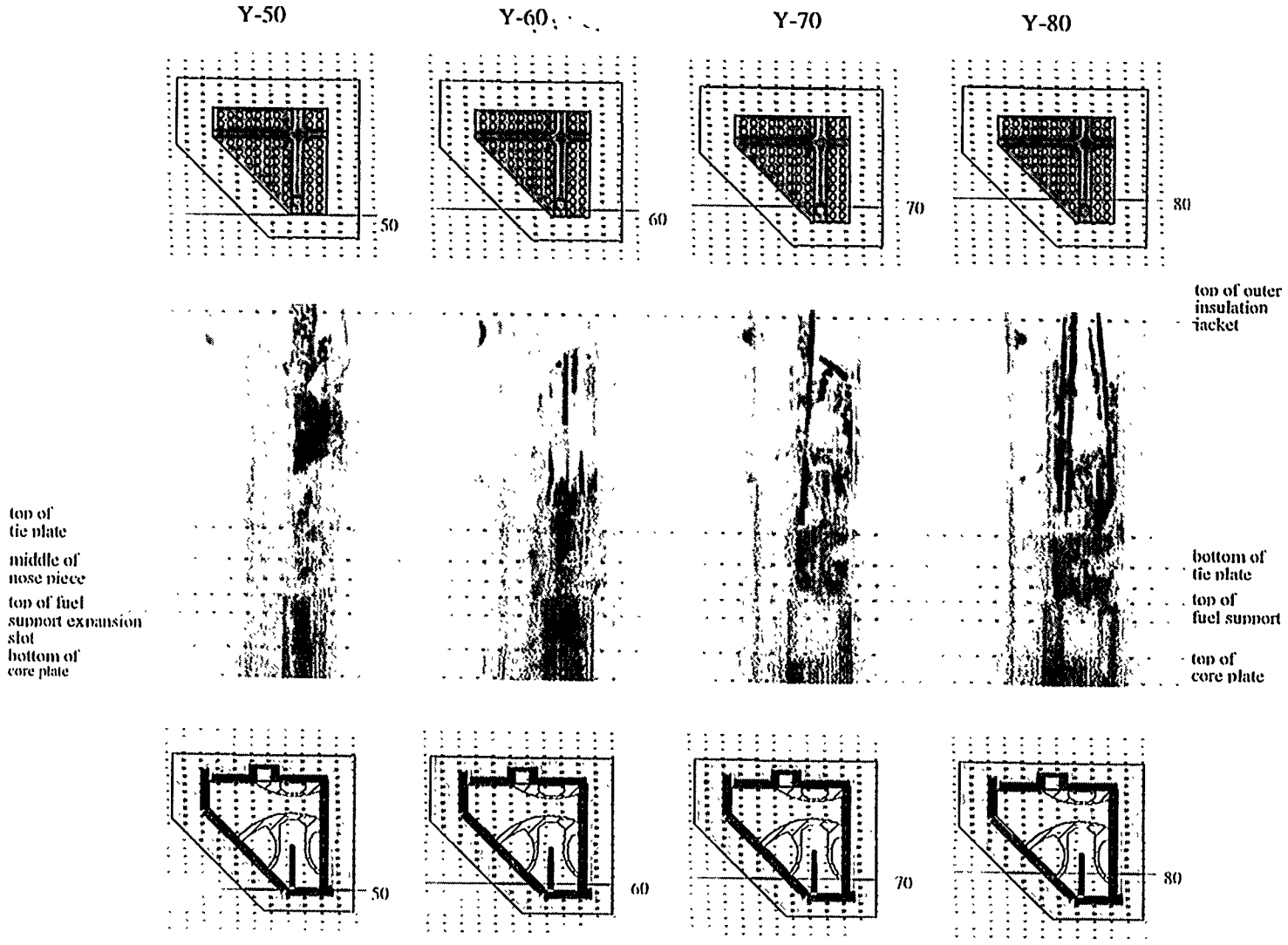

Figure 3-20: Axial x-ray tomographic slices through the XR2 test package (Y-50 through Y-80).

Figure 3-21: Axial x-ray tomographic slices through the XR2 test package (Y-90 through Y-120).

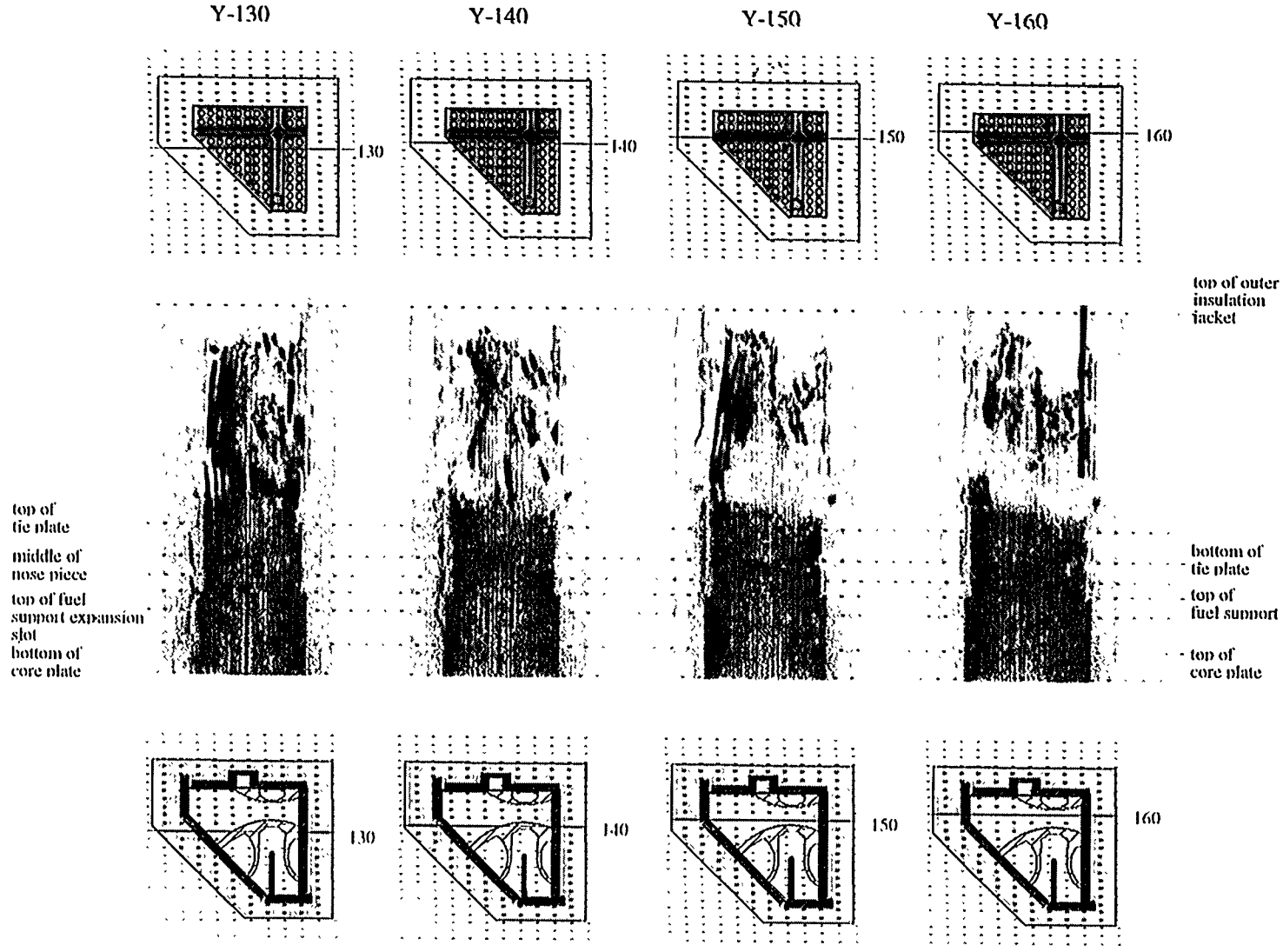

Figure 3-22: Axial x-ray tomographic slices through the XR2 test package (Y-130 through Y-160).

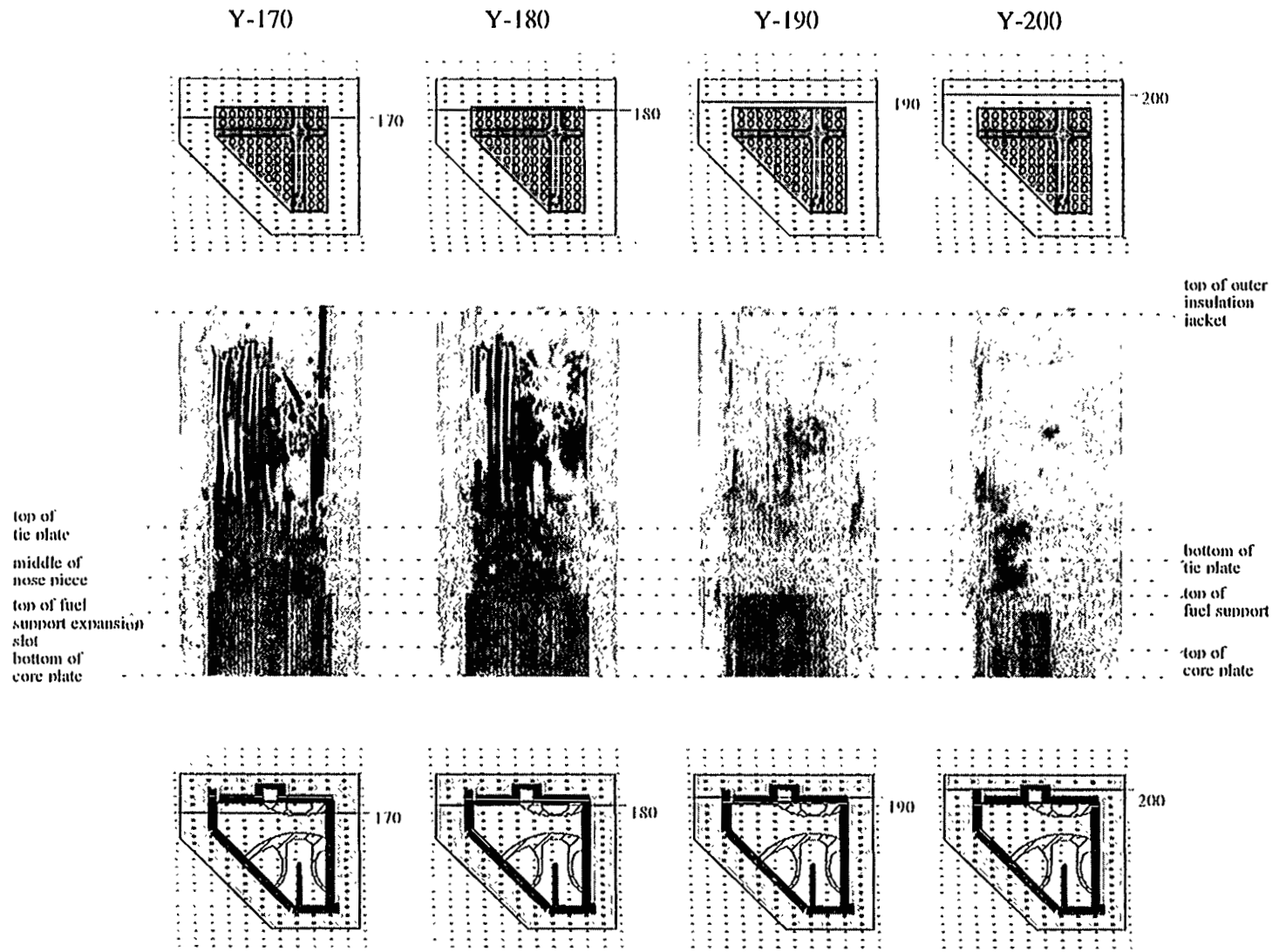

Figure 3-23: Axial x-ray tomographic slices through the XR2 test package (Y-170 through Y-200).

Table 3-3. Post-test material balance.

Molten Material Identified at Post Test		Molten Material Available for Relocation During Test	
Location	Volume (liter)	Molten material available	Volume (liter)
Material found below the core plate	**7.06**	Introduced as wire feed	**8.6**
Catcher box	2.9	SS/B_4C composite wire	2.7
On velocity limiter	3.2	Zircaloy wire	5.9
Inlet nozzle	0.96	Test section structural material (excluding UO_2)	**1.5**
Material above core plate	**1.7**	Active control blade	0.19
Above core plate	.62	Fuel rod cladding	1.0
In nosepieces	.77	Fuel canister walls	0.31
Control blade gap	.31		
Volume accounted for:	**8.76**	Total volume available:	**8.6 - 10.1**
Volume unaccounted for:	**-0.16 - 1.34**		

3.6 Summary of the XR2 test

The following table (Table 3-4) summarizes the chronology and explanation of significant events that were presumed to transpire during the XR2-1 experiment. Even though the physical explanation of these events may be somewhat subjective in nature, they were deduced from the thermocouple signatures, real-time X-ray images, and the post-test examination of the test package.

Table 3-4. XR2-1 test summary.

Event	Time (hr)	Time (sec)
Initialize data recording.	0	0
Stage 1: Begin package preheat, melter at 1700 K.	1:50	6600
Package preheat accomplished.	3:34	12,840
Close melter gate and heat melter to operating temperature.	3:42	13,320
Melter reaches operating temperatue of 2650 K.	4:45	17,100
Stage 2: Open melter gate and start feeding stainless steel wire.	4:46	17,213
Material at the top of package (most likely steel springs and fuel rod spacers) melt and relocate to the bottom of the fuel rods.	4:47	17,230
Indications of some molten material reaching the core plate and the top of the fuel support pieces before flow to the core plate is choked off by blockages above.	4:47	17,240
The upper 1/3 of the control blade may have melted by now. Relocated material has been detected in the gaps between the control blade and the can walls as low as 6 inches above the tie plate (nearly 2/3 down the active control blade). The bottom 1/3 of the control blade gap is still largely open. Material is accumulating in the unbladed gap above the nose piece. However, there are no indications of a sustained accumulation of material on the core plate.	4:49	17,360
There is an extensive melt relocation to the bottom of the short control blade. In addition, there is a significant mass of material (probably zircaloy melting at the tops of fuel bundles) that drips all the way to the tie plate. Material is collecting between fuel rods.	4:52	17,500
Molten control blade material completely fills in gaps around the lower control blade at the tie plate elevation. Molten material in the fuel bundle relocates to the bottom of the nose piece. It is uncertain whether the material accumulating in the nose piece is control blade material that has breached the can walls and is draining to the nose piece or zirconium melting at the tops of the fuel bundle.	4:57	17,840
The gap between the fuel assemblies on the bladed channel fills in completely above the fuel support pieces. There is a very large mass of material that relocates to the core plate.	4:59	17,940
Stage 3: Terminate stainless steel wire feed and initiate Zr wire feed.	5:03	18,212
Material has nearly filled the bottom third of the half assembly above the tie plate forming a pool around fuel rods. Some material drips past the tie plate onto the nose piece.	5:06	18,340
A large mass of molten material retained above the nose piece breaks free and relocates to the lower package. Material pours down the can wall onto the core plate heating the tops of the fuel support structures and nose pieces. Material also drains out the coolant inlet nozzles in the fuel support structure. Material has also drained down the short control blade guide tube in the single fuel support structure into the catcher, though there are no indications of material draining down the long control blade channel.	5:10	18,610
The level of material accumulation on the core plate is much higher than the top of the fuel support piece and molten zirconium has probably melted previously deposited control blade material that was blocking the bladed channel. Material is now draining down the control blade channel onto the control blade velocity limiter and into the catcher.	5:18	19,100
Terminate zircaloy wire feed and close melter gate.	5:19	19,158

4. MERIS ASSESSMENT OF THE XR2 TEST

The XR2-1 test characterization to this point has been described in terms of assessments of available experiment diagnostics: thermocouple transients, real-time X-ray images, and post-test tomography. These techniques have provided invaluable insight into the chronology and extent of events taking place in the test. In the following section the MERIS[4] code analyses of the test progression will be compared to the XR2-1 test results. This analysis is intended to provide additional interpretive insight into the observed behavior and to provide additional theoretical rationale for the subjective interpretations of the test events. Perhaps most importantly, the MERIS analysis of the XR2-1 test provides a tool with which to synthesize the effects of parameters not explored in the XR2-1 test, such as the impact of a different axial thermal gradient, and a means to extrapolate the test results beyond the test end-state in order to explore the core degradation beyond the XR2-1 end state. These latter issues are beyond the scope of this study. Without this analysis, we risk overlooking important details of late-phase reactor accidents and miss an opportunity to verify current reactor safety models against a well-controlled, well-instrumented, prototypic experiment[5]. MERIS (Melt Relocation in Core Structures) was the computer code used to model the XR2 experiment.

4.1 Overview of the MERIS Model

MERIS is a computer code being developed at Sandia National Laboratories which is intended as a tool to better understand and simulate the events and processes which would occur during the metallic melt-down phase of a severe nuclear reactor accident. It was developed with two major objectives in mind: as an analysis tool for the XR experiment program, and as a reactor accident model to be incorporated into other NRC reactor safety analysis codes. For a complete description of specific formulations incorporated into the MERIS code, the reader is referred to the more detailed discussions of the MERIS code development referenced above. However, some of the more notable features of the MERIS code include the following:

1. The primary variables are geometry-independent, cell-averaged properties. Details of the cell geometry enter into the model as closure relationships for the heat and mass-transfer equations.

2. The current modeling in MERIS treats seven material components (UO_2, Zr, ZrO_2, Fe, steel-B_4C, Fe-Zr eutectic, and Zr-UO_2 eutectic) together with UO_2-Zr and Fe-Zr material interactions.

3. Solid and liquid materials are treated separately. Currently, only liquid motion is modeled.

4. Both axial and lateral liquid motion is modeled. Significant forces effecting relocation are: **axially** - inertia, gravity, and viscous resistance, and **laterally** - viscous resistance and the hydrostatic pressure caused by local pools accumulating above blockages.

5. Radiation heat transfer is handled as a modification to the effective thermal conductivity and radiation across a single empty or nearly-empty cell is modeled.

Perhaps the most distinctive feature of the MERIS code is the way in which the local cell geometry is handled. In this regard, the MERIS model resembles the porous media models which inspired it. The details of the model geometry enter the calculations through closure relationships to the heat and mass-transfer equations. Each cell is assigned a geometry parameter (see Figure 4-1) which is used in determining liquid/solid contact area, the liquid layer thickness, connectivity tensors for heat transfer, and boundaries to liquid mass flow. For example, material cannot flow into a cell of type igeo=2 from the cell to the left (lower values of x) until a sufficient fraction of the wall thickness has melted away. Likewise, liquid material in a cell of type igeo=2 cannot flow into cells to the left (lower values of x) of that cell. In addition, heat can be conducted axially through a cell of type igeo=2 or in the y-direction but cannot be conducted to the right of that cell, though heat may radiate in that direction. Heat may or may not be conducted to the left of this cell, depending on the type of cell that resides there.

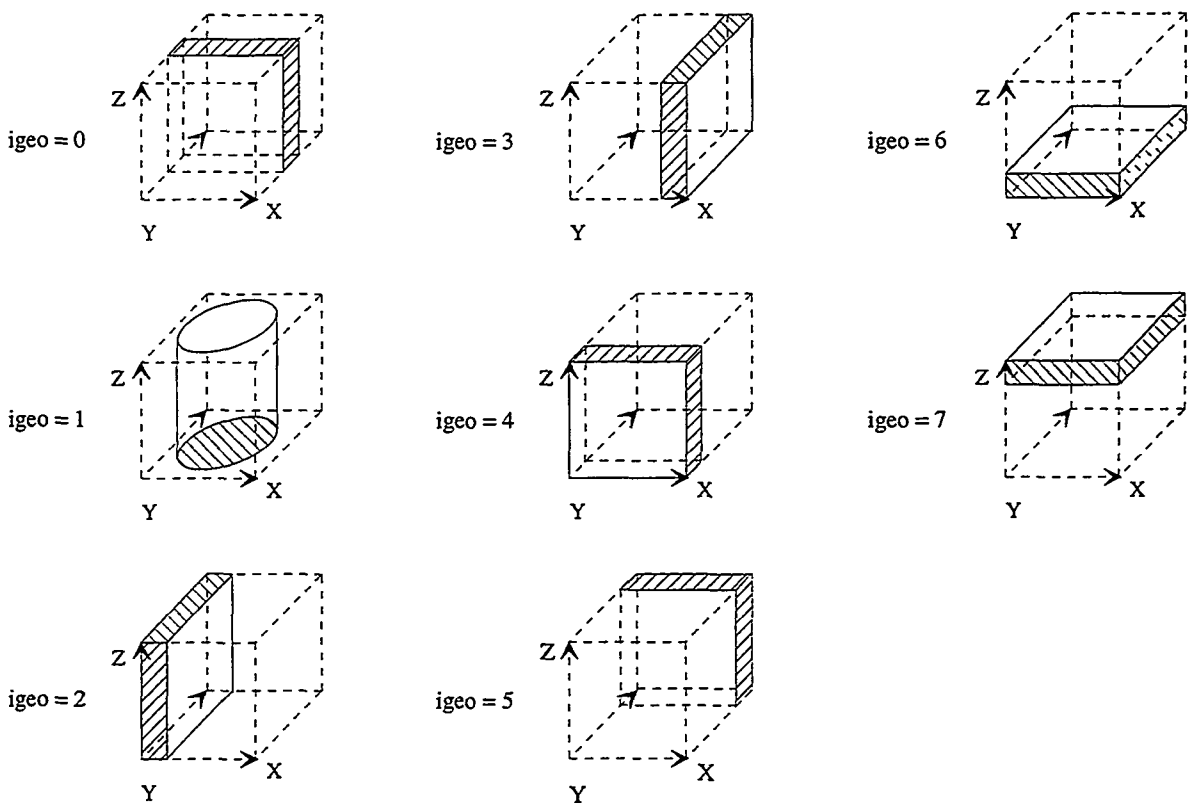

Figure 4-1. MERIS nodal geometry types.

The MERIS code has already been applied to an analysis of the XR1-1 and XR1-2 experiments[6] showing mixed success in predicting thermal trends and material relocation characteristics for those experiments. MERIS was able to adequately describe the general behaviour of the molten flow through the bladed and unbladed channels as well as the formation of blockages. However, it was not able to predict the subsequent failure of those blockages and resulting flow of material.

A possible explanation for this shortcoming is a failure of the code to properly address the dynamics of material interactions.

The XR2 test is a much more complicated geometry to model arising in more complicated flow paths and includes a high temperature zirconium melt pour. This test geometry can provide a more thorough assessment of MERIS for modeling melt relocation in BWR geometries.

4.2 MERIS Representation of the XR2 Experiment

The MERIS model developed here is intended to model the lower package during the stainless steel/B_4C wire phase of the XR2 experiment. The test package, extending from the lower surface of the core plate to the top of the fuel rods has been explicitly described in this model. The problem was nodalized and boundary conditions were selected to adequately describe this phase of the analysis. However, more detail in the lower structures will be required to model the zircaloy wire phase of the experiment.

4.2.1 Problem Nodalization

The XR2 geometry is adequately represented by a 28x28x36 X-Y-Z nodalization. On an XY planar cross-section at the fuel assembly elevation, this grid (see Figure 4-2) was chosen to correspond with significant features of the XR2 fuel pin lattice. For example, each fuel pin has been assigned its own cell and cells have been chosen to correspond to physical boundaries such as can walls and control blades. This is to ensure that when the local geometry parameter, igeo, is properly chosen, the MERIS model accurately describes both heat transfer and barriers to mass transfer for the local geometry. Cells outside the physical boundaries of the package (such as i=28, j=28) are treated as null cells and do not participate in the calculation. Cells along the XR2 package physical boundary, yet not at the edge if the XY grid (such as i=16, j=28) are treated as boundary cells and boundary conditions are applied at those cells.

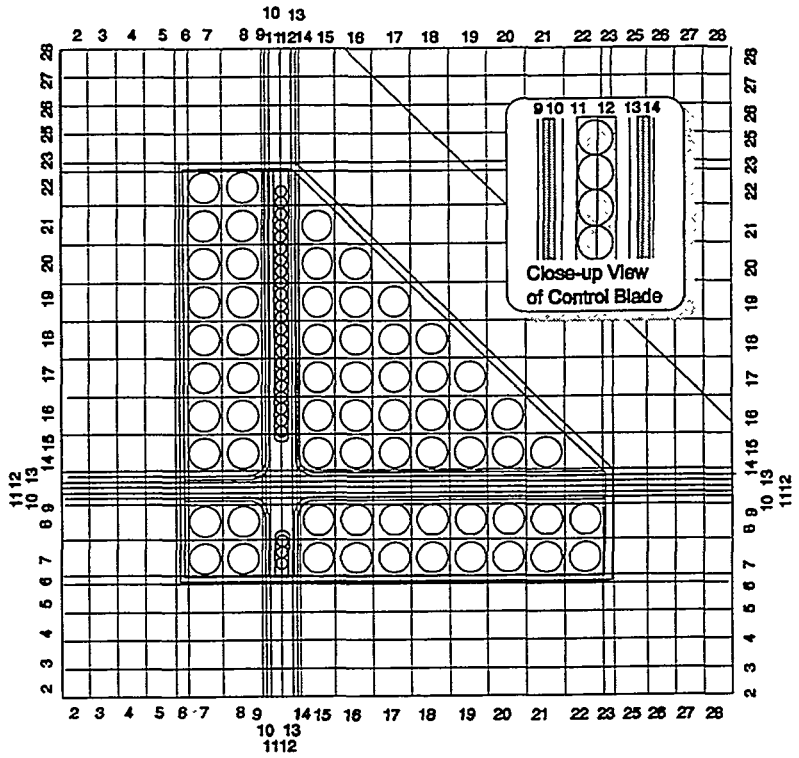

Figure 4-2. XY nodalization in the MERIS representation of the XR2-1 experiment.

The XR2 package has been modeled using 36 axial nodes (see Figure 4-3). Twenty-two of those nodes are located within the fuel assemblies resulting in an axial spacing of about 2.25 cm (≈ 1 inch) along the fuel rods and the active control blades. Below the fuel bundle, the axial spacing must be defined small enough to adequately describe the axially changing cross sections of lower structures. Note that because the current version of MERIS allows only structures that are orthogonally oriented, obliquely aligned surfaces have been approximated from orthogonal surfaces. Finer nodalization can achieve closer approximations to the actual geometry. Figure 4-3 shows lateral cross sections of lower structures at selected axial elevations in the MERIS model.

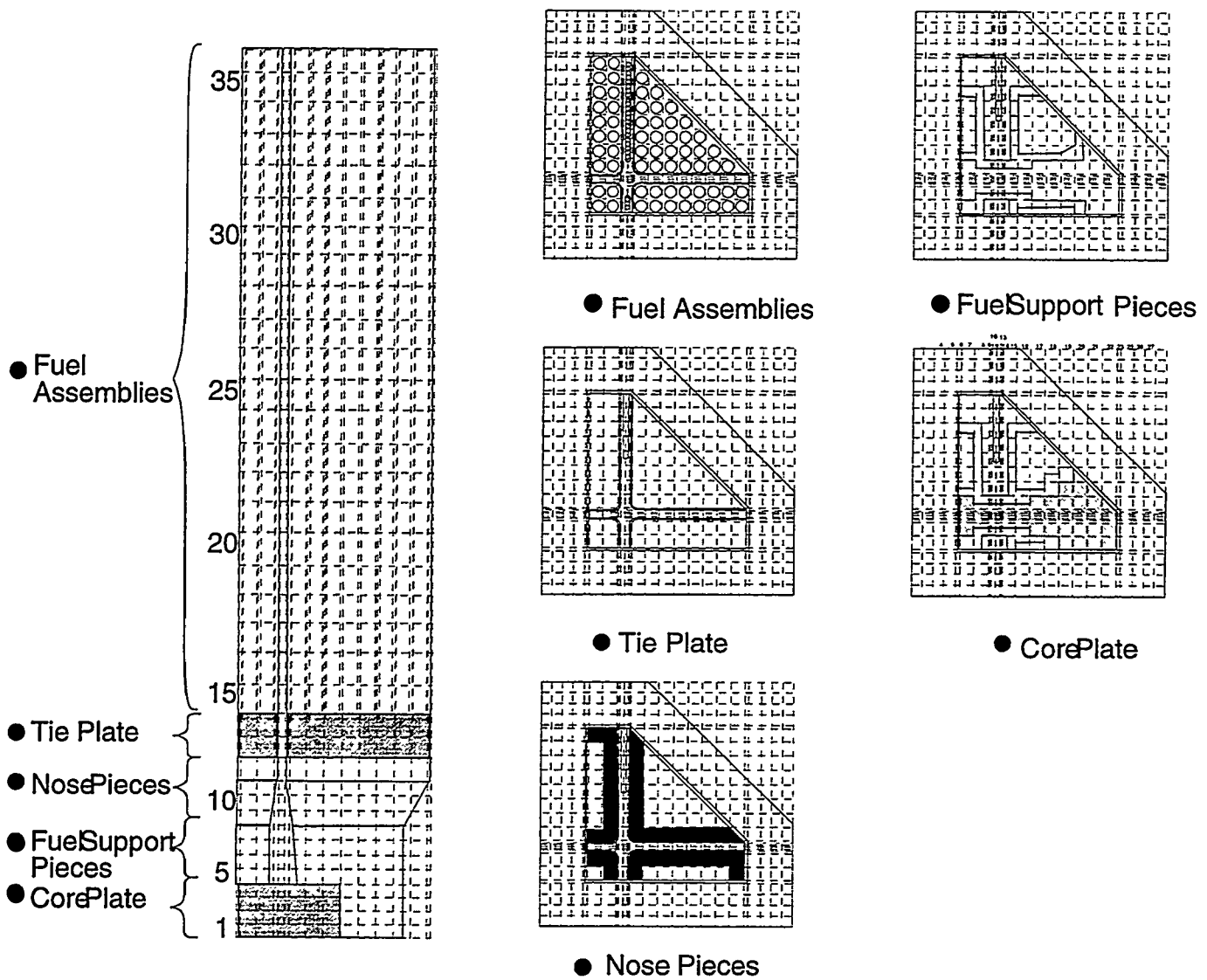

Figure 4-3. Axial MERIS nodalization.

4.2.2 Thermal and Physical Boundary Conditions

The thermal boundary conditions applied to the MERIS model are somewhat idealized models that utilize measured thermal conditions in the test package, wherever possible. For example, the lower boundary condition is that of a fixed sink temperature, where the boundary temperature used is taken from data recorded for thermocouples at the bottom surface of the core plate. This boundary condition is adequate during the steel/B_4C composite wire stage, where the temperature of the lower surface of the core plate does not vary much but would not be acceptable during the zircaloy wire stage since material relocating to the core plate heats the lower surface significantly.

This calculation also models heat conduction out the insulated sides of the package. The insulation is explicitly included in the model and a radiant boundary condition is applied at the outer surface of the insulation. Where the outer nodes are defined as null cells, the program searches for interior non-null regions where this boundary condition can be applied.

The top surface of the package receives the most significant external heat flux due to radiant heat transfer from the melter system above, and the calculation will be most sensitive to the boundary condition applied there. The radiant heat flux shining on the top of the package was estimated from data recorded for thermocouples and pyrometers in the melter system. Specifically, temperatures in the melter cavity and in the gate housing assembly were used in estimating the heat flux to the package.

In addition to thermal boundary conditions, the physical boundary conditions must also be defined. At the upper, open end of the package, molten material flows into the bladed channel at a predefined rate. This rate is known very well from the rate at which feed material is fed from the wire spools into the melter system (Figure 3-1). The distribution of molten material over the test package was assumed to correspond roughly to the wire guide pattern of Figure 2-2. Molten material was distributed uniformly over all cells directly below the wire guide tubes. The flow boundaries at the sides and bottom of the package are implemented through the local geometry parameter, igeo. Molten material cannot flow out the can walls unless the can walls have been degraded sufficiently by melting or material interaction. In addition, the core plate provides a lower boundary to flow. Material may exit the system only by passing through the opening in the fuel support piece or the control blade slot.

4.3 Results of the MERIS Modeling of the XR2 Experiment

The calculated MERIS results are to be discussed both qualitatively and quantitatively in light of previous observations for this experiment. The MERIS results should be able to qualitatively predict general material flow patterns that are consistent with the real-time x-ray images and the thermocouple characterization discussed above. It should also be able to quantitatively predict the gradual temperature adjustment in the package due to the change in the radiant heat flux when the gate is opened. More rigorously, it should be able to estimate both the timing and the extent of thermal transients recorded by thermocouples due to molten material dynamics. Finally, it should predict an end-state for the package that is consistent with the state of the package as determined by the post-test tomography.

4.3.1 Qualitative Results of the MERIS Calculation

The MERIS calculation was carried out through both the steel/B_4C composite wire and the zircaloy wire stages. The model predicted flow patterns consistent with observations from thermocouple responses and real-time x-ray image views during the steel/B_4C composite wire stage. Initially the composite material flowed down the length of the control blade forming blockages midway along the blade and forcing molten material to flow laterally to the open, unbladed channel. Thermocouple responses during the test indicated that the downward flow of

material progressed much farther near the junction between the bladed and unbladed channels than it did near the outer edges of the packages (where the center of the cruciform control blade would be). In addition, real-time X-ray images clearly showed that the the gaps between the control blade and the can walls remained open at the tie-plate elevation until about 17,900 seconds at which time material completely filled these lower gaps. In the MERIS calculation, blockages midway up the control blade prevented material from relocating to the tie-plate elevation until at 17,820 seconds, when the blockages remelted due to increasing temperatures and in part, to the reduced melting point of the $FeZr_3$ eutectic resulting from material interactions. By 18,100 seconds, MERIS predicted that this gap was completely closed by the downward draining material, as indicated by measured data.

The MERIS calculation predicted a lateral flow of material along the unbladed gap above the tie-plate elevation between 17,400 seconds and 18,220 seconds. Material freezes at the nose-piece, forcing molten material to build up behind the blockage and then flow out farther along the channel. It also predicted occasional drips of material along the core plate as the molten material moved farther from the control blade channel which was consistent with thermocouple responses. However, the MERIS model was unable to predict the massive relocation of material onto the core plate which took place at 17,900 seconds, just before the end of the steel/B_4C phase. The images from the MERIS model indicate that molten material was unable to relocate to the core plate after 17,700 seconds because of blockages in the unbladed channel near the top of the nose-pieces. There does not appear to be any tendency for those blockages to remelt until after the start of the zircaloy phase of the test when high temperature zircaloy melt reaches the insides of the lower can walls.

The results of the MERIS model were disappointing during the zircaloy phase of the test. The MERIS model was unable to predict the extensive relocation of material to regions below the core plate that were so characteristic of the experiment. The code predicted only trace amounts of melt draining through the nozzle and the control blade slot. Instead, it predicted that molten zircaloy drained to the nose-piece where it solidified and blocked the further passage of material through the nose piece opening. The molten zircaloy then formed a pool inside the nose piece which heated the can walls and melted control blade material lodged between the fuel canisters. The molten control blade material began to react significantly with the can walls at 18,300 seconds, generating heat and forming the lower melting point $FeZr_3$ eutectic (see Figure 4-4). At 18,500 seconds, some of the molten material pooled up in the unbladed channel broke through the remelting blockages and molten material fell onto the core plate and the smaller, single fuel support piece. This agrees with the timing of a similar event observed in the XR2 test as will be discussed below. However, there was no corresponding sudden relocation of material through the nose piece as was observed at 18,600 seconds and it failed to predict the relocation of material down the control blade guide tube at 19,100 seconds. The molten pool continued to fill

the upper test section and even overflowed into the insulation at 18,700 seconds.

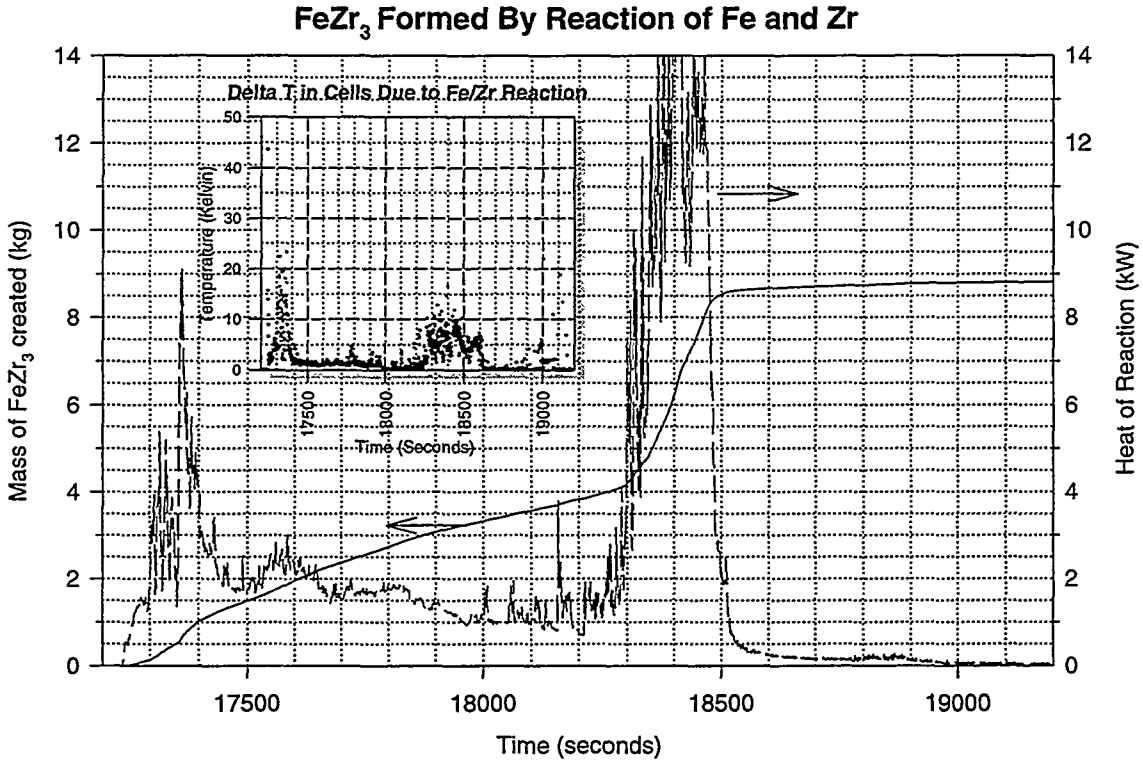

Figure 4-4. Interaction of Fe and Zr to form eutectic calculated by MERIS.

Animation sequences in MPEG format were generated for the fuel assembly and nose piece as well as both the bladed and unbladed channels extending from the bottom of the core plate to the top of the test assembly. These images indicate the volume of material that moves into a cell — the darkness of each pixel is proportional to the fraction of the cell's available volume (the total volume less the volume of any unmelted test package material) that is filled with relocated material. In addition, the pixel may be colored in order to indicate the composition or phase of the relocated material — black is for a cell containing more than 99 percent solid material of any composition, green is for 99 percent liquid zircaloy, magenta is for 99 percent liquid steel/B_4C composite material, and red is for liquid material composed of zircaloy, steel/B_4C, and possibly other eutectics. These images provide very detailed and relatively unambiguous views of the calculated material relocation dynamics and material phase changes for the downward flowing metallic melt in the BWR geometry.

Figure 4-5 and Figure 4-6 show selected frames from the MPEG files generated by MERIS for the steel/B_4C composite wire and the zircaloy wire stages, respectively. These figures indicate that MERIS predicted temporary blockages between the control blade and the can walls early in the test. Molten material was then forced to flow laterally along the control blade into the unbladed channel where it was free to flow downward to the core plate. Blockages also formed

near the nose piece in the unbladed channel within the first 90 seconds, restricting flow to the core plate below. Molten material pooled up in the bladed channel over the next 3 minutes until the top of the pool approached the top of the can walls. At about 17,420 seconds, material flowed down and laterally across the unbladed channel. Small quantities of melt arrived at the core plate at about 17,470 seconds, but again, blockages formed above the core plate near the top of the fuel support piece. At 17,740 seconds some of the blockages in the bladed channel began to remelt and material began to drain from the molten pool, arriving near the bottom of the nose piece structures at about 17,820 seconds where it again froze, forming blockages that prevented the further transfer of material to the core plate. These figures show projections of relocating material within the fuel canisters and in the nose pieces. Structural materials, i.e. cladding and the spacer grid near the top of the fuel canisters, melted early from the intense radiant heat flux above. This can be seen in these figures as material collected and solidified between fuel rods above the tie plates. Additionally, during the steel/B_4C phase, control blade material was found to relocate into the fuel canisters as the can walls were degraded by material interactions and the intense heat flux above.

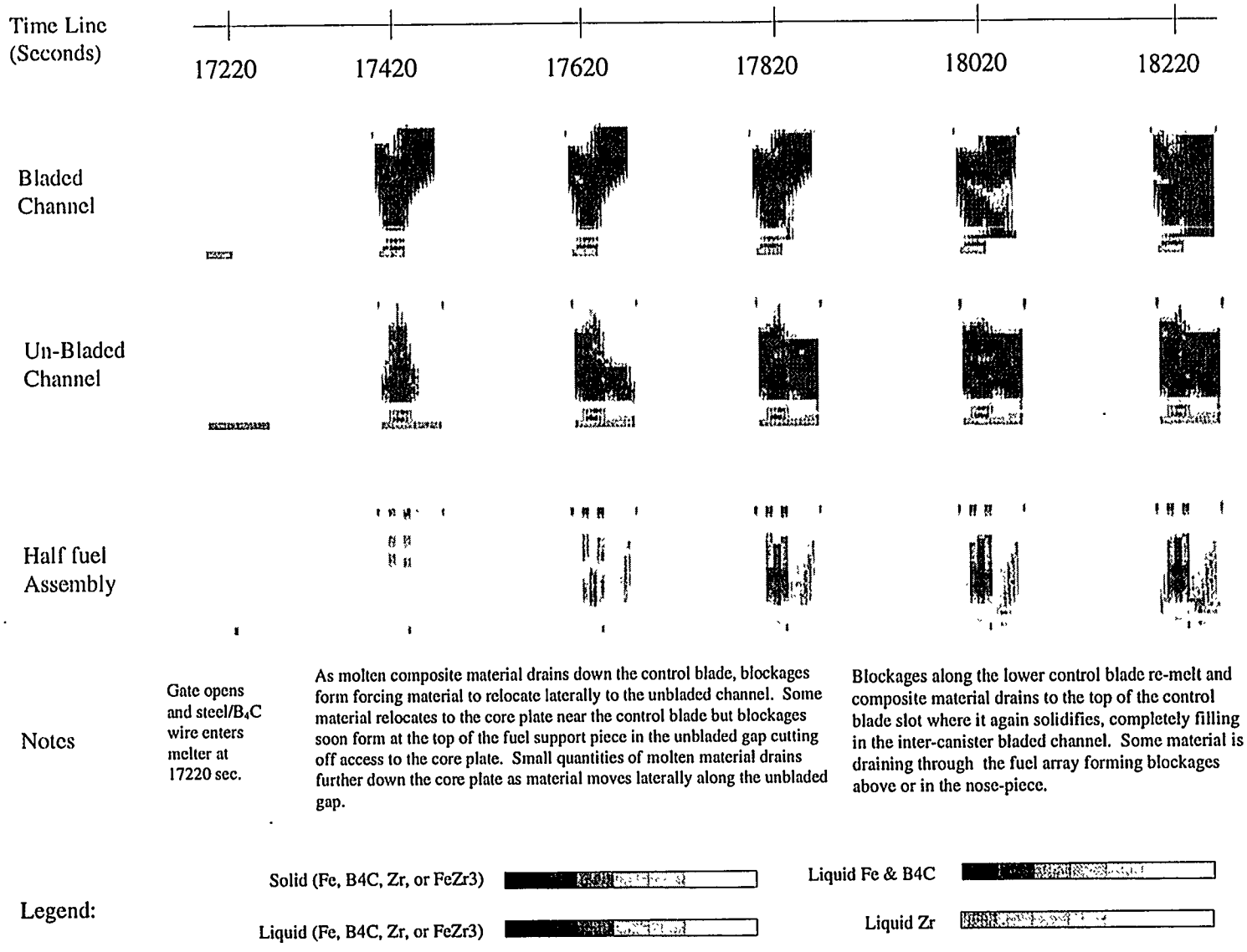

Figure 4-5. MERIS MPEG frames during composite wire feed.

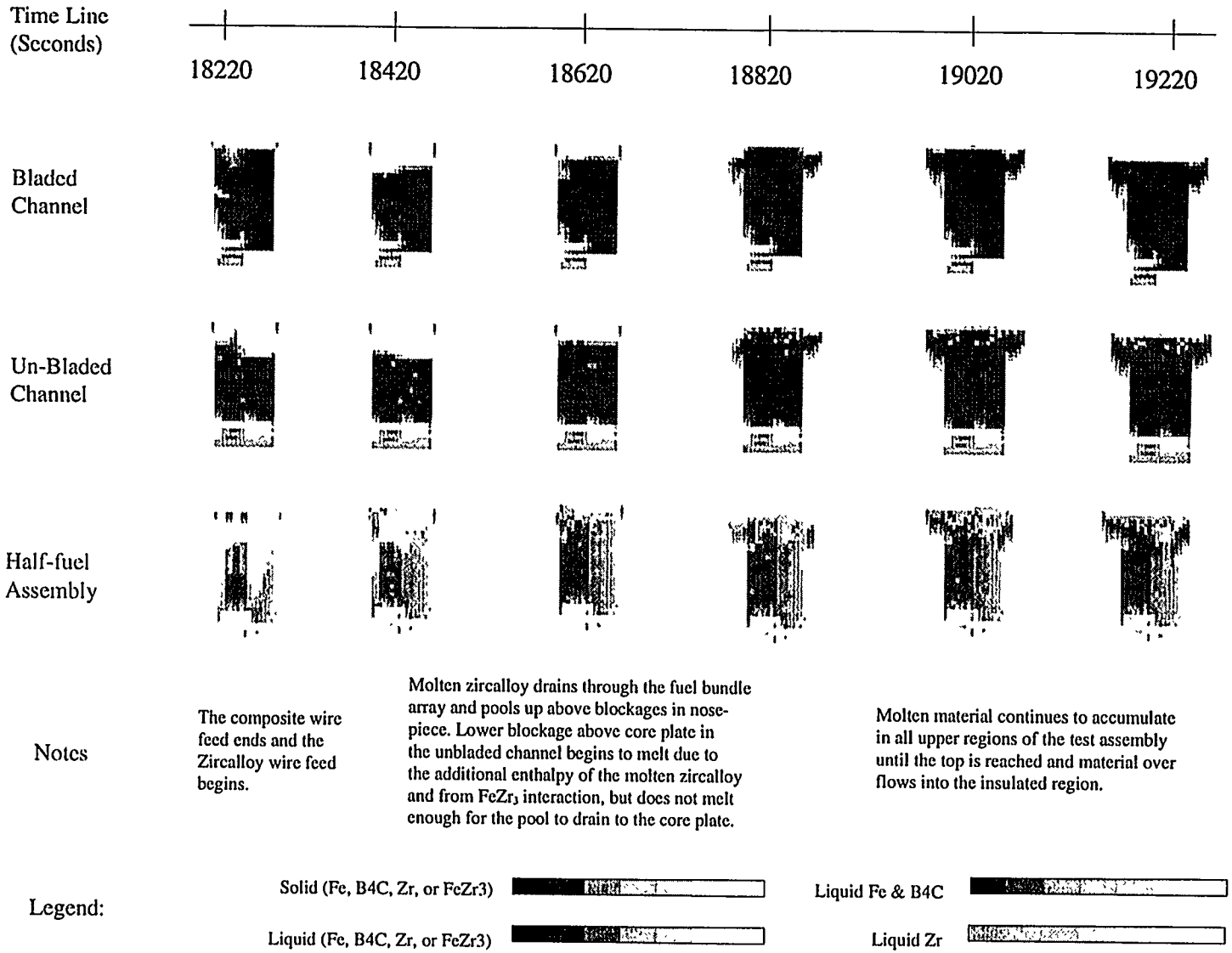

Figure 4-6. MERIS MPEG frames during zircaloy wire feed.

4.3.2 Quantitative Results of the MERIS Calculation

As previously noted, qualitatively the MERIS model developed here was unable to predict many of the major relocation events which occurred during the zircaloy wire feed phase. Most importantly, it did not predict the final end state of the XR-2 test package where 70-80 percent of the volume of material available for relocation was found below the core plate. It did, however, qualitatively describe many of the flow characteristics observed during the steel/B_4C wire phase. Quantitatively, MERIS also showed mixed success in predicting the thermocouple responses for the XR2 experiment. As seen in Figure 4-7 and Figure 4-8, the temperatures predicted for the upper three zones showed some agreement with the collected data. Keep in mind that these thermocouples failed above 2000 K, so there is no means of confirming the maximum temperatures attained in the top thermocouples. Agreement between calculated and observed temperatures for core region 3, CR3, did break down near 18,000 seconds, when the observed temperatures were about 200 K higher than expected. At core region 4 the calculated temperatures were much higher than measured temperatures until 18,700 seconds. This may be an indication that blockages in the bladed channel occured much higher than predicted by MERIS resulting in less material relocating to the core region 4 thermocouples.

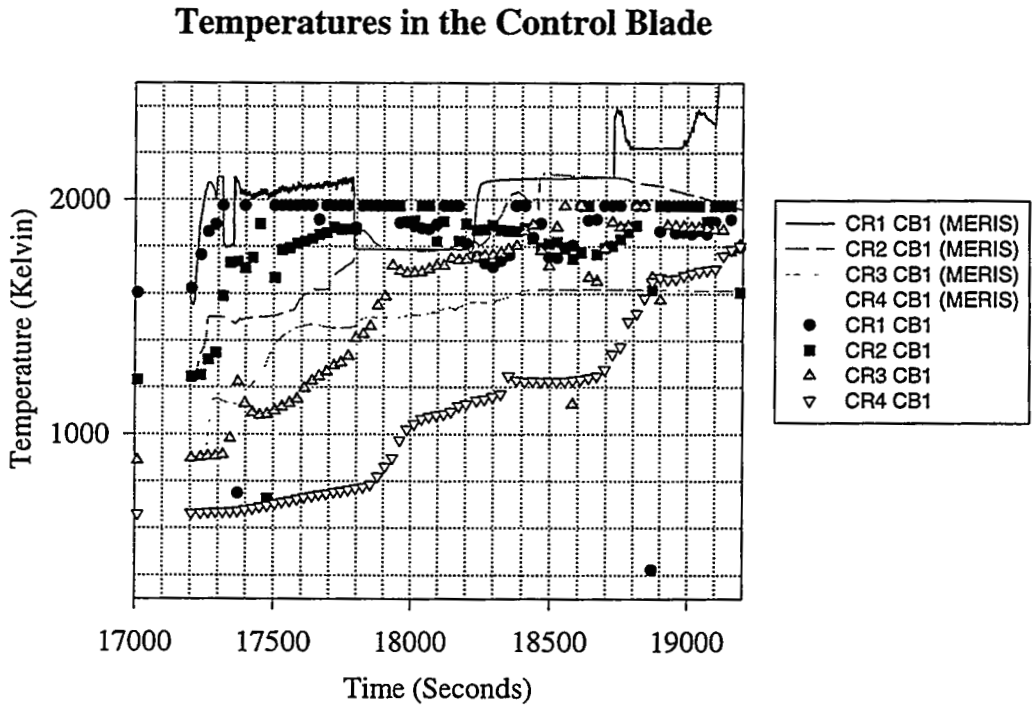

Figure 4-7. MERIS calculated temperatures in the control blade (CB1).

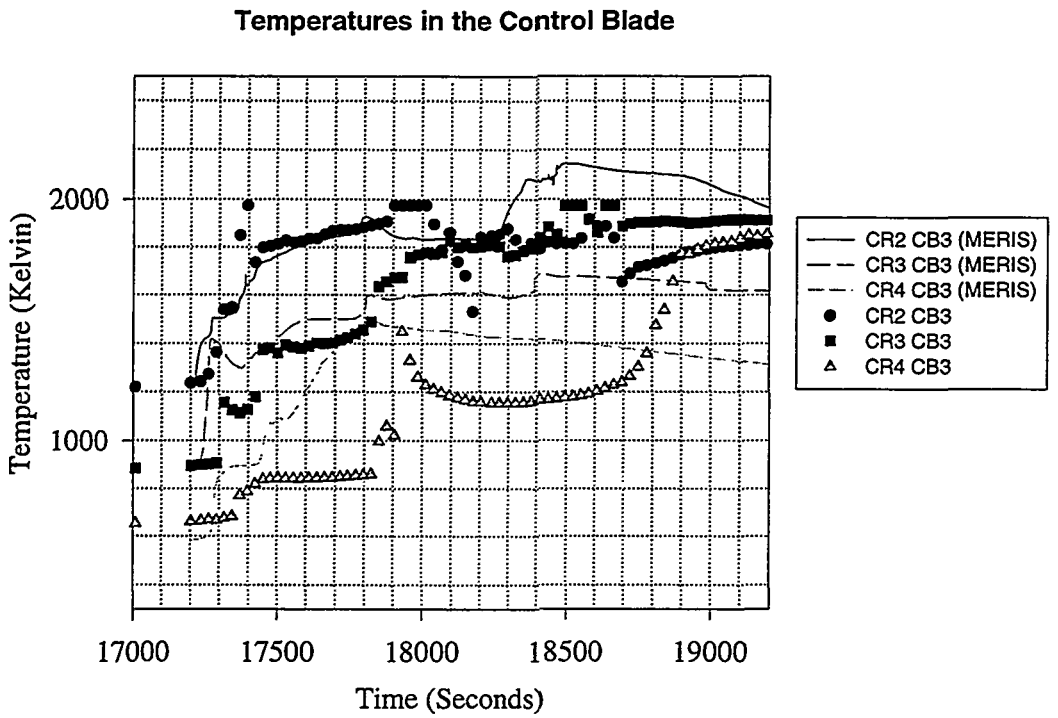

Figure 4-8. MERIS calculated temperatures in the control blade (CB3).

Measured temperature responses in the core plate give indications of the timing and extent of material relocation onto that structure. Figure 4-9 shows the comparison between the calculated thermocouple responses and the observed thermocouple responses in the XR-2 core plate structure during both the steel/B_4C wire phase and the zircaloy wire phase. MERIS correctly predicts a large thermal response in the CPT3 thermocouple shortly after beginning the steel/B_4C phase, though the predicted response is not as large as observed. The observed response also appears to dampen more slowly with two or three smaller temperature rises superimposed on the tail of the initial spike, indicating that material continued to fall to the core plate near CPT 3 until about 17,500 seconds. The relocation of material to the core plate in the MERIS calculation is curtailed early on due to the formation of a blockage near the top of the nose piece. This blockage apparently forms too soon and is apparently effective in preventing molten material to reach the core plate.

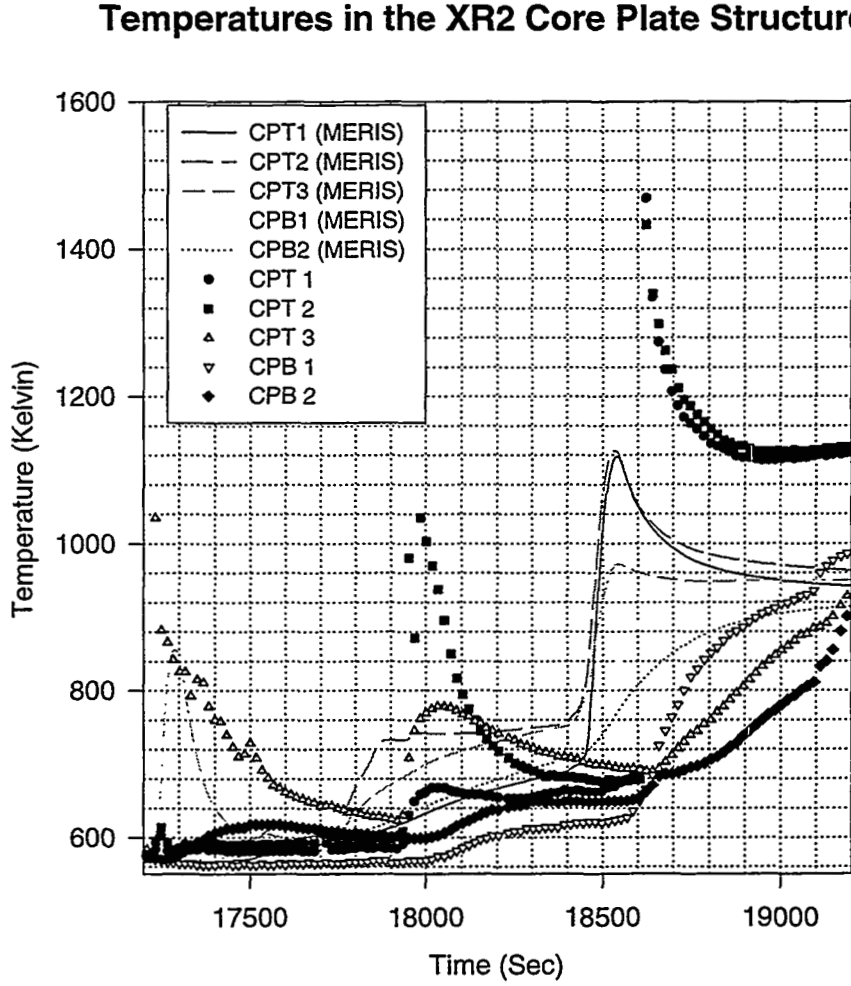

Figure 4-9. Thermocouple responses in the core plate structure.

At 17,990 seconds, there was a large and sudden rise in the temperature recorded for CPT2 and to a lesser extent, CPT3 and CPT1. MERIS predicted a similar though smaller and much more gradual increase in these core plate temperatures occurring 250 seconds earlier. The slow response is probably explained by the fact that the molten material freezes just above the core plate and the heat is conducted slowly to the core plate below.

Finally, at 18,600 seconds, shortly after the zircaloy wire phase had begun, measured temperatures in the core plate rose quite dramatically indicating an extensive relocation of molten material to the core plate. MERIS predicted a similar relocation at 18,500 seconds, though it was not as extensive and did not lead to the filling of the area above the core plate as seen in the final end-state. This calculated relocation event resulted from

the gradual erosion and liquefaction of blockages in the unbladed channel at the top of the nose piece releasing a small amount of molten material to the core plate.

There were other similarities found in the time-temperature plots for locations in the fuel support pieces. It was previously noted that MERIS predicted that the flow of material down the open junction between the bladed and unbladed channels is quickly curtailed as blockages form at the top of the nose piece. This resulted in a smaller and shorter temperature response in the core plate just after the start of the steel/B_4C composite wire phase. Likewise, the calculated temperature response in the fuel support piece near the control blade slot is also not as extensive (see Figure 4-10).

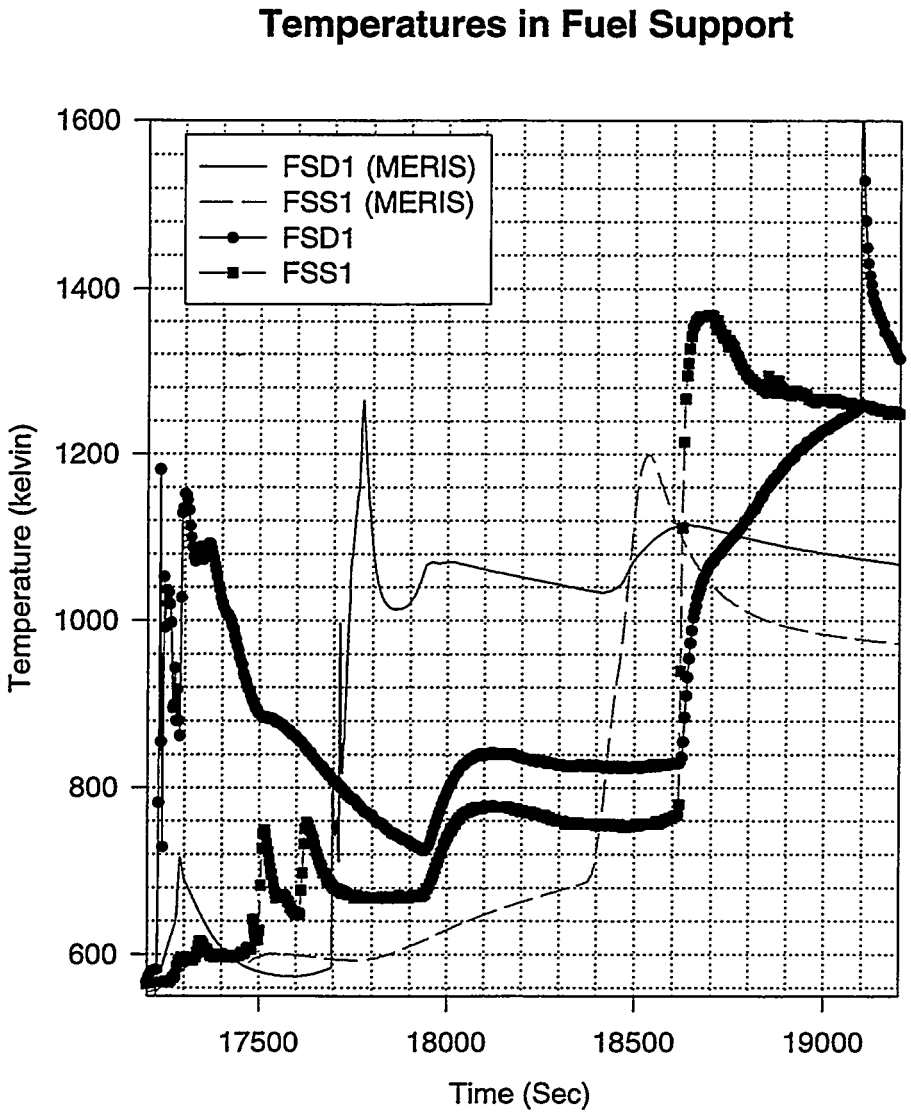

Figure 4-10. Thermocouple responses in fuel support pieces.

4.4 Summary of the MERIS Assessment of the XR2 Test

Though the MERIS model developed for this assessment was unable to predict the large-scale relocation of material to regions below the core plate that clearly characterizes the XR2 test, it was capable of describing many of the flow characteristics observed early on in the steel/B_4C composite wire phase. Solid-liquid heat transfer, liquid mass transfer, and material interactions all play important roles in describing the formation of blockages, the formation of molten pools, the failure of blockages and the subsequent drainage of molten pools. Both qualitative and quantitative evidence indicates that many of the important physical processes for heat transfer and material relocation are modeled in these calculations. However, the model is not yet able to predict the subsequent failure of blockages that leads to the draining of molten material below the core plate. The current MERIS model may not adequately describe the dynamics of material interactions which lead to lower melting point eutectics and would result in the erosion of solid blockages.

The scope of this work did not allow a thorough parameter sensitivity analysis to determine the effects of varying user-defined parameters. For instance, the degree to which the liquid flow contacts solid materials is crucial in determining the location of blockages and the extent to which materials relocate below the core plate. This parameter determines not only the heat transfer between solid and liquid phases, but also the axial drag coefficient. These calculations assumed a film flow approximation, overstating the heat transfer between solid and liquid phases and also overstating the drag coefficient. The lateral drag coefficient is also not very well known and it has been assumed to be very small in these calculations. Furthermore, the degree of superheat in the dripping molten material is also unknown and should be varied, though calculations have shown that molten droplets falling through the melter cavity probably do not receive more than 20-50 K of superheat. Further variations of these and other parameters may also result in a more accurate representation of the experiment and lead to a more extensive drainage of materials to regions below the core plate.

5. CONCLUSIONS

In the Ex-Reactor testing program, three melt progression tests have been performed, two simple channel tests (XR1-1 and XR1-2), and one full geometry test (XR2-1) characterized as a highly realistic and full scale representation of the lower BWR reactor core region. The Ex-Reactor tests are nearly full-scale, both with respect to the geometry and the melt mass involved, and make use of prototypic materials to simulate as faithfully as possible the accident conditions expected for a Short Term Station Blackout (STSB) accident in a US BWR. Similar general behavior was observed in all of the tests, the most significant being the initial formation of blockages by the draining metallic melts, and the subsequent catastrophic failure of those blockages, resulting in the sudden drainage of melt to lower regions. The drainage can result in metallic materials bypassing the core plate region by several different natural flow paths in the BWR lower core region (see Figure 1-2).

It is also clear from these tests that the BWR fuel canister/bypass geometry is degraded early in the core melt progression when the channel walls are destroyed by the highly aggressive eutectic action of the molten control blade alloy. Additionally, the subsequently draining zircaloy melt was observed in the XR2-1 test to cause significant disruption of the fuel rod configuration, and may be an early initiator for the transition from a rodded to a rubblized core geometry. Transfer of molten metallic materials to the lower plenum region under reactor accident conditions may be significantly enhanced by the aggressive material interactions, especially the Fe-Zr eutectic behavior thought to have been important in the Ex-Reactor experiments.

Below the rodded region of the simulted core, the BWR structures appeared to retain their geometric integrity providing physical boundaries to the draining liquefied metals. There was no evidence of gross failure of the core plate, the fuel support pieces or the nose pieces. Even so, more than 70 percent of the total molten inventory either delivered to the XR2-1 package or generated in the package, relocated into regions beneath the core plate. Three relocation paths were idendified in Figure 1-2 that could result in such material transfer below the core plate, i.e., melt relocation through the nose piece into the inlet nozzle, melt relocation down the unbladed channel onto the core plate, and melt relocation through the bladed channel into the drive tube. There is evidence that all three of these relocation paths contributed to the overall relocation of material to the lower catch basin.

Material completely filled the nose pieces and inlet nozzles in the fuel support pieces. Temperature responses of thermocouples at the bottom of the inlet nozzle indicate that this event took place at 18,600 seconds and was probably the first large-scale relocation event that deposited molten material into the catch basin. Coincidental timing of thermocouple responses at the bottom of the inlet nozzle and temperature responses in the catch basin would confirm this as a pathway for molten materials (most likely zircaloy through this pathway) into the catch basin. Subsequently, at 19,100 seconds, material drained rapidly

through the drive tube onto the velocity limiter, and then into the catch basin. Post-test images of the control blade guide tube and velocity limiter show that molten material drained out along the velocity limiter, eventually accumulating nearly 10 kg of material that solidified on the velocity limiter. Again, the coincidental thermal responses in the velocity limiter and a very substantial temperature response in the catch basin substantiates this also as a path for material to access the lower catch basin.

Evidence also indicates that a considerable inventory of material accumulated on the core plate. While the nose piece and core plate remained intact throughout the test, as expected, the material on the core plate accumulated to elevations much higher than the top of the control blade guide tube and most likely contributed to the mass of material draining down the guide tube onto the velocity limiter. Although the composition of material below the core plate is unknown, it is likely that material relocating through these pathways would be composed of both control blade material and zircaloy as well as "eutectic" mixtures.

The XR2-1 experiment has for the conditions explored, demonstrated the tendency for molten metal relocation to the lower plenum in a BWR core through existing pathways in the lower core structures. More than 70 percent of the relocating molten metals ultimately drained to regions below the core plate. The balance of the metallic melt was found to have formed non-coherent partial blockages in regions on and just above the lower core plate. Continued decay heating (under real accident conditions) could be expected to result in further draining of the remaining core region metallic materials to the lower vessel region. In this investigation, the XR2-1 results resemble the "continuous drainage" pathway illustrated in Figure 1-1.

Earlier analysis of the XR1-1 and XR1-2 tests and even analysis of the XR2 test demonstrate the ability of the MERIS code to describe many features of the melt progression during the early stages of the STSB accident, i.e., before the zircaloy metals relocate to the bottom of the fuel assemblies. However, MERIS was unable to predict the extensive relocation of molten materials below the core plate during the zircaloy melt phase. MERIS predicted that blockages form in the nose piece and the top of the control blade slot, preventing material from draining to the lower head. Even the XR1-1 and XR1-2 tests demonstrated the failure of MERIS to predict crust failure. A possible explanation for this shortcoming is a failure of the code to properly address the dynamics of material interactions. Further analysis is necessary to identify reasons for this important discrepancy.

Finally, the information from XR2-1 concerning the core plate thermal response can be used to evaluate the failure behavior of the core plate under the physical loading conditions expected in a reactor accident. Subsequent analyses making use of the XR2-1 end state observations should consider the effects of fuel pellet agglomeration by zircaloy and the possible U-Zr-O "metallo-ceramic" material composition, and the likelihood that the draining metallic materials have effectively fused the core plate to the control blade drive tubes. Both effects could influence the net distribution of the core weight load over the core plate and drive tube structures. The current results can be further projected into the reactor scale regime by additional analyses. Quantitative extrapolation of the experiment results to a reactor evaluation will require the use of a tool like MERIS. The analysis would account for

sustained heating from above, embedded decay heating, and the differences in radial heat transfer. Such analyses were beyond the scope of this work, but could be accomplished with additions or modifications to the MERIS model.

6. REFERENCES

[1] F.P. Grifin and L.J. Ott, *Development of the BWR Dry Core Initial and Boundary Conditions for the SNL XR2 Experiments*, ORNL/NRC/LTR-94/38, Oak Ridge National Laboratory, Oak Ridge, TN, 1994.

[2] P. Hofmann, M.E. Markiewicz, and J.L. Spino, Reaction Behavior of B_4C Absorber Material with Stainless Steel and Zircaloy in Severe Light Water Reactor Accidents, *Nuclear Technology*, 90, 226, 1990.

[3] R.O. Gauntt, M. J. Rightley, R.C. Schmidt and S.C. Bourcier, *Data Report on the XR1-1 and XR1-2 BWR Metallic Melt Relocation Experiments,* NRC FIN L-1468, Sandia National Laboratories, Albuquerque, NM, 1994.

[4] R.C. Schmidt, *MERIS: A Model for Melt Relocation in Core Structures of Nuclear Reactors During Severe Accident Conditions,* NRC FIN L-2452, Sandia National Laboratories, Albuqerque, NM, October 1993.

[5] R. W. Wright, Status of Technical Issue Resolution: Core Degradation and Melt Progression, *Trans. ANS*, 73, October 1995.

[6] R.C. Schmidt and L.L. Humphries, *Analysis of the XR1-1 and XR1-2 Melt Progression Experiments with the MERIS Computer Code: Results and Assessment of Models,* NRC FIN L-2452, Sandia National Laboratories, Albuquerque, NM, January 1997.

APPENDIX A

Radiant Heat Transfer Model

Contents

Figures

APPENDIX A

Radiant Heat Transfer Model

The radiant heat transfer model for the melter cavity and the melter exit duct (see Figure A-1) were critical in determining coil power requirements, as well as in predicting temperatures in the lower XR2 package and in the wire guide tubes entering the melter upper end. In its simplest description, the XR2 melter system can be described as a large insulated tube closed on the upper end and open or closed on the lower end, depending on the position of the gate. The radiant heat loss out the open end becomes increasingly more important as either the length over diameter ratio of the tube decreases or as the temperature gradient along the axis increases. Even when the length of the tube is large in comparison to its diameter, heat exchange within a few diameters of the open end of the tube will be severely impacted by the lower environment. A significant complication to this simplistic description results from the two chamber design of the XR2 melter, i.e., the lower chamber or exit duct has a smaller (not even cylindrical) internal cross section than the upper radiant cavity. This discontinuous internal cross section leads to an obstruction of the view between locations on the upper and lower chambers which complicates the calculation of the view factors. The following is a short discussion of the radiant heat transfer model used in the analysis for the XR2 experiment. For a more thorough understanding of radiant heat transfer methods the reader is referred to a number of textbook discussions on the subject. [A-1,A-2,A-3]

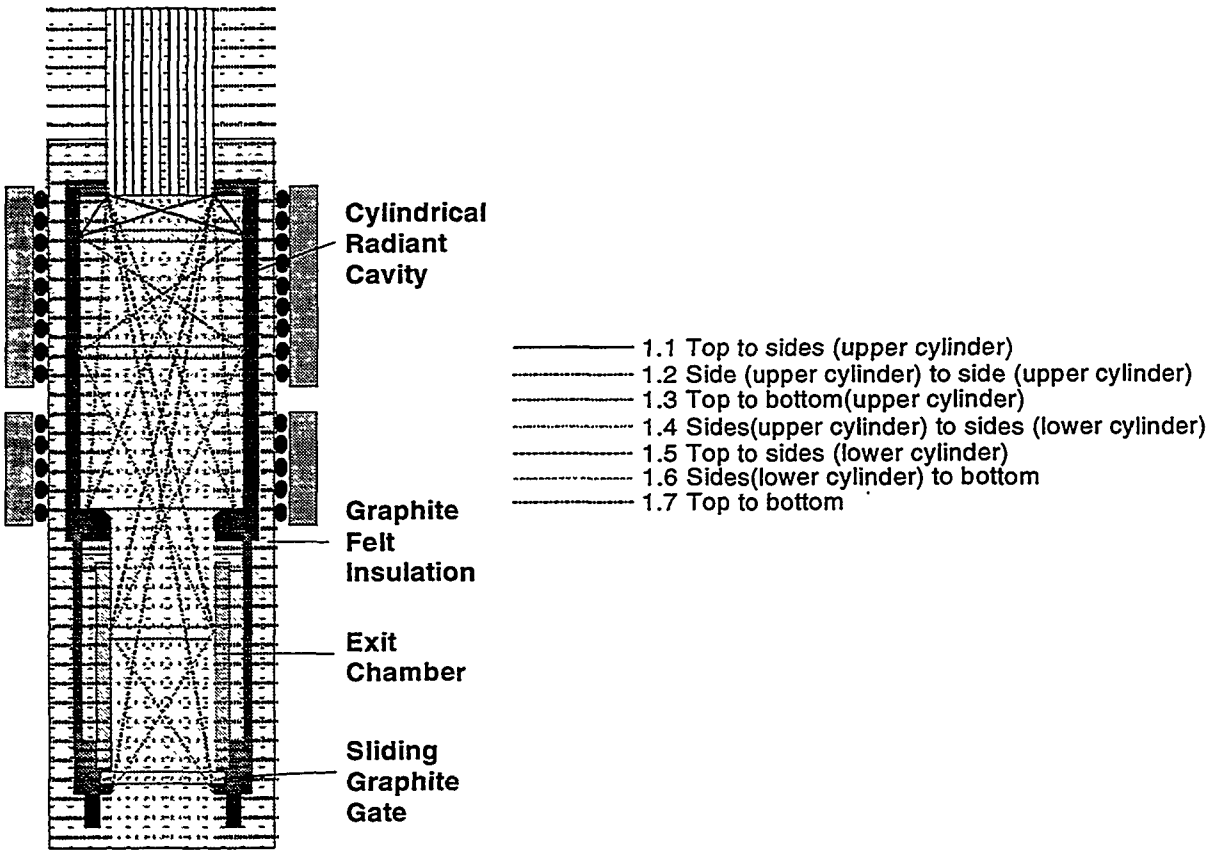

Figure A-1. Melter system and radiant heat transfer geometries.

Assuming that radiant exchange between internal surfaces is not greatly affected by the intervening argon fill gas and that all radiating surfaces are diffuse, gray emitters and reflectors, we can write the following equation for the net radiation heat flux at the location $\vec{x}$:
where B, the outgoing radiant energy or radiosity is calculated from:

$$q''(\vec{x}) = \frac{\varepsilon(\vec{x})}{1-\varepsilon(\vec{x})}\left[\sigma T_w^4(\vec{x}) - B(\vec{x})\right]$$

$$B(\vec{x}) = \varepsilon(\vec{x})\sigma T_w^4(\vec{x}) + (1-\varepsilon(\vec{x}))\left[\int_{\substack{bottom\\end}} B(\vec{\zeta}_{bot})F_{dA_x \to A_{bot}} + \int_{\substack{top\\end}} B(\vec{\zeta}_{top})F_{dA_x \to A_{top}} + \int_{\substack{upper\\cylinder}} B(\vec{\zeta})dF_{dA_x \to dA_\zeta} + \int_{\substack{lower\\cylinder}} B(\vec{\zeta})dF_{dA_x \to dA_\zeta}\right]$$

or

$$B(\vec{x}) = \alpha(\vec{x}) + (1-\varepsilon(\vec{x}))\left[\int_{\substack{all\\surfaces}} B(\vec{\zeta})dM\right],$$

where

$$\alpha(x) = \varepsilon(\vec{x})\sigma T_w^4(\vec{x}) + (1-\varepsilon(\vec{x}))\left[\int_{\substack{bottom\\end}} B(\vec{\zeta}_{bot})F_{dA_x \to A_{bot}} + \int_{\substack{top\\end}} B(\vec{\zeta}_{top})F_{dA_x \to A_{top}}\right].$$

The assumptions upon which this equation is based are quite good for monatonic gases such as argon and the graphite surfaces that exist in the XR2 melter design. Emissivity properties for graphite and other materials are included in Appendix D.

This integral equation can be cast in finite difference form as follows:

$$M_{i,j} = F_{dA_i \to dA_j} \cdot (1-\varepsilon_i),$$

where

$$\alpha_i = \sigma\varepsilon_i T_i^4$$
$$\overline{B} = \overline{\alpha} + \overline{B}\,\overline{\overline{M}}$$
$$\overline{B} = \left[\overline{\overline{I}} - \overline{\overline{M}}\right]^{-1} \cdot \overline{\alpha}.$$

The matrix $\overline{\overline{M}}$ contains view factor information for the given geometry. The view factor is defined as the fraction of diffusely distributed radiation leaving surface dA_i that is intercepted by surface dA_J. The net radiant heat flux can then be calculated as a function of position $\vec{x}$ by first calculating view factors between nodal surface areas and then solving for matrix $\overline{B}$ by performing the required matrix inversion.

The XR2-1 melter has been nodalized as shown in Figure A-1. There are 27 axial cells in the upper melter cavity and 34 cells in the lower exit duct. In the TAC2D model of the melter, the net radiant heat flux at each internal surface was calculated for each time step from the above equations and used as boundary conditions to complete the definition of the heat transfer problem. Critical to this calculation is the determination of view factors between surfaces. These view

factors contain only geometric information and therefore, need only to be evaluated once in the TAC2D calculation. The following discussion addresses the formulation of view factor equations for the various surfaces shown in Figure A-1 from simple, well-known view factor formulas and some view factor algebra.

A.1 Calculation of Surface View Factors

A.1.1 Top surface elements to side surface elements (upper cylinder) [see Figure A-2]

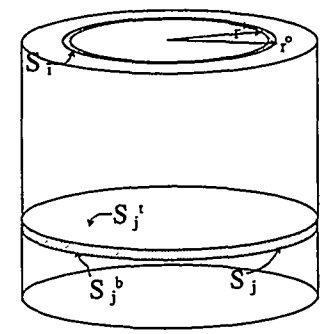

Figure A-2. Top to sides (upper cylinder) geometry.

In terms of view factor algebra, the view factor from surface S_i to S_j (the shaded surfaces in Figure A-2) is calculated as the difference between the view factor from surface S_i to surface S_j^t (the disk which bounds surface S_j at the top), and the view factor from surface S_i to surface S_j^b (the disk which bounds surface S_j at the bottom). This is equivalent to saying that the radiation emitted from surface S_i that enters the upper surface S_j^t, must either reach surface S_j or surface S_j^b. A similar "algebraic" procedure is used in determining the view factors from surfaces S_i , the circular annular ring to surface S_j^t (or S_j^b). First the view factor from disk S_j^t to surface S_i, $F_{S_j^t \to S_i}$, is calculated, and then the reciprocity relationship is used to find $F_{S_i \to S_j^t}$, i.e.,

$$F_{S_i \to S_j^t} \cdot Area_{S_i} = F_{S_j^t \to S_i} \cdot Area_{S_j^t}$$

$F_{S_j^t \to S_i}$ is also calculated algebraically from $F_{S_j^t \to S_i} = F_{S_j^t \to S_i^o} - F_{S_j^t \to S_i^i}$, where the superscript o refers to the circular disk whose perimeter corresponds to the outer perimeter of the annular ring S_i and the superscript i refers to the circular disk whose perimeter corresponds to the inner perimeter of S_i. Finally the equation for the view factor for this geometry can be written as:

$$F_{S_i \to S_j} = \left(F_{S_j^t \to S_i^o} - F_{S_j^t \to S_i^i}\right)\frac{Area_{S_j^t}}{Area_{S_i}} - \left(F_{S_j^b \to S_i^o} - F_{S_j^b \to S_i^i}\right)\frac{Area_{S_j^b}}{Area_{S_i}}.$$

For this case, view factor algebra together with reciprocity relationship have been utilized to formulate the view factor for radiation from a circular annular ring element to a concentric cylindrical ring element using only the formula for view factors between parallel concentric circular disks. The formula for the disk-to-disk view factor is readily found in the above references and is included here for completeness:

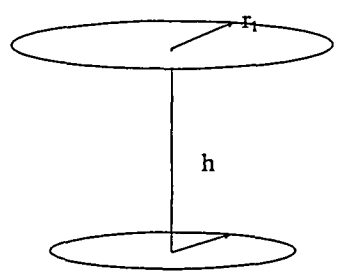

$$R_1 = \frac{r_1}{h} \quad R_2 = \frac{r_2}{h}$$

$$X = 1 + \frac{1 + R_2^2}{R_1^2}$$

$$F_{1 \to 2} = \frac{1}{2}\left[X - \sqrt{X^2 - 4\left(\frac{R_2}{R_1}\right)^2}\right].$$

A.1.2 Side surface elements to side surface elements (same cylinder) [see Figure A-3]

The view factor for surface S_i, the cylindrical segment at axial location i, to surface S_j, the cylindrical segment at axial location j, is the difference between the view factor from surface S_i to the disk which bounds surface j at the bottom, S_j^b, and the viewfactor from the surface S_i to the disk which bounds surface j at the top, S_j^t, i.e.,

$$F_{S_i \to S_j} = F_{S_i \to S_j^b} - F_{S_i \to S_j^t} .$$

Likewise,

$$F_{S_j^t \to S_i} = F_{S_j^t \to S_i^t} - F_{S_j^t \to S_i^b}$$

$$F_{S_j^b \to S_i} = F_{S_j^b \to S_i^t} - F_{S_j^b \to S_i^b} .$$

Finally, using the reciprocity relationship for view factors, i.e.,

$$F_{S_i \to S_j^t} \cdot Area_{S_i} = F_{S_j^t \to S_i} \cdot Area_{S_j^t}$$

We obtain the following equation for the view factor between segments of a cylinder in terms of view factors between the concentric parallel disks that prescribe the ends of those segments:

$$F_{S_i \to S_j} = \left[\left(F_{S_j^b \to S_i^t} - F_{S_j^b \to S_i^b} \right) - \left(F_{S_j^t \to S_i^t} - F_{S_j^t \to S_i^b} \right) \frac{Diameter}{4dz_i} \right]$$

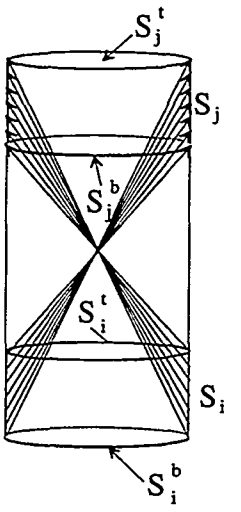

Figure A-3. Side to side (same cylinder) view factor geometry.

A.1.3 Top surface elements to bottom surface elements (upper cylinder)

The view factor for radiant exchange from the top end of the upper cylinder to the lower end of that cylinder is also derived from simple view factor algebra and reciprocity relationships:

$$F_{S_i \to S_j} = \left(F_{S_j^o \to S_i^o} - F_{S_j^o \to S_i^i} \right) \frac{Area_{S_j^o}}{Area_{S_i}} - \left(F_{S_j^i \to S_i^o} - F_{S_j^i \to S_i^i} \right) \frac{Area_{S_j^i}}{Area_{S_i}}$$

where the subscript i refers to an annular ring on the upper surface, the subscript j refers to an annular ring on the lower surface, the superscript o refers to the disk whose perimeter corresponds with the outer perimeter of the annular ring, and the superscript i refers to the disk whose perimeter corresponds with the inner perimeter of the annular ring.

A.1.4 Side surface elements (upper cylinder) to side surface elements (lower cylinder) [see Figure A-4]

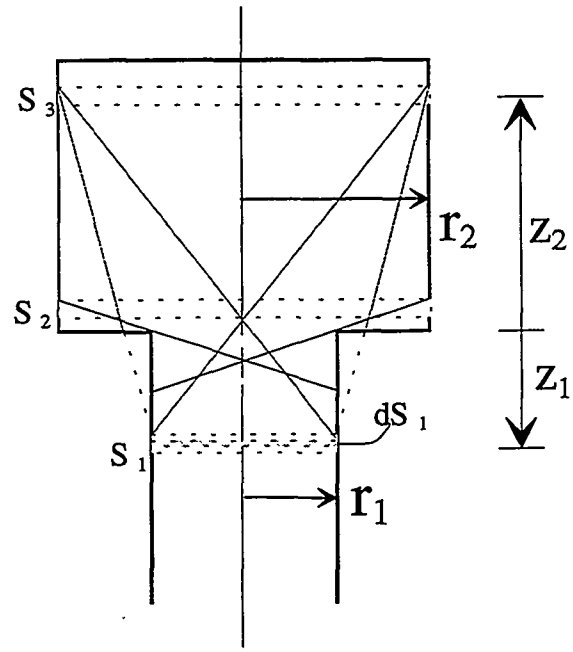

Figure A-4. Side (upper cylinder) to side (lower cylinder) geometry

This particular case poses more difficulty than previous cases and requires a little more attention. Since the internal surface is convex for this geometry, the view of positions in the narrow cylinder are either partially or fully obstructed from positions along the upper cylinder and the methods described above no longer apply. For example, surface S_1^t is totally obscured from the view of surface S_2 and there is no radiation transport between these surfaces. However, because surface S_3 is located farther away from the junction of the two cylinders, its view of surface S_1^t is only partially obstructed. Leuenberger[A-4] derived an equation describing the view factor from a differential surface area (a circular ring element of differential height in this case) on the smaller cylinder to a normal section through the larger cylinder (a disk bounding surface S_3 at either the top or bottom in this case) for these partially obstructed views, i.e.,

When $\frac{z_2}{z_1} \geq \frac{1}{2}\left(\frac{r_2}{r_1} - 1\right)$, then

$$F_{dS_1 \to S_3^b} = 2r_1 \left(\begin{array}{l} \dfrac{Z_1^2+2}{\sqrt{Z_1^2+4}} \tan^{-1}\left[\dfrac{B\sqrt{Z_1^2+4}}{\sqrt{(A+Z_2)^2 - R^2 Z_1^2}}\right] - z_1 \sin^{-1}\left[\dfrac{BZ_1}{2\sqrt{AZ_2}}\right] \\ + \dfrac{A}{2}\left\{\left[\dfrac{A^2+R^2+1}{\sqrt{(A^2+R^2+1)^2 - 4R^2}}\right]\cos^{-1}\left[\dfrac{(B^2-A^2)(2Z_2 - Z_1B^2}{2RA(Z_2A + R^2 - 1)}\right] - \cos^{-1}\left[\dfrac{Z_1B^2 - 2Z_2}{2RZ_2}\right]\right\} \end{array} \right).$$

where

$$Z_1 = \frac{z_1}{r_1}$$

$$R = \frac{r_2}{r_1}$$

$$Z_2 = \frac{z_2}{r_1}$$

$$A = Z_1 + Z_2$$

$$B = \sqrt{R^2 - 1}$$

This equation can be integrated over the height of S_1 to arrive at the equation for the view factor from S_1 to S_3:

$$F_{S_1 \to S_3} = \int_{z_{1,low}}^{z_{1,high}} F_{dS_1 \to S_3^b}\, dz_1 - \int_{z_{1,low}}^{z_{1,high}} F_{dS_1 \to S_3^t}\, dz_1 .$$

A.1.5 Top surface elements to side surface elements (lower cylinder) [see Figure A-5]

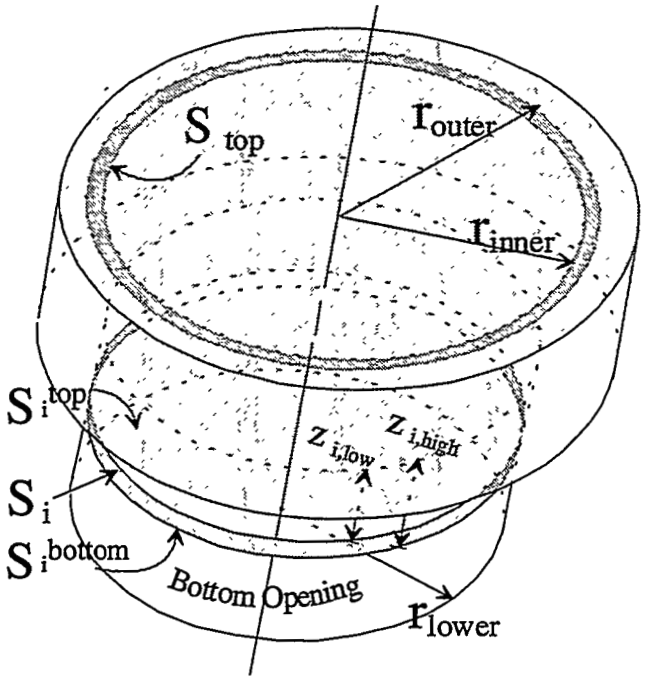

Figure A-5. Top surface to side surface (lower cylinder) geometry.

Again, because of the convex nature of the radiating surfaces, the view of the lower cylinder side walls may be partly obscured from the top surface of the upper cylinder, depending on the locations of the two surfaces. Of course if the outer diameter of the top surface element is less than or equal to the diameter of the lower cylinder, then the view factor is unaffected by any other surfaces and it can be calculated as it was in A.1.1. However, when the outer, and for the sake of

discussion,the inner diameter are larger than the diameter of the lower cylinder, the view is again partially obstructed and the view factor "algebra" methods no longer apply.

$$F_{S^{top}\to S_i} = \left(\int_{z_{i,low}}^{z_{i,high}} F_{dS_i \to S^{top}_{outer}}\, dz_i - \int_{z_{i,low}}^{z_{i,high}} F_{dS_i \to S^{top}_{inner}}\, dz_i \right) \frac{Area_{S_i}}{Area_{S_{top}}}$$

A.1.6 Bottom surface elements to side surface elements (lower cylinder)

This particular case is the logical equivalent to A.1.1 for radiation from the top surface to the sides of the upper cylinder.

$$F_{S_i \to S_j} = \left(F_{S^b_j \to S^o_i} - F_{S^b_j \to S^i_i} \right) \frac{Area_{S^b_i}}{Area_{S_i}} - \left(F_{S^t_j \to S^o_i} - F_{S^t_j \to S^i_i} \right) \frac{Area_{S^t_j}}{Area_{S_i}}$$

A.1.7 Top surface element to bottom surface element [see Figure A-6]

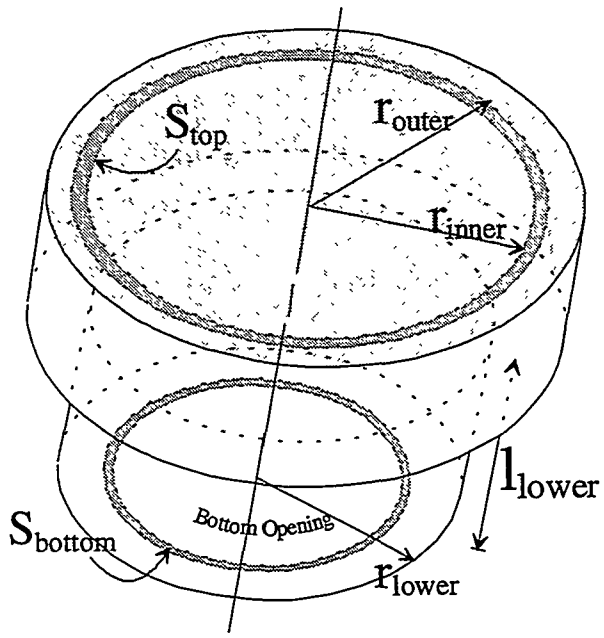

Figure A-6. Top surface to bottom surface geometry.

If the outer diameter of the top surface element is less than, or equal to, the diameter of the lower cylinder, then the view factor is unaffected by any other surfaces and it can be calculated simply by use of view factor "algebra"as it was in A.1.3. However, when the outer and, for the sake of discussion, the inner diameter of the top surface element are greater than the diameter of the smaller cylinder, then the view factor was estimated as follows. The view factor from the upper surface element to the total lower opening was calculated using view factor algebra and the view factor correlation by Leuenberger:

$$F_{S_{top}\to S_{opening}} = \left[\left(F_{S_{top}^{outer}\to S_{junction}} - \int_{\substack{length\\lower\\cylinder}} F_{dS_j\to S_{top}^{outer}}\, dz_1 \frac{2r_{lower}l_{lower}}{r_{outer}^2} \right) \frac{Area_{S_{top}^{outer}}}{Area_{S_{top}}} - \left(F_{S_{top}^{inner}\to S_{junction}} - \int_{\substack{length\\lower\\cylinder}} F_{dS_j\to S_{top}^{inner}}\, dz_1 \frac{2r_{lower}l_{lower}}{r_{inner}^2} \right) \frac{Area_{S_{top}^{innerr}}}{Area_{S_{top}}} \right].$$

An approximation, the only approximation used thus far, is introduced at this point to arrive at the final results. It was assumed that the temperature at the lower opening is uniform across the entire area. This assumption is quite good considering the high temperatures and tube bundle array at the top of the XR package. Using this approximation, the view factor from a surface element on the upper lid to a surface element on the bottom opening is estimated as:

$$F_{S_{top}\to S_{bottom}} = F_{S_{top}\to S_{opening}} \frac{Area_{S_{bottom}}}{Area_{opening}}.$$

These equations were implemented into the TAC2D models of the XR2 melter radiation cavity and exit region.

A.2 Estimate of Heat Flux Out the Bottom of the Melter Exit Duct

For early design estimates, the heat flux out the bottom of the melter exit duct was estimated by introducing some simple approximations into the integral equations for the net radiant heat flux presented above. If it can be assumed that no heat is lost from the melter walls (the walls are adiabatically insulated), that the system reaches steady state, that the upper cavity achieves a uniform temperature, and that the upper surfaces of the XR2 package also achieve a uniform temperature, then the equations above can now be written as:

$$q''(\vec{x}) = \frac{\varepsilon(\vec{x})}{1-\varepsilon(\vec{x})}\left[\sigma T_w^4(\vec{x}) - B(\vec{x})\right]$$

$$B(\vec{x}) = \varepsilon(\vec{x})\sigma T_w^4(\vec{x}) + (1-\varepsilon(\vec{x}))\left[\sigma T_{bot}^4 F_{dA_x\to A_{bot}} + \sigma T_{top}^4 F_{dA_x\to A_{top}} + \int_{\substack{exit\\duct}} B(\vec{\zeta}) dF_{dA_x\to dA_\zeta}\right]$$

$$B(\vec{x}) = \varepsilon(\vec{x})\sigma T_w^4(\vec{x}) + \alpha 2(\vec{x}) + (1-\varepsilon(\vec{x}))\left[\int_{\substack{exit\\duct}} B(\vec{\zeta}) dM\right],$$

or

$$\sigma\overline{T_w^4} = \overline{B} = \left[\left[\overline{\overline{I}} - \overline{\overline{M}}\right]^{-1}\overline{\alpha 2} + \left[\overline{\overline{I}} - \overline{\overline{M}}\right]^{-1}\cdot\varepsilon\sigma\overline{T_w^4}\right],$$

where $$\alpha 2(\vec{x}) = (1-\varepsilon(\vec{x}))\left[\sigma T_{bot}^4 F_{dA_x \to A_{bot}} + \sigma T_{top}^4 F_{dA_x \to A_{top}}\right].$$

In these equations, the term involving the wall surface temperature has not been absorbed into the definition of the function α, as it was before since the objective is to solve for this value. It is now possible to estimate the axial temperature profile in the exit duct for a given cavity temperature and an assumed temperature at the top of the XR2 package. In matrix form, the implicit form for the equation for the radiosity, $\overline{B}$, is written:

$$\overline{B} = \varepsilon(\vec{x})\sigma\overline{T_w^4} + \overline{\alpha 2} + \overline{B}\overline{\overline{M}},$$

or explicitly: $$\overline{B} = \left[\overline{\overline{I}} - \overline{\overline{M}}\right]^{-1} \cdot \overline{\alpha 2} + \left[\overline{\overline{I}} - \overline{\overline{M}}\right]^{-1} \cdot \varepsilon\sigma\overline{T_w^4}.$$

This equation is now substituted into the equation for the local radiant heat flux which results in an implicit equation for the local wall surface temperature along the exit duct.

Explicitly, the equation for the local wall surface temperature is written:

$$T_w^4 = \frac{1}{\sigma}\left[\overline{\overline{I}} - \varepsilon\left[\overline{\overline{I}} - \overline{\overline{M}}\right]^{-1}\right]^{-1} \cdot \left[\overline{\overline{I}} - \overline{\overline{M}}\right]^{-1} \cdot \overline{\alpha 2}.$$

Finally, the wall surface temperature is used in calculating the heat flux out the lower opening:

$$q_{bottom} = 2\pi r\sigma \int_{\substack{length \\ of\ exit \\ duct}} \varepsilon(z, T_w^4(z))\left(T_w^4(z) - T_{bot}^4(z)\right) F_{dA(\vec{x}) \to A_{bot}}\, dz + \pi r^2 \sigma\varepsilon(T_{bot})\left(T_{topt}^4 - T_{bot}^4\right) F_{A_{top} \to A_{bot}}.$$

This approximation was used in assessing the effectiveness of increasing the length of the melter exit duct in reducing the heat flux to the XR2 package. The assumption of adiabatic insulation leads to an overstatement of the heat radiated to the package since heat losses in the duct will lead to lower temperatures at the bottom end of the exit region. Figure A-7 shows a plot of the ratio of the heat loss to the lower package with an exit duct of varying length to the heat loss without the exit duct. The exit duct was made of graphite and graphite fibrous insulation. Further reductions could be made by making the lower half of the exit duct out of ZrO_2, which is nearly a diffuse scatterer and has a lower emissivity than graphite. Since graphite has a large emissivity, nearly 1, graphite scatters very little radiation from its surface. A material like ZrO_2 has a smaller emissivity and can scatter some of the radiation coming from the melter back into the melter. The second curve shows the effect of fabricating the bottom end of the exit duct from ZrO_2. Note that a minimum occurs when the bottom half of the duct is made of ZrO_2. This method was not used as a means of reducing the heat load to the package in this design because of the level of complication introduced resulting in only a minimal gain in performance.

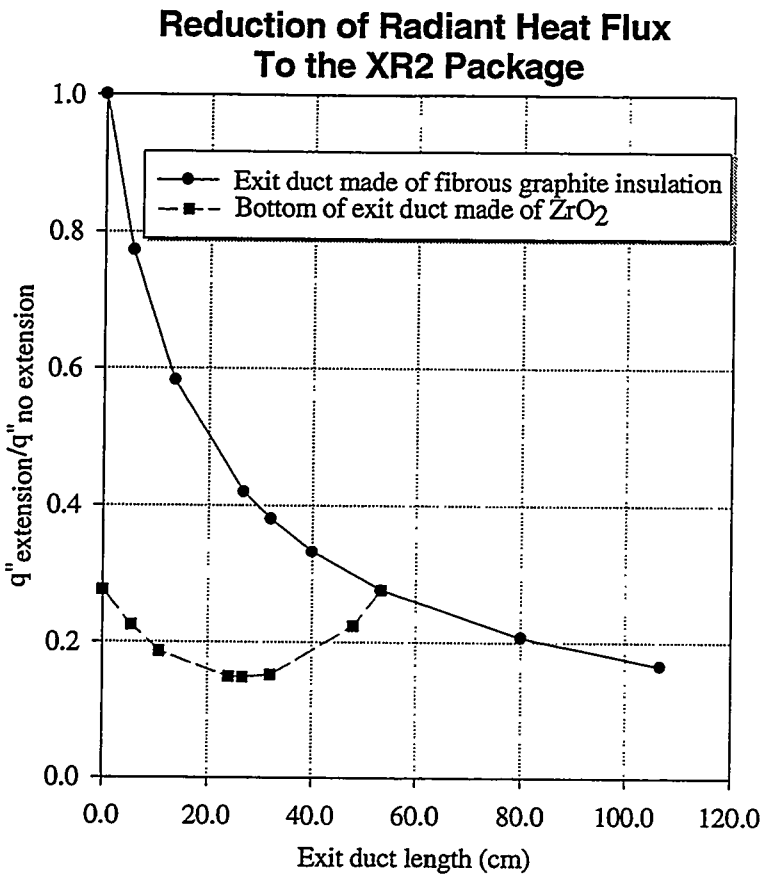

Figure A-7. Reduction in heat flux to lower package due to the exit duct.

APPENDIX A

References

A-1 E.M. Sparrow, *Radiation Heat Transfer*, Hemisphere Publishing Co., Washington, 1978.

A-2 R. Siegel and J. R. Howell, *Thermal Radiation Heat Transfer*, McGraw Hill Book Co., New York, 1972.

A-3 *ASM Handbook of Engineering Mathematics*, American Society for Metals, Ohio, 1983.

A-4 H. Leuenberger, *Compilation of Radiation Shape Factors for Cylindrical Assemblies*, American Society of Mechanical Engineers, New York, 1957.

APPENDIX B

XR2 Data EXCEL Workbook

Figures

APPENDIX B

XR2 Data EXCEL Workbook

The data set from the XR2-1 experiment is quite large, consisting of over 100 channels with more than 1000 entries per channel. In addition to the experimental data, it is also desired to compare calculated data to this experimental data, more than doubling the extent of the data of interest. In order to make analysis of this data more tractable to users, more accessible to users with varying levels of familiarity with the experiment, and prove a convenient means of archiving the data for future use, a graphical user's interface was developed using Microsoft Excel® version 5.0. This Workbook utilizes several useful macros which make retrieving and comparing data much more user-friendly. The underlying macros have been written in visual basic and the interface is the familiar Windows® interface with dialogue boxes, drop-down menus, and toolbars (see Figure B-1).

On opening the XR2Data.xls workbook, the subroutine Auto_Open found in Module1 (initially hidden from user) is executed. This subroutine sets up the XR2 toolbar and the XR2 menu along with some additional housekeeping activities. The toolbar and menu provide the user access to the necessary macros. The three macros currently supported are TOC (short for Table of Contents) which is the main engine for generating Excel® charts, Chart Manager for automatically deleting user-generated charts, and MERIS which post-processes the data collected from a MERIS calculation into a form useable by this workbook. The subprograms called by these macros reside on sheets Module2 and Module3.

The macro TOC enables the user to do any of four activities: inspect the experimental data set in spreadsheet form, view one of a number of prepared trend charts for the XR2 experiment, generate customized trend charts, or generate charts of customized axial plots. In generating customized charts the user has access to both the experimental data and the calculated data over any time range included on the data spreadsheets. Figure B-2 shows the initial dialogue box presented the user upon calling the Macro TOC. The user simply checks the type of plot desired and whether or not to generate a comma-delimited output file. This output file can then be used by other applications.

If the user chooses to view the Data sheet, the macro finds the Data sheet and places it in collapsed form. All similar channels are collapsed so that only one channel from each group of similar channels is visible, e.g., the only fuel rod channel visible is for fuel rod 1 at core region 1. If the columns are expanded one level, then a column for each fuel rod, can wall, and control blade appears, but the data for all but one core level is hidden. Finally, if the columns are fully expanded, the data for all channels are made visible. This provides a simple means for viewing only the data of interest reducing the time needed in

scrolling through the data. In addition, the rows are collapsed into four regions: those times before the steel composite wire are fed into the XR2 experiment, during the steel composite wire feed, during the Zr wire feed, and after the test was terminated.

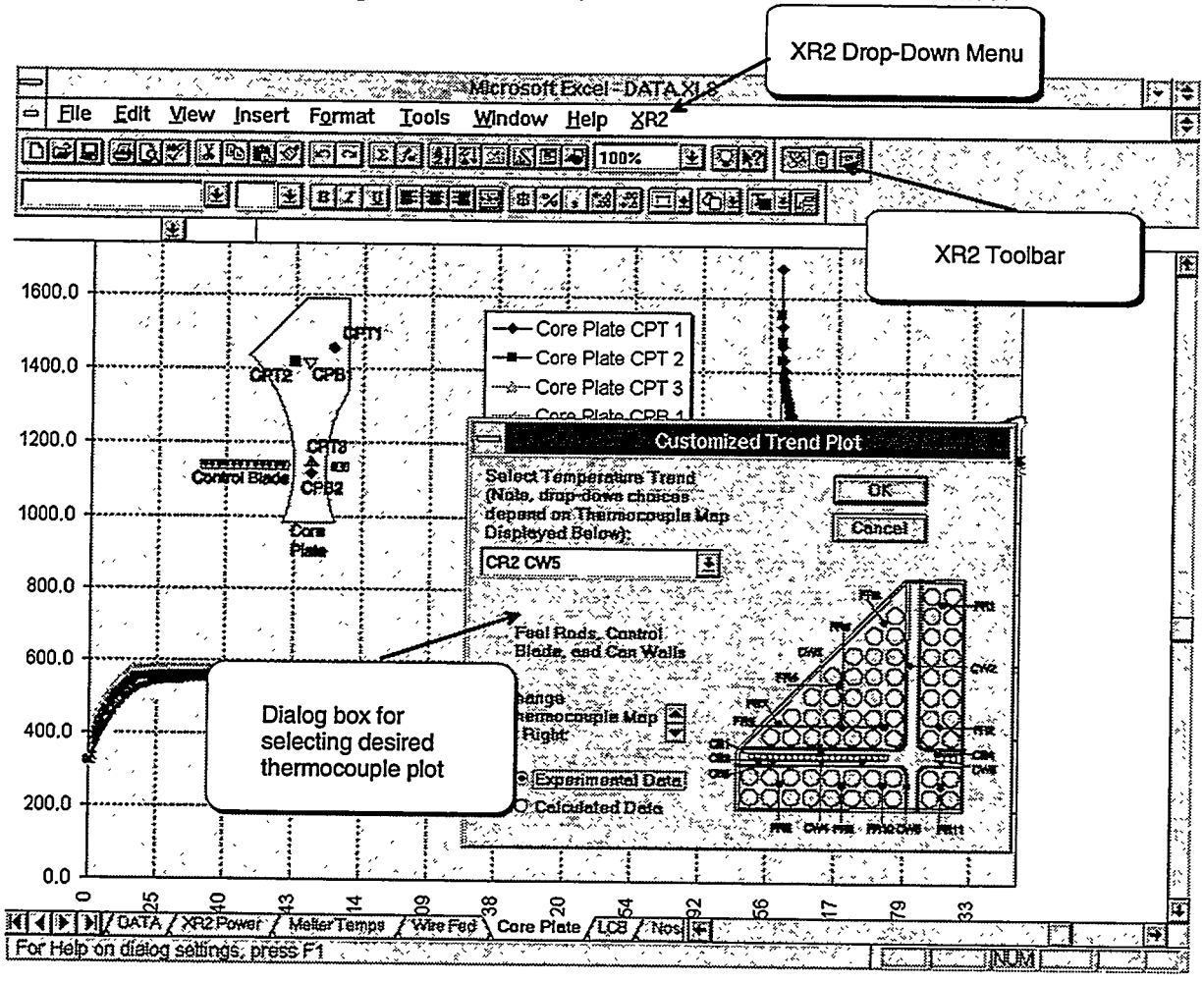

Figure B-1. XR2Data.xls data interface.

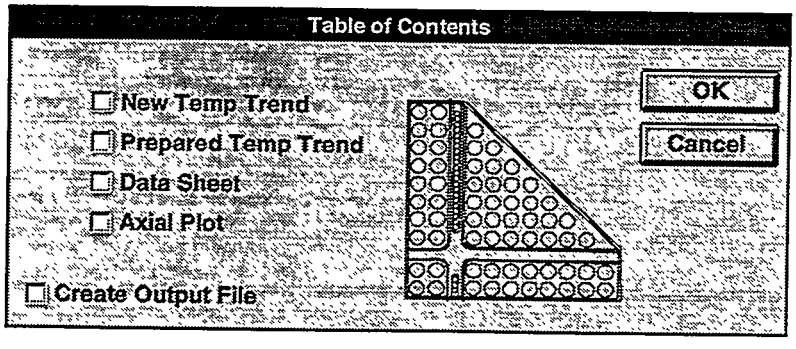

Figure B-2. TOC dialogue box 1.

If the user chooses, he may view one of several prepared Data charts. These charts display trends for similar channels plotted over the entire XR2 test (including both pre-heat and cool-down).

The user may also choose to generate customized trend plots using user-specified channels, over user-specified time ranges. The dialog box of Figure B-3 provides the means for specifying the time range and the name of the output file. The box requesting the name of the output file will be shadowed unless the user selected this option in the previous dialog box. No extension is allowed since the Macro automatically gives it the ".out" extension. The upper drop-down box is also shadowed. This drop-down box is used only when generating axial plots. The number of trends to plot on this chart are input in the following dialog box.

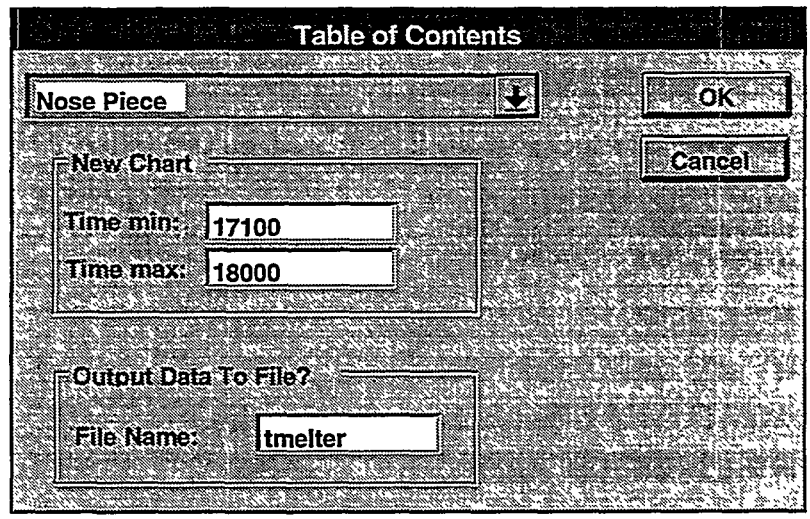

Figure B-3. TOC dialog box 2.

Finally, the Dialog box of Figure B-4 is used to specify the desired channel and whether experimental or calculated data is desired. The embedded scroll bar is used to select the thermocouple map displayed at the right. The thermocouple map is provided as a graphical aid to finding the desired thermocouple location. The user may choose between the XR2 bundle, the core plate, the lower control blade, the nose pieces, or the fuel support pieces. As the thermocouple map changes, so do the thermocouples available in the drop-down box. This provides a means for narrowing the search for the desired thermocouple. Notice that since the type of data (experimental or calculated) is specified on the same dialog box that the desired thermocouple is specified, the user can plot both experimental and calculated data on the same chart.

If the user selects to plot axial profiles in the TOC dialog box 1, then the dialog box of Figure B-5 appears rather than that of Figure B-4. For this dialog box the time is entered for each selected thermocouple location so that axial profiles at various points in time can be compared. In this case, the temperature range in TOC dialog box 2 is disabled.

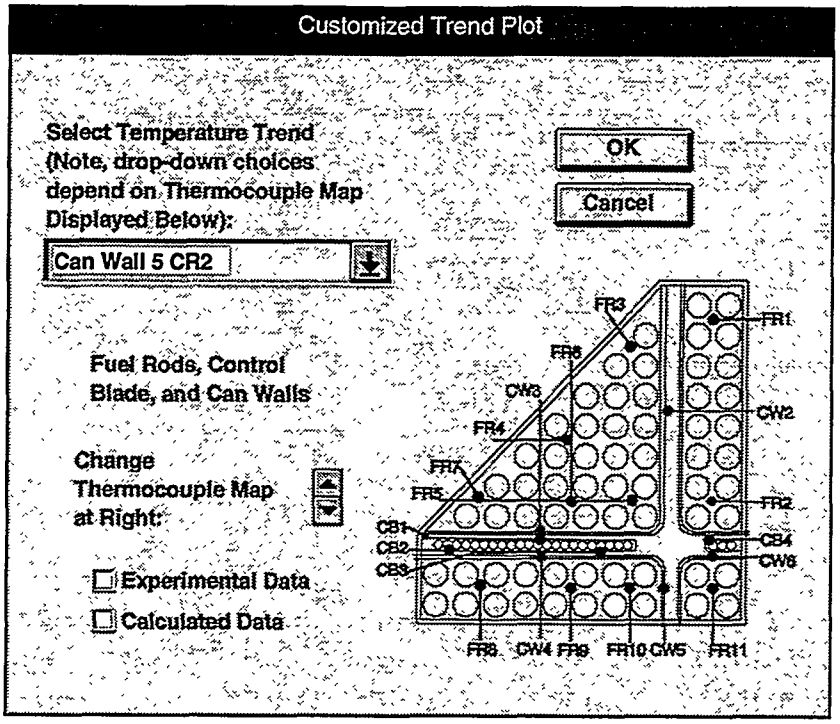

Figure B-4. Customized trend plot dialog box.

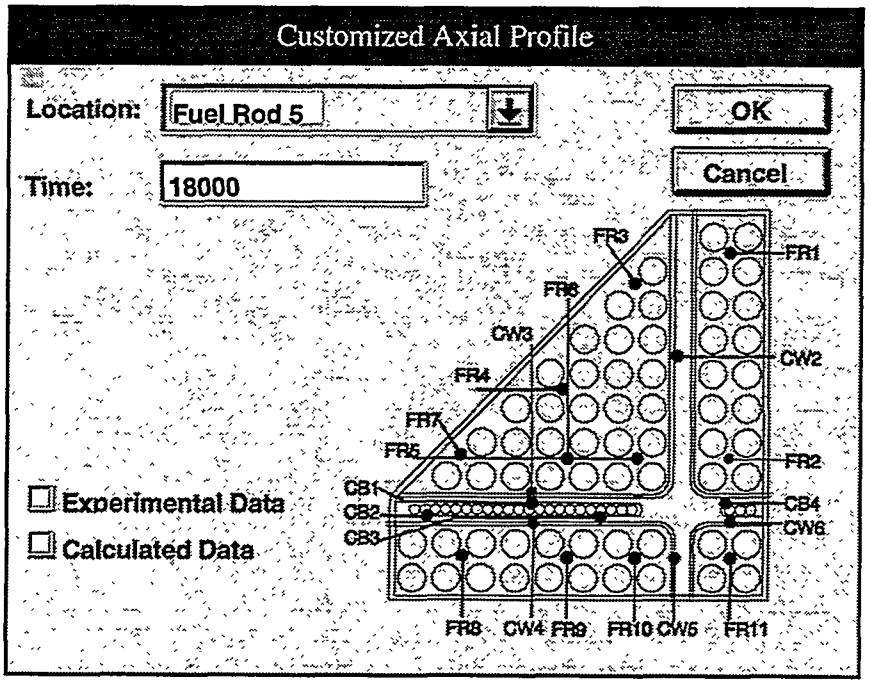

Figure B-5. Customized axial profile dialog box 2.

Since axial plots are associated with temporary worksheets, there is some housekeeping associated with deleting or renaming charts and their associated scratch files. The purpose of the Charts Manager macro is to provide a convenient means of maintaining charts generated in a session that is as transparent as possible to the user.

The user may decide to save generated charts on closing for later sessions. On closing, the subroutine Auto_Close is executed automatically. This subroutine does all the final housekeeping, including discarding all user-generated charts for that session. The user can over-ride deletion of a chart and rename the chart for later sessions via the dialog box of Figure B-6. If any of the charts to be retained are axial plots, then this should be indicated on that dialog box since there is a scratch file that was created on opening XR2Data.xls that Excel will need to rename and save for later sessions.

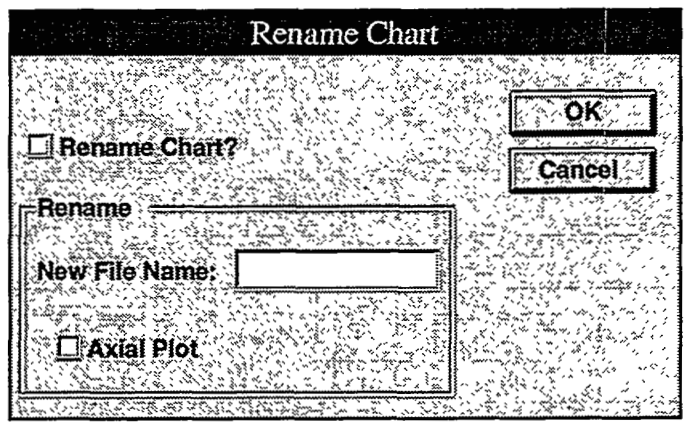

Figure B-6. Rename chart dialog box.

The XR2Data workbook provides a convenient means of accessing the data from the XR2 test and making meaningful comparisons. Once a chart is generated, it can be further edited with Excel to provide a highly customized chart that can be imported into various word processors. It can also output user-defined subsets of the XR2 data into comma-delimited data files for use in other applications. Many of the plots reproduced in this report were generated from this Workbook.

APPENDIX C

Thermophysical Properties of Materials

Contents

Figures

Tables

APPENDIX C

Thermophysical Properties of Materials

This appendix summarizes the thermal physical material property correlations used in the XR2 experiment analyses, i.e., the preliminary TAC2D design calculations or the post-test MERIS analysis. Experimental data is also referenced and plotted alongside these correlations wherever possible.

Values for thermal conductivities, specific heats and melting points for materials found in the XR2 melter facility and package are presented in the figures that follow.

C.1 Effective Thermal Conductivities for Porous Materials.

Effective thermal conductivities for porous insulating materials are estimated using a correlation developed by Sadahisa Imura and Eisyun Takegoshi for packed spherical beds[C-1] and a radiation model developed by Vortmeyer[C-2], i.e.,

$k_{eff} = k_{cond} + k_{rad}$

where

$k_{rad} = 4\varepsilon_r \sigma \pi d_p T^3 \eta$

ε_r = emissivity of the solid

σ = Stefan-Boltzmann constant

d_p = mean particle diameter

η = an empirical parameter (.25 was used)

and

$$k_{cond} = \psi\, k_g + \frac{1-\psi}{k_o\, \omega + k_g(1-\omega)}\, k_\sigma k_g$$

where

$$\omega = 0.3\, \alpha_g^{1.6} \left[\frac{k_s}{k_g}\right]^{-0.044},$$

$$\psi = \frac{\alpha_g - \omega}{1-\omega},$$

$$k_\sigma = \frac{1}{\alpha_s + \alpha_l}\left[\alpha_s \sum_j Y_{s,j} k_{s,j} + \alpha_l \sum_j Y_{l,j} k_{l,j}\right]$$

and

α_g is the volume fraction occupied by gas.

The conductivity k_σ is seen to be the volume averaged thermal conductivities of both the solid and liquid components of all species.

C.2 Thermal Conductivity of Materials

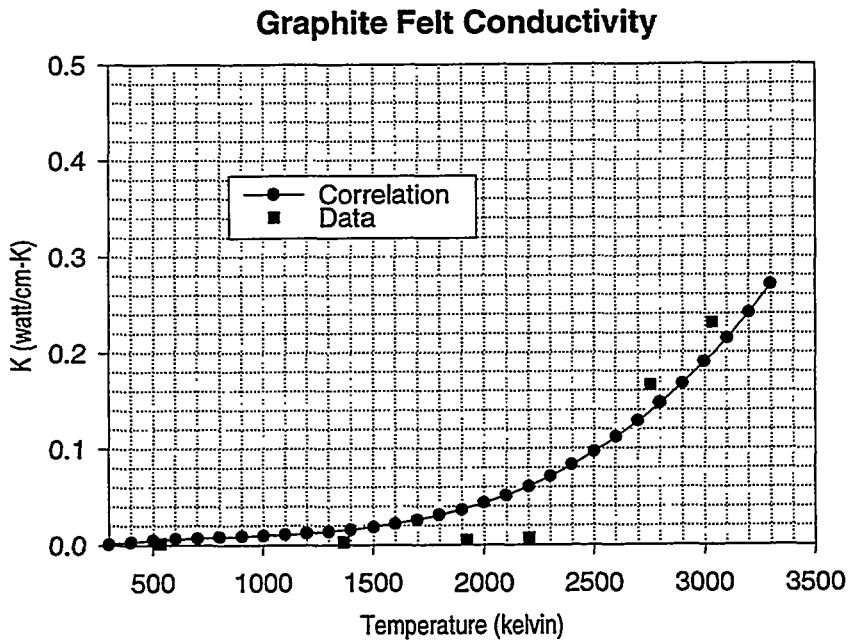

$$k_{gr}(t) = -8.54207 \cdot 10^{-3} + t\left(4.2807 \cdot 10^{-5} + t\left(-4.09243 \cdot 10^{-8} + 1.6217 \cdot 10^{-11} \cdot t\right)\right) \quad \frac{watt}{cm \cdot K}$$

Figure C-1. Thermal conductivity of graphite felt.

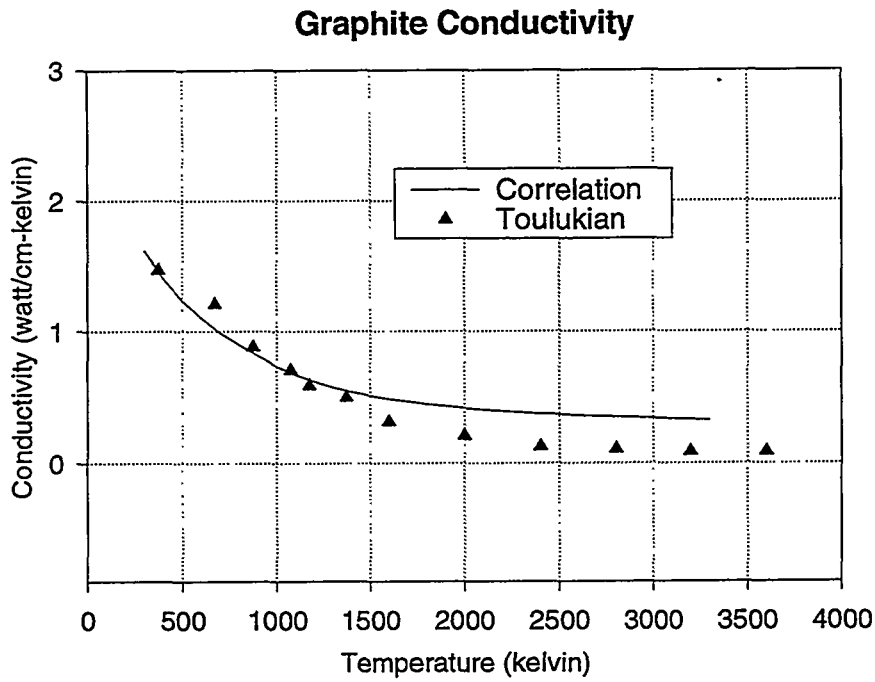

$$k_{graphite}(t) = \begin{cases} t < 1000 & -6.39652 + 13.8956 \cdot t^{-0.0964107} \\ t \geq 1000 & .243884 + 14287.3 \cdot t^{-1.48748} \end{cases} \quad \frac{watt}{cm \cdot K}$$

Figure C-2. Thermal conductivity of graphite.

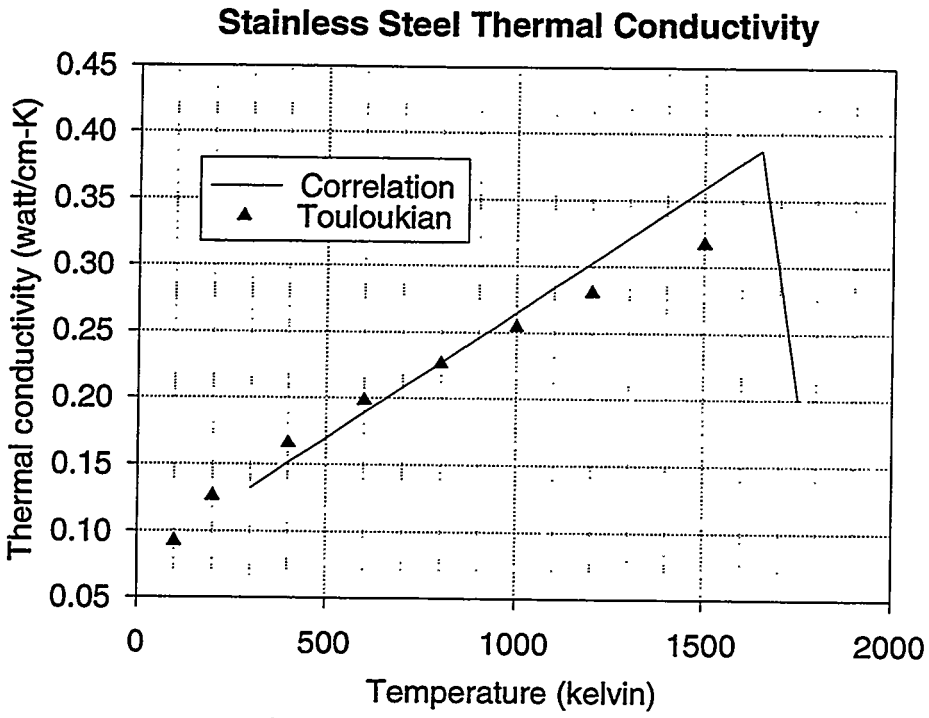

$$k_{ss}(t) = \begin{cases} t < 1671°K & .0758 + 0.000189 \cdot t \\ t \geq 1671°K & 6.109393 - 0.003421767t \end{cases} \frac{watt}{cm \cdot K}$$

Figure C-3. Thermal conductivity in stainless steel.

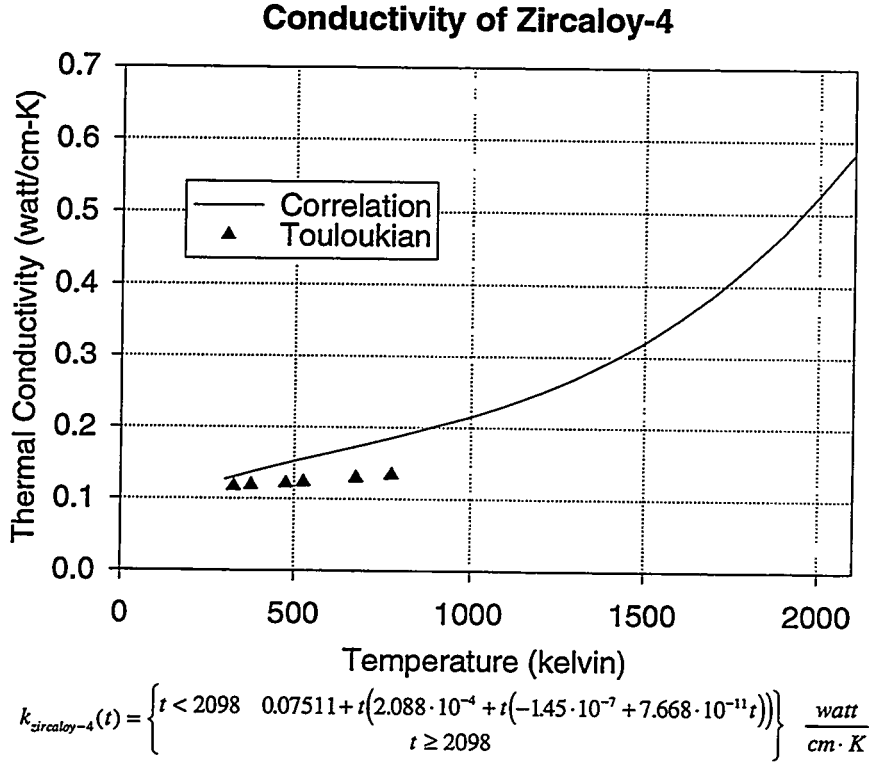

$$k_{zircaloy-4}(t) = \begin{cases} t < 2098 & 0.07511 + t\left(2.088 \cdot 10^{-4} + t\left(-1.45 \cdot 10^{-7} + 7.668 \cdot 10^{-11} t\right)\right) \\ t \geq 2098 & \end{cases} \frac{watt}{cm \cdot K}$$

Figure C-4. Thermal conductivity of zircaloy-4.

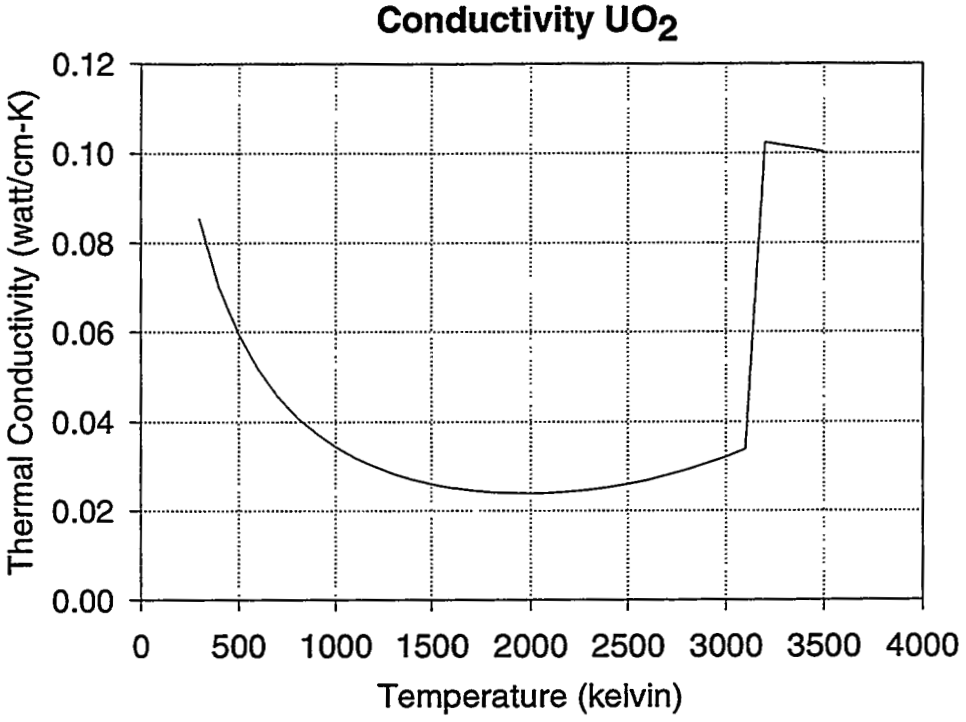

$$k_{UO_2}(t) = \left\{ \begin{array}{ll} t < 3138K & pct2(t,td) \times \left(\dfrac{1}{4 + 2.57 \cdot 10^{-2} \times t} + .73 \cdot 10^{-12} \times t^3 \right) \\ t \geq 3138K & 2.5 \cdot 10^{-2} \times \rho_l(t,td) \times 5 \times pct2(t,td) \end{array} \right\} \quad \frac{watt}{cm \cdot K}$$

$$where \quad \rho_l(t,td) = td \times \frac{10.97}{1 + 9.3 \cdot 10^{-5} \times (t - 273)}$$

$$pct2(t,td) = \begin{array}{lll} & t < 1600 & pct(td) \\ td < .95 & t < 3138 & 1 - (1 - pct(x)) \times \dfrac{3138 - t}{3138 - 1600} \\ & t \geq 3138 & 1.0 \\ td \geq .95 & & pct(td) \end{array}$$

$$pct(td) = \begin{array}{ll} td < .9 & \dfrac{td}{1 + .5 \cdot \dfrac{(1 - td)}{.875}} \\ td \geq .9 & \dfrac{1 - 2.5 \cdot (1 - td)}{.875} \end{array}$$

Figure C-5. Thermal conductivity of UO_2

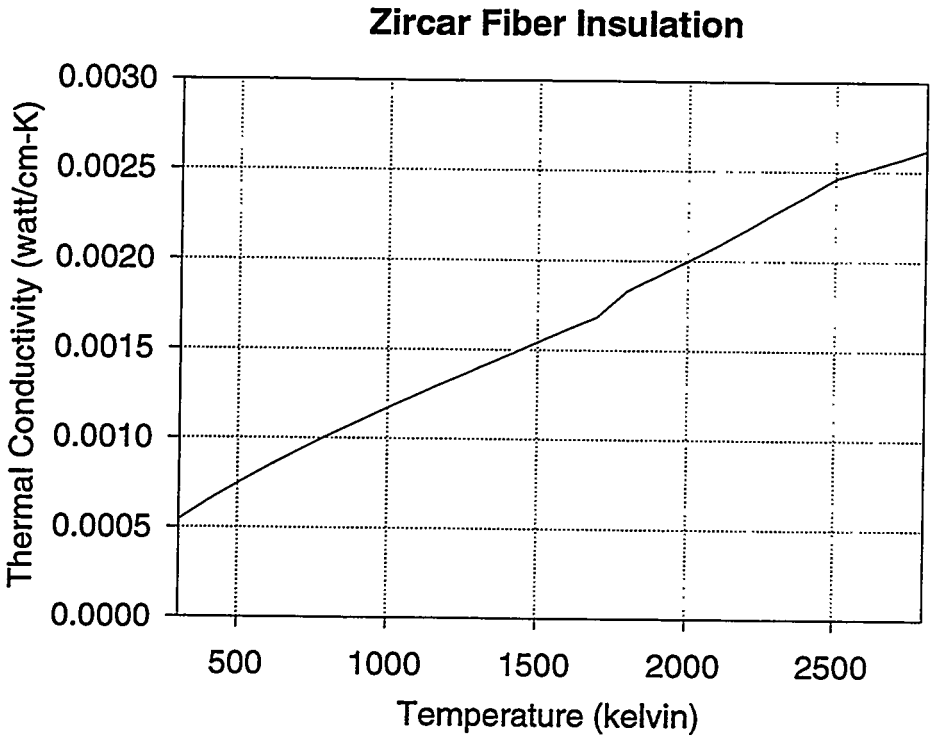

Figure C-6. Thermal conductivity of Zircar fiber insulation.

C.3 Specific Heat of Materials

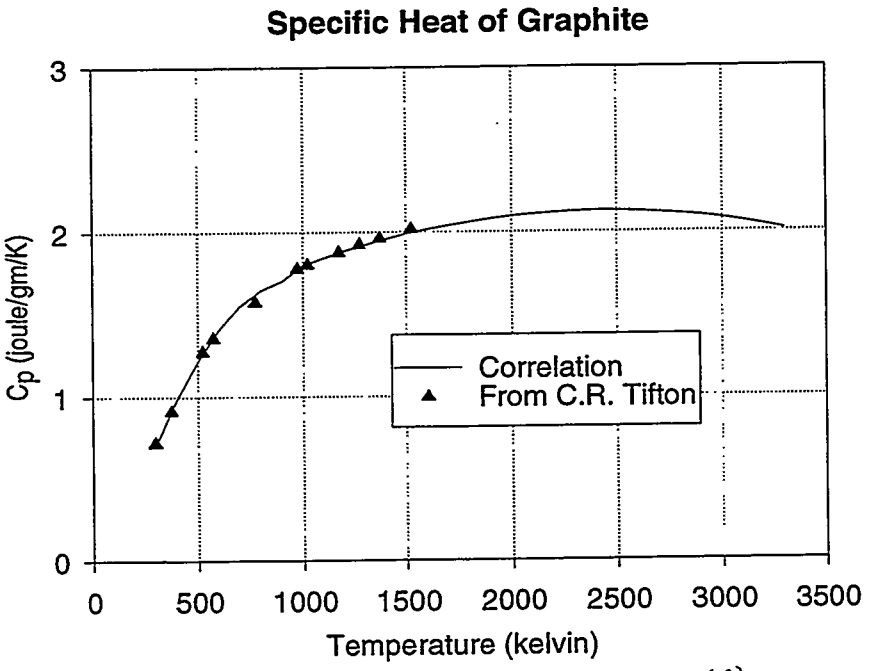

$$C_p^{graphite}(t) = \begin{cases} t < 1000°K & -.390075 + 4.334274 \cdot 10^{-3} t - 2.24196 \cdot 10^{-6} t^2 \\ t \geq 1000°K & 1.20279 + 7.54778 \cdot 10^{-4} t - 1.54435 \cdot 10^{-7} t^2 \end{cases} \frac{Joule}{gm \cdot K}$$

Figure C-7. Specific heat of graphite.

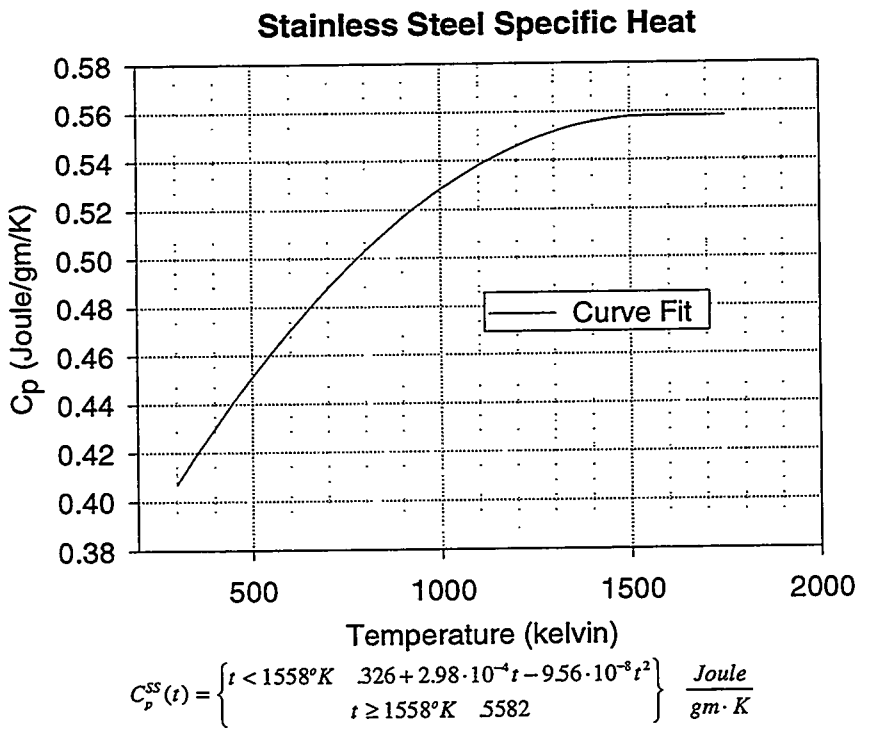

$$C_p^{SS}(t) = \begin{cases} t < 1558°K & .326 + 2.98 \cdot 10^{-4} t - 9.56 \cdot 10^{-8} t^2 \\ t \geq 1558°K & .5582 \end{cases} \frac{Joule}{gm \cdot K}$$

Figure C-8. Specific heat of stainless steel.

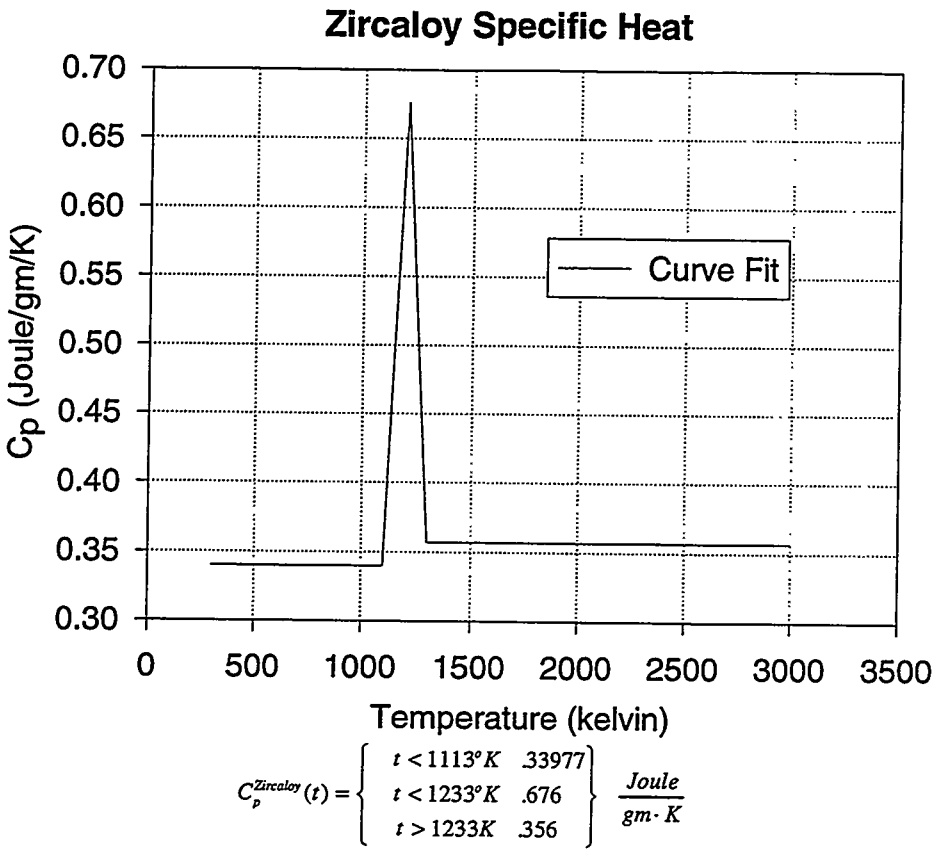

$$C_p^{Zircaloy}(t) = \left\{ \begin{array}{ll} t < 1113^\circ K & .33977 \\ t < 1233^\circ K & .676 \\ t > 1233K & .356 \end{array} \right\} \frac{Joule}{gm \cdot K}$$

Figure C-9. Specific heat of zircaloy.

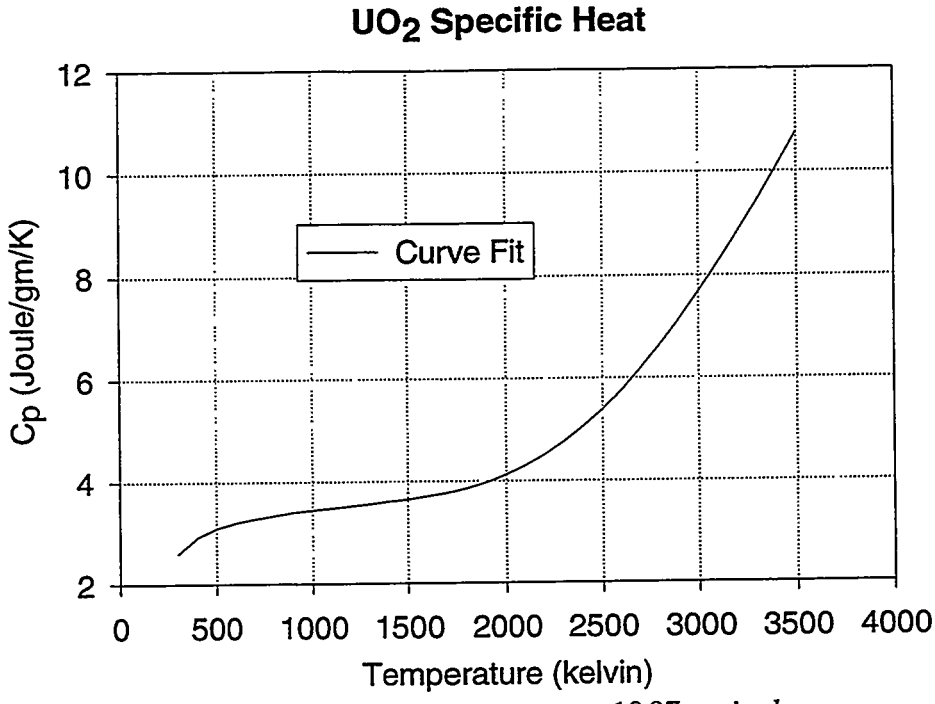

$$Cp_{UO_2}(t) = \left(C_e(t) + C_V(t) + C_d(t)\right) \times \frac{10.97}{1000} \quad \frac{joule}{gm \cdot K}$$

$$where \quad C_e(t) = \frac{8.50135 \cdot 10^7 \times e^{\frac{535.285}{t}}}{\left(t \times \left(e^{\frac{535.285}{t}} - 1\right)\right)^2}$$

$$C_V(t) = .0243 \times t$$

$$C_d(t) = \frac{1.658692 \cdot 10^{12}}{t^2} \times e^{\frac{-1.89673 \cdot 10^4}{t}}$$

Figure C-10. Specific heat of UO_2.

C.4 Fe/Zr Phase Diagram and Melting Points of Materials

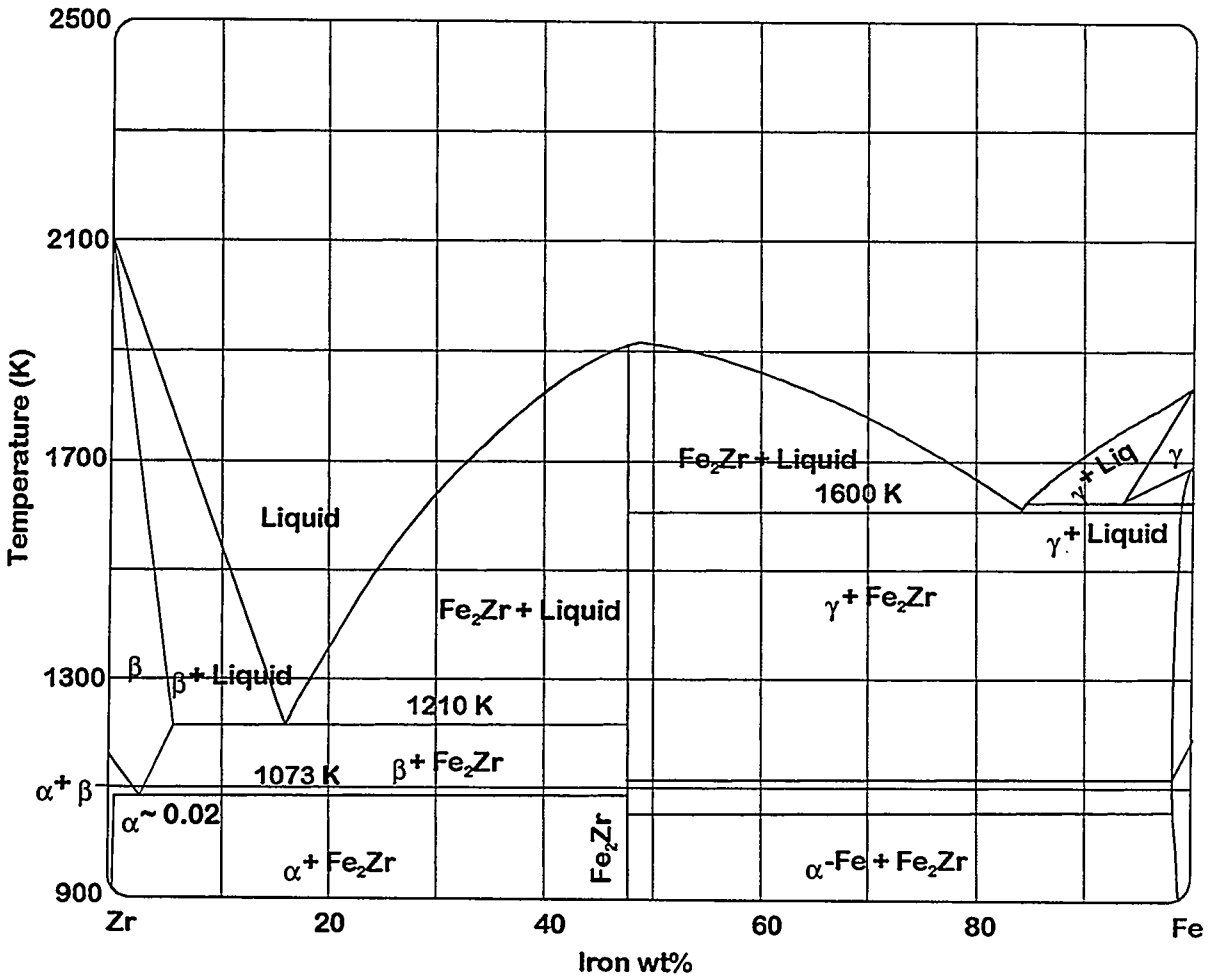

Figure C-11. Fe/Zr phase diagram.

Table C-1. Melting points for materials used in the analysis of the XR2 test.

Material	Solidus (K)	Liquidus (K)
UO_2	3110	3115
Zr	2095	2100
Fe	1671	1727
Fe/B_4C	1500	1525
Fe/Zr	1600	1650

APPENDIX C

References

C-1 S. Imura and E. Takegoshi, Effect of Gas Pressure on the Effective Thermal Conductivity of Packed Beds, *Heat Transfer Japanese Research*, Vol. 3, No. 4, p.13, 1974.

C-2 D. Vortmeyer, Radiation in Packed Solids, *Proc. 6th Int. Heat Transfer Conference*, Toronto, Vol. 6, pp. 525-539.

APPENDIX D

XR2 Thermocouple Data

Figures

APPENDIX D

XR2 Thermocouple Data

The thermocouple data collected for the XR2-1 experiment has been plotted over the entire length of the experiment and is presented in this appendix. The reader is referred to Section 5.1 above for a complete description of thermocouple locations. The reference in these figures to CR1, CR2, CR3, or CR4 indicates the axial elevation in the test package, CR1 being at the top and CR4 at the bottom. All fuel rod thermocouples at elevation CR1 or CR2 were type C thermocouples and all can wall thermocouples at elevation CR2 were also type C. Other than the two lower thermocouples for can wall 2 (both type C), the balance of thermocouples were of type K.

An Excel spreadsheet has been written to archive this database for simplified access and the user's guide is presented in Appendix B. More detailed views of some of the more notable temperature trends during the melt phase of the experiment are presented throughout this report.

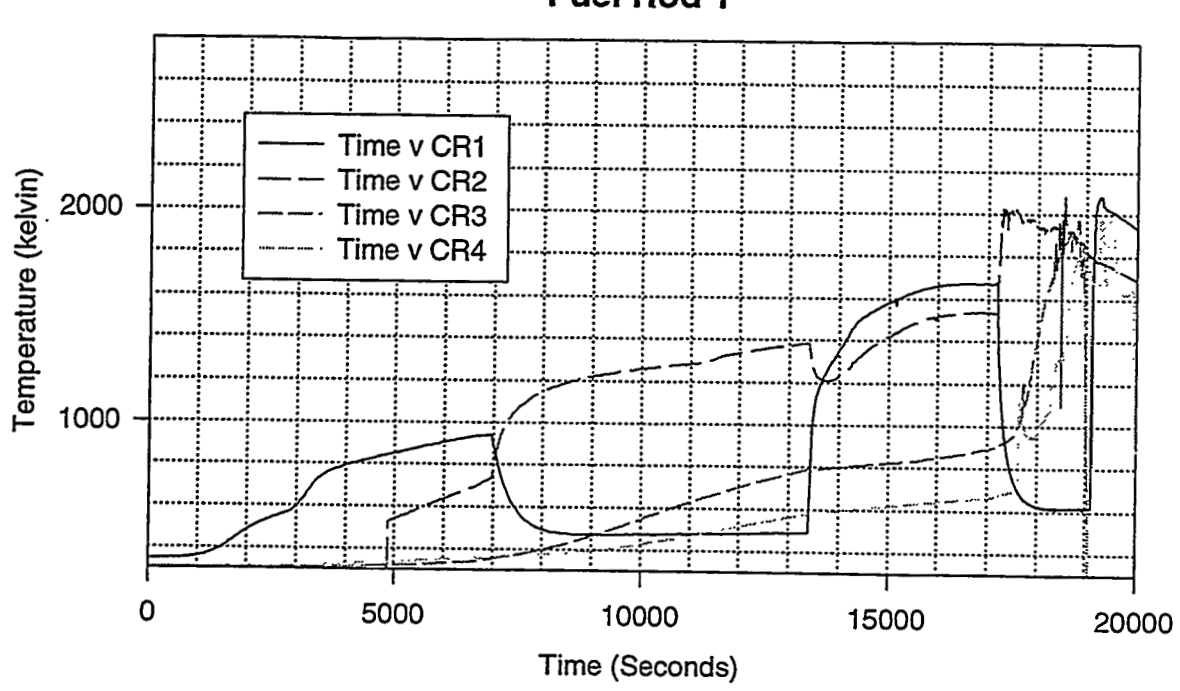

Figure D-1. Temperature data for fuel rod 1.

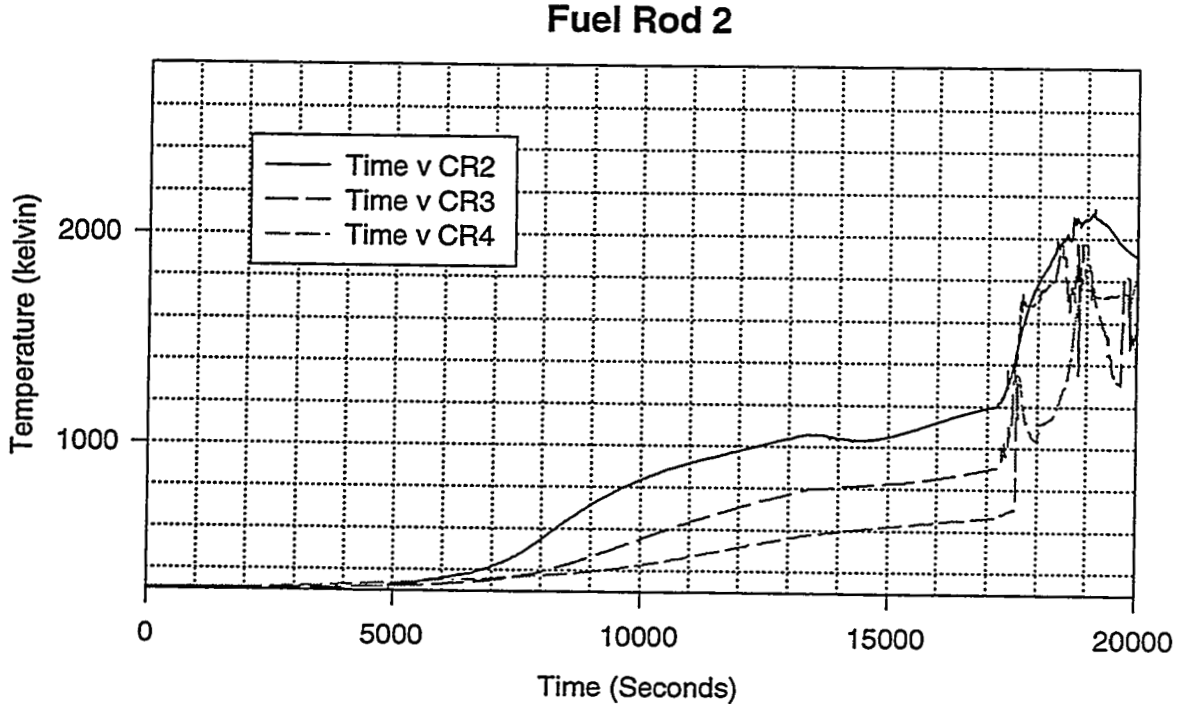

Figure D-2. Temperature data for fuel rod 2.

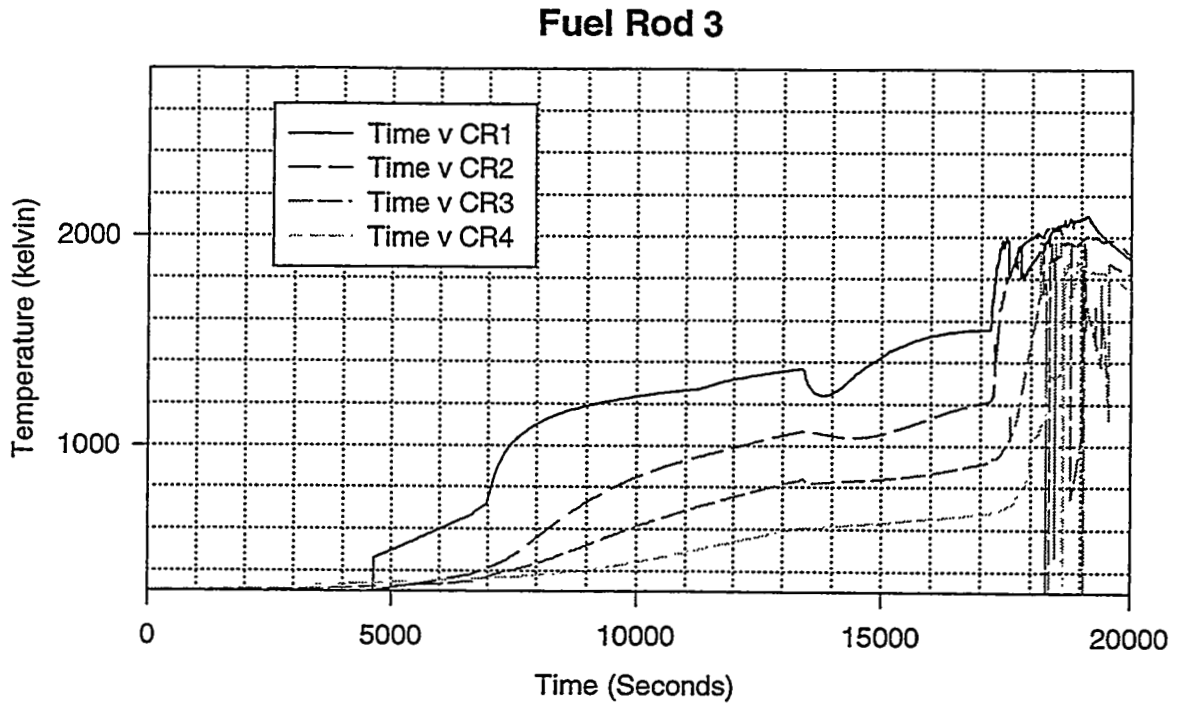

Figure D-3. Temperature data for fuel rod 3.

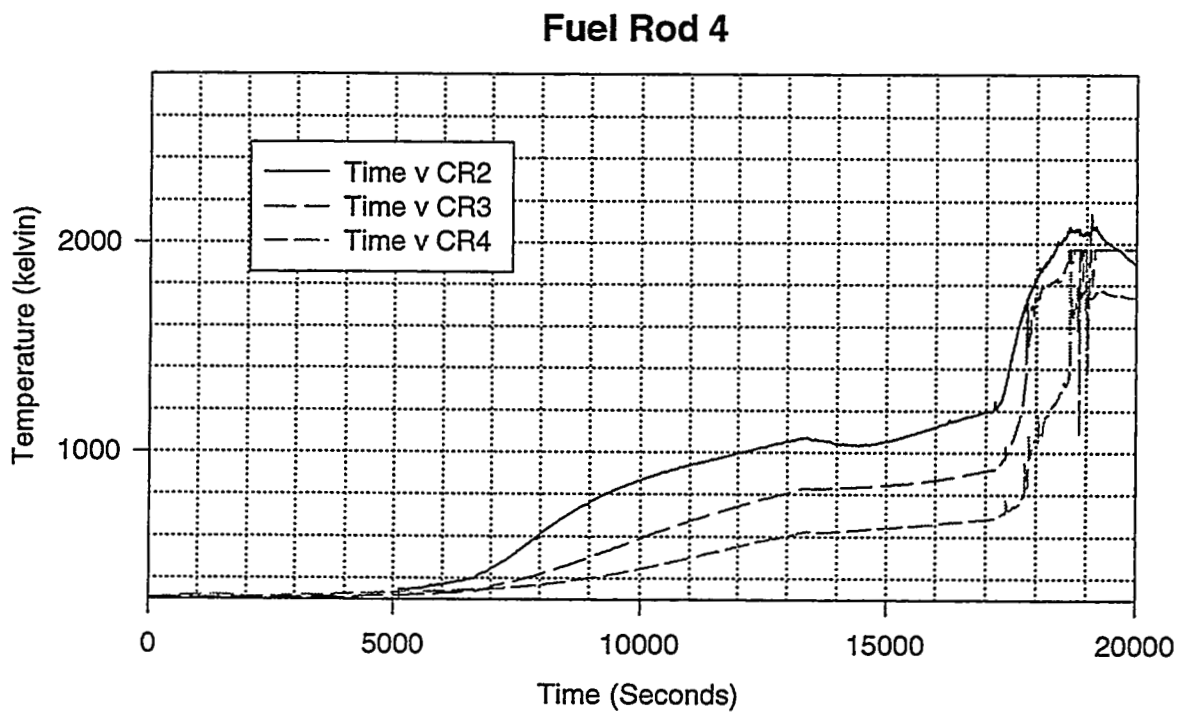

Figure D-4. Temperature data for fuel rod 4

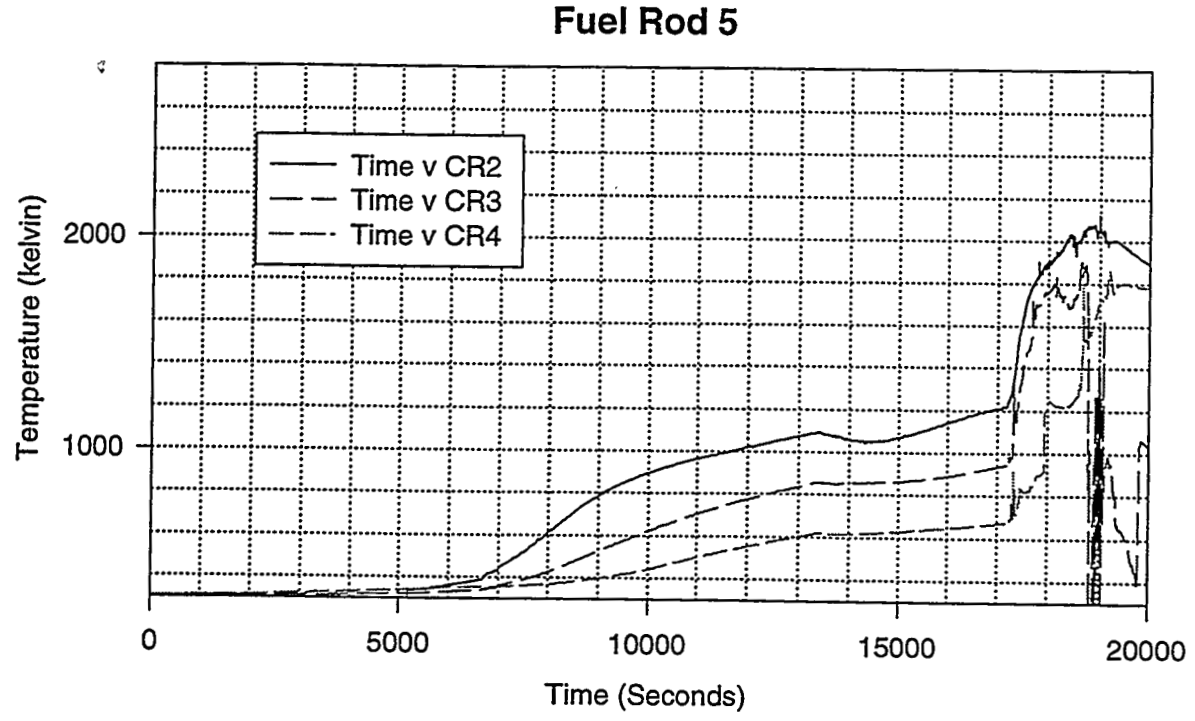

Figure D-5. Temperature data for fuel rod 5.

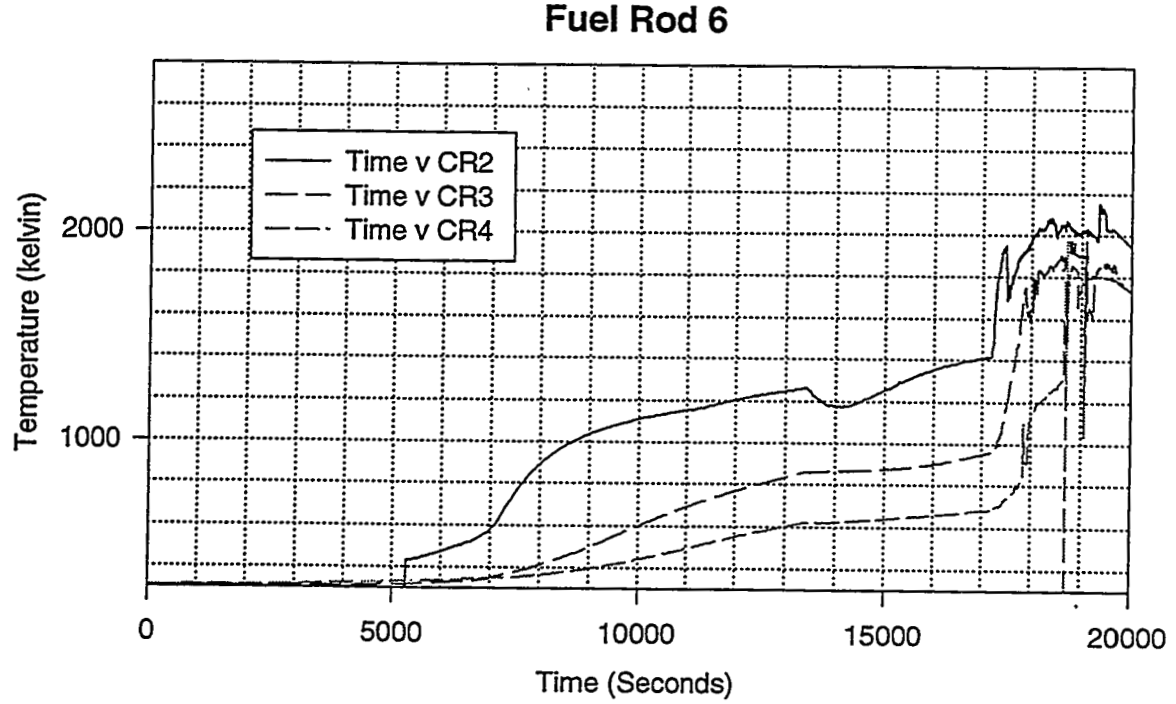

Figure D-6. Temperature data for fuel rod 6.

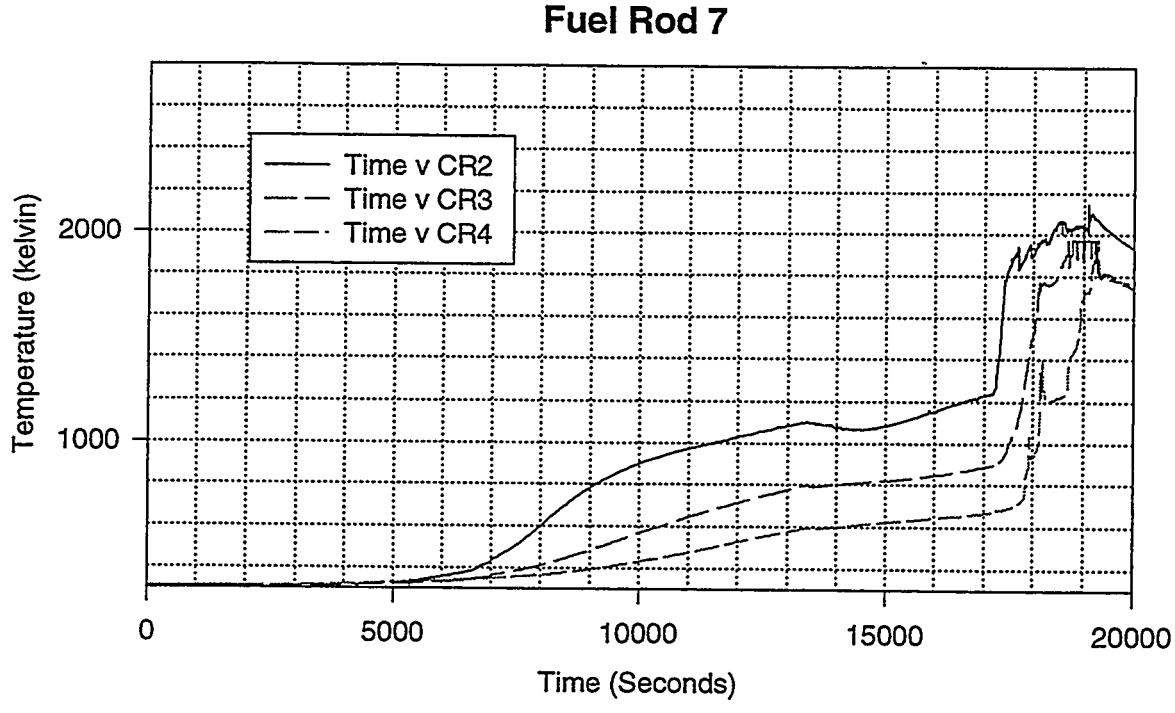

Figure D-7. Temperature data for fuel rod 7.

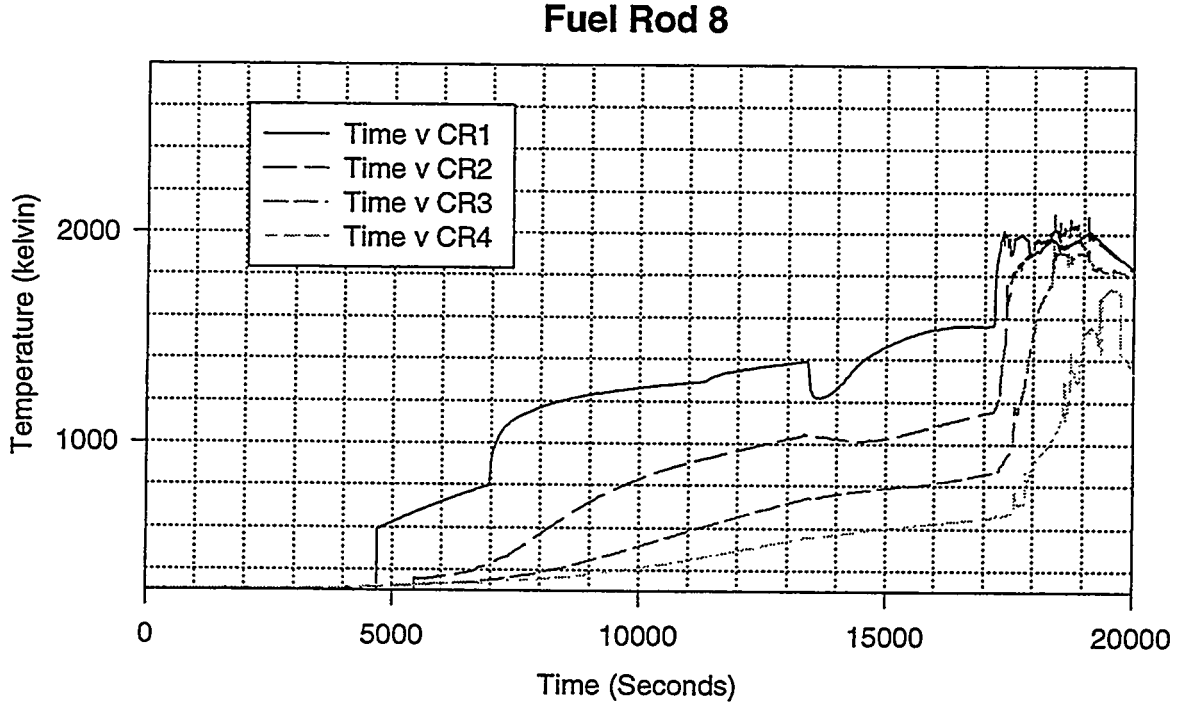

Figure D-8. Temperature data for fuel rod 8.

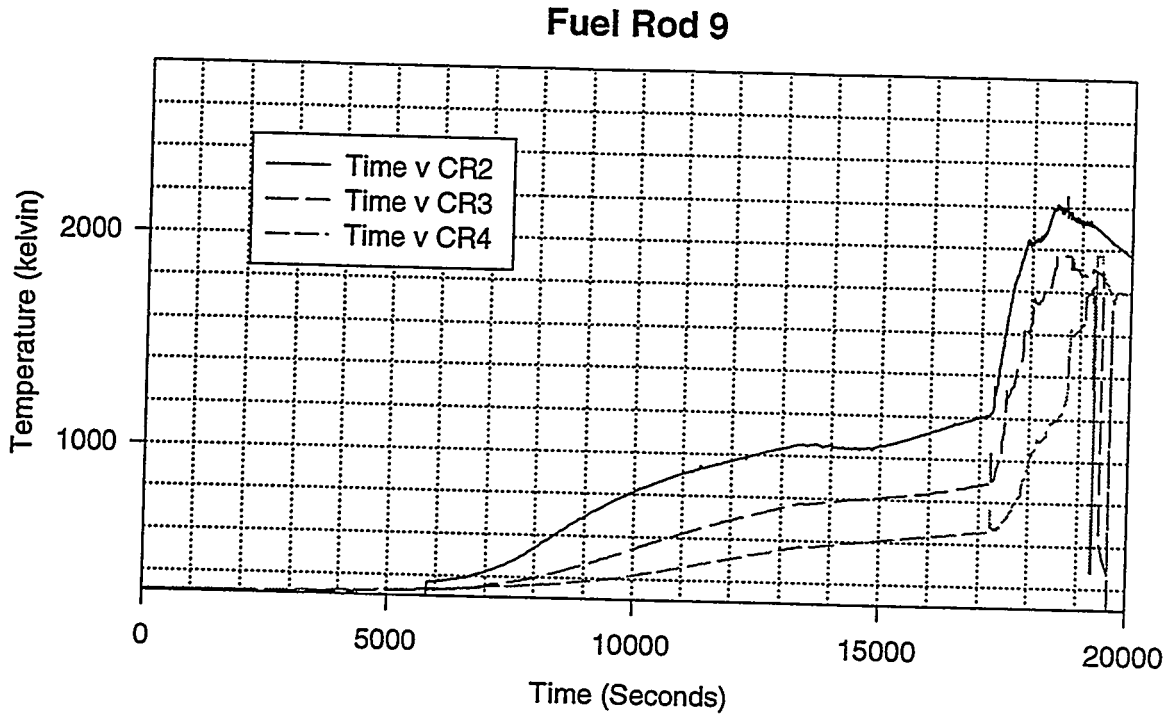

Figure D-9. Temperature data for fuel rod 9.

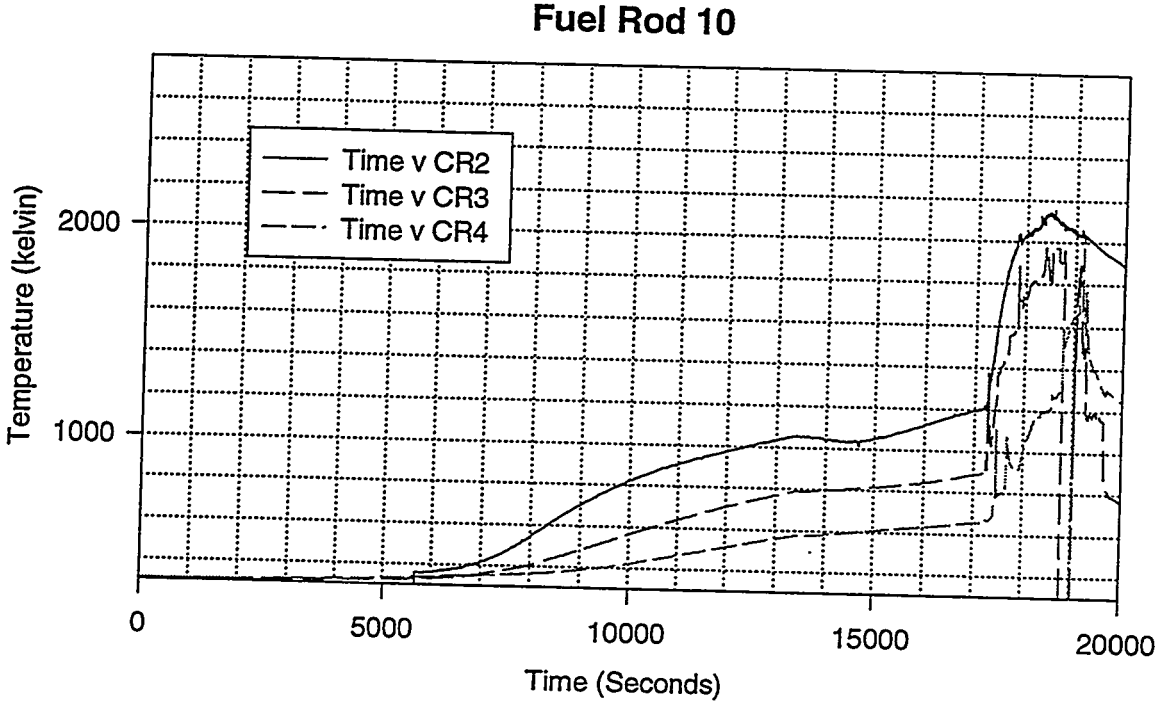

Figure D-10. Temperature data for fuel rod 10.

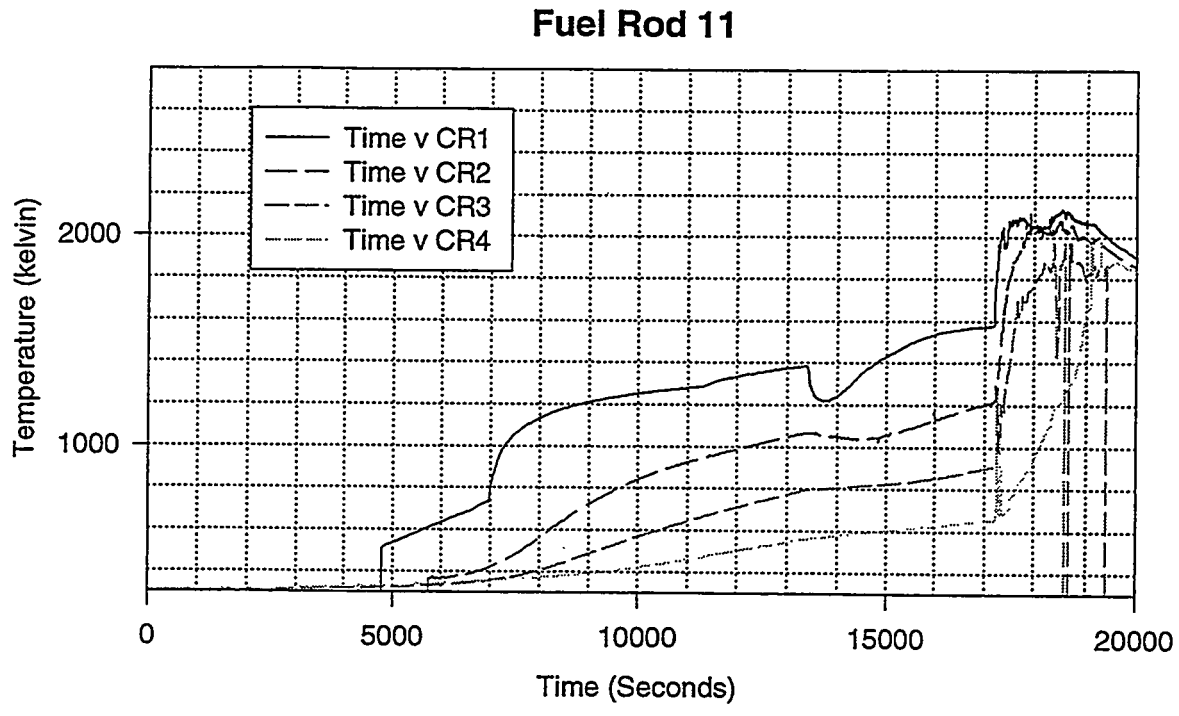

Figure D-11. Temperature data for fuel rod 11.

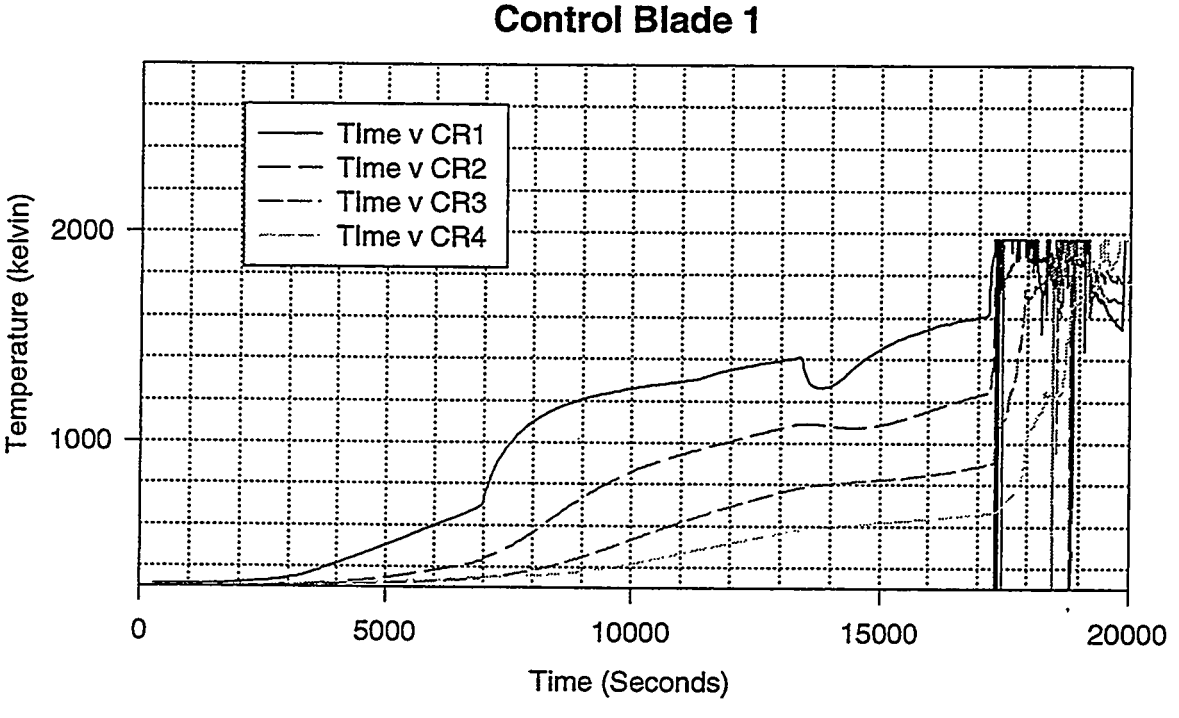

Figure D-12. Temperature data for control blade 1.

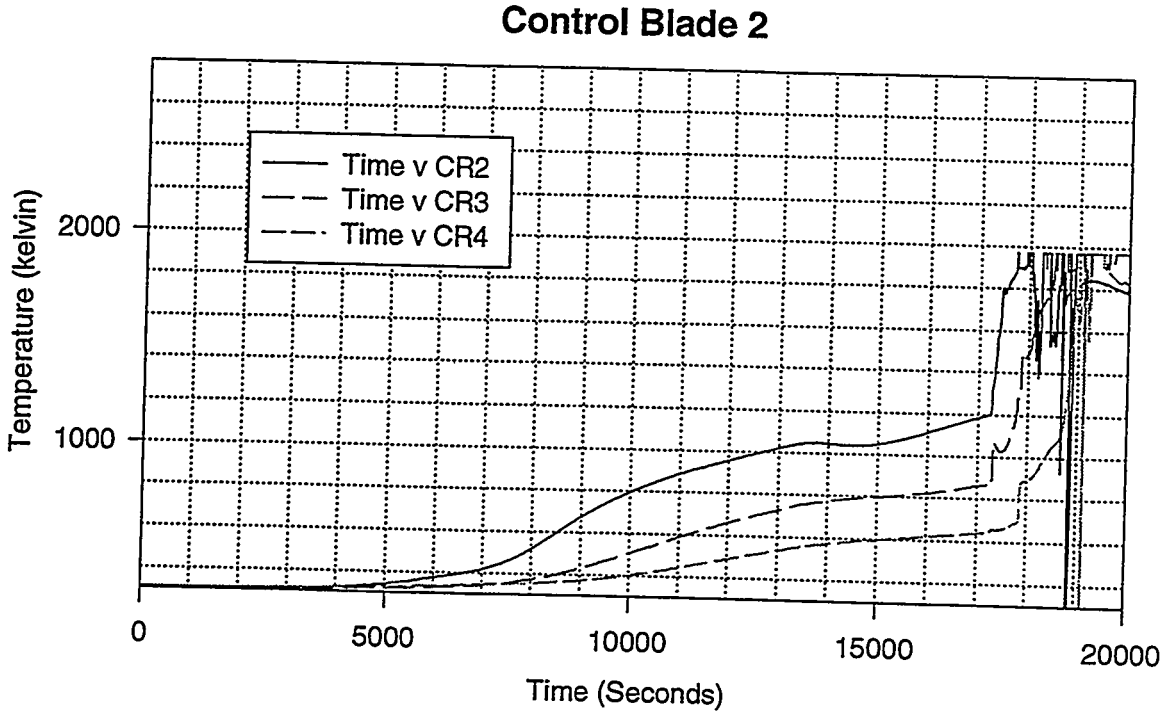

Figure D-13. Temperature data for control blade 2

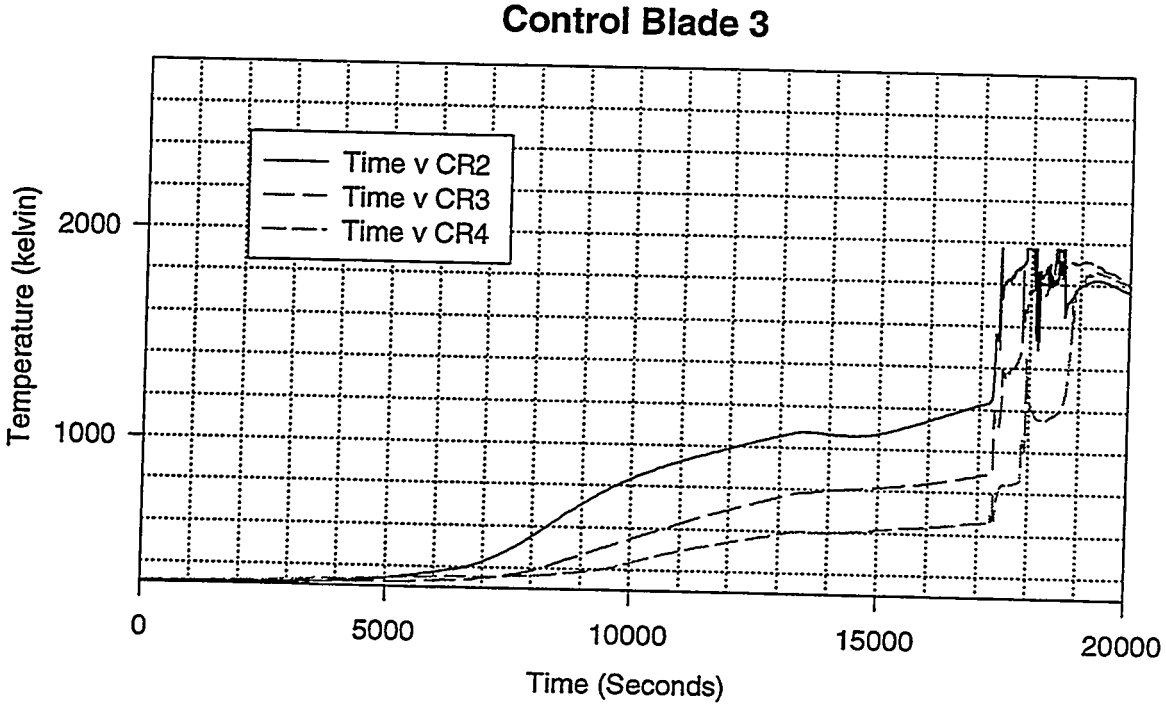

Figure D-14. Temperature data for control blade 3.

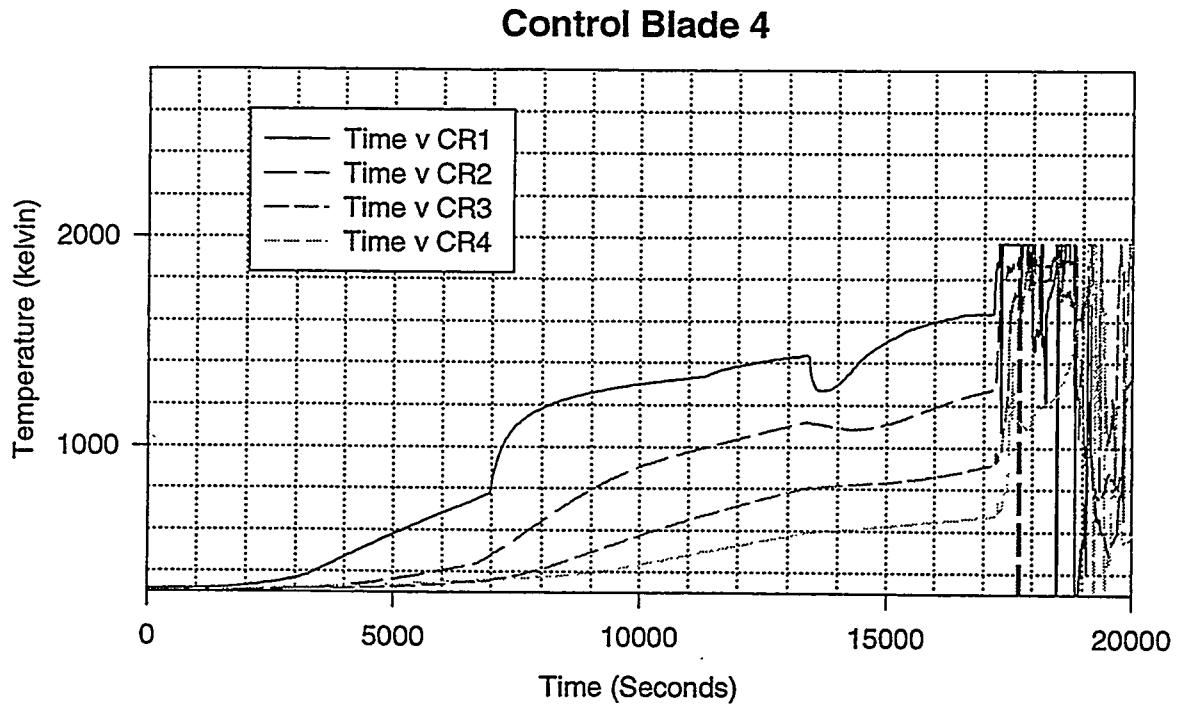

Figure D-15. Temperature data for control blade 4.

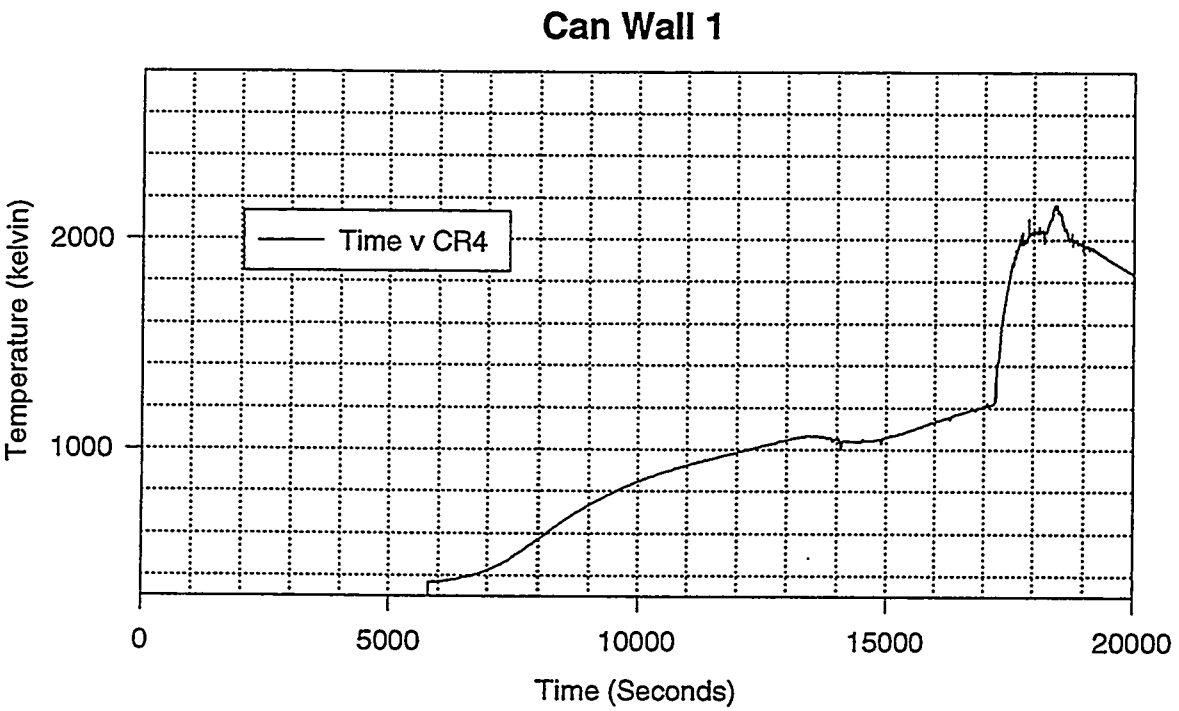

Figure D-16. Temperature data for can wall 1.

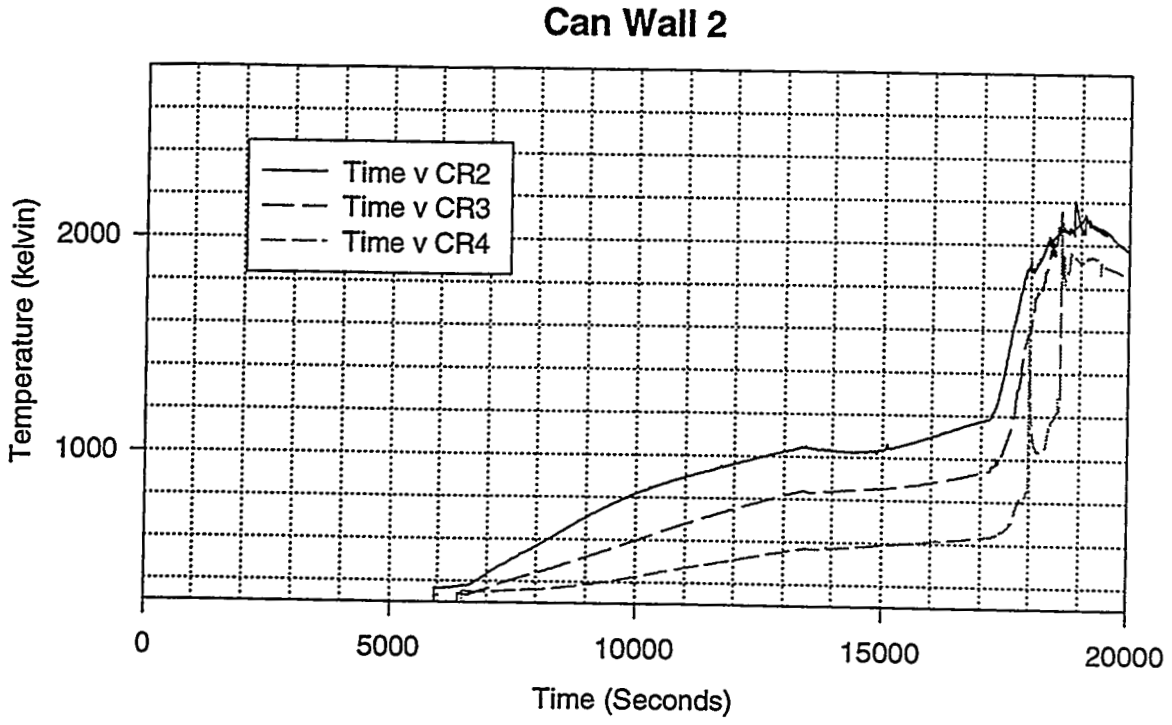

Figure D-17. Temperature data for can wall 2.

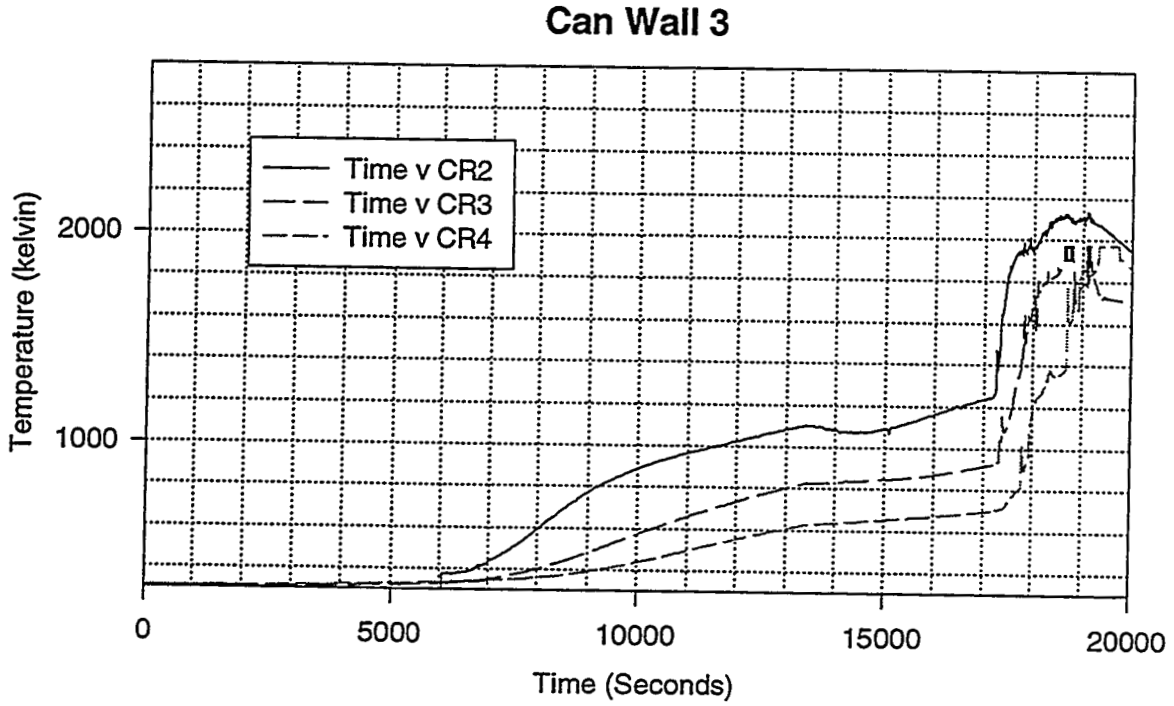

Figure D-18. Temperature data for can wall 3.

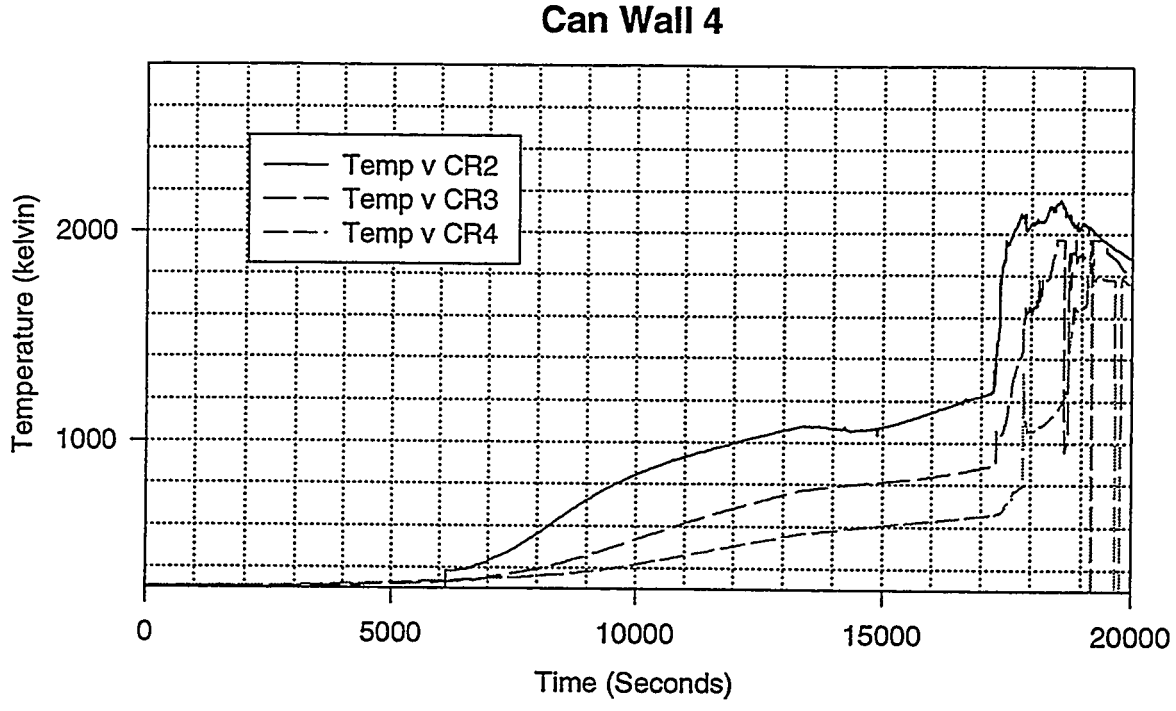

Figure D-19. Temperature data for can wall 4.

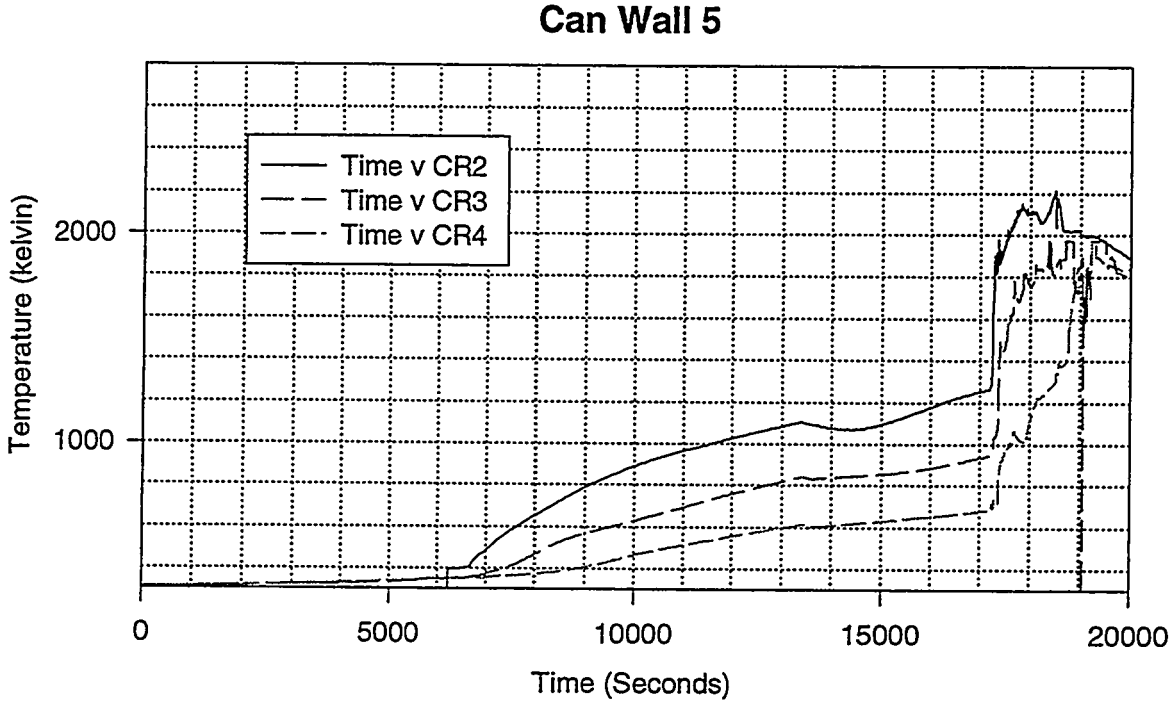

Figure D-20. Temperature data for can wall 5

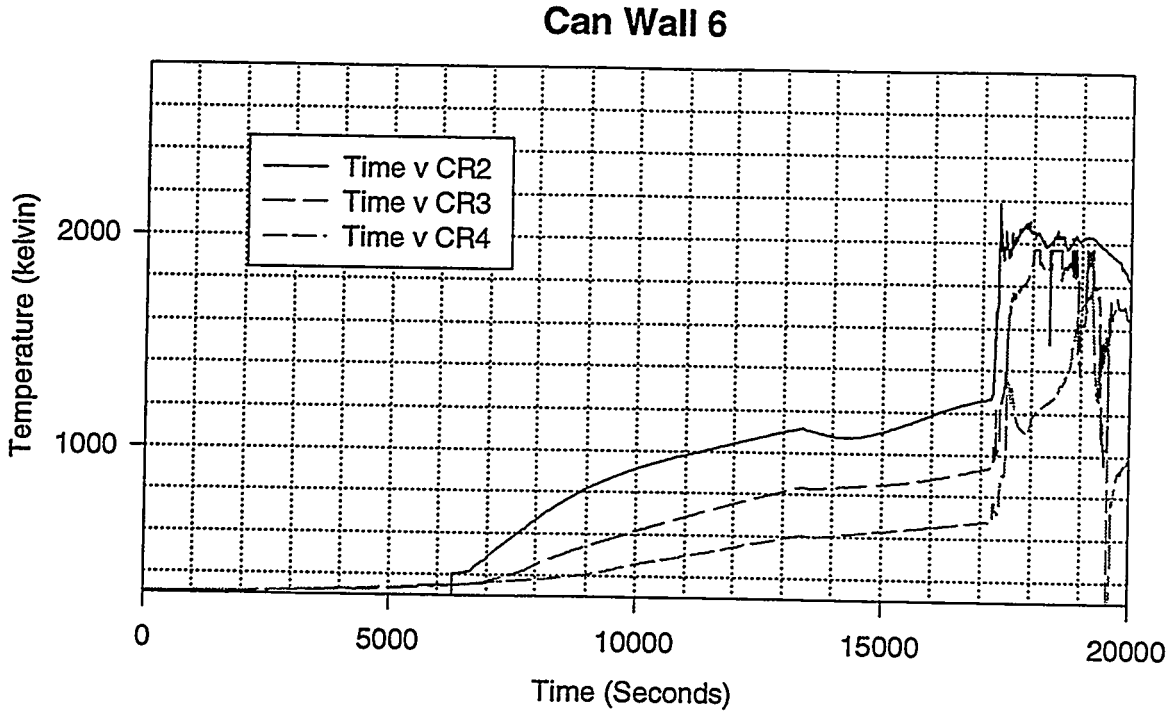

Figure D-21. Temperature data for can wall 6

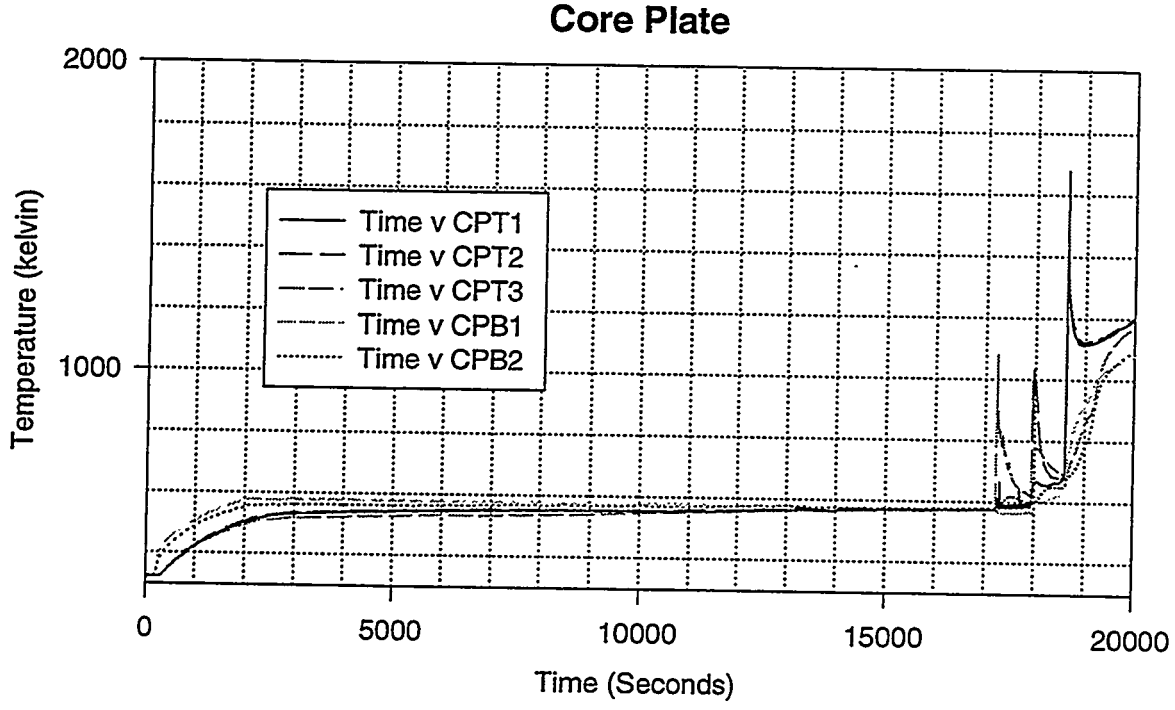

Figure D-22. Temperature data for the core plate.

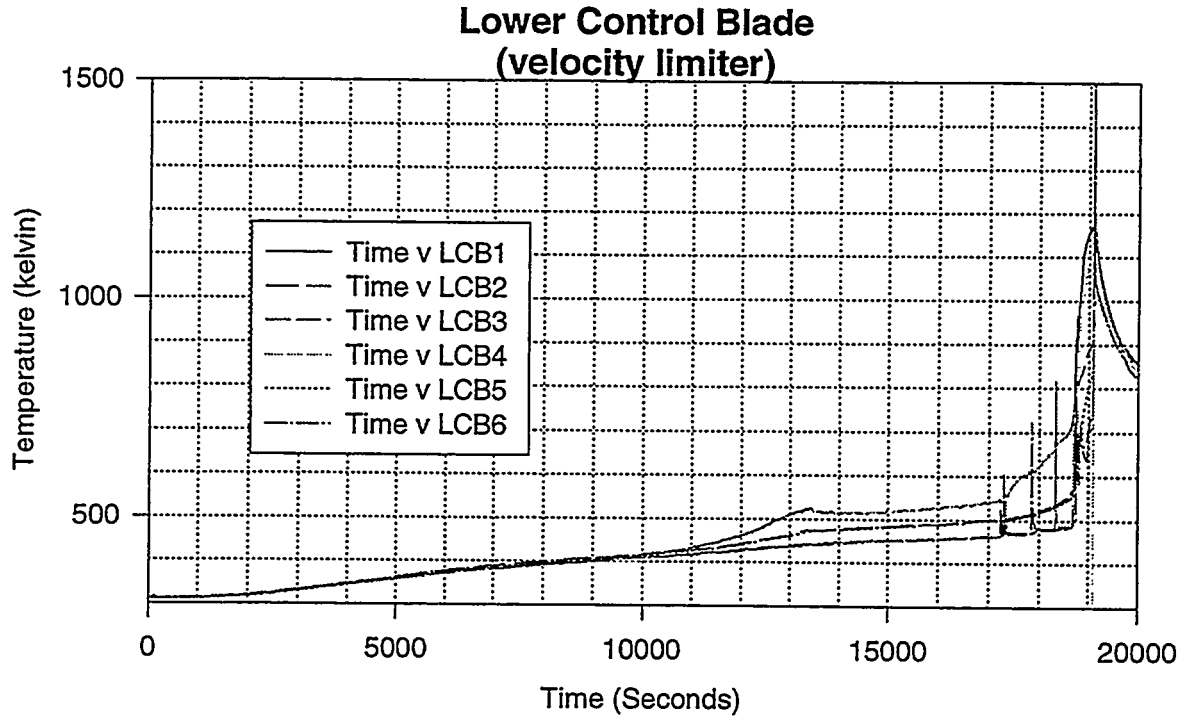

Figure D-23. Temperature data for the lower control blade (velocity limiter).

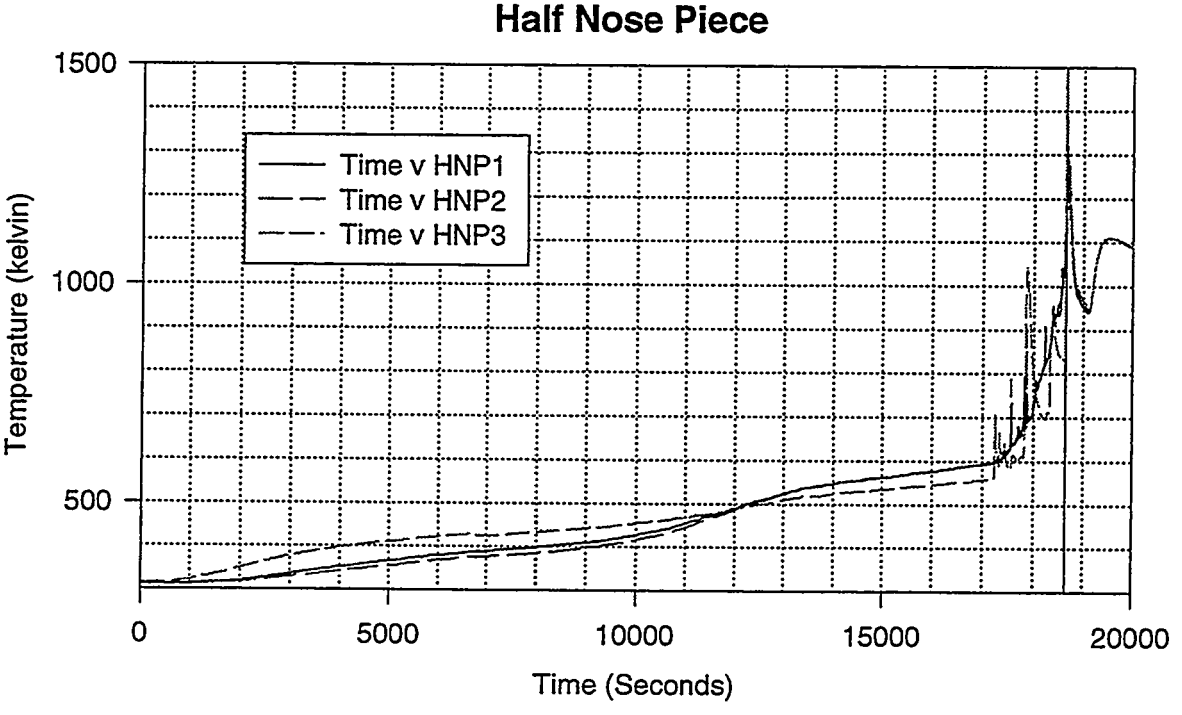

Figure D-24. Temperature data for the half nose piece

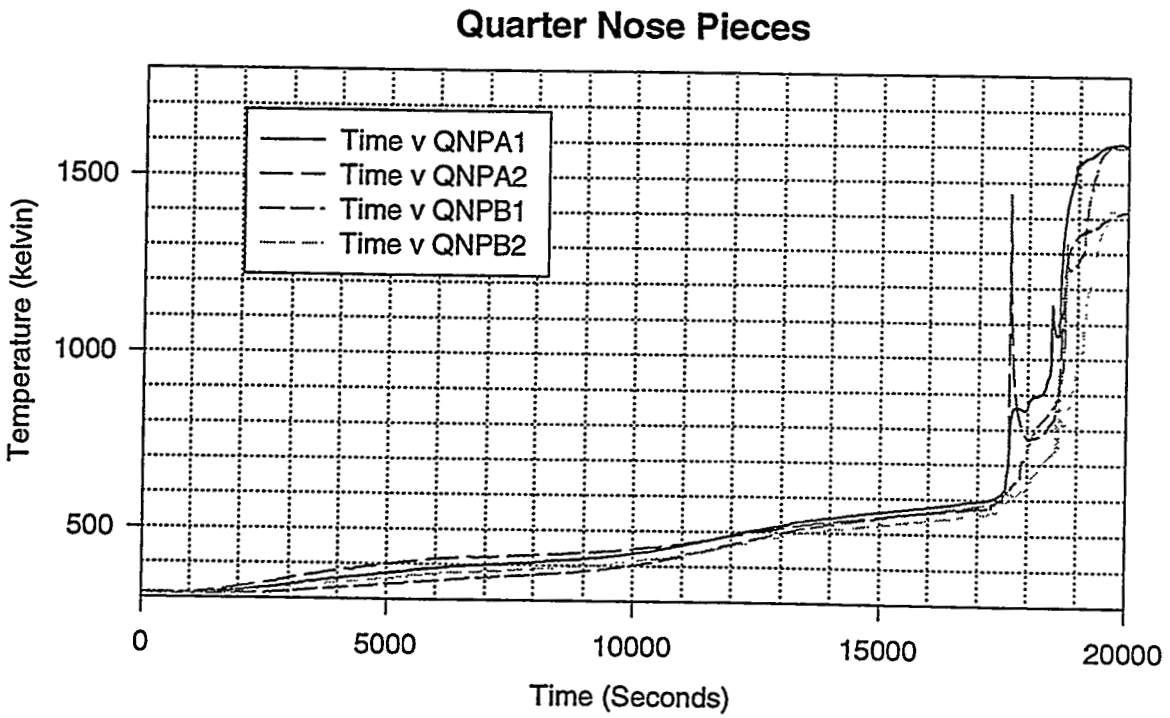

Figure D-25. Temperature data for the quarter nose pieces.

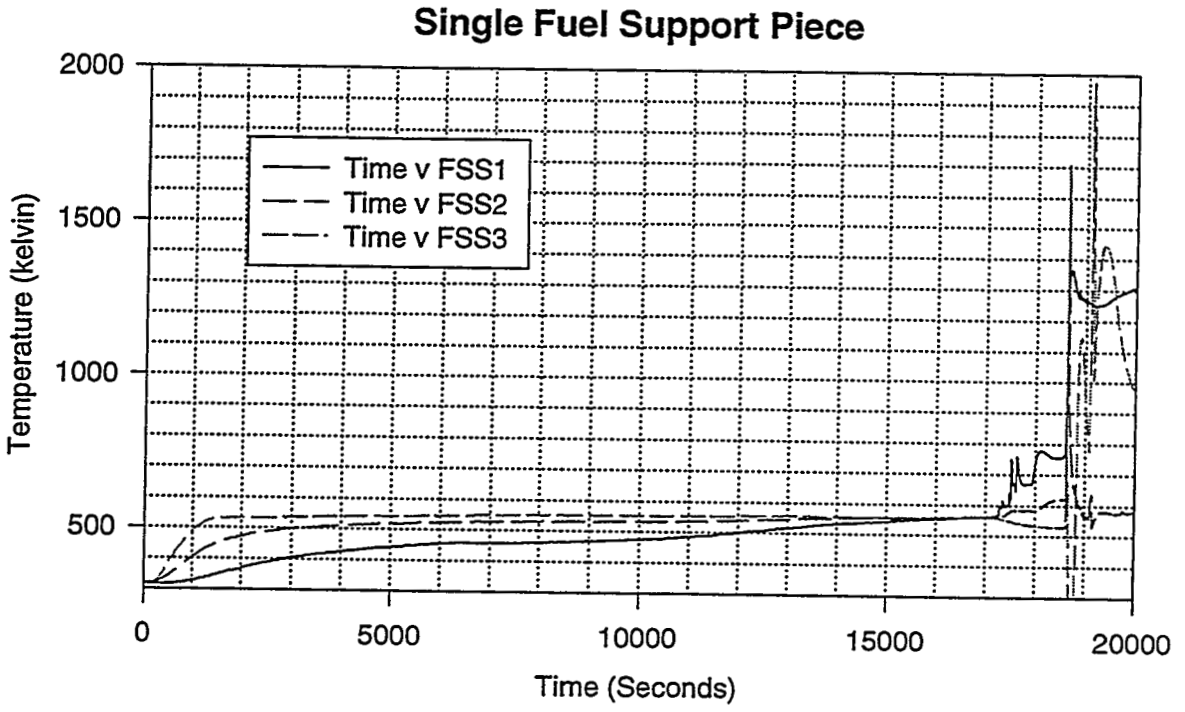

Figure D-26. Temperature data for the single fuel support piece.

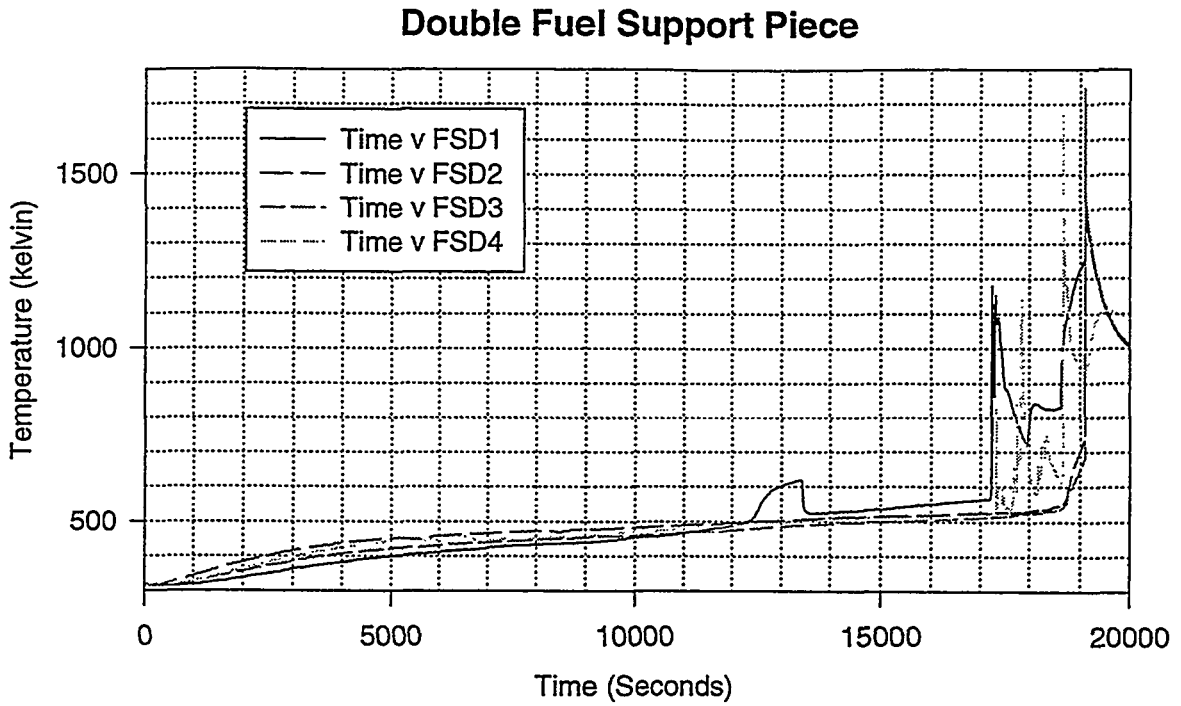

Figure D-27. Temperature data for the double fuel support piece

Appendix E

XR2 Drawings

Figures

Appendix E

XR2 Drawings

This Appendix contains a set of engineering drawings for the XR-2 package. Parts included here are the frame, the core plate, the containment wall, the spacer grids, the can wall, the nosepieces, the fuel support pieces, the control blade, fuel rods, tie rods, and water rods together with their end noses, the guide tubes, and the reinforcing plate.

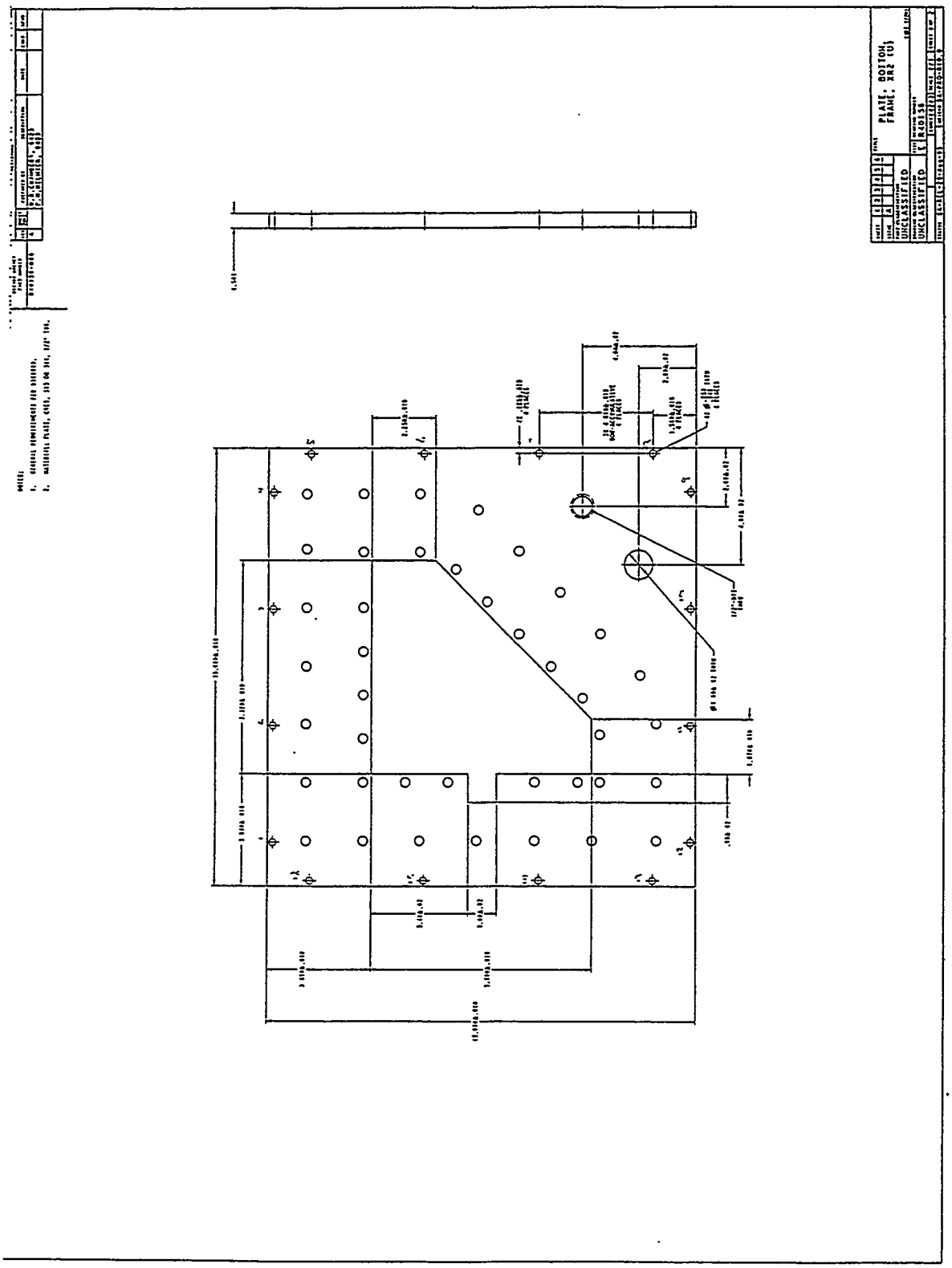

Figure E-1: Bottom XR2 Frame Plate.

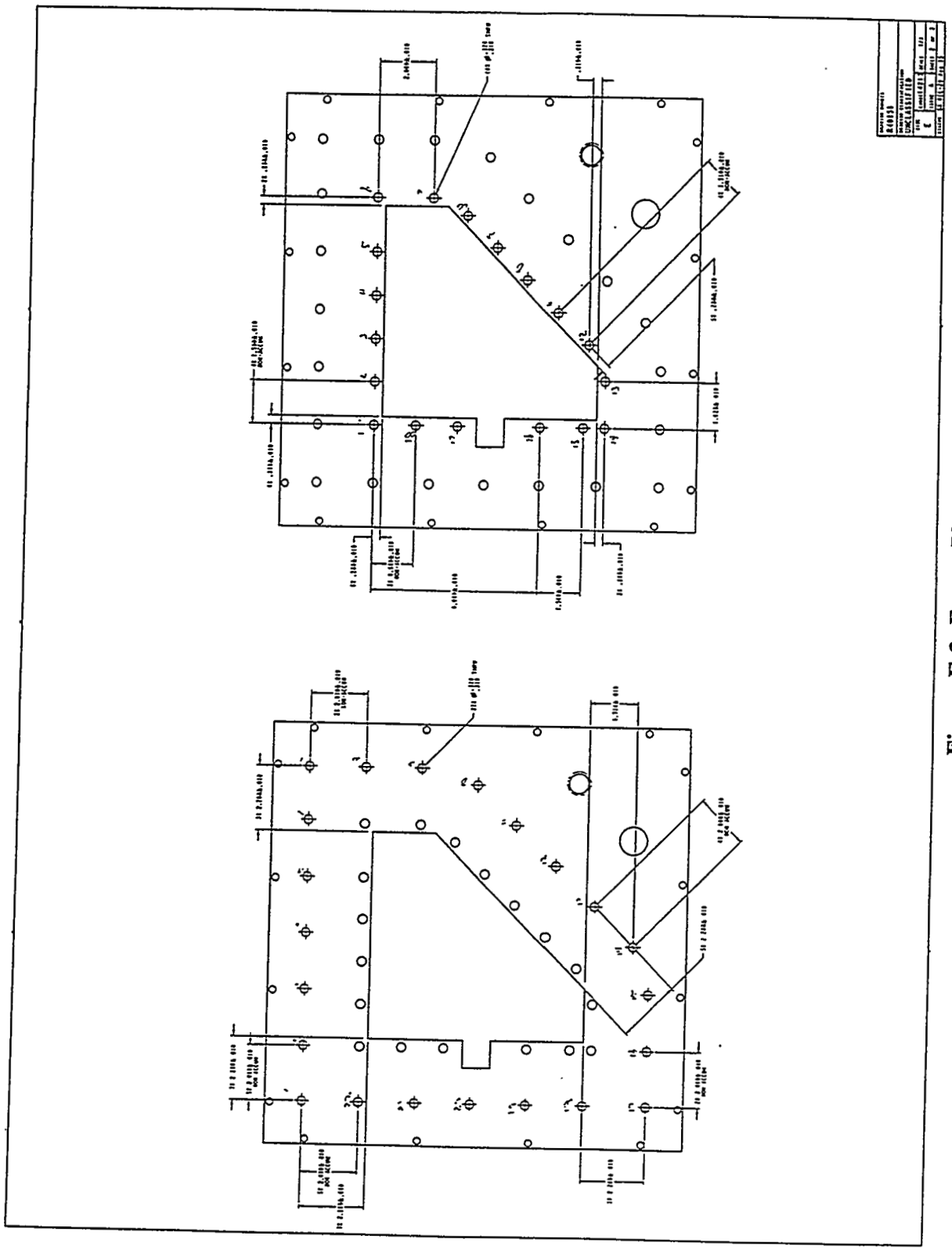

Figure E-2: Frame Plate.

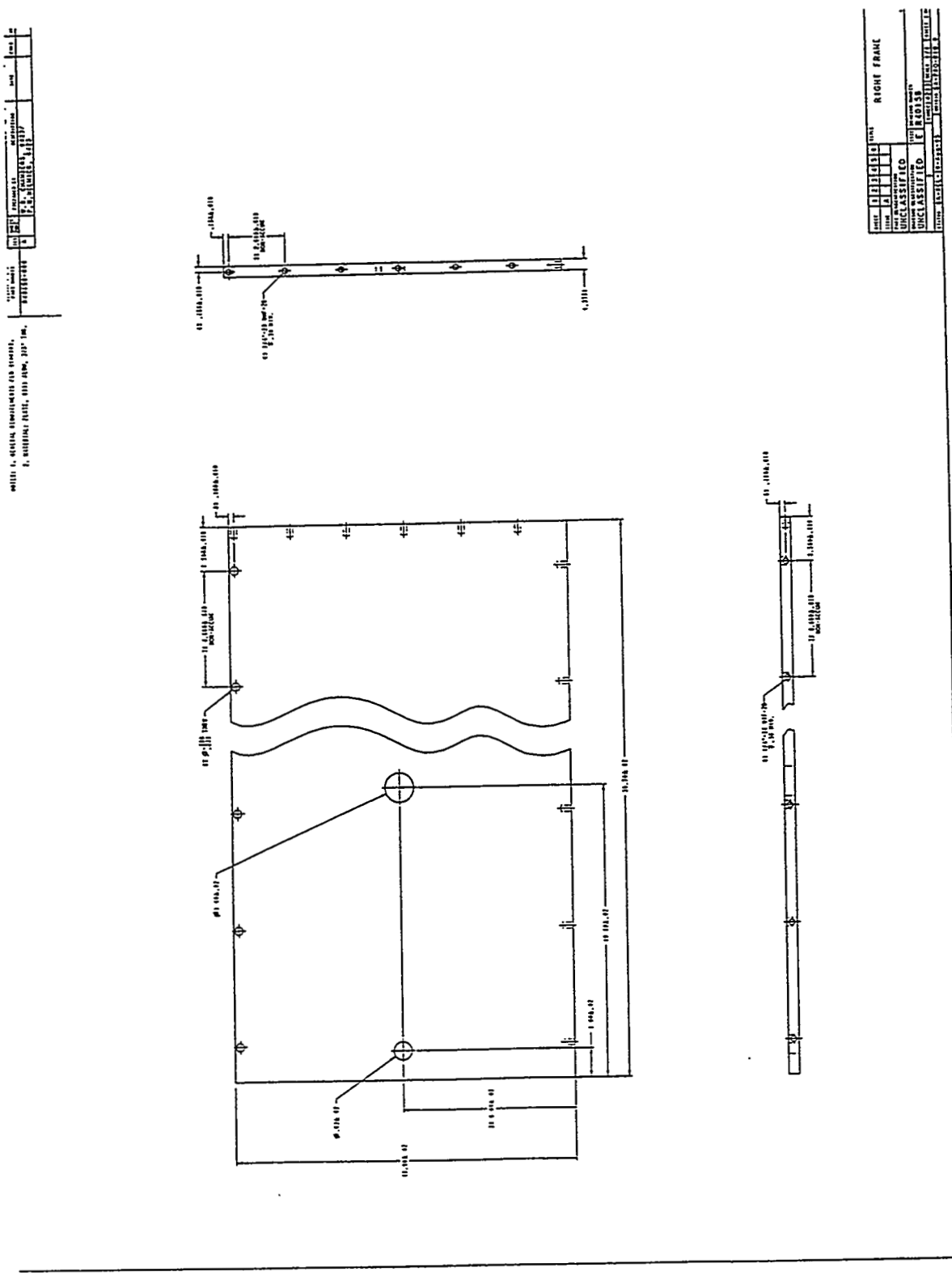

Figure E-3: Right Frame.

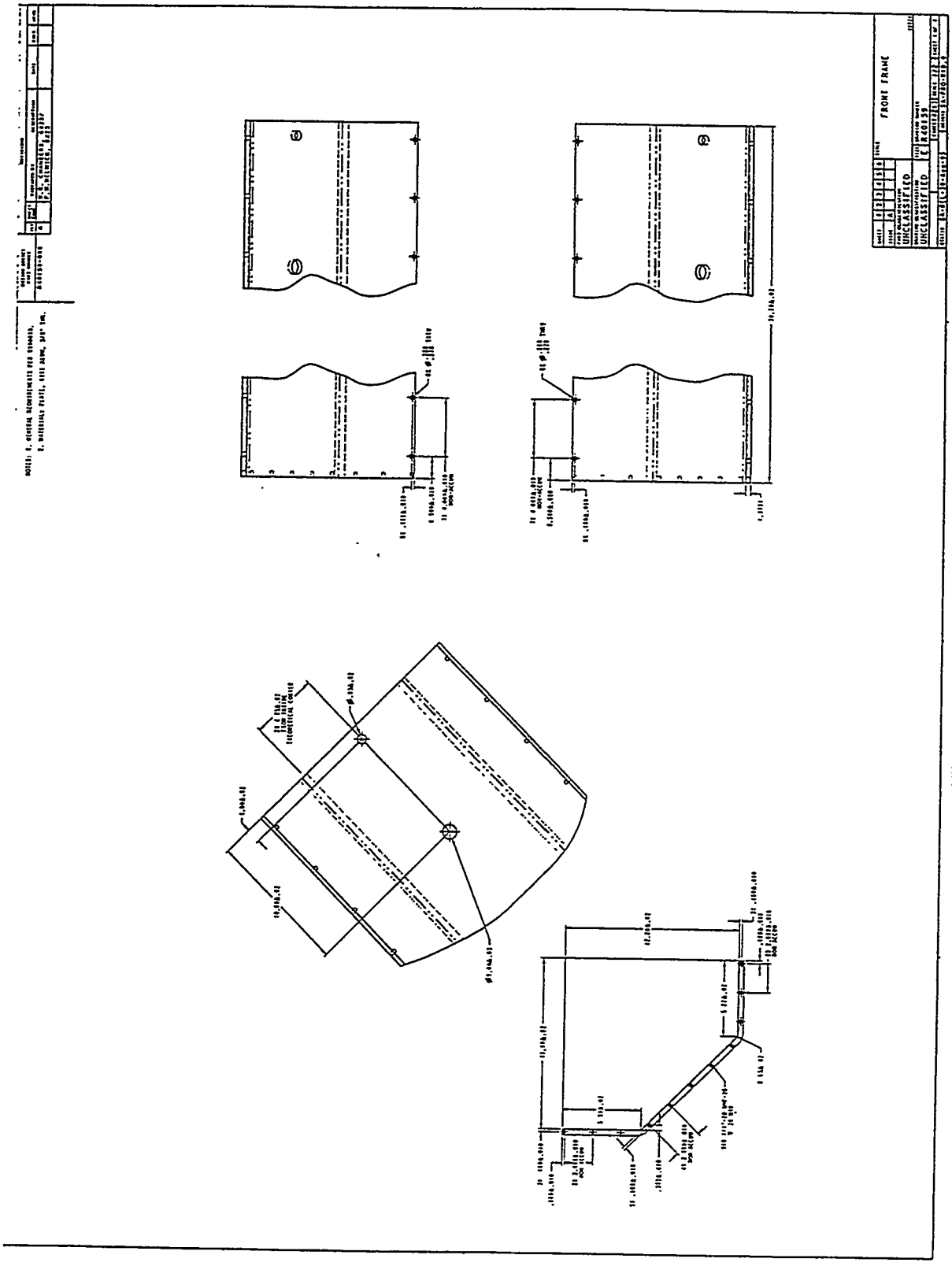

Figure E-4: Front Frame.

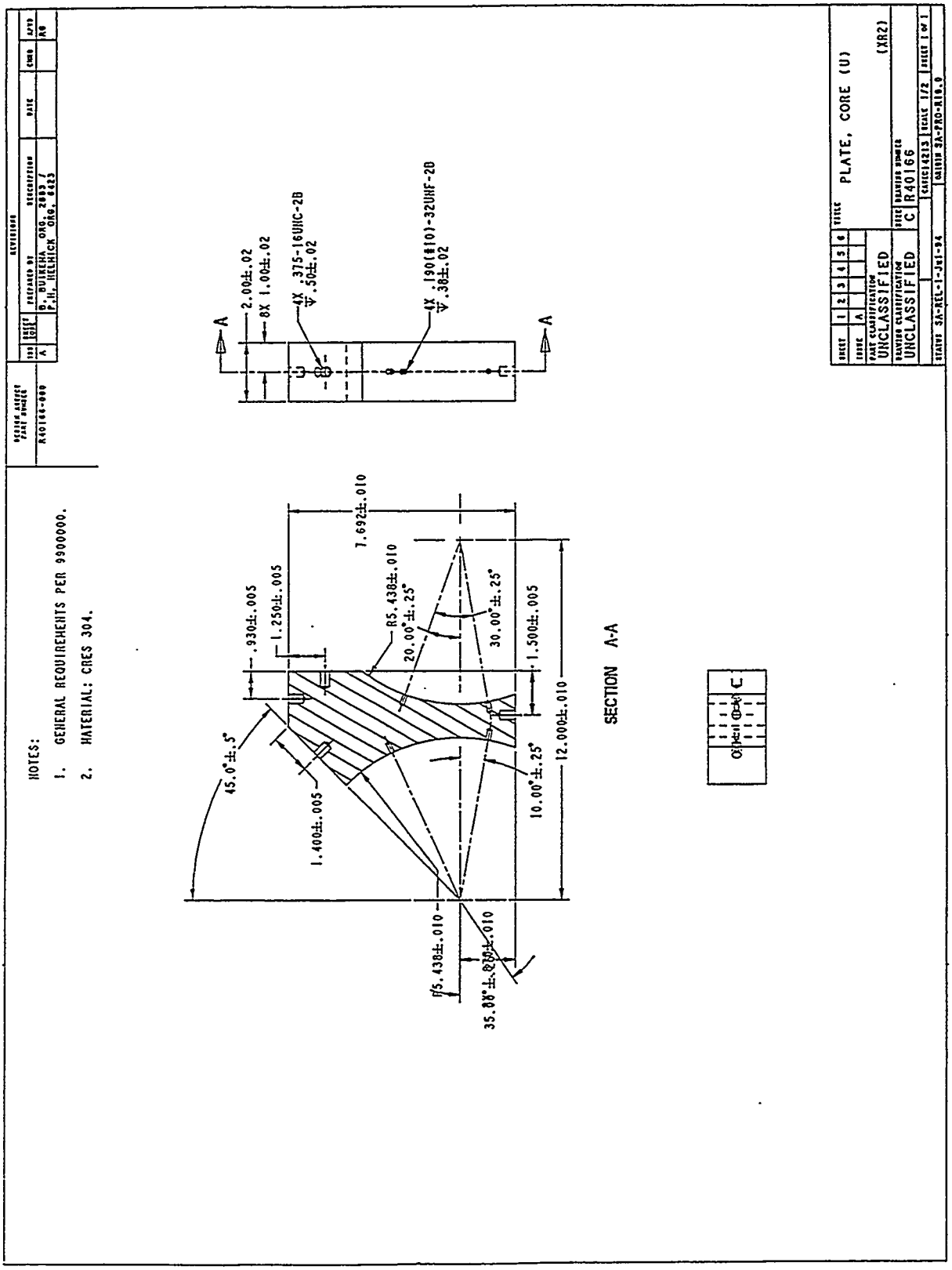

Figure E-5: Core Plate.

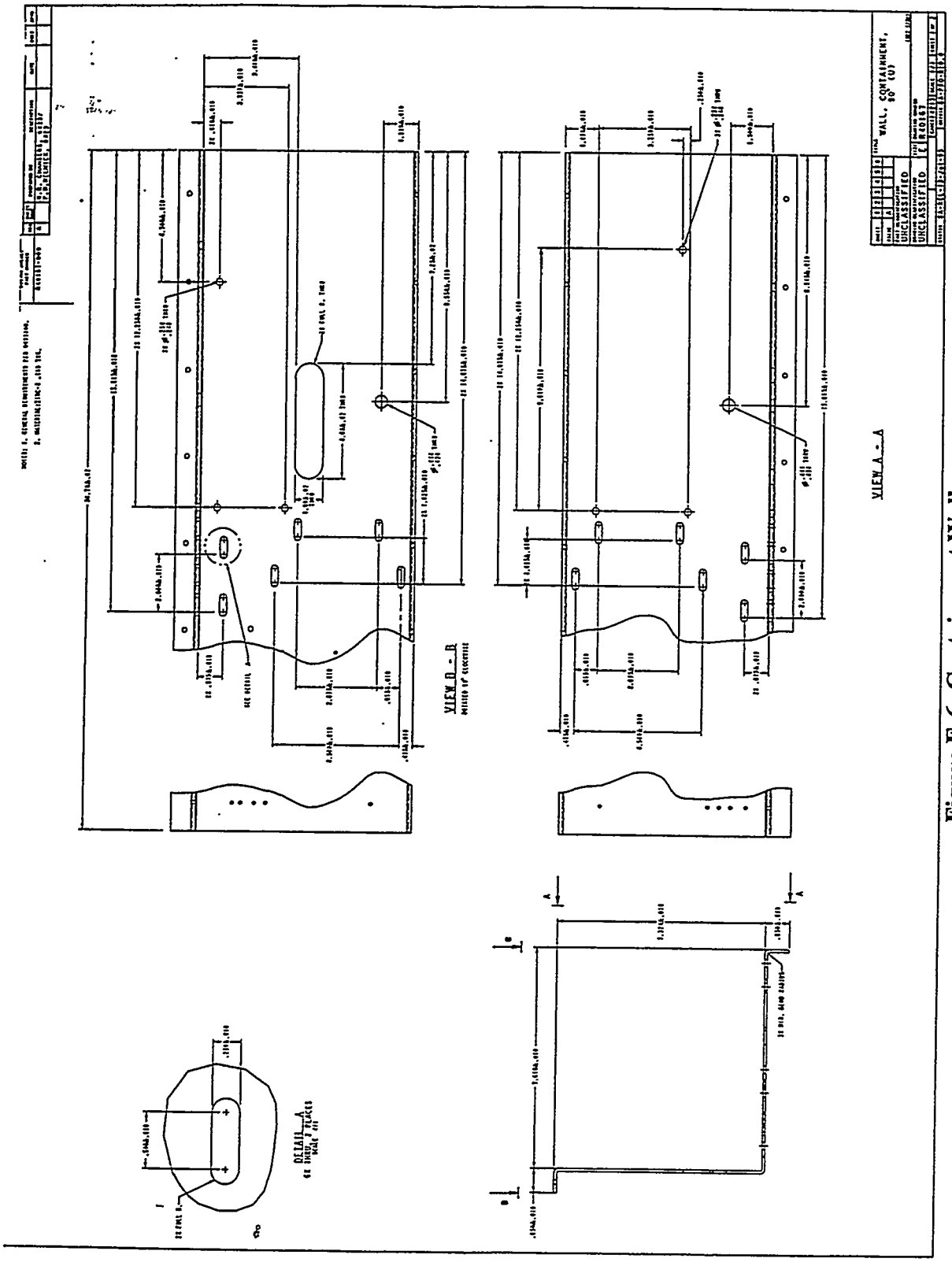

Figure E-6: Containment Wall.

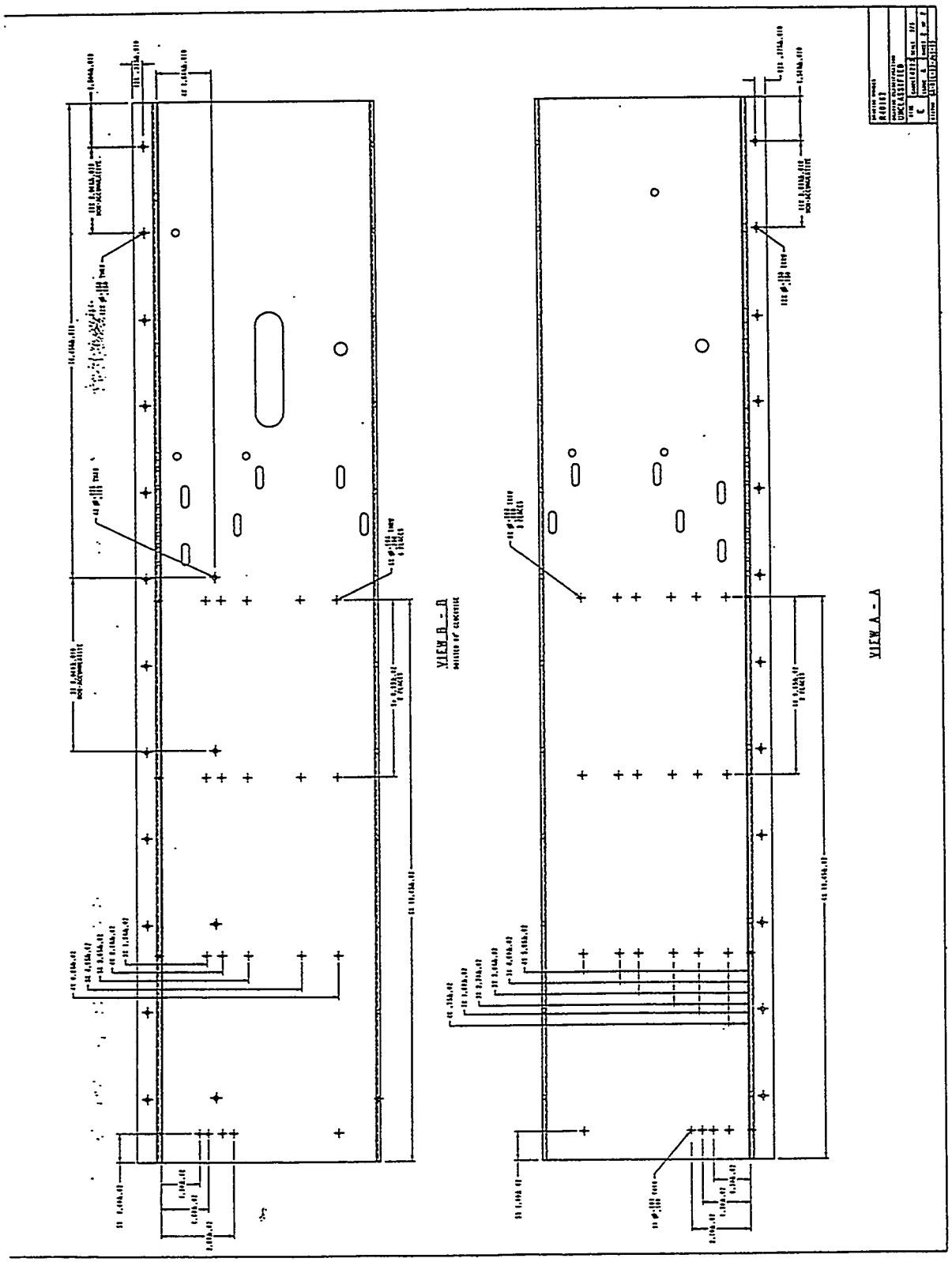

Figure E-7: Containment Wall.

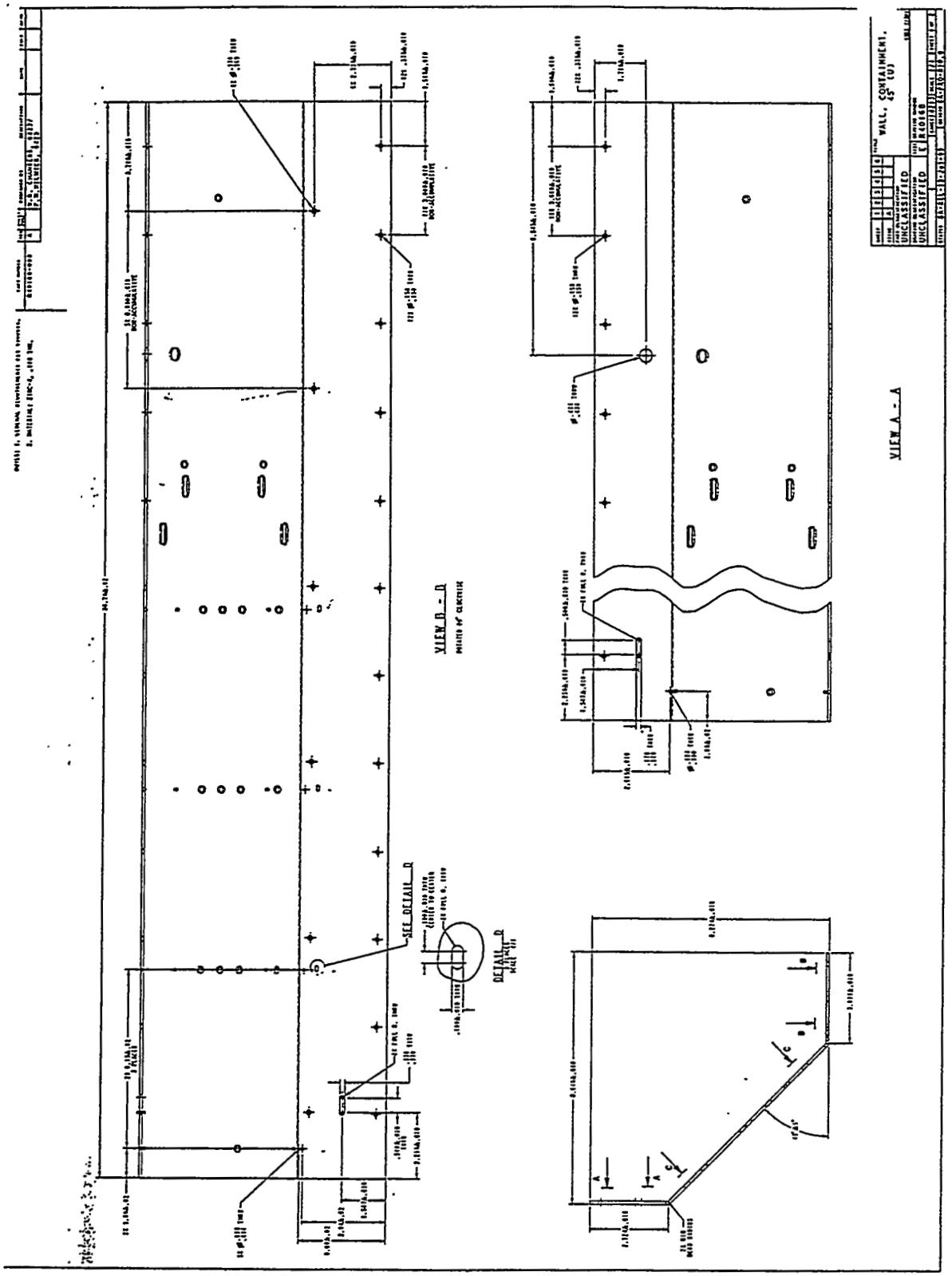

Figure E-8: Containment Wall.

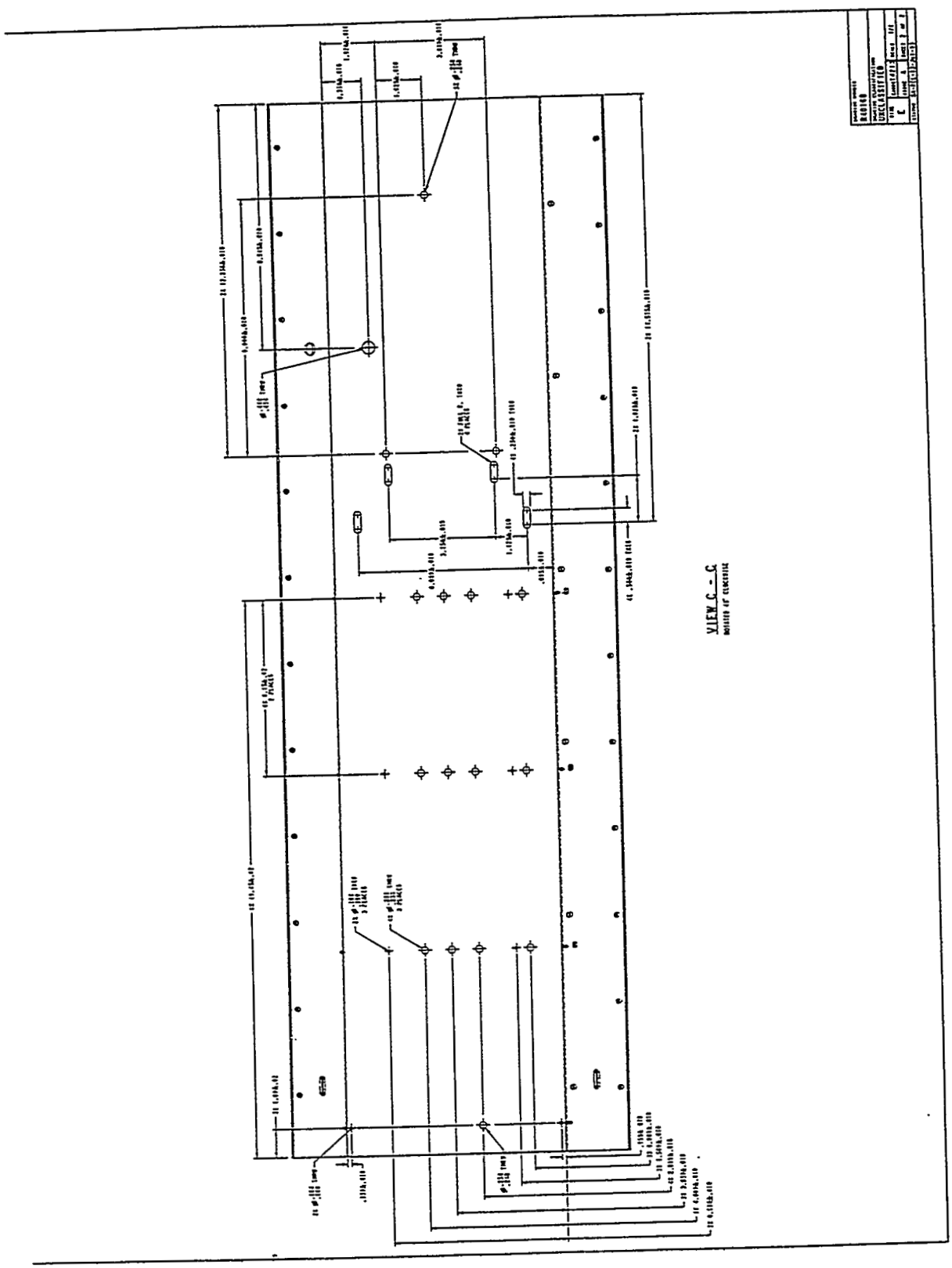

Figure E-9: Containment Wall.

NOTES:

1. GENERAL REQUIREMENTS PER 9900000.
2. MATERIAL: CUT EXISTING FUEL SPACER AS SHOWN. TO BE OBTAINED FROM DIV 6423.

DESIGN AGENCY PART NUMBER	REVISIONS					
	ISS	SHEET ZONE	PREPARED BY DESCRIPTION	DATE	CHKR	APVD
R40169-000	A		B. BUIKEMA ORG. 2883/ P.H. HELMICK ORG. 6423			

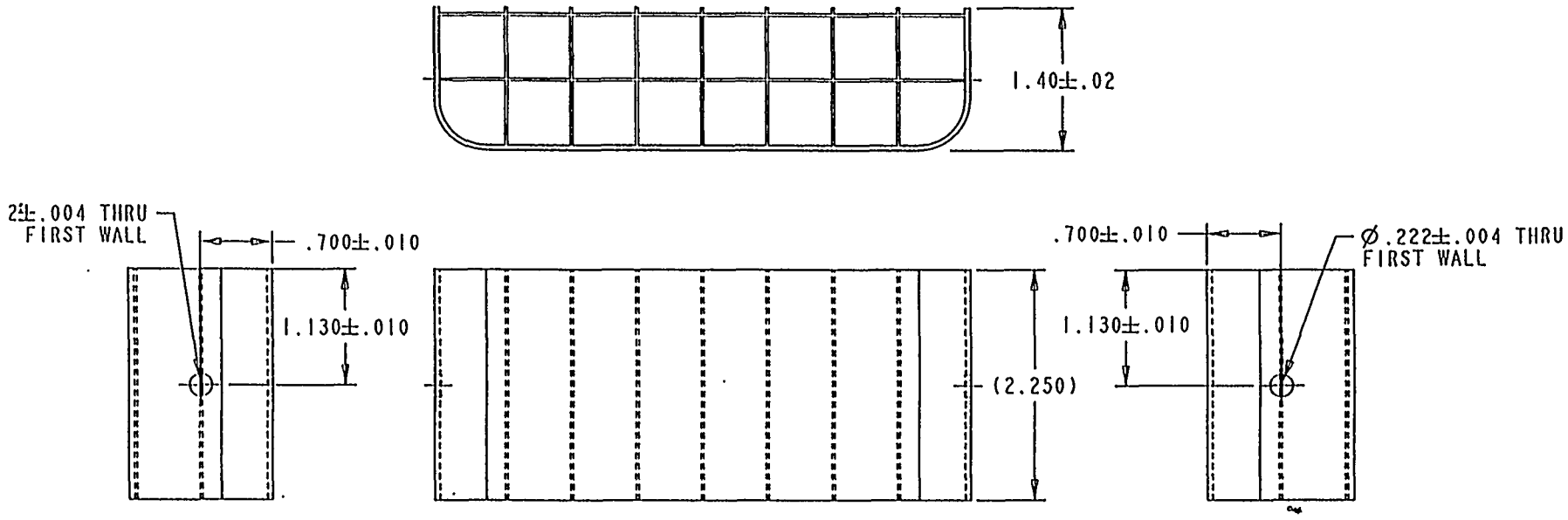

SHEET	1	2	3	4	5	6	TITLE SPACER, FUEL BUNDLE, QUARTER (U)
ISSUE	A						
PART CLASSIFICATION UNCLASSIFIED							(XR2 1/2H)
DRAWING CLASSIFICATION UNCLASSIFIED							SIZE B DRAWING NUMBER R40169
							CAGEC 14213 SCALE 1/1 SHEET 1 OF 1
STATUS SA-REL-1-Jul-94							ORIGIN SA-PRO-R10.0

Figure E-10: Quarter Fuel Bundle Spacer.

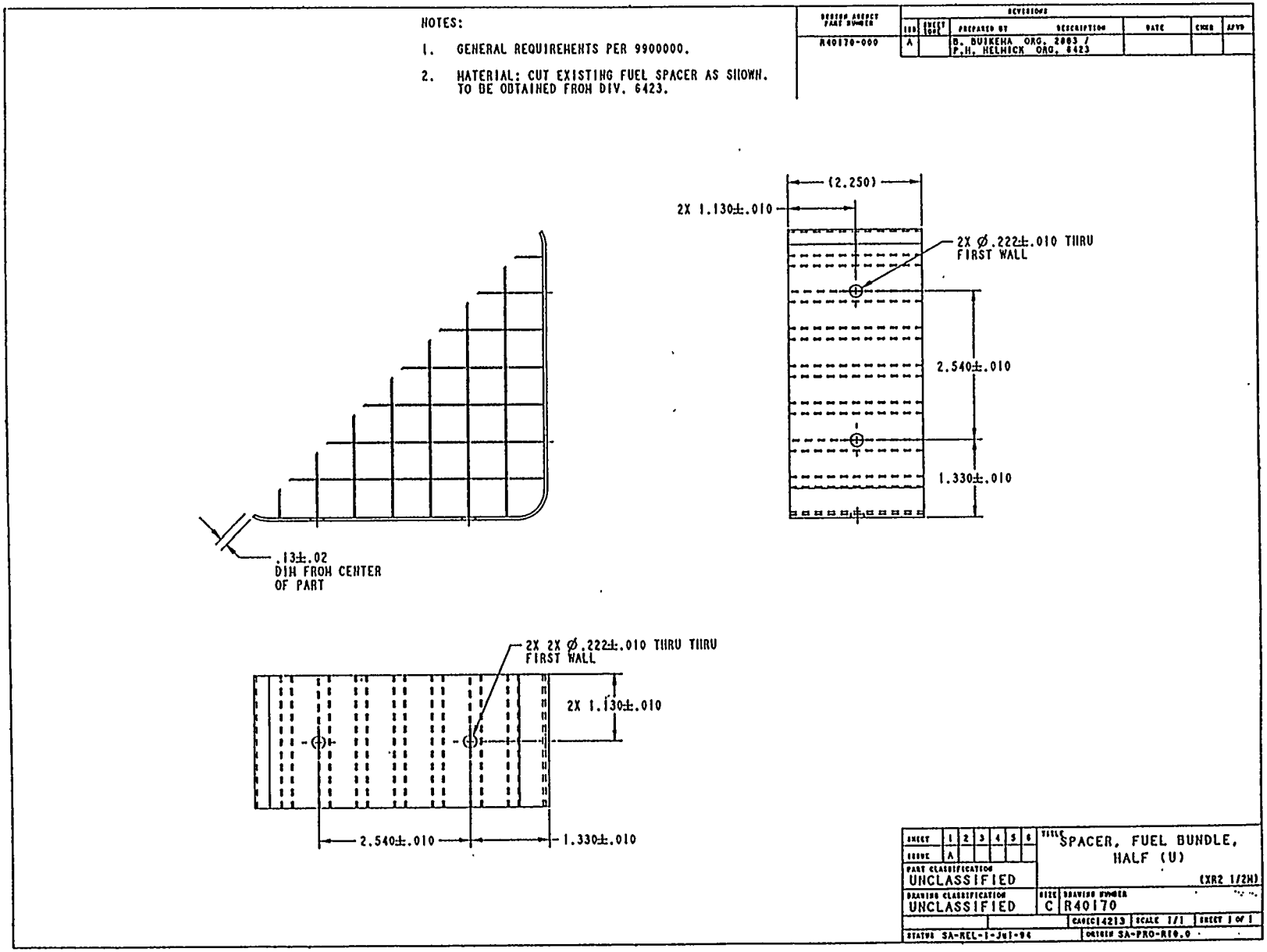

Figure E-11: Half Fuel Bundle Spacer.

NOTES:

1. GENERAL REQUIREMENTS PER 9900000.
2. MATERIAL: CUT EXISTING FUEL SPACER AS SHOWN. TO BE OBTAINED FORM DIV. 6423.

DESIGN AGENCY PART NUMBER	REVISIONS					
	ISS	SHEET ZONE	PREPARED BY DESCRIPTION	DATE	CHKR	APVD
R40171-000	A		B. BUIKEMA ORG. 2883/ P.H. HELMICK ORG. 6423			

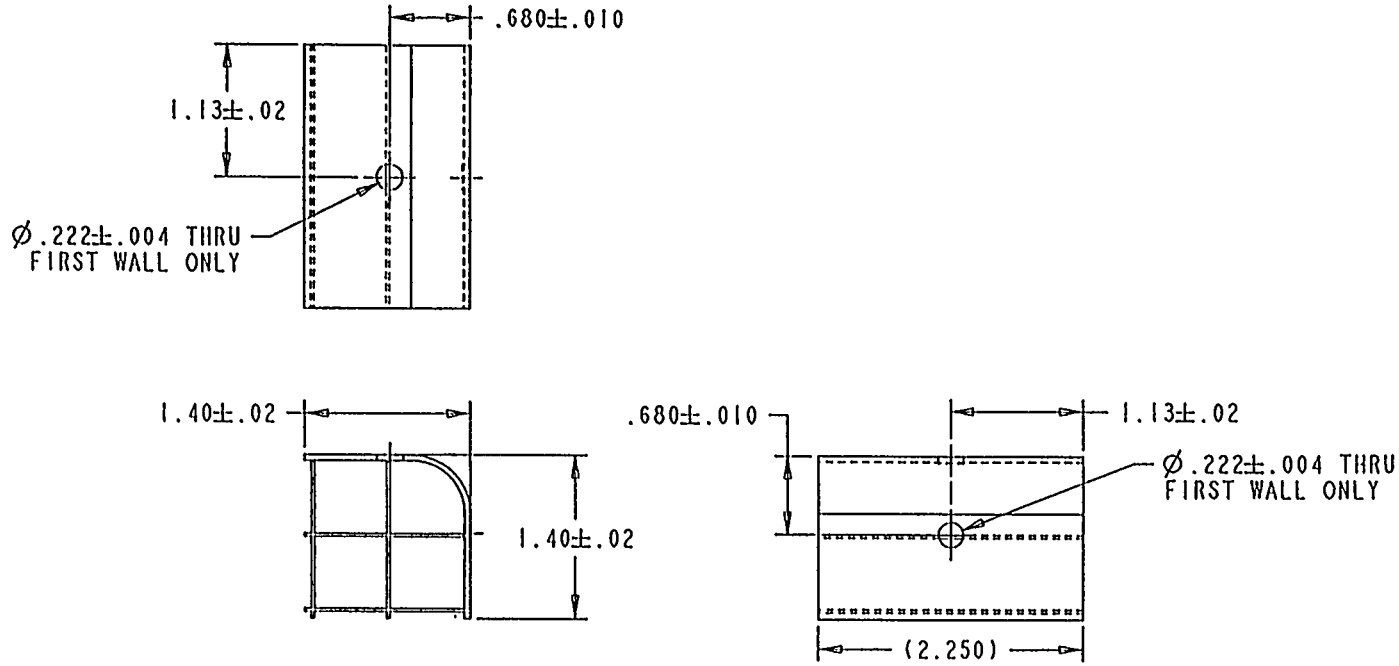

SHEET	1	2	3	4	5	6	TITLE SPACER, FUEL BUNDLE, DUMMY (U)
ISSUE	A						
PART CLASSIFICATION UNCLASSIFIED							(XR2 1/2H)
DRAWING CLASSIFICATION UNCLASSIFIED							SIZE B DRAWING NUMBER R40171
							CAGEC 14213 SCALE 1/1 SHEET 1 OF 1
STATUS SA-REL-1-Jul-94							ORIGIN SA-PRO-R10.0

Figure E-12: Dummy Fuel Bundle Spacer.

NOTES:

1. GENERAL REQUIREMENTS PER 9900000.
2. MATERIAL: CUT EXISTING FUEL SPACER AS SHOWN. TO BE OUTAINED FORM DIV. 6423.

DESIGN AGENCY PART NUMBER	REVISIONS					
	ISS	SHEET ZONE	PREPARED BY DESCRIPTION	DATE	CHKR	APVD
R40171-000	A		B. BUIKEMA ORG. 2883/ P.H. HELMICK ORG. 6423			

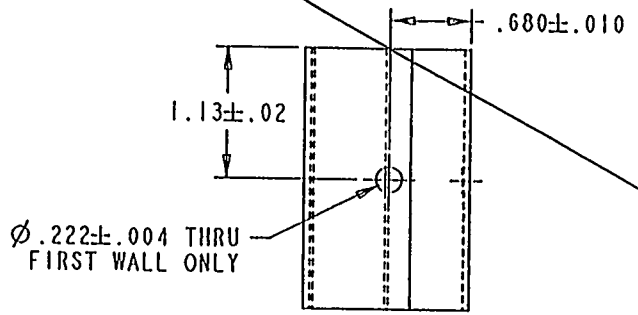

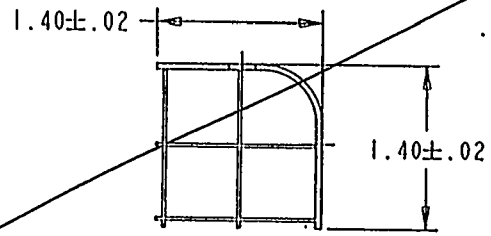

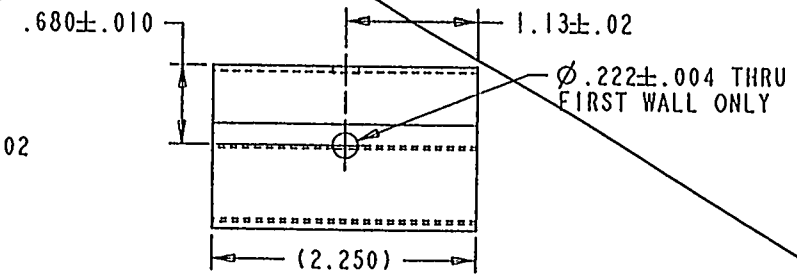

SHEET	1	2	3	4	5	6	TITLE: SPACER, FUEL BUNDLE, DUMMY (U)
ISSUE	A						
PART CLASSIFICATION: UNCLASSIFIED							(XR2 1/2H)
DRAWING CLASSIFICATION: UNCLASSIFIED							SIZE: B; DRAWING NUMBER: R40171
							CAGEC 14213; SCALE 1/1; SHEET 1 OF 1
STATUS SA-REL-1-Jul-94							ORIGIN SA-PRO-R10.0

Figure E-12: Dummy Fuel Bundle Spacer.

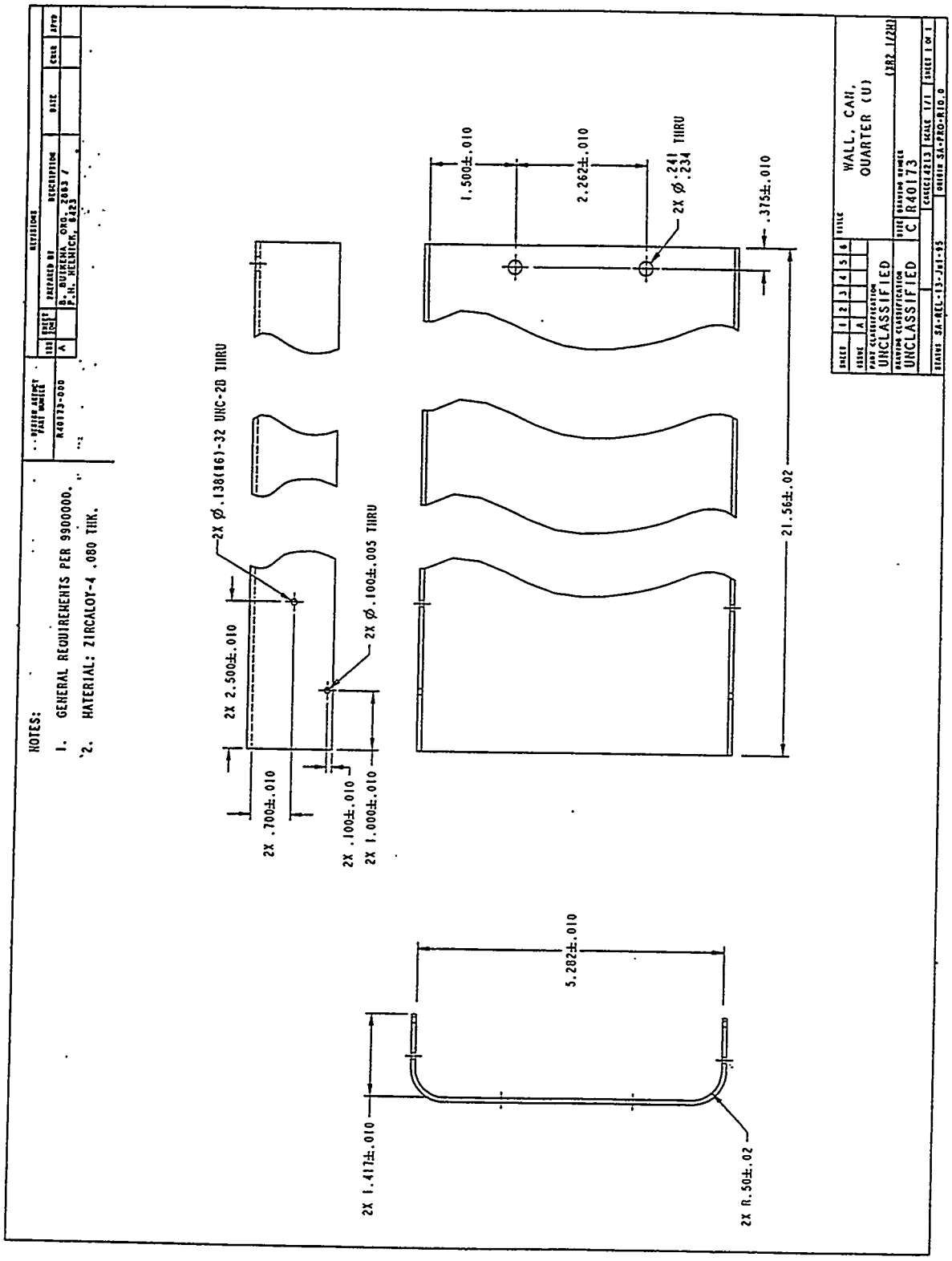

Figure E-14: Quarter Can Wall.

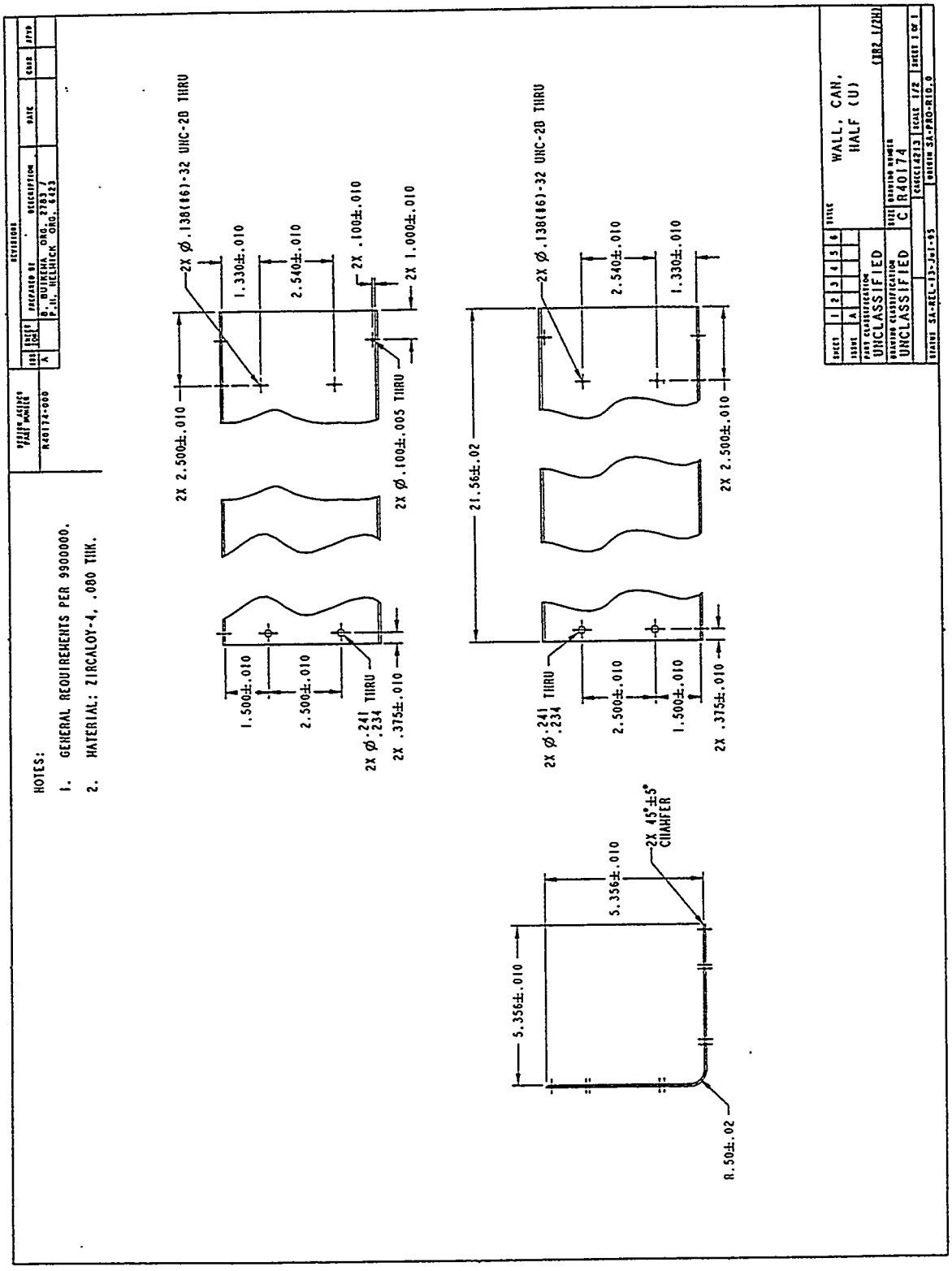

Figure E-15: Half Can Wall.

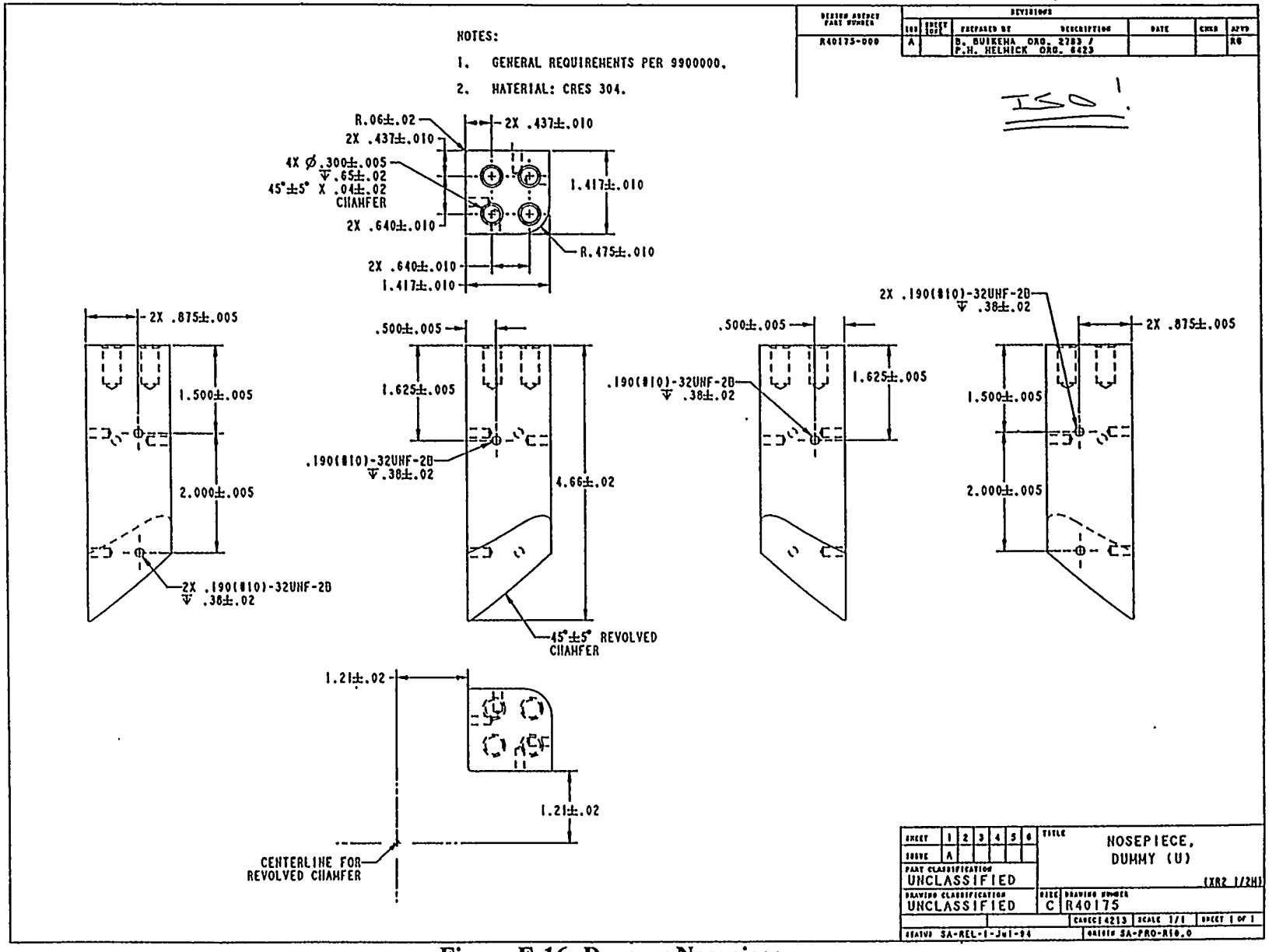

Figure E-16: Dummy Nosepiece.

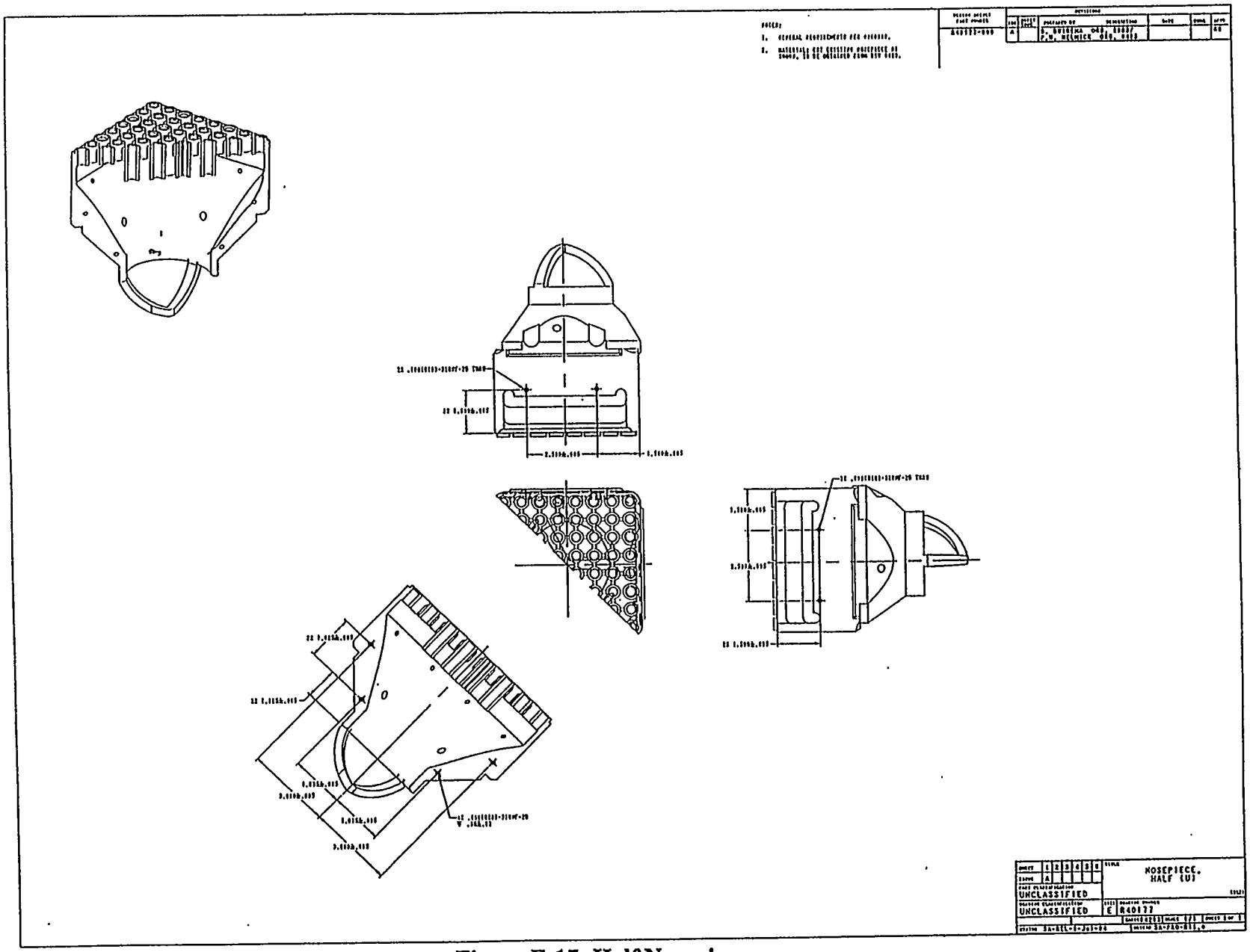

Figure E-17: Half Nosepiece.

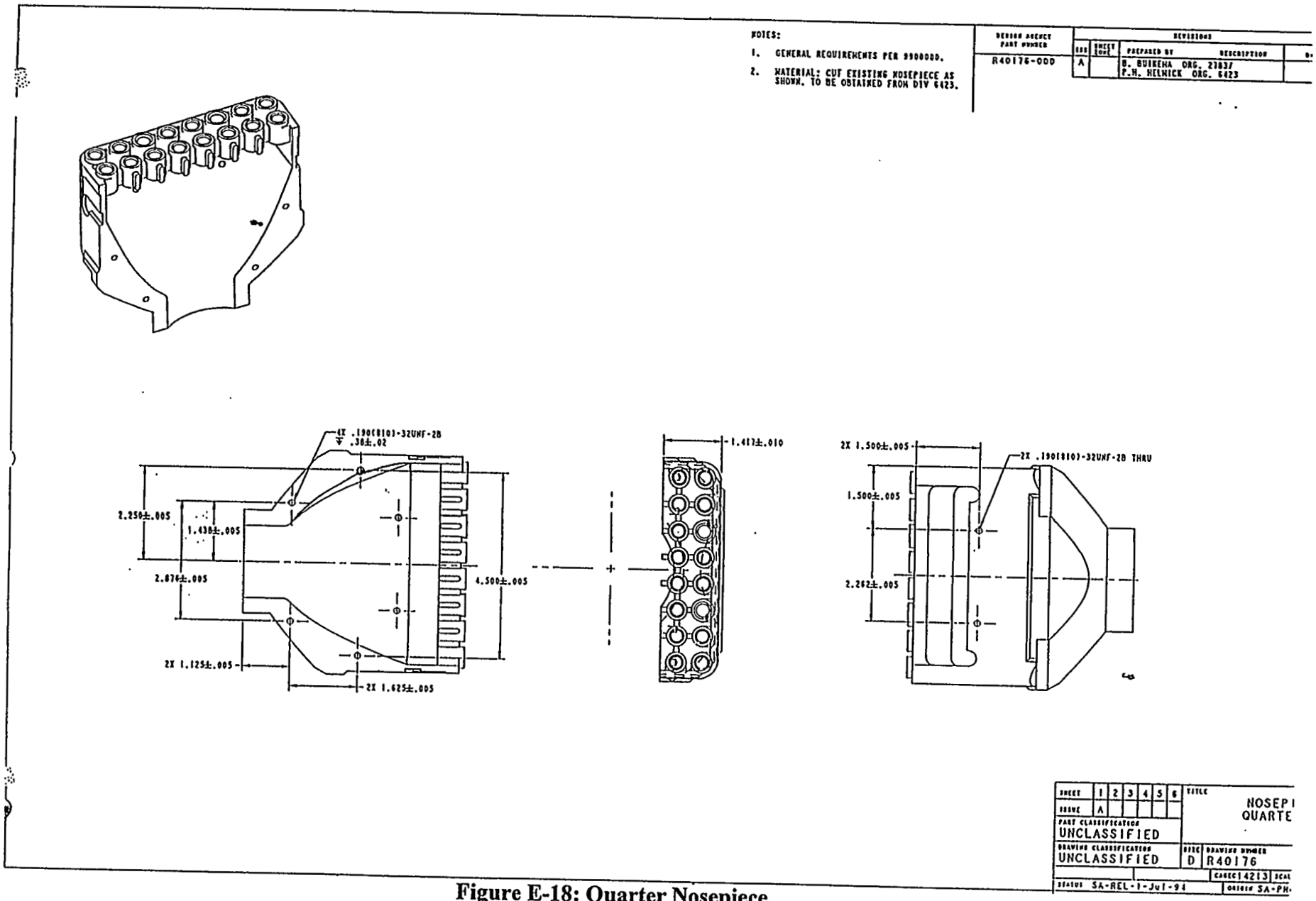

Figure E-18: Quarter Nosepiece.

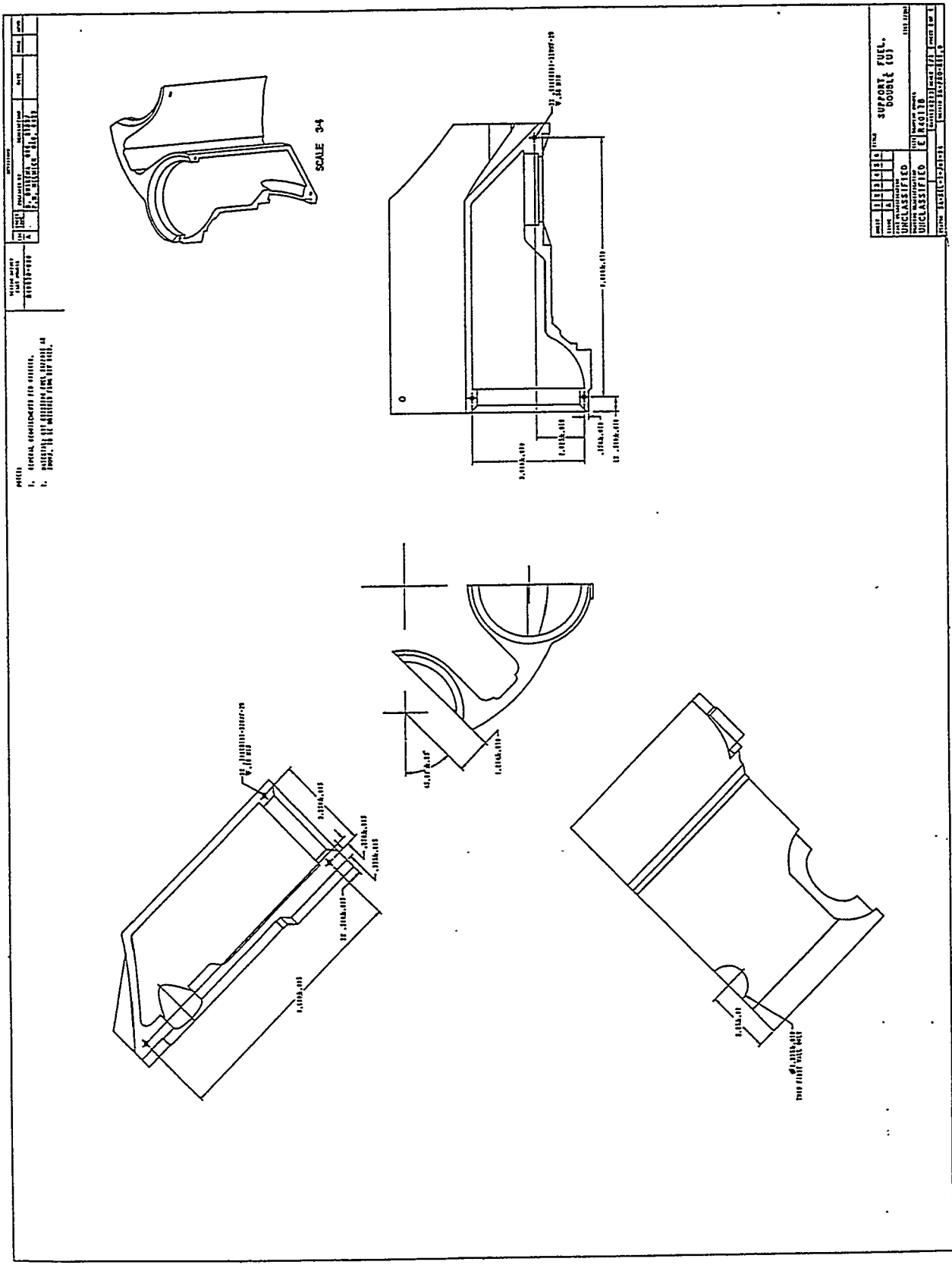

Figure E-19: Double Fuel Support Piece.

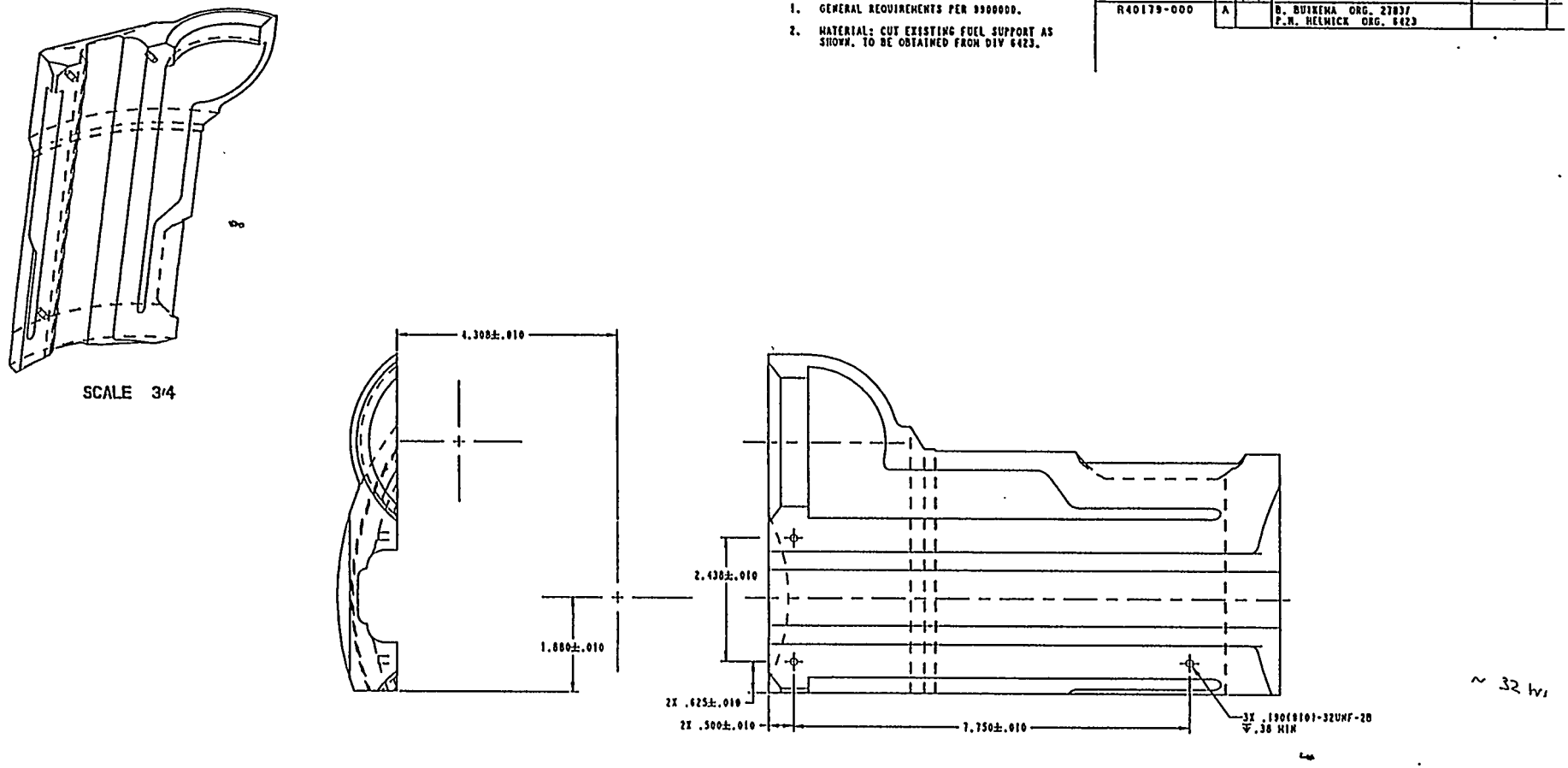

Figure E-20: Single Fuel Support Piece.

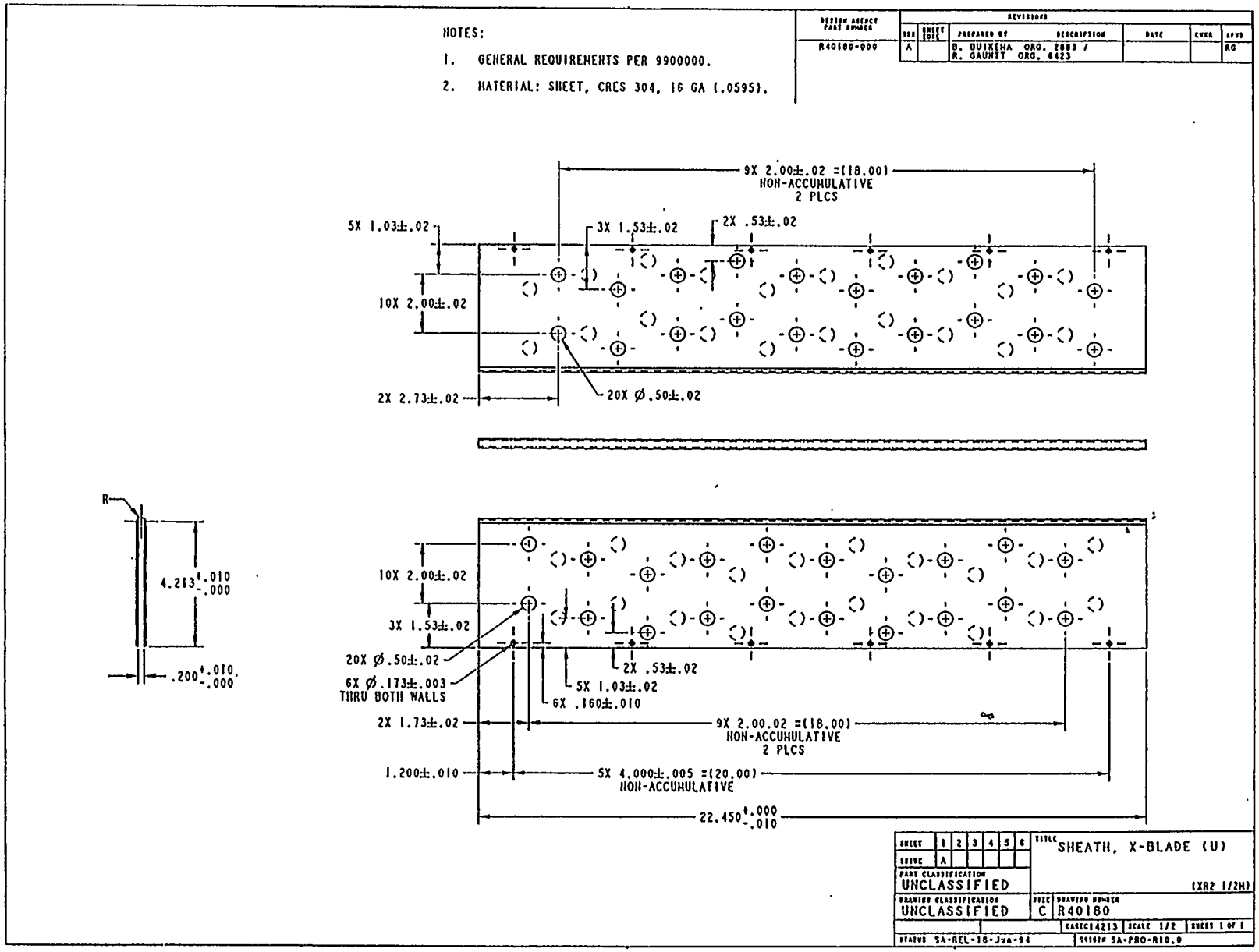

Figure E-21: Control Blade Sheath.

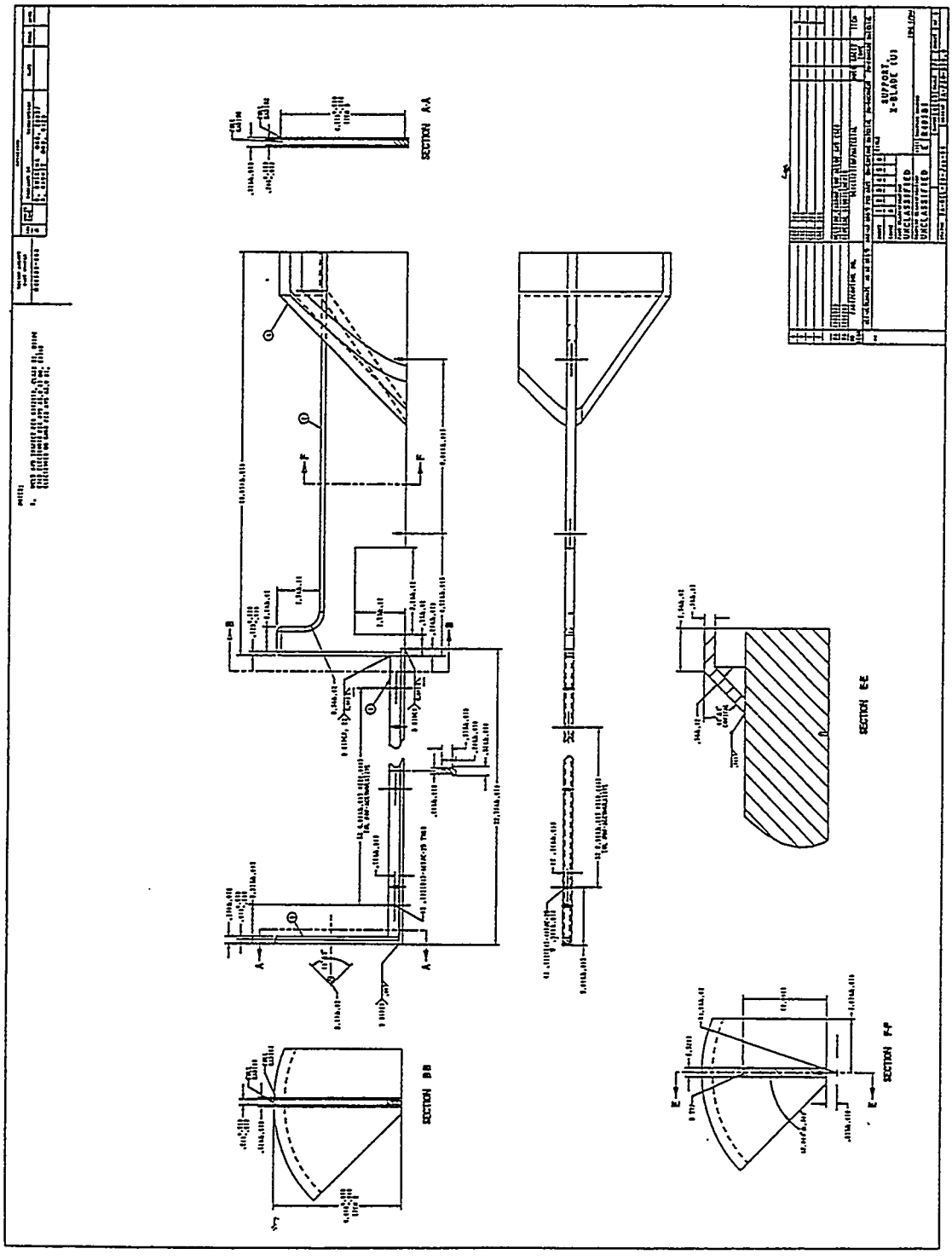

Figure E-22: Control Blade Support.

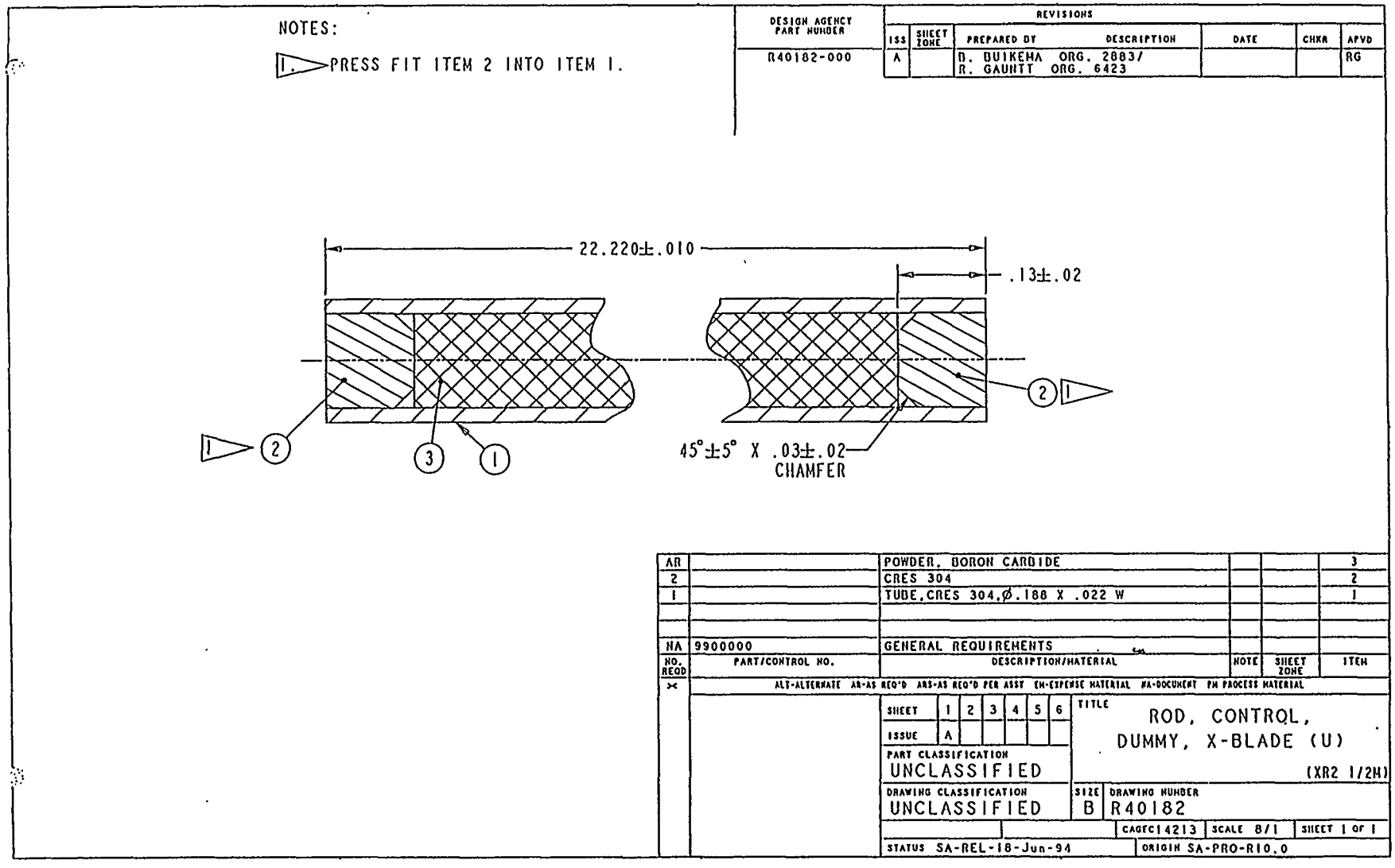

Figure E-23: Dummy Control Blade Control Rod.

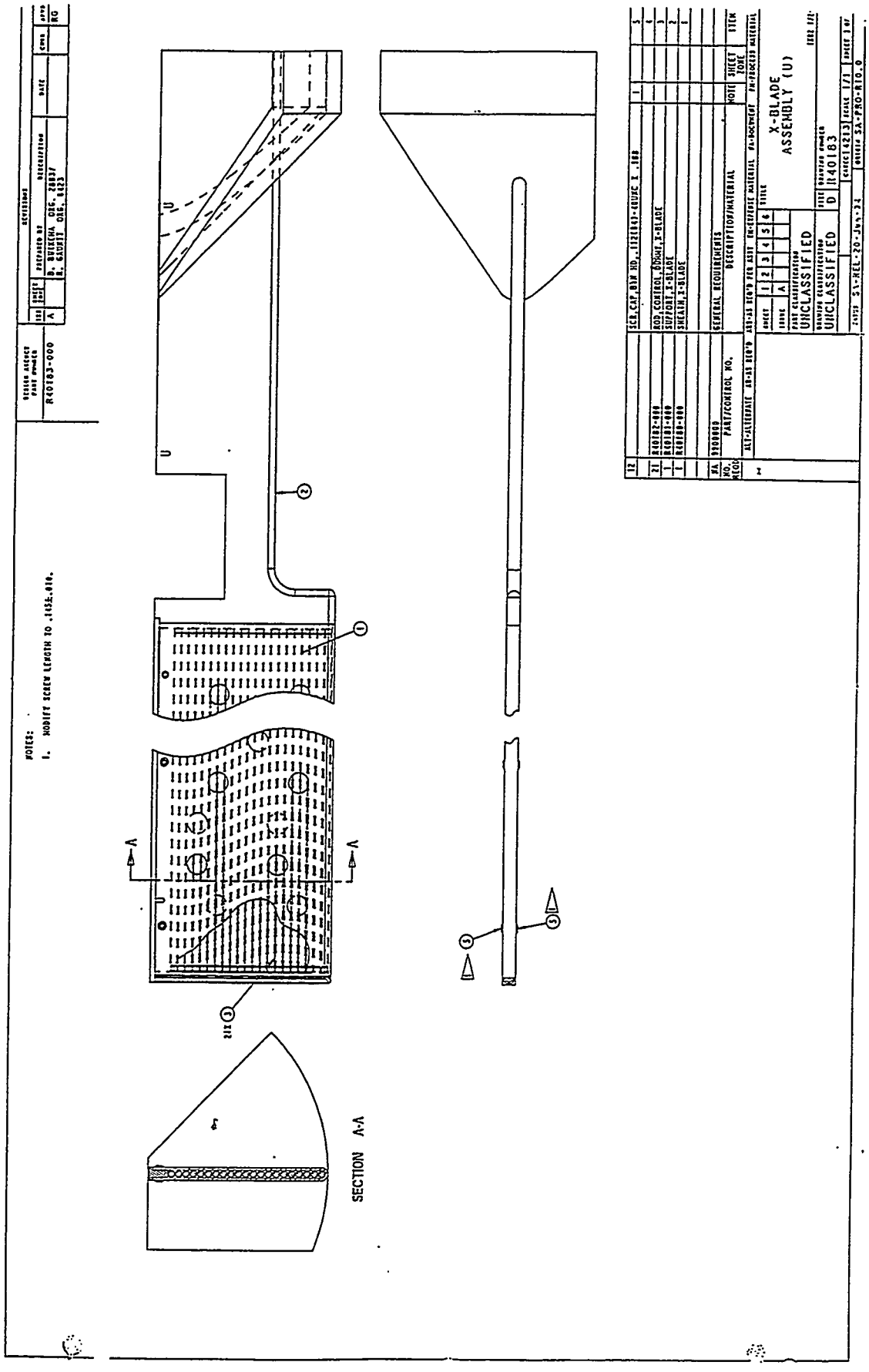

Figure E-24: Control Blade Assembly.

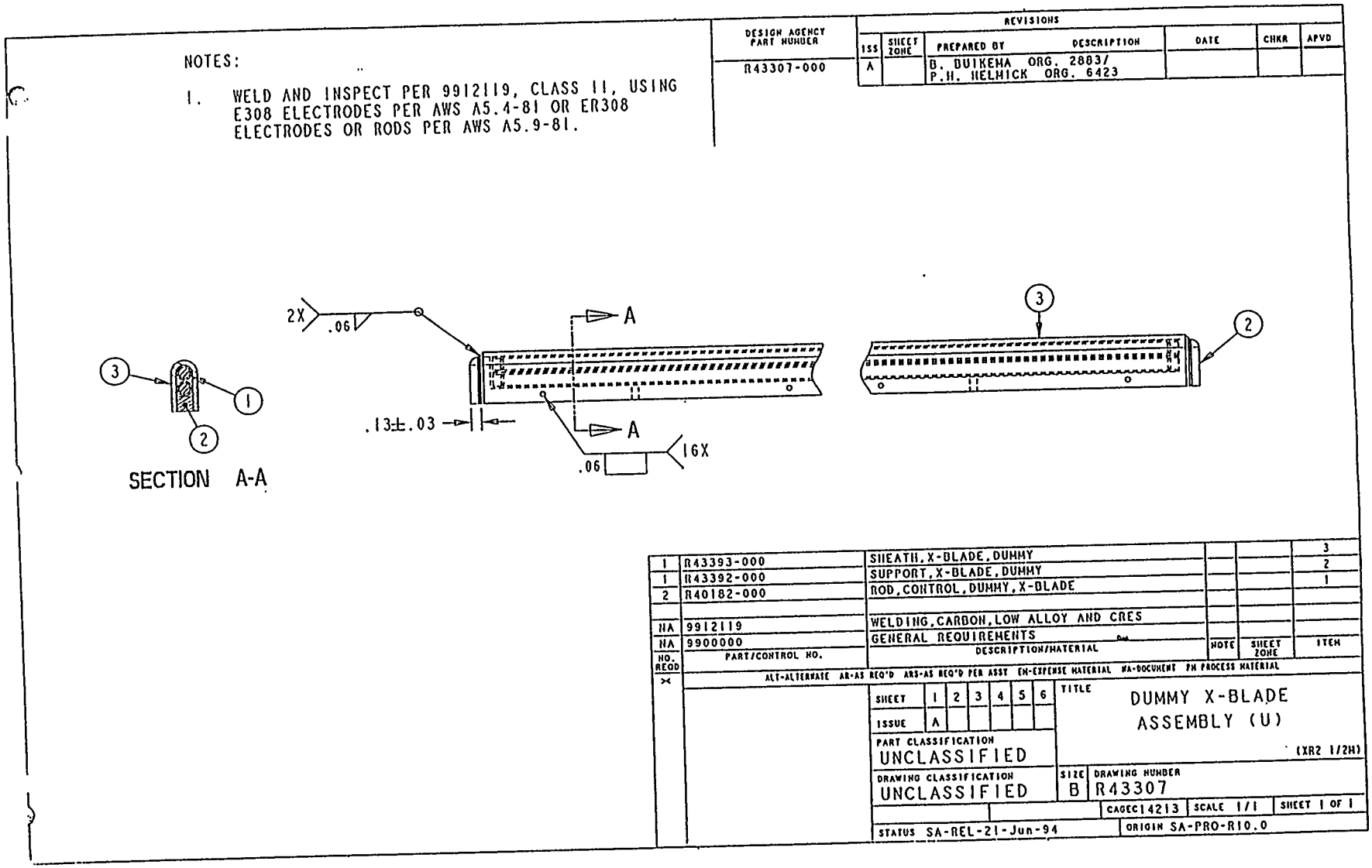

Figure E-25: Dummy Control Blade Assembly.

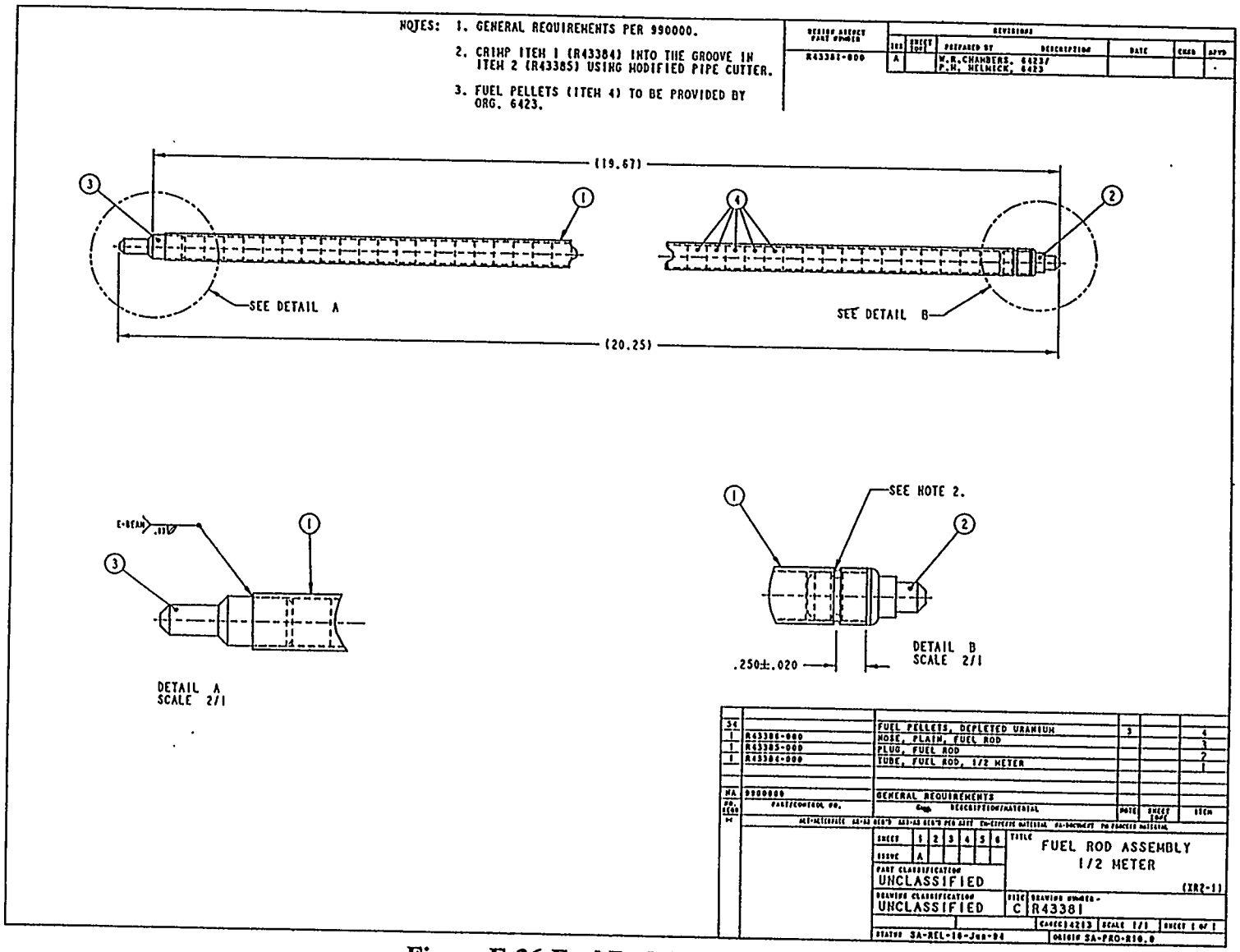

Figure E-26:Fuel Rod Assembly.

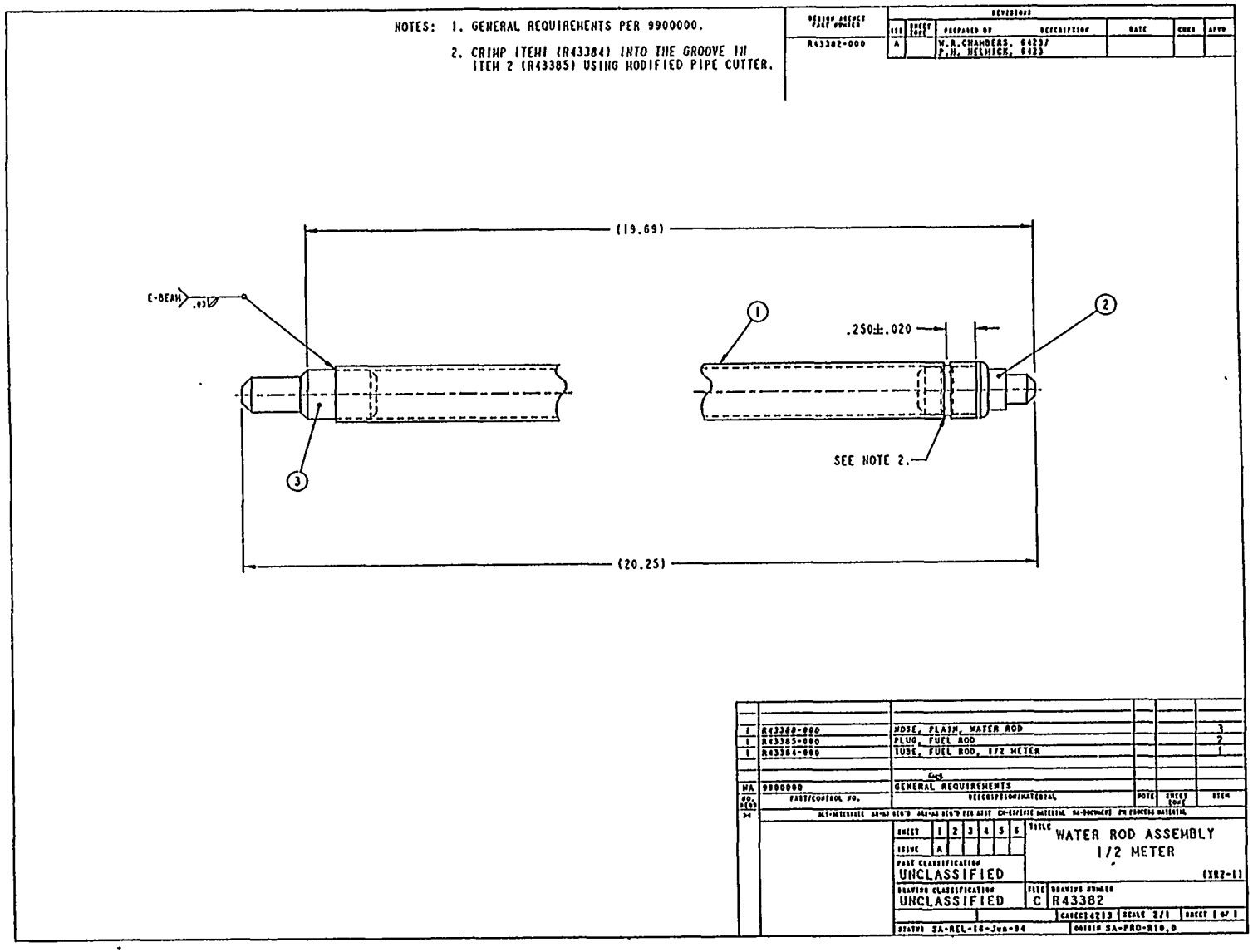

Figure E-27: Water Rod Assembly.

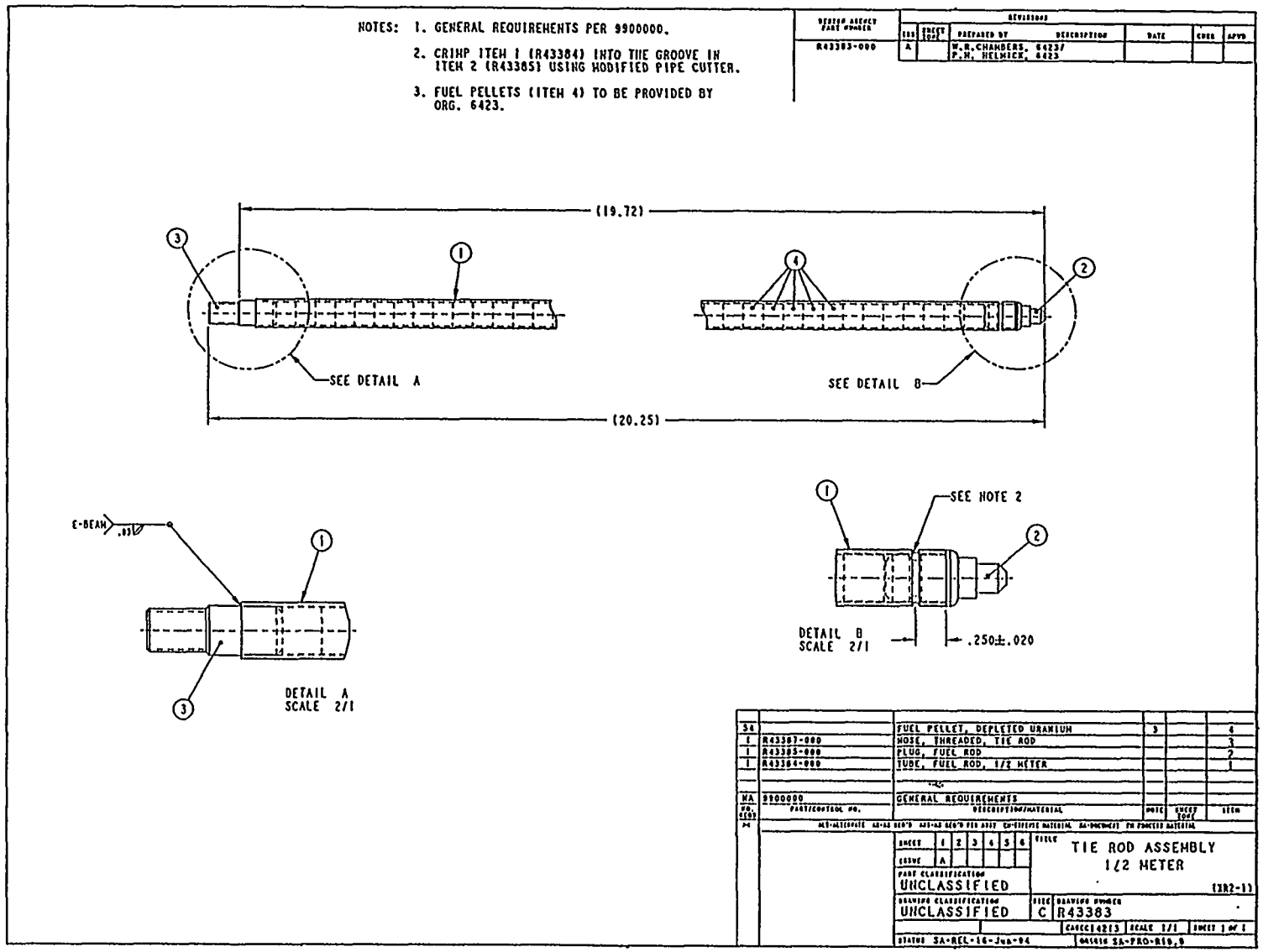

Figure E-28: Tie Rod Assembly.

NOTES: 1. GENERAL REQUIREMENTS PER 9900000.

2. MATERIAL: ZIRCALOY 2 TUBING TO BE SUPPLIED BY ORG. 6423.

DESIGN AGENCY PART NUMBER
R43384-000

REVISIONS						
ISS	SHEET ZONE	PREPARED BY	DESCRIPTION	DATE	CHKR	APVD
A		W.R CHAMBERS, 6423/ P.M. HELMICK, 6423				

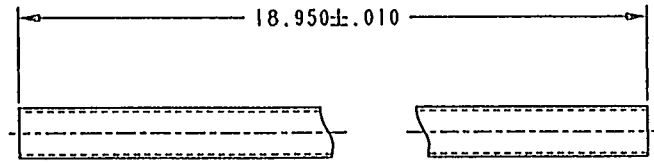

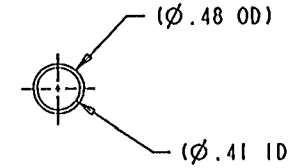

SHEET	1	2	3	4	5	6	TITLE: TUBE, FUEL ROD, 1/2 M.
ISSUE	A						
PART CLASSIFICATION: UNCLASSIFIED							(XR2-1)
DRAWING CLASSIFICATION: UNCLASSIFIED							SIZE: B; DRAWING NUMBER: R43384
							CAGEC 14213; SCALE 1/1; SHEET 1 OF 1
STATUS SA-REL-16-Jun-94							ORIGIN SA-PRO-R10.0

Figure E-29: Fuel Rod Tube.

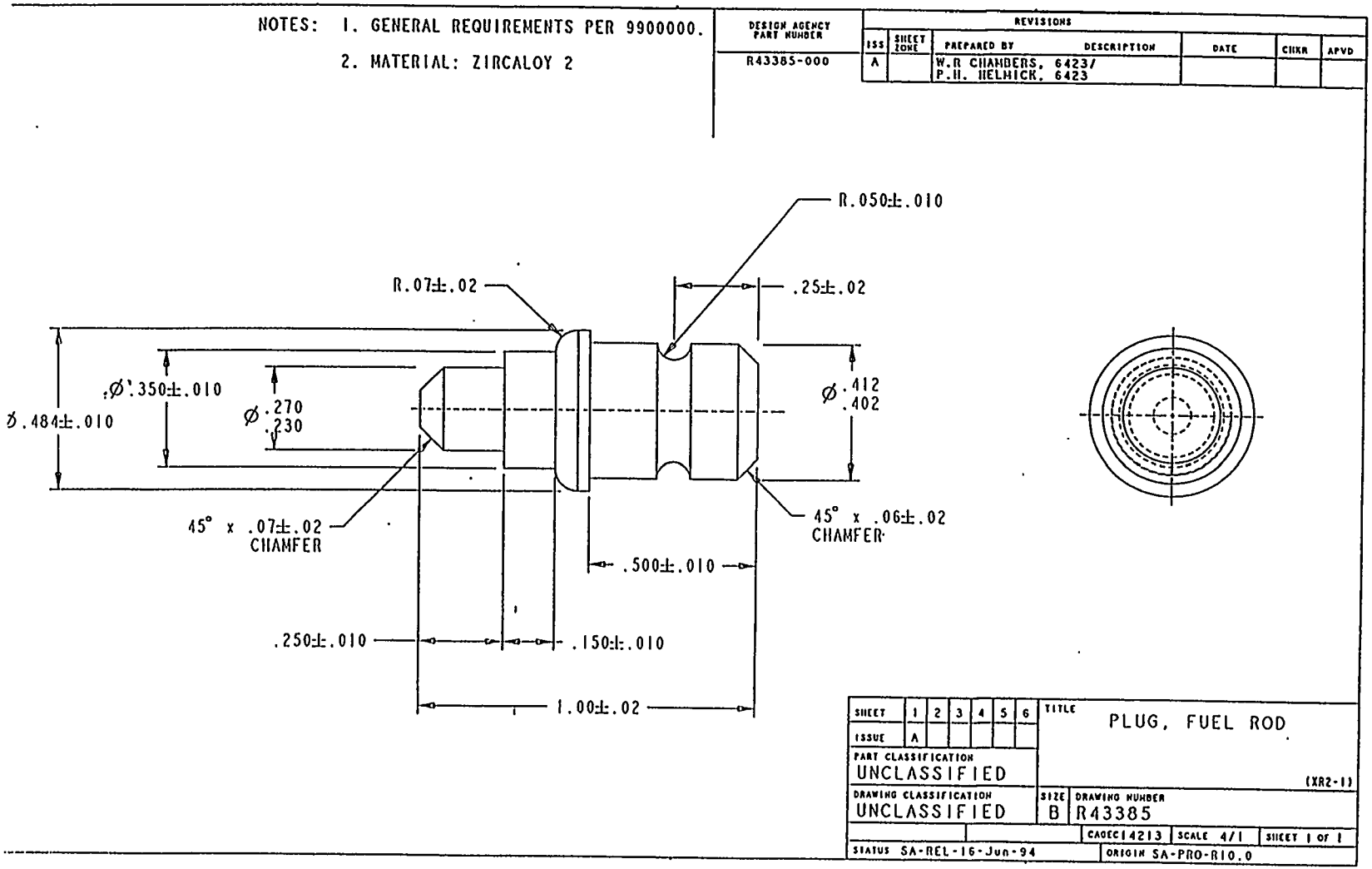

Figure E-30: Fuel Rod Plug.

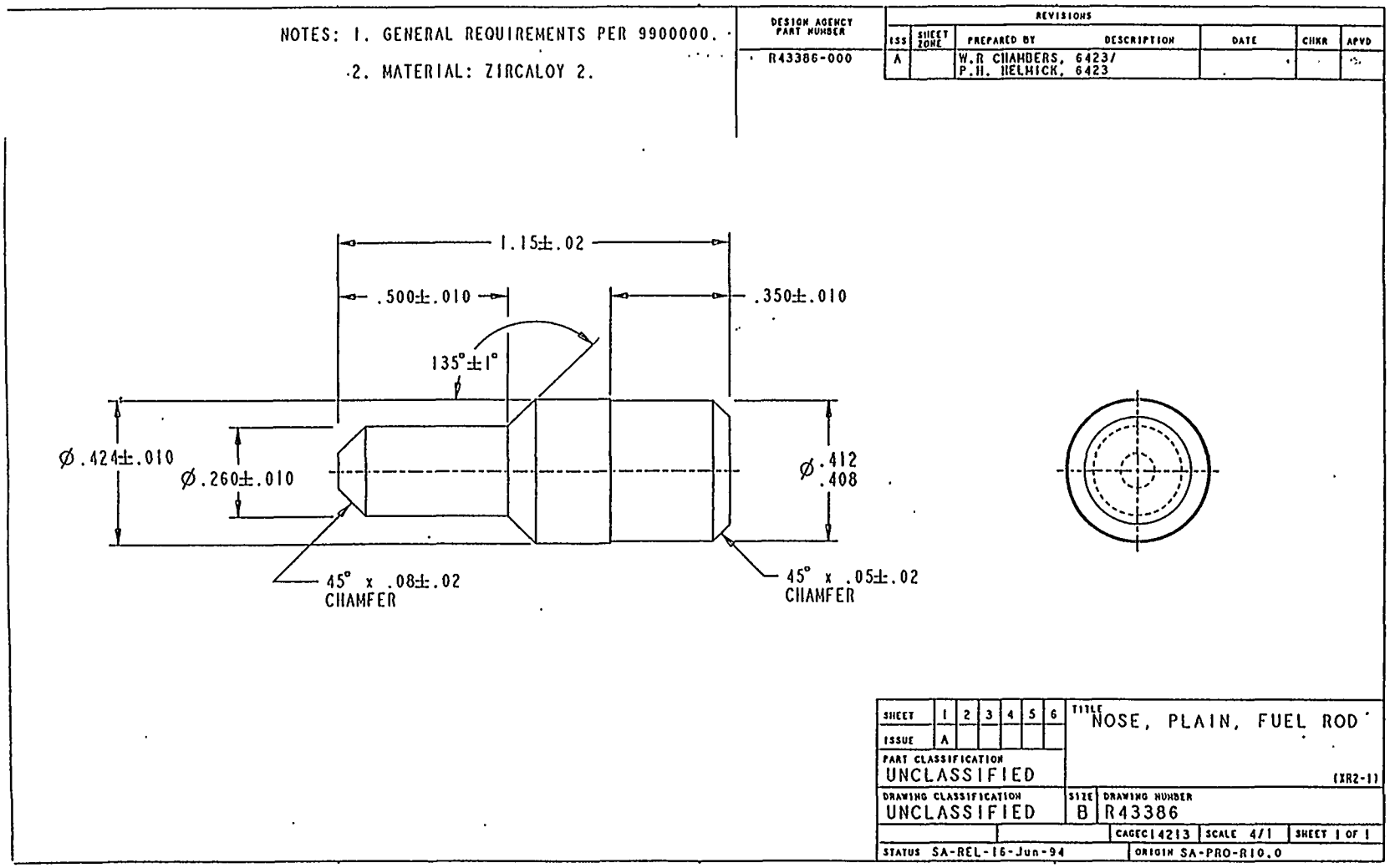

Figure E-31: Fuel Rod Nose.

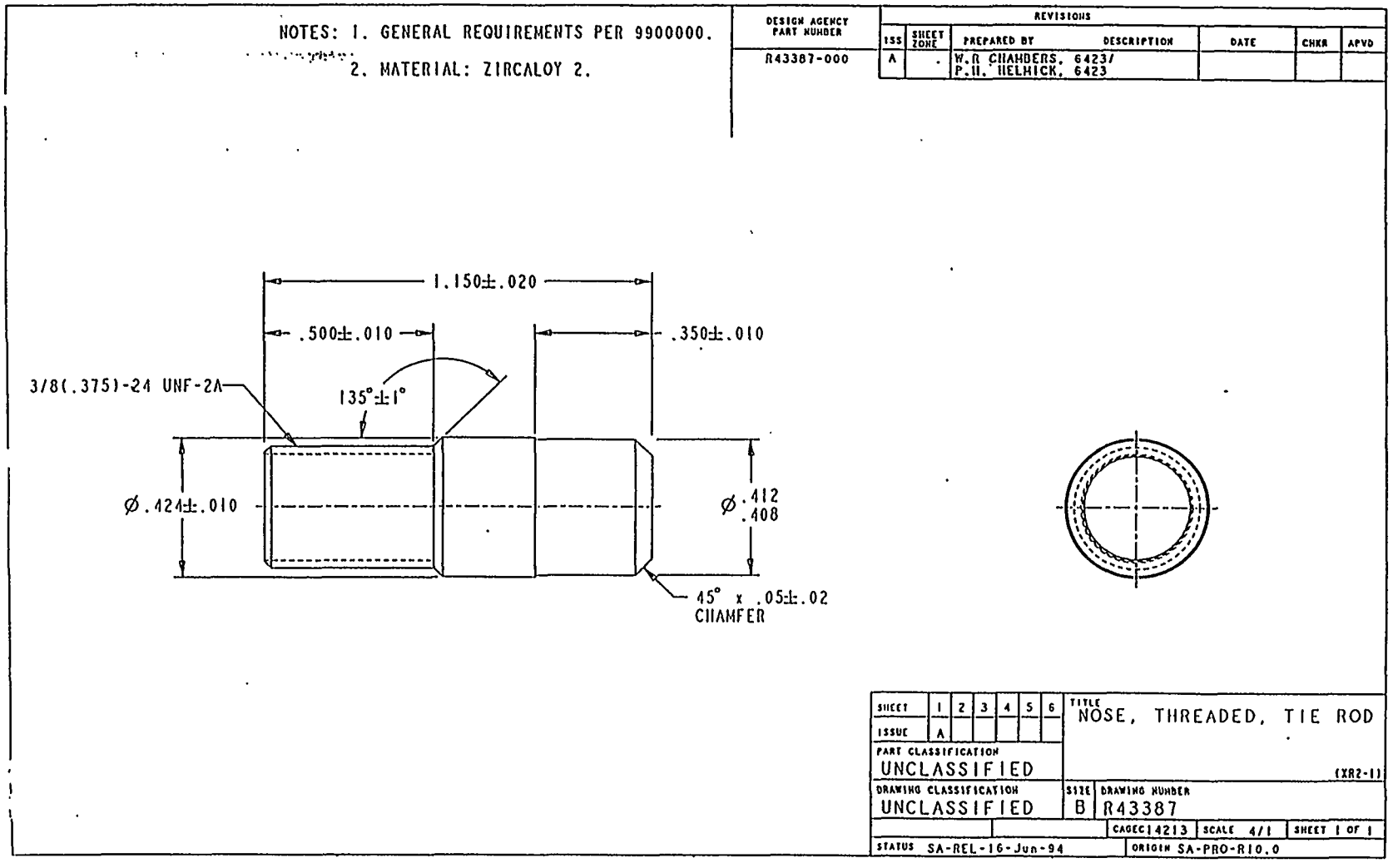

Figure E-32: Tie Rod Nose (threaded).

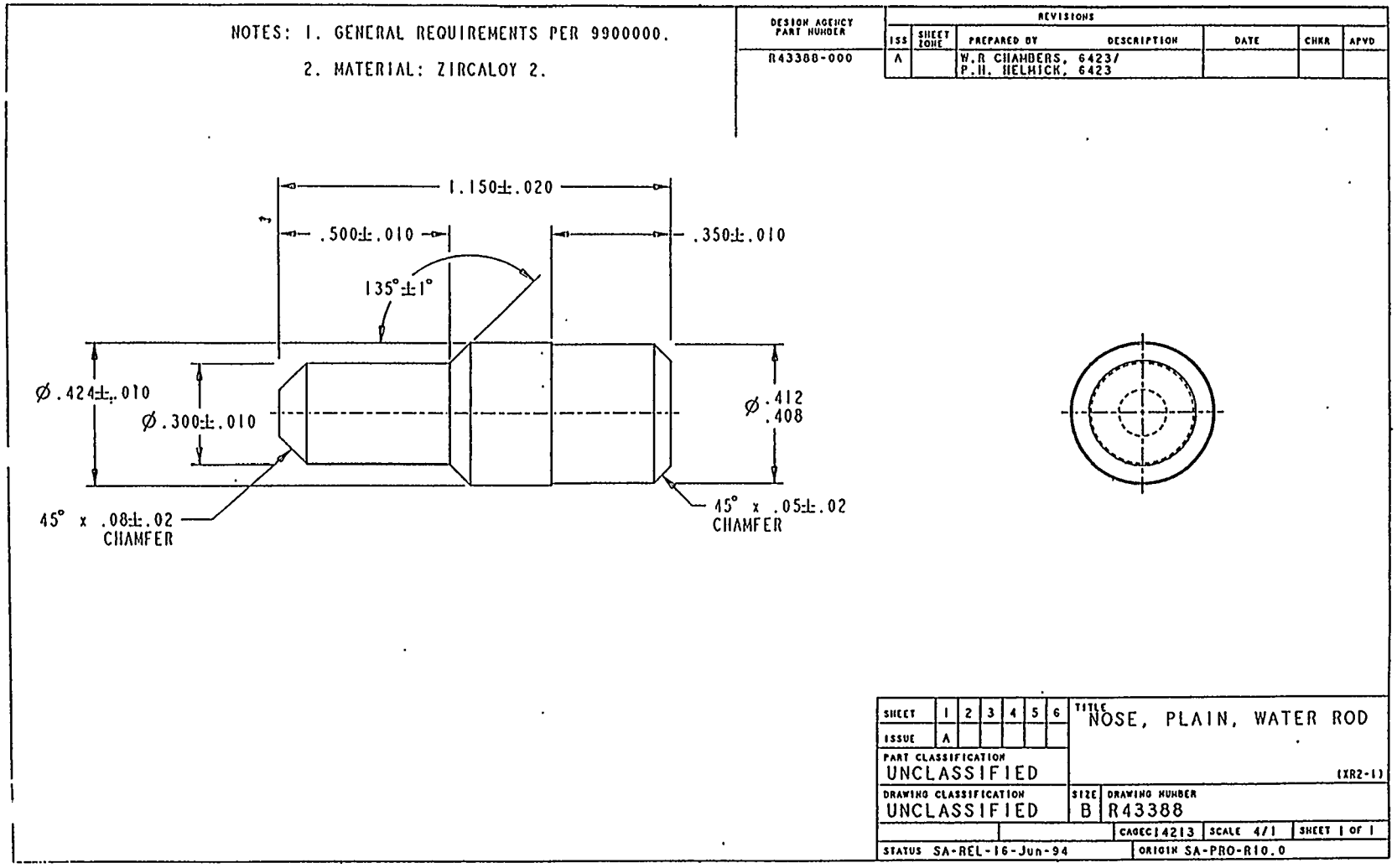

Figure E-33: Water Rod Nose.

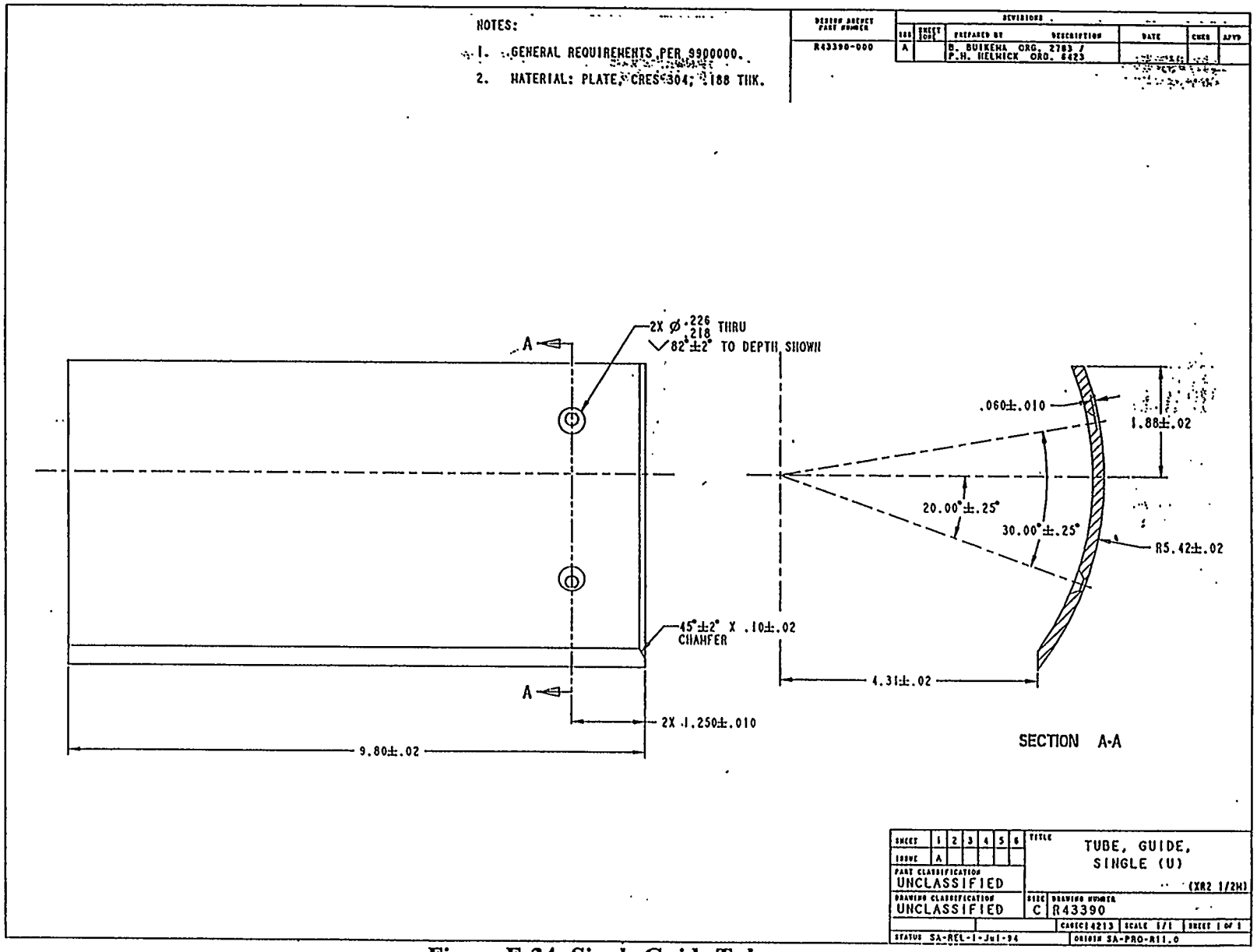

Figure E-34: Single Guide Tube.

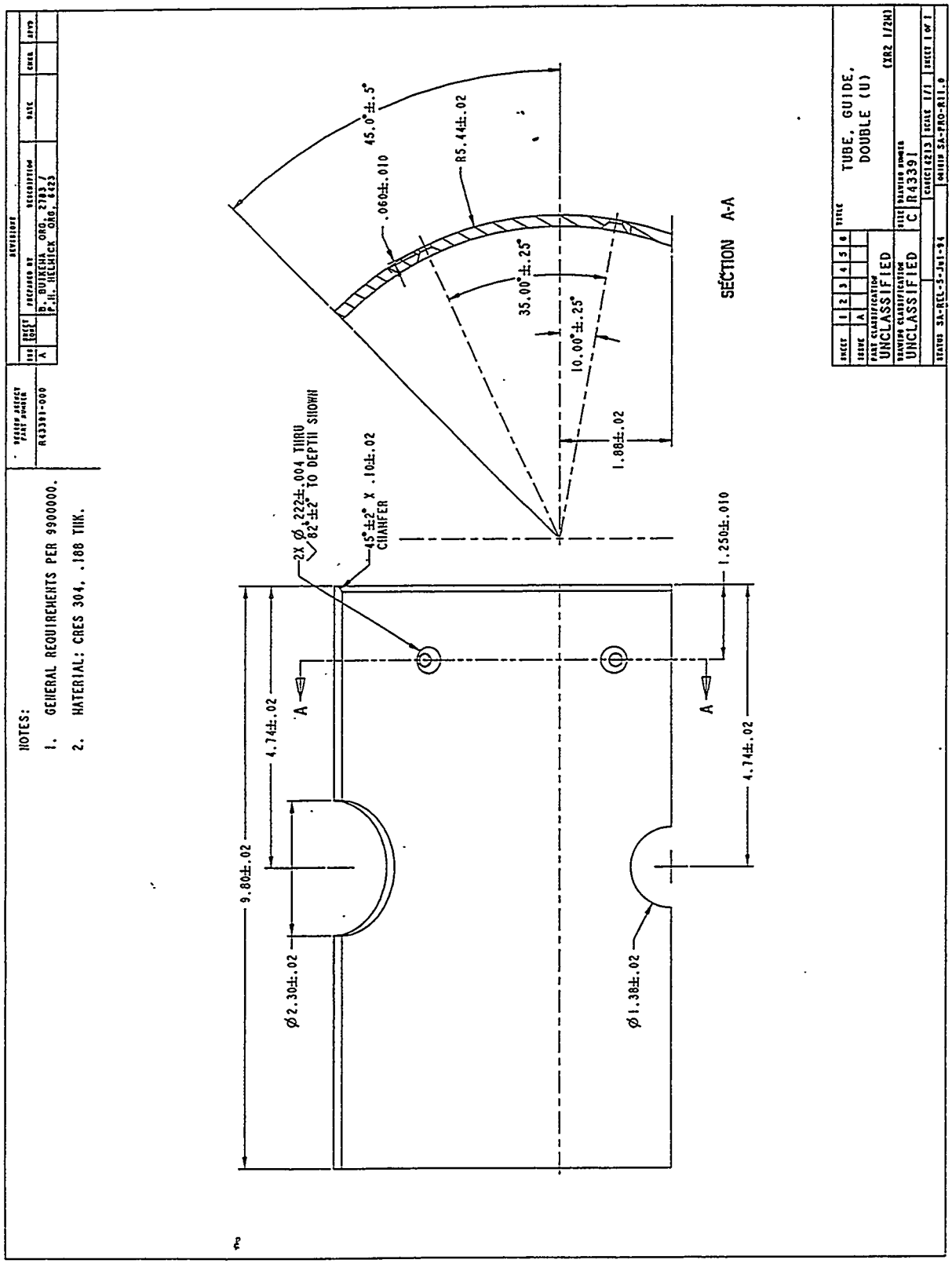

Figure E-35: Double Guide Tube.

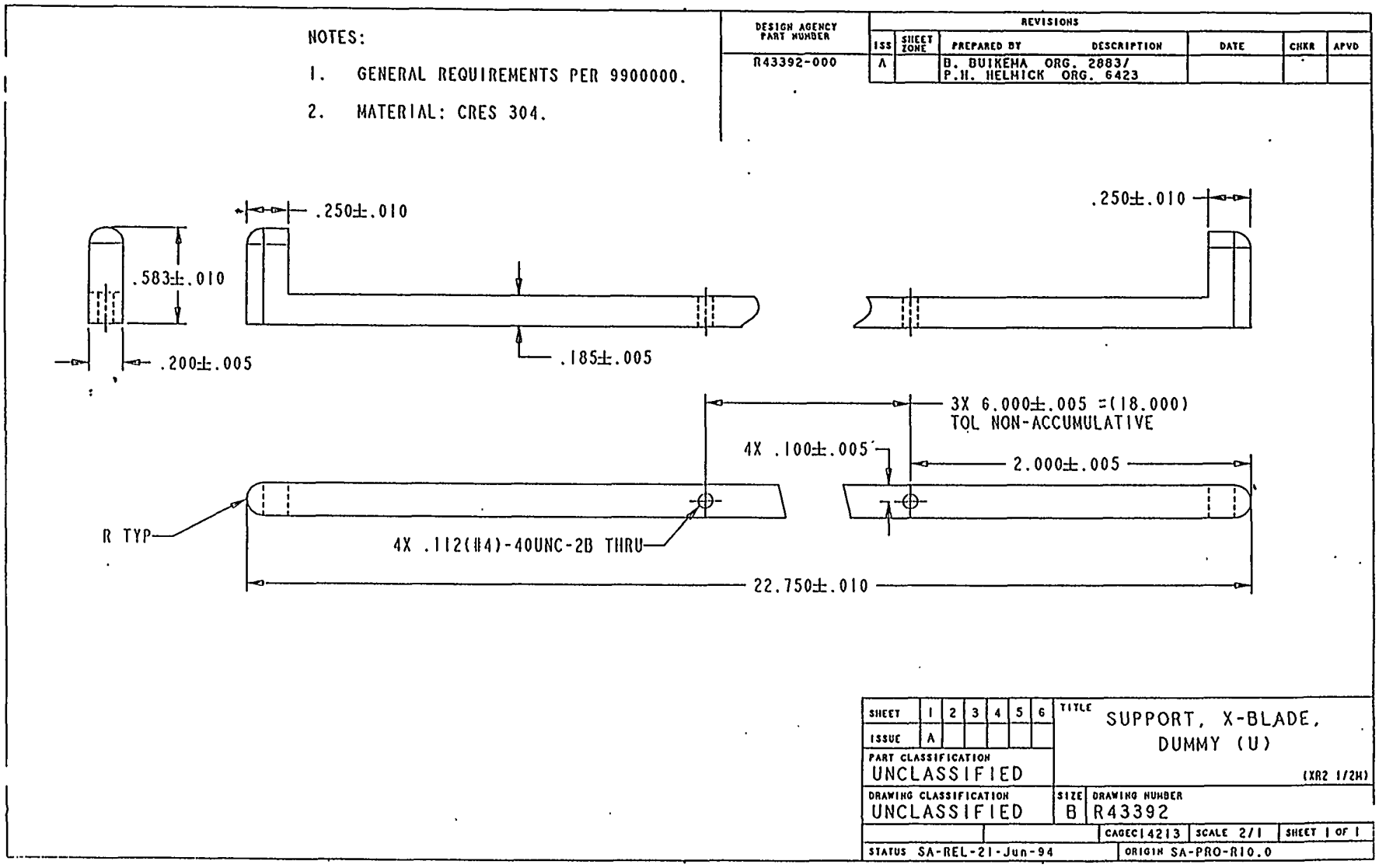

Figure E-36: Dummy Control Blade Support.

NOTES:

1. GENERAL REQUIREMENTS PER 9900000.
2. MATERIAL: SHEET, CRES 304, 16 GA (.0595).

DESIGN AGENCY PART NUMBER	REVISIONS					
	ISS	SHEET ZONE	PREPARED BY DESCRIPTION	DATE	CHKR	APVD
R43393_U	A		B. BUIKEMA ORG. 2883/ P.H. HELMICK ORG. 6423			

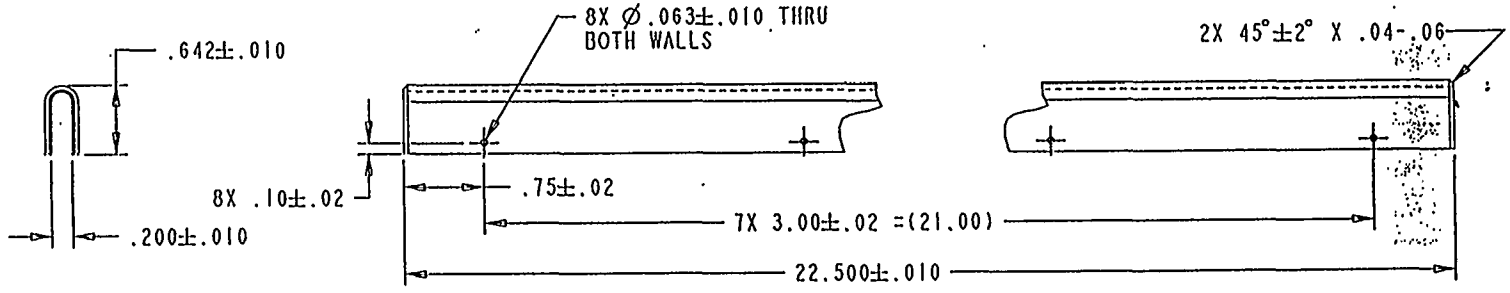

SHEET	1	2	3	4	5	6	TITLE	SHEATH, X-BLADE, DUMMY (U)
ISSUE	A							
PART CLASSIFICATION	UNCLASSIFIED							(XR2 1/2H)
DRAWING CLASSIFICATION	UNCLASSIFIED						SIZE B	DRAWING NUMBER R43393
							CAGEC 14213	SCALE 1/1 SHEET 1 OF 1
STATUS SA-REL-21-Jun-94							ORIGIN SA-PRO-R10.0	

Figure E-37: Dummy Control Blade Sheath.

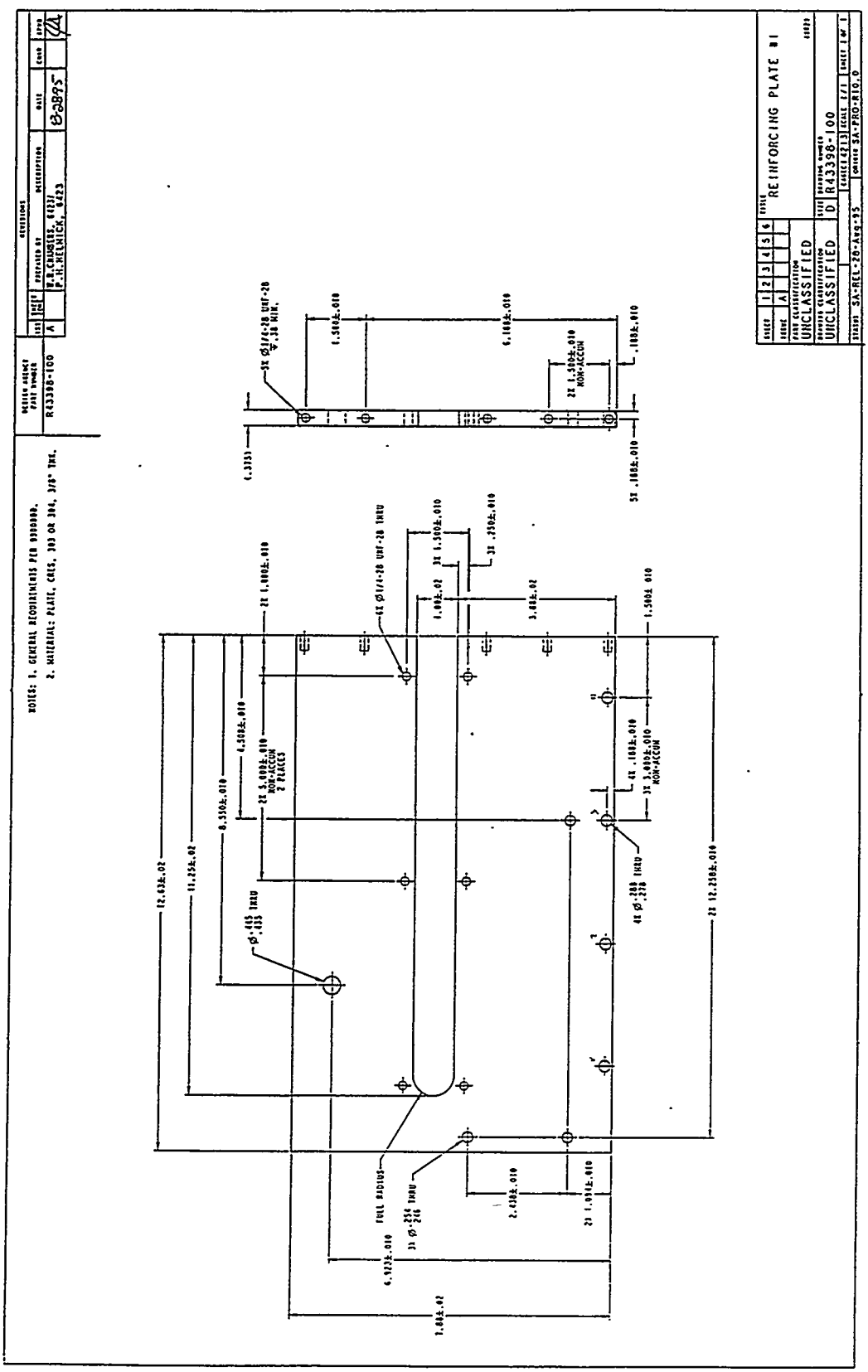

Figure E-38: Reinforcing Plate #1.

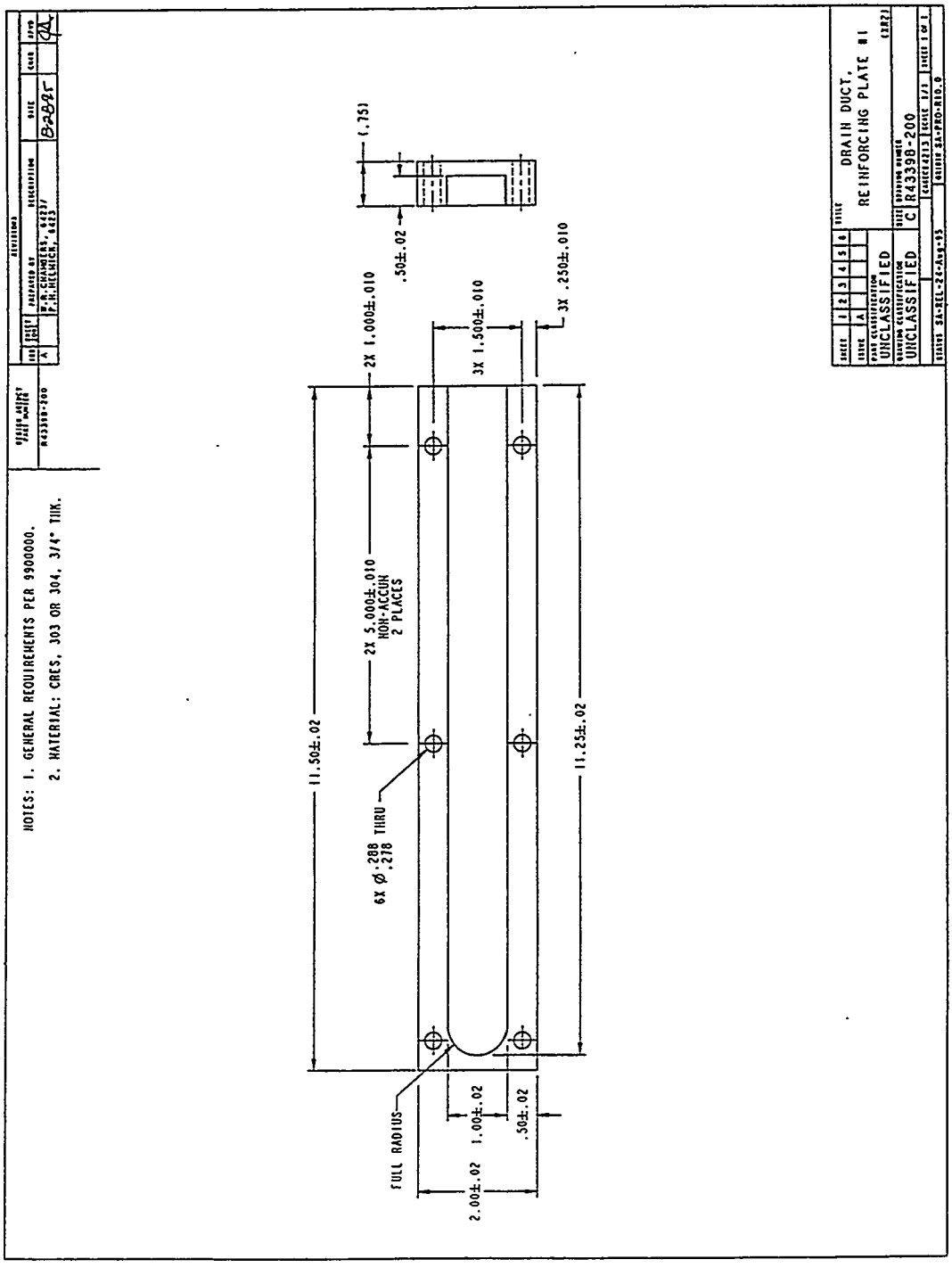

Figure E-39: Reinforcing Plate Drain Duct.

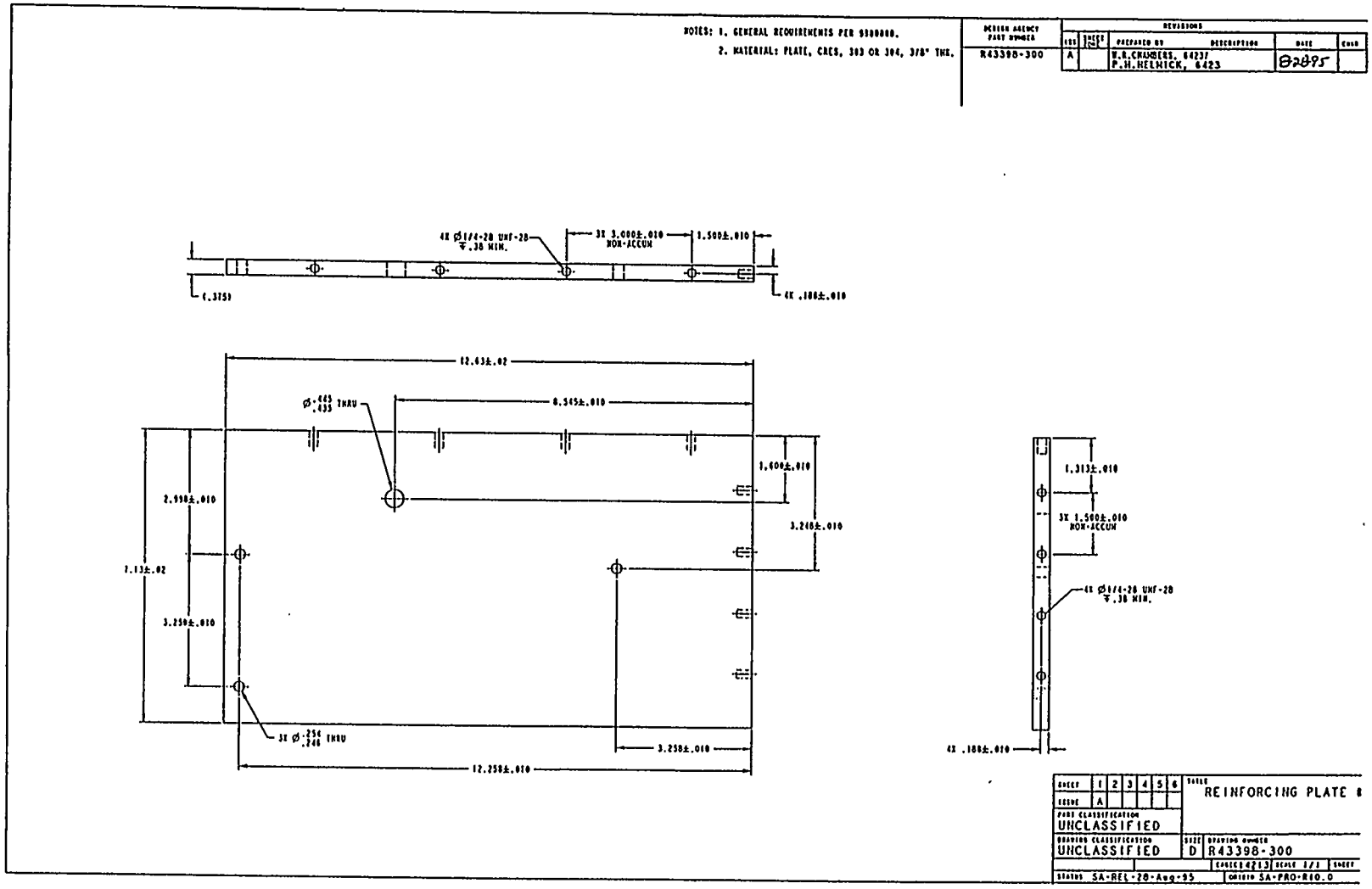

Figure E-40: Reinforcing Plate #2.

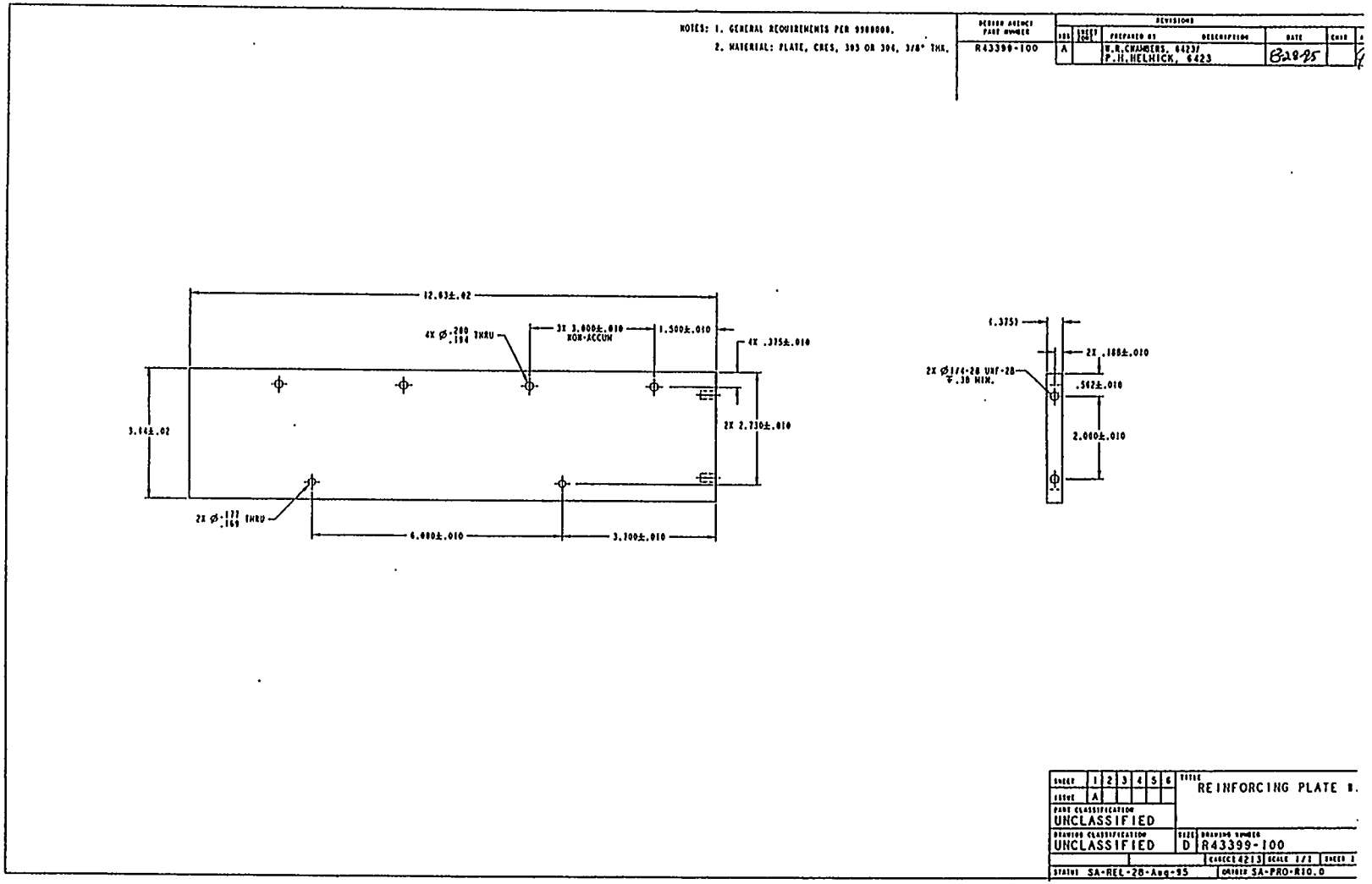

Figure E-41: Reinforcing Plate # 3.

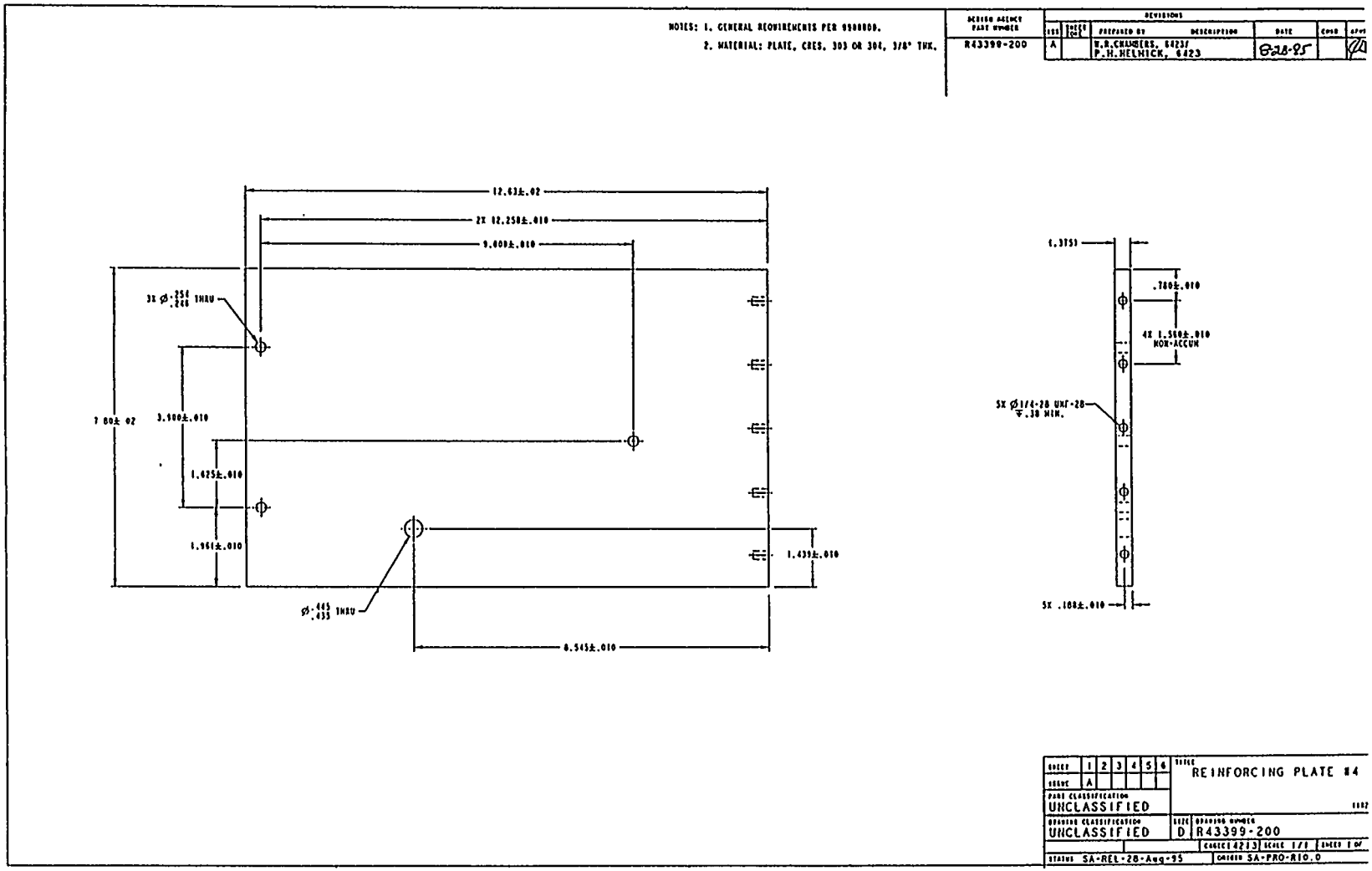

Figure E-42: Reinforcing Plate # 4.

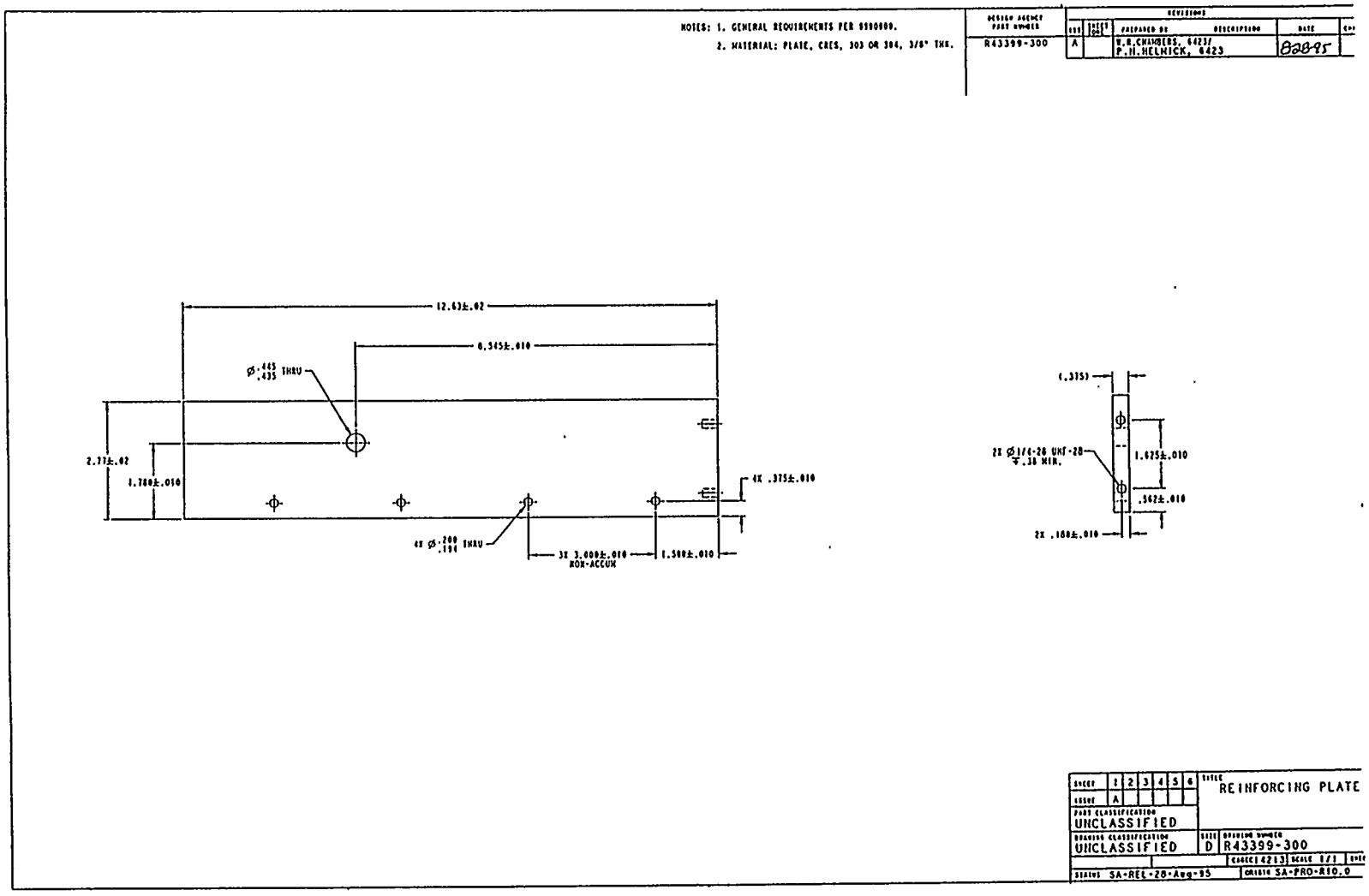

Figure E-43: Reinforcing Plate # 5.

NRC FORM 335 (2-89) NRCM 1102, 3201, 3202

U.S. NUCLEAR REGULATORY COMMISSION

BIBLIOGRAPHIC DATA SHEET

(See instructions on the reverse)

1. REPORT NUMBER (Assigned by NRC. Add Vol., Supp., Rev., and Addendum Numbers, if any.)
SAND97-1039
NUREG/CR-6527

2. TITLE AND SUBTITLE
Final Results of the XR2-1 BWR Metallic Melt Relocation Experiment

3. DATE REPORT PUBLISHED
MONTH: August
YEAR: 1997

4. FIN OR GRANT NUMBER
L1468

5. AUTHOR(S)
R. O. Gauntt, SNL

L. L. Humphries, SAIC

6. TYPE OF REPORT
Technical

7. PERIOD COVERED *(Inclusive Dates)*

8. PERFORMING ORGANIZATION – NAME AND ADDRESS *(If NRC, provide Division, Office or Region, U.S. Nuclear Regulatory Commission, and mailing address; if contractor, provide name and mailing address.)*

Sandia National Laboratories
Albuquerque, NM 87185

Science Applications International Corp.
Albuquerque, NM 87106

9. SPONSORING ORGANIZATION – NAME AND ADDRESS *(If NRC, type "Same as above"; if contractor, provide NRC Division, Office or Region, U.S. Nuclear Regulatory Commission, and mailing address.)*
Division of Systems Technology
Office of Nuclear Regulatory Research
U. S. Nuclear Regulatory Commission
Washington, D. C. 20555-0001

10. SUPPLEMENTARY NOTES
Y. Chen, NRC Project Manager

11. ABSTRACT *(200 words or less)*

This report documents the final results of the XR2-1 boiling water reactor (BWR) metallic melt relocation experiment, conducted at Sandia National Laboratories for the U.S. Nuclear Regulatory Commission. The objective of this experiment was to investigate the material relocation processes and relocation pathways in a dry BWR core following a severe nuclear reactor accident such as an unrecovered station blackout accident. The imposed test conditions (initial thermal state and the melt generation rates) simulated the conditions for the postulated accident scenario and the prototypic design of the lower core test section (in composition and in geometry) ensured that thermal masses and physical flow barriers were modeled adequately. The experiment has shown that, under dry core conditions, the metallic core materials that melt and drain from the upper core regions can drain from the core region entirely without formation of robust coherent blockages in the lower core. Temporary blockages that suspended pools of molten metal later melted, allowing the metals to continue draining downward. The test facility and instrumentation are described in detail. The test progression and results are presented and compared to MERIS code analyses.

12. KEY WORDS/DESCRIPTORS *(List words or phrases that will assist researchers in locating the report.)*
Severe Nuclear Reactor Accidents - Experiments
Unrecovered Station Blackout Accidents
Metallic Melt Relocation
Core Degradation
Melt Progression
Boiling Water Reactors (BWRs)
MERIS

13. AVAILABILITY STATEMENT
Unlimited

14. SECURITY CLASSIFICATION
(This Page) Unclassified
(This Report) Unclassified

15. NUMBER OF PAGES

16. PRICE